UNIVERSITY OF CAPE TOWN
IYUNIVESITHI YASEKAPA • UNIVERSITEIT VAN KAAPSTAD

The effect of venting configuration on the blast response of an aircraft unit load device.

Shaun Kriek
Supervisor: Prof. Genevieve Langdon
Co-supervisor: Prof. Gerald Nurick

Dissertation submitted in partial fulfilment
of the requirements for the degree

MSc (Eng)

October 2019

Blast Impact and Survivability Research Unit
Department of Mechanical Engineering
Faculty of Engineering and the Built Environment
University of Cape Town

Declaration

I hereby declare that:

(a) I know the meaning of plagiarism and declare that all the work in the document, save for that which is properly acknowledged, is my own.

(b) This dissertation has been submitted to the Turnitin module and I confirm that my supervisor has seen my report and any concerns revealed by such have been resolved with my supervisor.

Signed on 15 October 2019

.....

Shaun Kriek

This page is intentionally left blank.

Abstract

The inclusion of venting areas in aircraft unit load devices (ULDs) as a potential blast mitigation technique is investigated in this work. Damage to the ULD, such as large deflections or container rupture, from an internal explosion threatens to tear the aircraft skin and cause fuselage decompression. The loading within a luggage container was expected to be reduced when the explosive products were vented into the adjacent ULDs. Although previous work has investigated the effect of venting on ULD blast loading, this has only considered a single venting side and not multiple venting configurations. To determine if a multiple-venting system would be beneficial in ULDs, experimental blast testing was performed by subjecting a 1:6 scaled ULD box to representative blast loads with different venting configurations. The blast response of the side of the ULD which would be positioned closest to the fuselage was measured. Numerical simulations were established to provide insight into the blast loading effects not measured experimentally. The loading within the ULD box, in terms of the number and magnitude of blast wave reflections, and internal pressure build-up, was reduced when introducing venting areas. Final deformations were reduced by 11% and 22% when using a single- and double-venting configuration, respectively. Further deformation reduction was expected if more venting area was made available: unconfined blasts tests (demonstrating complete absence of ULD confinement) reduced deformations by 44%. The fully-confined (no venting) blast test resulted in rupture failure when blasted with a 20 g explosive, whereas the vented tests exhibited no tearing when blasted with higher charge masses. The double-venting configuration demonstrated better blast mitigation than the single-venting configuration. However, since both reduced the deformations and rupture probability of the container, the implementation of a multiple-venting system within aircraft ULDs would improve the survivability of the ULD container during a blast event.

This page is intentionally left blank.

Acknowledgements

I would like to extend my gratitude to the following:

My supervisor, Prof. Genevieve Langdon, for your guidance, patience and good humour, and for providing me with invaluable knowledge, advice and encouragement when I needed it.

My co-supervisor, Prof. Gerald Nurick, for sharing your tremendous insight and knowledge, and being an unrelenting source of calm reassurance.

The National Research Fund, Postgraduate Funding Office and Mechanical Engineering Department for the financial assistance needed to complete this work.

Pierre Smith and the workshop staff, especially Peter Jacobs, for manufacturing, modifying and transporting the Heavy Box.

The BISRU staff and students, for inspiring success, growth and comradery in the office and creating an environment of serious work, serious discussions and serious laughs. I would particularly like to thank Vinay Shekhar and Dr Richard Curry for your indispensable help with LS DYNA and running the simulations, and Sherlyn Gabriel for teaching me how to use DIC.

Roy Horwitz, for your solid friendship, advice and readiness to talk through work problems and everything else, and ultimately making postgrad bearable.

Kate Burling and Cai Nebe (my Cape Town family), for providing me with a pet-friendly home, many lengthy conversations, even more food, and most importantly, the opportunity to *get on with it*.

My parents and siblings, for providing me with unwavering love and support, and being impressed when I spoke about my research.

This page is intentionally left blank.

Table of Contents

This page is intentionally left blank.

List of Figures

List of Tables

6 Blast Model Development

7 Numerical Results

8 Discussion

9 Conclusions

Glossary

ALE	Arbitrary Lagrangian Eulerian
BISRU	Blast Impact and Survivability Research Unit
CJ	Chapman-Jouguet
CPU	Central Processing Unit
DIC	Digital Image Correlation
EOS	Equation of State
FC	Fully-Confined
FEM (FEA)	Finite Element Method (Finite Element Analysis)
FSI	Fluid-Structure Interaction
FV	Fully-Vented
JWL	Jones-Wilkins-Lee
MMALE	Multi-Material Arbitrary Lagrangian Eulerian
PE4	Plastic Explosive no. 4
SOD	Stand-Off Distance
TNT	Trinitrotoluene
UC	Unconfined
ULD	Unit Load Device
UTS	Ultimate Tensile Strength

This page is intentionally left blank.

Nomenclature

Roman

A	Plate area [m^2]
b	Plate width [m]; Friedlander decay coefficient
B	Plate half-width [m]
c	Speed of sound [m/s]
$C_p,\ C_v$	Specific heat at constant pressure and volume, respectively [$J/kg \cdot K$]
C_R	Reflected pressure coefficient
d	Charge diameter [m]
D	Detonation velocity [m/s]
E	Elastic/Young's modulus [Pa]; Energy per unit volume [J/m^3]
F	Force [N]
F_p	Programmed burn model
G	Shear modulus [Pa]
H	Plate thickness [m]
H^d	Heat of detonation [J/kg]
I	Impulse [$N \cdot s$]
l	Plate length [m]
L	Plate half-length [m]
m	Charge mass [kg]
M	Mach number
P	Pressure [Pa]

Q	Explosive energy [J]
r	Charge radius [m]
R	Stand-off distance [m]; Gas constant [J/kg · K]
R_n	Zhao dimensionless response number
t	Time [s]
T	Temperature [K]
v	Velocity [m/s]
V	Volume [m^3]
W	Charge mass (Hopkinson-Cranz scaling) [kg]
Z	Hopkinson-scaled distance [$m/kg^{1/3}$]

Greek

α	Johnson non-dimensional damage number
β	Plate aspect ratio; Beta burn model
Γ	Jones loading factor
γ	Ratio of specific heats
δ	Final midpoint deflection [m]
ε	Strain
$\dot{\varepsilon}$	Strain rate
ζ	Scaled venting area
λ	Blast scaling factor; Jones dimensionless initial kinetic energy
μ	Coefficient of friction; Plate mass per unit surface area [kg/m^2]
ν	Poison's ratio
ξ_0	Jones geometry parameter
ρ	Density [kg/m^3]
σ	Stress [Pa]
ϕ	Plastic hinge angle
Φ	Nurick dimensionless damage number

Johnson and Cook Parameters

A	Yield stress [Pa]
B	Strain hardening coefficient
n	Strain hardening exponent
C	Strain-rate sensitivity coefficient
m	Thermal sensitivity exponent

Jones-Wilkins-Lee Equation of State Parameters

A, B	Material-specific pressure terms [Pa]
E	Detonation energy per unit volume [J/m^3]
R_1, R_2, ω	Material-specific non-dimensional terms
V	Relative volume/density ratio

This page is intentionally left blank.

1 Introduction

Understanding the phenomenon of explosions is required for improving the survivability of structures subjected to blast loading. Investigation into the blast response of containers, such as the luggage containers onboard an aircraft, provides additional understanding of the effect on the resultant blast load when an explosive is detonated within a confined space. Furthermore, the effects of reducing the degree of confinement, by allowing the explosive products to be vented from the container – instead of building up internal pressure – can be investigated, potentially improving the container survivability. Controlled venting into the adjacent containers can possibly improve aircraft survivability and ensure passenger safety.

1.1 Background and Motivation

Although the frequency of airline bombings has reduced in the past fifty years, onboard detonations of explosives have still occurred in recent history. Figure 1.1 illustrates the number of aircraft bombing incidents occurring each year between 1967 and 2017 [1,2,3]. The motives for most aircraft bombings remain unknown: acts of terrorism account for approximately 37% of bombings, and 16% are due to fraudulent exploitation of life insurance schemes [1].

One case of an aircraft bombing disaster is the Lockerbie bombing of 1988, in which a Boeing 747 was destroyed in-flight by the successful detonation of an onboard explosive [4]. The bomb was located within the left luggage container near the front of the hold and the explosion created a large hole through the aircraft skin, resulting in decompression of the fuselage. The destruction took place above Lockerbie, Scotland and resulted in 270 fatalities, comprising all 259 occupants of the plane, and 11 people on the ground [4].

With improvised explosive devices becoming more sophisticated, explosive screening technology requires constant improvement. Even though airline security is one of the strictest in the world, it remains difficult to guarantee that no aircraft bombings will take place in the

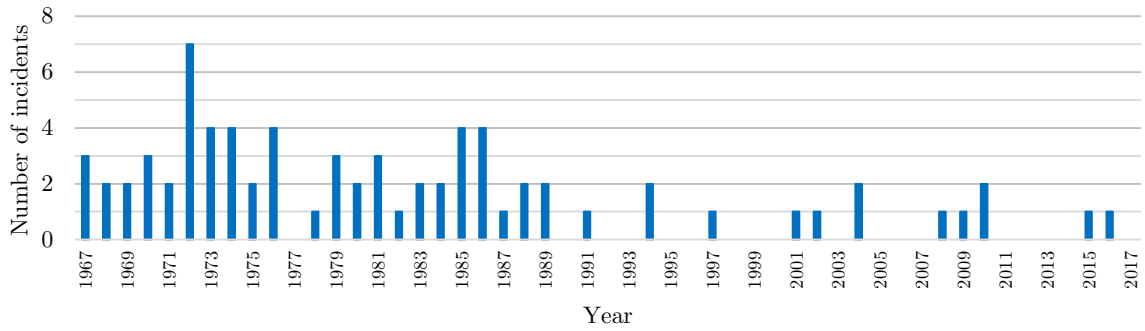

Figure 1.1: Graph of the frequency of aircraft bombing incidents from 1967 to 2017 [1,2,3].

future. It is therefore necessary to investigate the ways in which aircraft can be better designed to improve the blast survivability following an onboard explosion. One potential location of an explosive device is within a luggage container, which can cause catastrophic failure of an aircraft should the explosive gases rupture the container and tear through the fuselage skin.

A unit load device (ULD) is used to contain a large amount of luggage within a wide-bodied aircraft, and greatly reduce the number of units to be loaded onto the plane by the ground crew, making flight departures more efficient. ULDs are divided into two types: a pallet and a container, however, most commercial aircraft use container-type ULDs to store freight and passenger luggage [5]. Freight stored in containers are generally loosely packed, and the access hatch is closed by a solid door to prevent luggage from escaping. Figure 1.2 depicts the cross-section of an Airbus A300, loaded with ULD containers [6].

Figure 1.2: Photograph of Airbus A300 cross-section, with two ULD containers loaded in the lower deck [6].

The venting of an explosion into adjacent ULDs (and away from the fuselage and passengers) may mitigate the damage resulting from a detonation within the luggage container. It is expected that the venting of explosive gases will reduce the blast loading within the ULD, preventing the container from rupturing and the blast wave from tearing the fuselage skin. The diagonal side of the ULD is positioned closest to the fuselage and therefore of particular interest since rupture of this face presents the greatest risk to fuselage damage.

1.2 Objectives of the Dissertation

The main aim of this project was to determine the effect of the venting configuration (or degree of confinement) on the blast response of an aircraft unit load device. The investigation would be performed by subjecting scaled specimens with a representative geometry of a ULD, at various venting configurations, to blast loading, and assessing the resulting failure, in terms of deformation or rupture. To ensure the aim of the project was fulfilled, the following objectives were determined:

- Design and manufacture a scaled model of a ULD. The geometry must be representative of ULDs used in practice and accommodate blast testing of the box.
- Perform experimental blast testing of the ULD box with various venting configurations. Final and, where possible, transient deformation results shall be recorded for all the blast tests.
- Perform material characterisation of the target plate to assist with the material definitions used in the numerical simulations.
- Establish working numerical models, capable of simulating transient blast responses due to the different loading and venting conditions used in the experimental blast tests.
- Use the experimental and numerical blast results to elucidate the effect of charge mass and venting configuration on the loading and blast response of one of the ULD faces.

1.3 Scope and Limitations

Blast testing was performed on the scaled ULD box in the Blast Impact and Survivability Research Unit (BISRU) blast chamber, located at the University of Cape Town. The size of the ULD box was therefore influenced by the size of the blast chamber. The test setup and results were limited by the available testing equipment and measurement devices, respectively. Due to the security risks of publishing the manufacturing specifications of aircraft ULDs, the

design of the scaled ULD box was limited by the scarcity of such details available in the public domain.

Only the blast response of the diagonal side of the ULD was investigated: severe damage to this face would immediately affect the fuselage due to the proximity created by the ULD positioning. Only the effects of varying the explosive charge masses and venting configurations were investigated, with all other test parameters remaining constant. The blast load was generated using only Plastic Explosive no. 4 (PE4) material shaped into spherical charges; no other charge shape or explosive material were used. The effect of luggage capacity and the location of the explosive was not investigated; only the blast testing of empty ULD boxes with a centrally-located explosive was performed. The blast results were concerned only with the ULD box containing the explosive, and no investigation into the ULDs receiving the vented explosive products was performed.

The material of the target plate used for blast testing was restricted to one grade of locally-sourced aluminium. The thickness of the target plate remained constant. Material characterisation was performed to assess only the work-hardening effects of the aluminium, requiring only quasi-static tensile tests to be performed. The strain-rate sensitivity and influence of thermal effects were not measured experimentally, but rather obtained from published literature.

LS DYNA®, a commercial finite element analysis (FEA) package, was used to simulate the blast tests. The fluid-structure interaction between the explosive and target plate were modelled for each of the venting configurations. Only the experimentally-tested configurations were simulated numerically.

1.4 Dissertation Outline

The work presented in this project was structured to ensure the objectives of the dissertation were addressed. A review of published literature is presented in the next chapter. The literature covered includes the theory of explosions and blast waves, the laws of blast scaling, the different blast loading categories, previous blast testing of ULDs, the theoretical predictions of blast loaded quadrangular plates, the experimental blast testing of aluminium plates, and the blast testing of (confined) box structures.

Chapter 3 describes the process taken to design a ULD model suitable for blast testing. This process includes a description of the type of ULD chosen for investigation, the possible venting

configurations to be tested and the scale to which the model should be designed. The experimental methodology is also described, detailing the setup of each of the blast tests and the methodology of using high-speed cameras and Digital Image Correlation (DIC) to capture and measure the dynamic response of the target plate during the blast tests.

The fourth chapter documents the results of the experimental blast tests. The target plate final midpoint and midline deformation results are presented for each test. The transient deformation results of the successful DIC tests are also provided.

The procedure performed to characterise the material of the target plate is presented in Chapter 5. Details of the tension test setup, and the procedure to obtain the relevant material constants, are provided. The simulated tension test is included to demonstrate the numerical implementation of the material model to provide a representative material response.

Chapter 6 details the development of the numerical blast models. The material properties and equations of state, where relevant, for the air, explosive and structural components are provided. The procedure to model the interactions between the fluid and structures, as well as the contact between the structural components, is described. A mesh independence study is performed to assess the effect of mesh refinement on the simulated solutions, and to select suitable mesh resolutions for the blast models.

The numerical results are presented in Chapter 7. The evolution of the blast load is shown to demonstrate the interaction between the explosive and target plate. The transient and final deformations of the target plate for all the tests are provided, as well as the pressure history at selected points on the target plate.

Chapter 8 presents a discussion of the results from the experimental and numerical tests. The discussion includes an assessment of the tests to produce results consistent with theoretical predictions and existing experimental work. The simulated results are compared to the experimental outcomes to assess the accuracy of the numerical models. An assessment of the effect of the venting configuration on the blast response of the target plate, the practical applications of the project findings, and the limitations faced in the project are presented.

The ninth chapter documents the conclusions drawn from the work performed in this project. An assessment of the factors influencing the plate response is presented, the meeting of the project objectives is evaluated, and the application of the project outcomes is reviewed.

The final chapter lists the recommendations for further work related to the project. Suggestions are provided for the experimental testing, material characterisation and numerical modelling.

This page is intentionally left blank.

2 Literature Review

The effects of blast loading have been widely examined. An understanding of the response of various structures to blast loading is important for mitigating the damage which usually results from an explosion. Furthermore, from this understanding, structural members can be designed and appropriate materials can be selected to improve the survivability of the structure.

This review of published literature begins with simple theory of blast waves and explosive loading. The methods used to scale and predict blast loads, particularly for the application of blast testing, is investigated. The different types of blast loading and the effect of blast confinement are described. The previous design and blast testing of hardened unit load devices is studied. Finally, the blast loading of quadrangular plates is investigated with particular focus on the predicted response to dynamic loading,

2.1 Explosions and Blast Waves

An explosion is often described as the sudden release of rapidly accumulated energy. This release arises from, but is not limited to, the detonation of an explosive charge, the rupture of a pressurised vessel, or an uncontrolled high-speed nuclear reaction [7]. The accumulated energy dissipates into the surrounding medium in the form of a blast wave and impinges on any nearby structures. Understanding the behaviour and properties of the blast wave is necessary to designing structures which can withstand explosive loadings.

The detonation of a solid explosive is a stable, highly exothermic chemical reaction which moves through the explosive at the detonation velocity. This speed is supersonic and dependent on the type of explosive used. The reaction converts the solid explosive into a very dense, high-pressure gas which almost immediately occupies the small volume of the explosive. This sudden conversion becomes the source of the resultant blast wave as the explosive products rapidly expand into the surrounding medium [8].

2.1.1 Shock Wave Behaviour

The blast wave propagates as a high-intensity shock front which moves radially outwards from the explosive. This shock front initiates a pressure discontinuity: a point located near the explosion will experience a sudden rise in pressure from ambient conditions. A sudden change in density and temperature is also created in the medium behind the shock front. The change in pressure, density and temperature is dependent on the speed at which the blast wave moves. The Mach number (M) is a non-dimensional term which relates the speed of the blast wave (v) to the speed of sound (c) in the medium in which the blast wave propagates, as described in Equation 2.1.

$$M = \frac{v}{c} \tag{2.1}$$

The pressure (P), density (ρ) and temperature (T) of the fluid immediately behind the shock wave (denoted by the subscript s) are related to the ambient conditions in front of the shock wave (denoted by the subscript o) by Equations 2.2 – 2.4 [9].

$$\frac{P_s}{P_o} = 1 + \frac{2\gamma}{\gamma + 1}(M^2 - 1) \tag{2.2}$$

$$\frac{\rho_s}{\rho_o} = \frac{(\gamma + 1)M^2}{(\gamma - 1)M^2 + 2} \tag{2.3}$$

$$\frac{T_s}{T_o} = \left(\frac{P_s}{P_o}\right) \Big/ \left(\frac{\rho_s}{\rho_o}\right) = \frac{(2\gamma M^2 - \gamma + 1)[(\gamma - 1)M^2 + 2]}{(\gamma + 1)^2 M^2} \tag{2.4}$$

where: γ is the ratio of specific heats, $\frac{C_p}{C_v}$.

The properties of the fluid diminish back to ambient conditions once the blast wave passes the point of interest. As the blast wave itself moves away from the source of the explosion, it decays in pressure magnitude and velocity, and the loading it exerts increases in duration. The true pressure history of the blast wave is complex and often idealised to analyse the effect of the pressure load on structural members.

2.1.2 Friedlander Pressure Waveform

The simplified pressure history of a typical far-field blast wave at an arbitrary point is illustrated in Figure 2.1 [8,10]. Once the explosive is detonated, a blast wave is produced and travels outwards, arriving at the point of interest at the arrival time (t_a). There is a near-instantaneous pressure rise; the peak overpressure (P_s) causes loading which, in addition to the atmospheric pressure (P_o), results in the peak incident pressure (P_{so}). As the blast wave moves past the point, the pressure exponentially decreases, reaching ambient conditions at t_p. The return to ambient pressure signifies the end of the positive phase of the loading, which has a duration equal to the difference between t_p and t_a. The pressure continues to drop below the atmospheric pressure, initiating the negative phase of the loading. The pressure returns to ambient conditions once more, indicating the end of the blast load. The total blast duration is the difference between the finish time (t_f) and the arrival time.

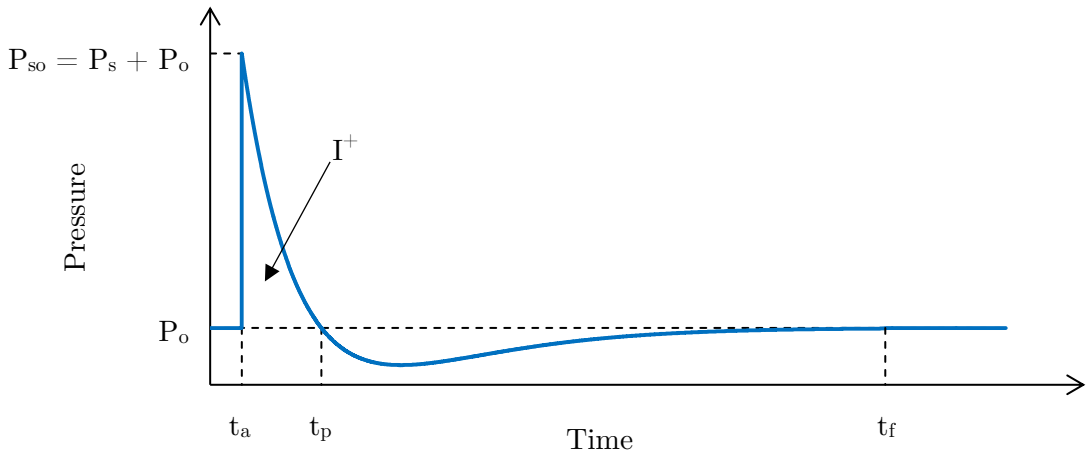

Figure 2.1: Graph of pressure vs time showing the Friedlander pressure waveform [10].

The pressure profile, taking the ambient pressure and arrival time as reference points, is described by the Friedlander equation, shown by Equation 2.5 [10].

$$P(t) = P_s \cdot e^{-\frac{bt}{t^+}}\left(1 - \frac{t}{t^+}\right) \tag{2.5}$$

where: P_s is the peak overpressure, b is a decay coefficient, and t^+ is the positive phase duration.

Equation 2.6 can be modified to include the ambient pressure condition and arrival time of the blast wave.

$$P(t) = \begin{cases} P_o & \text{for } t < t_a \\ P_s \cdot e^{-\frac{b(t-t_a)}{t^+}}\left(1 - \frac{t-t_a}{t^+}\right) + P_o & \text{for } t \geq t_a \end{cases} \tag{2.6}$$

The specific impulse (I^+), described by Equation 2.7, is calculated from the area under the positive phase of the pressure curve, as indicated in Figure 2.1, and is used as the measure of total impulse for the blast load. The effect of the ambient pressure is also removed from the impulse calculation because it is the change in pressure which causes the impulsive loading.

$$I^+ = \int_{t_a}^{t_p} (P(t) - P_o)\,\mathrm{d}t \tag{2.7}$$

For the Friedlander waveform, the specific impulse is calculated by Equation 2.8.

$$\begin{aligned} I^+ &= \int_{t_a}^{t_p} P_s \cdot e^{-\frac{b(t-t_a)}{t^+}}\left(1 - \frac{t-t_a}{t^+}\right)\mathrm{d}t \\ &= \frac{P_s t^+}{b^2}\left(b - 1 + e^{-b}\right) \end{aligned} \tag{2.8}$$

The impulse is therefore directly proportional to the peak overpressure and positive phase duration: increasing either would increase the specific impulse of the blast. A low pressure, long duration blast can produce comparable impulse to a high pressure, short duration blast.

2.1.3 Blast Wave Reflection

A blast wave reflection occurs when a blast wave interacts with the surface of a structure. The blast wave propagation and reflection are shown in Figure 2.2. As the blast wave moves radially outwards from the source, it travels towards and first impinges a surface at point A. A reflected wave is created and continues to develop as the incident wave continues to interact with the surface [9].

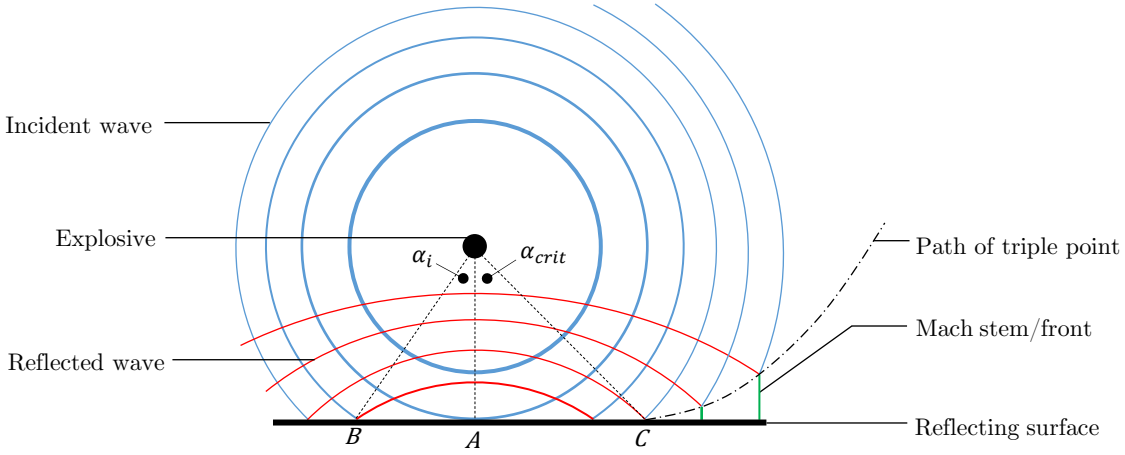

Figure 2.2: Schematic of a free air blast wave interacting with a reflecting surface [9].

The peak reflected pressure (P_{ro}) is dependent on the peak incident pressure and the angle of incidence (α_i). The angle of incidence is the angle between the blast wave velocity vector and the normal vector of the surface. The reflected pressure is larger than the incident pressure, as shown in Figure 2.3, and is the pressure for which structural members are designed [8,9].

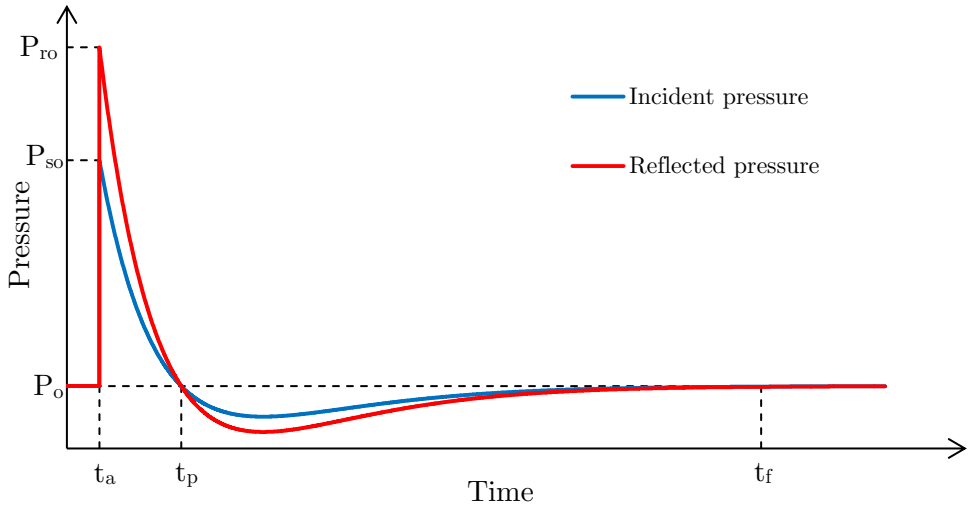

Figure 2.3: Graphs of incident and reflected pressure waveforms [9,10].

Equation 2.9 [8] defines the reflected pressure coefficient (C_R) as the ratio between the reflected overpressure (P_r) and the incident overpressure (P_s).

$$C_R = \frac{P_r}{P_s} \tag{2.9}$$

2.1.3.1 Normal Reflection

When a blast wave impinges a surface at an angle of incidence of 0°, such as at point A in Figure 2.2, a normal reflection is initiated which travels back towards the explosion source. The reflected pressure coefficient for a normal reflection is described by Equation 2.10 [9]. The reflected pressure coefficient is therefore not constant and is dependent on both the incident and atmospheric pressures.

$$C_R = 2\left(\frac{7P_o + 4P_s}{7P_o + P_s}\right) \tag{2.10}$$

Equation 2.10 implies that the C_R value varies between two and eight for low and high incident overpressures, respectively. However, experimental tests have recorded reflected pressure coefficients much greater than eight. At high pressures and temperatures, air does not behave as an ideal gas, an assumption made in the development of Equation 2.10 [8]. Figure 2.4 illustrates the increase in reflected pressure coefficient as the incident pressure increases [8].

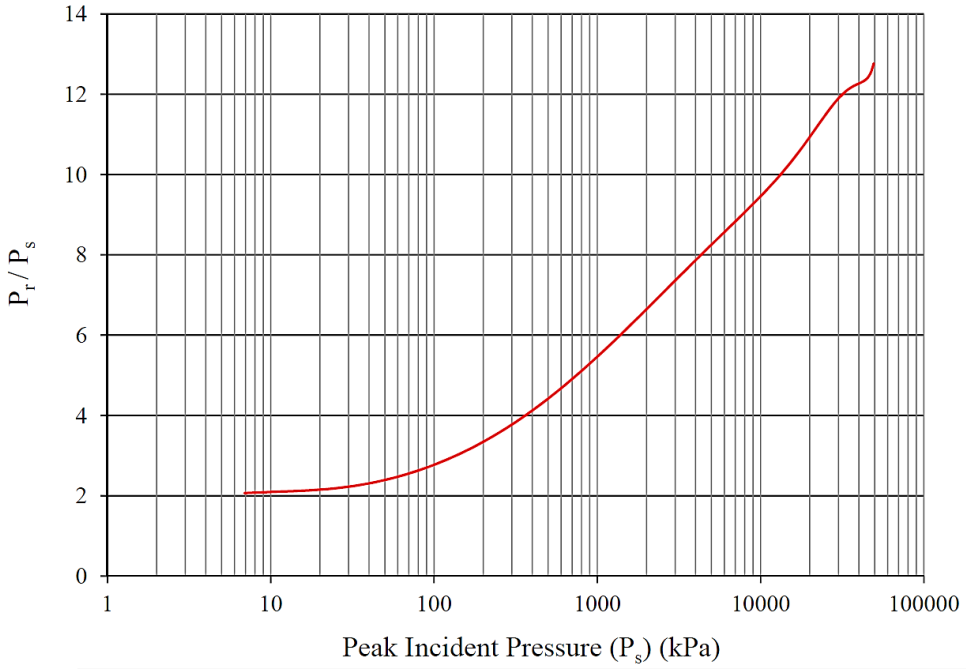

Figure 2.4: Graph of reflected pressure coefficient vs peak incident pressure for normal reflections [8].

2.1.3.2 Oblique Reflection

When a blast wave impinges a surface at any angle of incidence other than 0°, an oblique reflection occurs. An example of oblique reflection occurs at point B in Figure 2.2. The reflected pressure wave moves away from the incident wave at an angle called the reflection angle (α_r). As the incident angle increases, so too does the reflection angle [8, 9]. The reflected pressure coefficient varies for an oblique reflection, depending on the angle of incidence and the incident overpressure, as shown in Figure 2.5. Generally, the reflected pressure coefficient decreases as the incident angle increases, until a critical angle (α_{crit}) is reached, such as at point C in Figure 2.2, where the coefficient suddenly increases. This spike is the onset of a Mach reflection, where the incident and reflected waves coalesce to form a third wave known as a Mach stem, which is a region of increased pressure [10]. The point where the incident wave, reflected wave and Mach stem meet is called the triple point. The Mach stem grows as the angle of incidence exceeds the critical value forming a locus known as the triple point path. At lower overpressures (when P_s is less than 400 kPa) this increase results in an oblique reflection with magnitude greater than that of a normal reflection (where $\alpha_i = 0°$). As the angle of incidence approaches 90° the value of C_R tends to 1, indicating that the pressure experienced by the surface is equal to the incident pressure at that point.

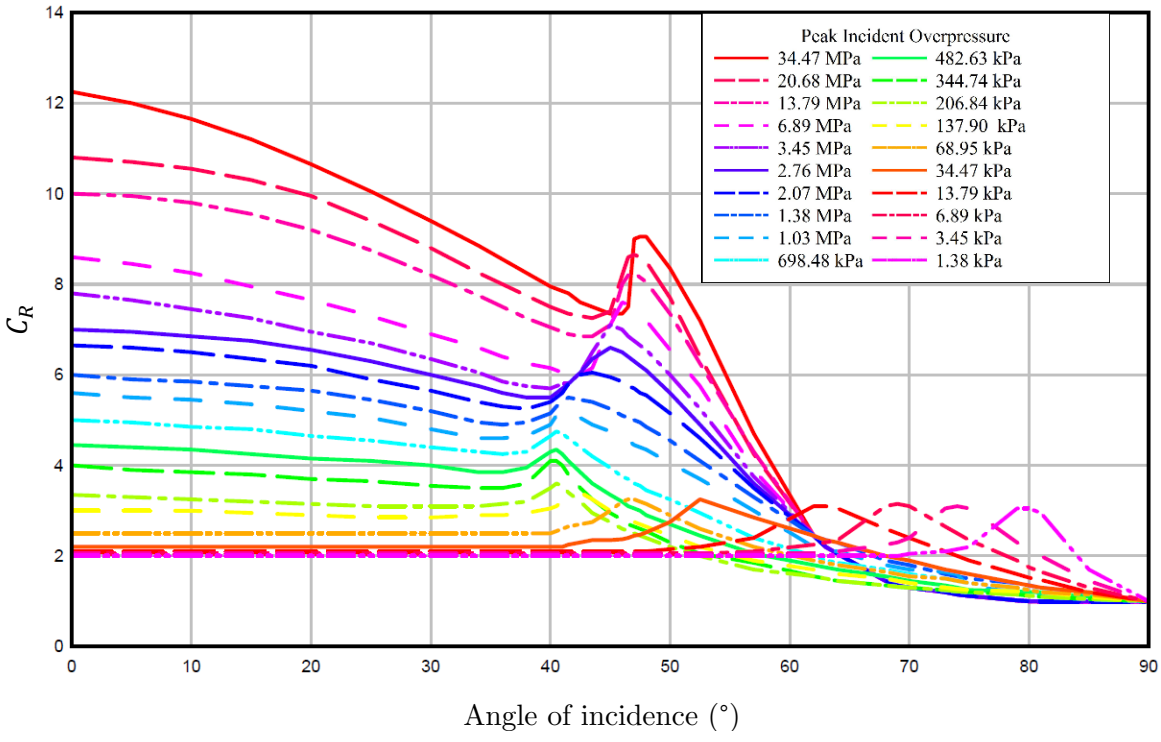

Figure 2.5: Graph of reflected pressure coefficient vs angle of incidence for peak incident overpressures [8,9].

2.2 Blast Scaling

Testing of large-scale explosions is often an undesirable endeavour due to the long set-up and preparation times. More expensive measurement instruments capable of surviving the greater impulses (due to larger explosives) are required to adequately record the results of the tests. These tests also require large spaces within which safe testing can take place. Consequently, large-scale results are usually performed outdoors, where a number of uncontrollable factors can cause variability in the results. It is therefore useful to perform scaled-down blast tests, which can then be used to predict the results of the full-scale setup on which they are based.

2.2.1 Hopkinson-Cranz Scaling Law

The most widely-used scaling law was formulated by Hopkinson [11] in 1915 and Cranz [12] in 1926, and is referred to as Hopkinson-Cranz scaling. According to this law, two explosives of scaled sizes, but of the same shape and explosive material, will produce self-similar blast waves at identically-scaled distances away from their centres [13]. Blast scaling is only meaningful if both the charge diameter and stand-off distances are scaled by the same factor.

The scaling factor (λ), as described by Equation 2.11, is the ratio of the charge diameters, d_1 and d_2, or the stand-off distances, R_1 and R_2.

$$\lambda = \frac{d_2}{d_1} = \frac{R_2}{R_1} \tag{2.11}$$

Baker et al. [13] evaluated the effect of Hopkinson-Cranz scaling. Two blast tests, of which one was a scaled version of the other, were investigated. Figure 2.6(a) illustrates the full-scale test, where the detonation of a spherical charge of diameter d produced, at a stand-off distance R, a blast wave with peak overpressure P. The pressure dissipated in magnitude over a blast duration T and resulted in a total impulse transfer i. The scaled test is shown in Figure 2.6(b), where a smaller spherical charge of diameter λd was detonated at a smaller stand-off distance λR, and produced a blast wave of peak overpressure equal to the full-scale test. However, the loading produced a shorter duration λT and smaller impulse λi. As intended by the scaling law, the overpressure remains unchanged, however, the impulse and duration are scaled according to the scaling factor. Hopkinson-Cranz scaling results in a number of blast arrangements which yield identical peak pressures, by scaling the charge size and stand-off distance. The scaled distance, in terms of a charge mass and a particular stand-off distance, is

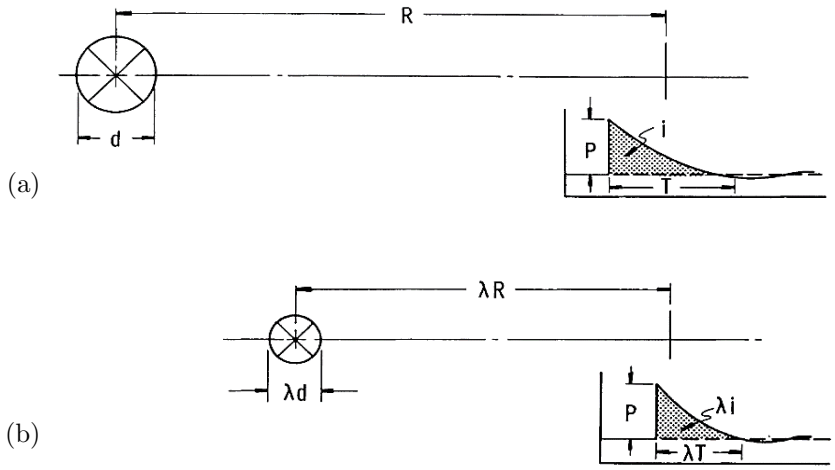

Figure 2.6: Schematic showing the effect of Hopkinson-Cranz blast wave scaling on the blast parameters of (a) full-scale and (b) scaled-down test arrangements [13].

often used to describe the blast arrangement, from which the expected pressure profile can be predicted. Due to the similar geometry of the two explosives, and in this case assuming spherical charges of the same explosive material with density ρ, the ratio of the charge masses, W_1 and W_2, is calculated as:

$$\frac{W_2}{W_1} = \frac{\frac{1}{6}\rho\pi {d_2}^3}{\frac{1}{6}\rho\pi {d_1}^3} = \left(\frac{d_2}{d_1}\right)^3 = \left(\frac{R_2}{R_1}\right)^3 \tag{2.12}$$

Re-arranging Equation 2.12 yields the scaled distance, which is constant for all scaled blasts of similar arrangements and described by Equation 2.13. Any test that is a scaled version of another will have the same scaled distance, and yield the same peak pressure. This outcome is often referred to as the Cube Root Scaling Law [14].

$$\frac{R_1}{\sqrt[3]{W_1}} = \frac{R_2}{\sqrt[3]{W_2}} = \text{constant} \tag{2.13}$$

From Equation 2.13 the equivalent charge mass, given the scaled distance, for a full-scale explosion with a similar pressure profile can be calculated. Furthermore, it is useful to define the Hopkinson-scaled distance Z such that:

$$Z = \frac{R}{\sqrt[3]{W_E}} \tag{2.14}$$

where: W_E is the TNT (Trinitrotoluene) equivalent charge mass.

Normalising the scaled distance of an explosive to TNT – a widely tested and understood explosive material – allows for better comparisons and predictions to be made, when using other types of explosives [8]. Calculating the TNT equivalent charge mass of explosives of different materials is discussed in Section 2.2.2.

Blast arrangements which have the same Z value will yield similar loading effects. This outcome is useful, not only for predicting the pressure and impulse resulting from a detonation of the same arrangement at a different scale, but for establishing informed safety measures regarding the use of explosives. For example, the Z value can be used as a guideline for the safe storage of explosive materials, as it provides an upper limit of the allowable quantity of explosive held at a storage facility. It can also provide minimum separation distances between the storehouse and other structures, such as blast testing facilities, residential houses, public buildings (hospitals, schools, etc.) and public transport routes [14].

2.2.2 TNT Equivalence

In order to calculate the blast parameters for any explosion, and considering the variety of explosive materials that currently exist, a standardised quantity is required. The majority of empirical blast test data, from which predictions can be drawn, are based on TNT explosives. TNT behaves similarly to most solid explosives and is a well-characterised explosive material [10]. As a result, an equivalent TNT charge mass is used as a universal reference when determining the blast wave characteristics of other high explosives. The equivalent TNT mass, calculated formally using Equation 2.15, is determined by scaling the charge mass of the chosen explosive using the ratio of the detonation energies of the two materials [10].

$$W_E = \frac{H_{exp}^d}{H_{TNT}^d} \cdot W_{exp} \tag{2.15}$$

where: W_E is the equivalent charge mass of TNT (kg), W_{exp} and H_{exp}^d are the charge mass (kg) and heat of detonation (J/kg) of the chosen explosive, respectively, and H_{TNT}^d is the heat of detonation of TNT (J/kg).

However, only some of the chemical energy stored in the explosive is released during detonation; most of the energy is slowly released during the combustion of the explosive products in the surrounding medium [10]. Subsequently, the equivalent charge mass calculated in Equation 2.15 may not necessarily produce the same blast wave parameters as those of the

Table 2.1: TNT equivalence of C4 explosive.

Explosive	TNT equivalence factor		
	Peak pressure [10]	**Impulse** [10]	**Detonation energy** [8]
Composition C4	1.37	1.19	1.13

chosen explosive. Table 2.1 lists the TNT equivalence factors for C4 based on an equivalent peak pressure, impulse and detonation energy.

2.2.3 Peak Overpressure Prediction Models

A number of equations have been developed to predict the blast response which results from the detonation of an explosive. The following equations are based on the Hopkinson-scaled distance Z (in $\mathrm{m/kg^{1/3}}$) of the blast arrangement to provide an estimation of the peak overpressure P_s (in kPa).

Brode [15] developed a model based on near field (for P_s greater than 1000 kPa) and medium to far field (for P_s between 10 kPa and 1000 kPa) cases. Equation 2.16 is used to calculate the overpressure for blasts within these two ranges.

$$P_s = \begin{cases} \dfrac{670}{Z^3} + 100 & \text{for } P_s > 1000\ \text{kPa} \\ \dfrac{97.5}{Z} + \dfrac{145.5}{Z^2} + \dfrac{585}{Z^3} - 1.9 & \text{for } 10 < P_s < 1000\ \text{kPa} \end{cases} \tag{2.16}$$

Newmark and Hansen [16] proposed a single formulation independent of detonation severity to predict the overpressure, as described by Equation 2.17.

$$P_s = \frac{678.4}{Z^3} + \sqrt{\frac{86490}{Z^3}} \tag{2.17}$$

Henrych [17] suggested three equations, each based on a range of scaled distances.

$$P_s = \begin{cases} \dfrac{1407.2}{Z} + \dfrac{554}{Z^2} - \dfrac{35.7}{Z^3} + \dfrac{0.625}{Z^4} & \text{for } 0.05 \le Z < 0.3\ \mathrm{m/kg^{1/3}} \\ \dfrac{619.4}{Z} - \dfrac{32.6}{Z^2} + \dfrac{213.2}{Z^3} & \text{for } 0.3 \le Z < 1\ \mathrm{m/kg^{1/3}} \\ \dfrac{66.2}{Z} + \dfrac{405}{Z^2} + \dfrac{328.8}{Z^3} & \text{for } 1 \le Z < 10\ \mathrm{m/kg^{1/3}} \end{cases} \tag{2.18}$$

Kinney and Graham [7] presented a formula, described by Equation 2.19, which determined the peak overpressure based on the atmospheric pressure P_o of the test.

$$P_s = P_o \cdot \frac{808\left[1+\left(\frac{Z}{4.5}\right)^2\right]}{\sqrt{\left[1+\left(\frac{Z}{0.048}\right)^2\right]\left[1+\left(\frac{Z}{0.32}\right)^2\right]\left[1+\left(\frac{Z}{1.35}\right)^2\right]}} \tag{2.19}$$

Mills [18] put forward a simpler expression, described by Equation 2.20, for calculating the peak overpressure.

$$P_s = \frac{108}{Z} + \frac{114}{Z^2} + \frac{1772}{Z^3} \tag{2.20}$$

Figure 2.7 is compiled from the prediction models presented in this section, comparing each of the peak overpressure estimates. All the curves, except for that developed by Mills, correspond well for scaled distances between 0.8 and 10 m/kg$^{1/3}$. Those suggested by Brode and Newmark diverge at smaller scaled distances, whereas the curves proposed by Henrych and Kinney show stable estimates over the entire range of presented scaled distances.

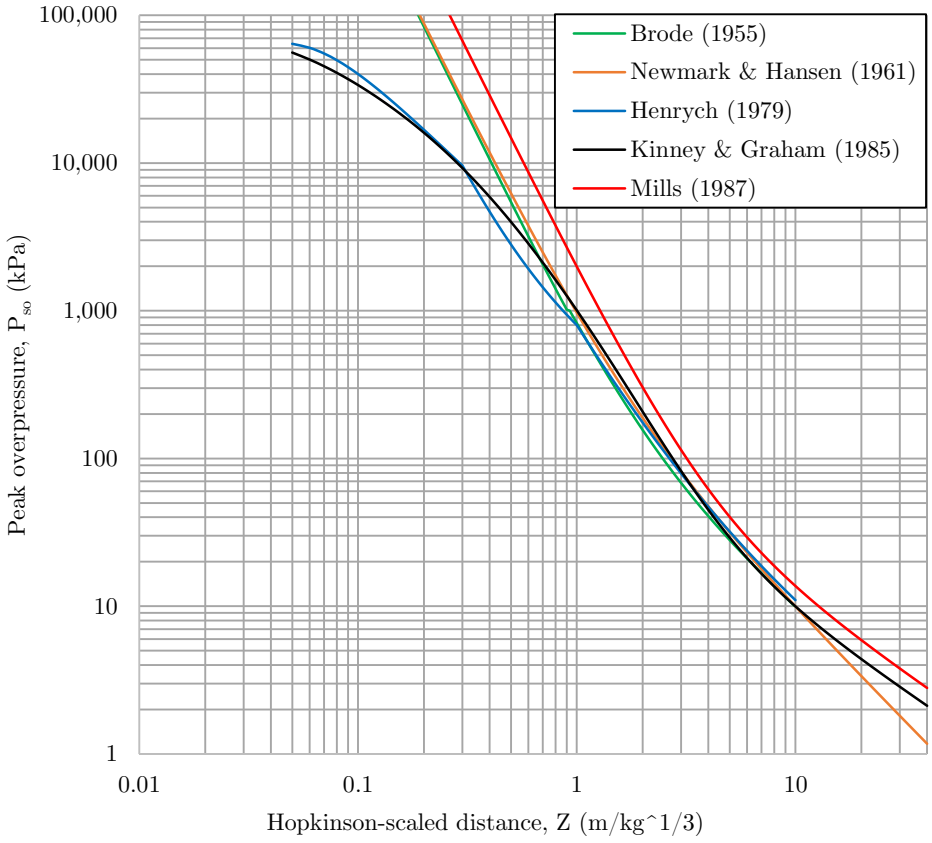

Figure 2.7: Prediction models for peak overpressure based on Hopkinson-scaled distance.

2.3 Blast Loading Categories

The type of blast loads that are exerted on structures are grouped into two categories: unconfined and confined explosions. Within these two groups are further divisions depending on the type of loading produced on the structure, which is based on the location of the explosive, the effect of any reflected blast waves and the configuration of the target structure.

2.3.1 Unconfined Blasts

An unconfined explosion is due to the detonation of an explosive charge located outside of the structure. Upon impingement, the blast wave is not affected by any prior interaction with the structure. The blast wave is only affected by the surrounding medium through which it travels and/or interactions with the ground surface. The type of unconfined blast is dependent on the location of the explosive charge relative to the ground and target structure, as illustrated in Figure 2.8 and explained in the following sections.

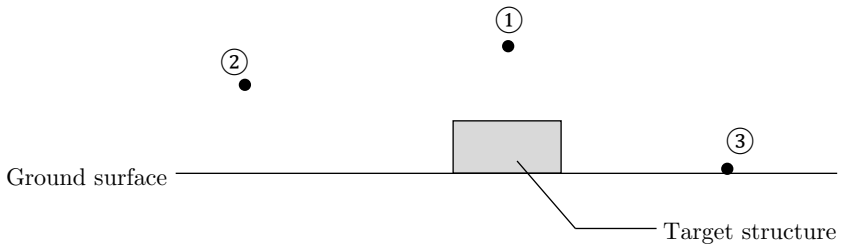

Figure 2.8: Location of explosive charges for three different types of unconfined blasts (1) free air burst, (2) air burst, and (3) surface burst.

2.3.1.1 Free Air Bursts

A free air burst occurs when an explosive is located above the target surface, or high enough above the ground, such that, when the explosive is detonated, the resulting blast wave strikes the surface without first interacting with the ground [8]. Since no wave reflections occur prior to impingement, the incident wave is unamplified when it strikes the surface.

2.3.1.2 Air Bursts

An explosive will create an air burst if it is placed away from the target structure and above the ground such that the blast wave is first reflected off the ground before it impinges the target structure. Due to the interaction with the ground, a Mach front is produced (as

described in Section 2.1.3.2) which travels towards the structure as a plane wave and impinges the structure with a uniform pressure (provided the height of the Mach stem is greater than the height of the structure) [8]. The incident wave acting on the surface is an amplification of the blast wave produced by the explosive.

2.3.1.3 Surface Bursts

When an explosive is detonated on or near the ground, the incidence wave is immediately amplified by the reflections off the ground. The resulting surface burst creates a single, hemispherical blast wave which is similar in nature to a Mach front [8]. The blast loading due to a surface burst is more severe than that of an air burst.

2.3.2 Confined Blasts

When an explosive is detonated within a structure or container, the resulting explosion is called a confined blast. The container can vary in confinement: fully-confined (with very little to no venting), partially-confined (with small openings to the atmosphere) and fully-vented (with large openings or faces open to the atmosphere). Figure 2.9 illustrates these three degrees of confinement.

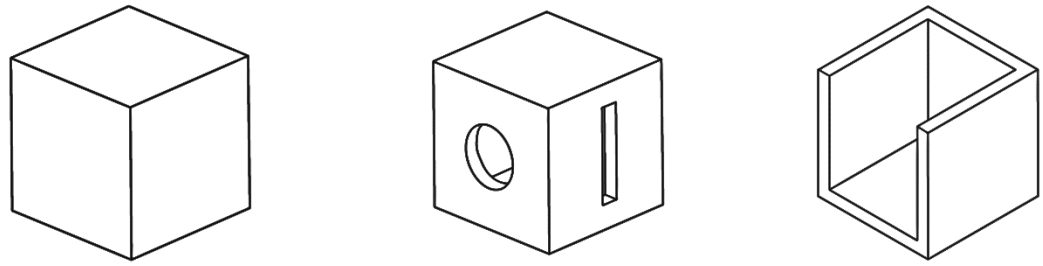

Figure 2.9: Cubicles of varying confinement (a) fully-confined, (b) partially-confined, and (c) fully-vented [8,32].

There are two types of loads that are created within the container when the explosive is detonated, with the severity of both being dependent on the degree of confinement. The first load is the short duration, high magnitude blast pressures exerted on the walls of the structure. The initial pressure wave is amplified by a reflection off the internal walls, which in turn exerts further high-amplitude reflections on the structure. The magnitude of the blast pressure diminishes quickly as the shock wave energy dissipates [8]. The second load is the rise in gas pressures within the confined structure resulting from the high temperature air and explosion

by-products due to the heat energy released by the detonation and afterburning reactions [8]. The peak gas pressure is much smaller than the peak blast pressure, but it is the duration of the gas pressure (t_g) compared to the duration of the reflected shock load (t_s) which determines the overall significant loading on the structure. The duration of these loads is affected by the degree of confinement, or the amount of venting, of the container. Keenan and Tancreto [19] developed a scaled venting area, denoted in Equation 2.21 as ζ, by normalising the amount of venting with the size of the container.

$$\zeta = \frac{A_v}{V^{\frac{2}{3}}} \tag{2.21}$$

where: A_v is the total venting area and V is the free volume within the container.

Keenan and Tancreto [19] investigated the blast environment of partially-confined and fully-vented cubicles and determined a critical value of the scaled venting area which indicated the transition between the two tested degrees of confinement. Table 2.2 summarises the blast and geometric requirements for the different confined blast cases.

Table 2.2: Definition of degree of confinement in terms of load durations and scaled venting area [19].

	Fully-confined	**Partially-confined**	**Fully-vented**
Load durations	$t_g \gg t_s$	$t_g > t_s$	$t_g \leq t_s$
Scaled venting area	$0.0 \leq \zeta < 0.001$	$0.001 \leq \zeta < 0.6$	$\zeta \geq 0.6$

Note: t_g refers to the duration of the internal gas pressure load and t_s refers to the duration of the shock loads.

2.3.2.1 Fully-Confined Blasts

At total (or near total) containment of an explosion within a structure, neither the shock waves nor the gas pressures are able to vent out to the atmosphere. Although the loading of the reflected blast pressure still decays quickly due to the energy attenuation of the shock waves, the gas pressures produce a very long duration loading on the structure. Kingery et al. [20] performed a number of tests to determine the internal pressure within containers with full and partial confinement. Figure 2.10 shows the resulting internal pressure history within a fully-confined cubicle.

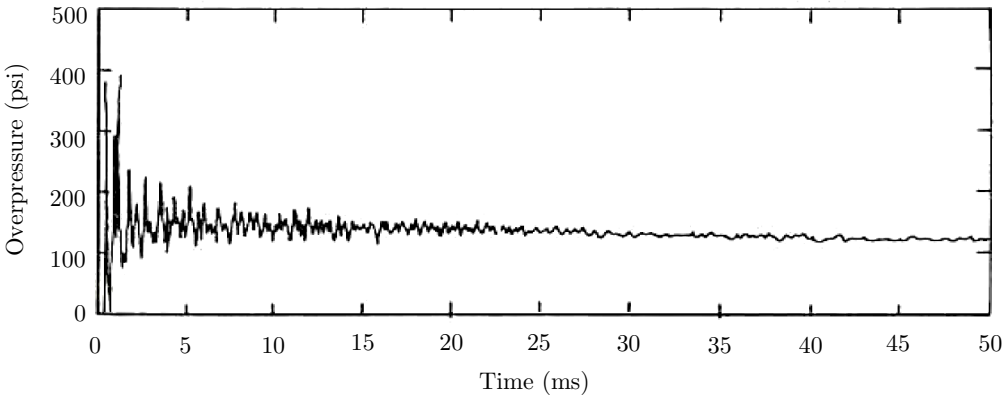

Figure 2.10: Graph of internal pressure vs time for a fully-confined cubicle [20].

The reflected blast pressures dominated the loading soon after detonation but diminished quickly. The total loading did not, however, disappear as the gas pressures exerted a much longer duration loading on the structure. Since there was no (or very little) venting present, the gas pressures exerted an almost constant loading on the structure, and slowly decreased as the internal temperature reduced (or the gas pressure slowly leaked out of the container).

2.3.2.2 Partially-Confined Blasts

When an explosive is detonated within a partially-confined container, there is limited venting of both the reflected shock wave and gas pressures. The degree of venting determines the significance of the gas pressure loading, however, for partially-confined blasts the venting area must be such that the duration of the gas pressure loading is greater than the duration of the shock wave loading [19]. Figure 2.11 shows the measured internal pressure history of a partially-confined cubicle, as tested by Kingery et al. [20].

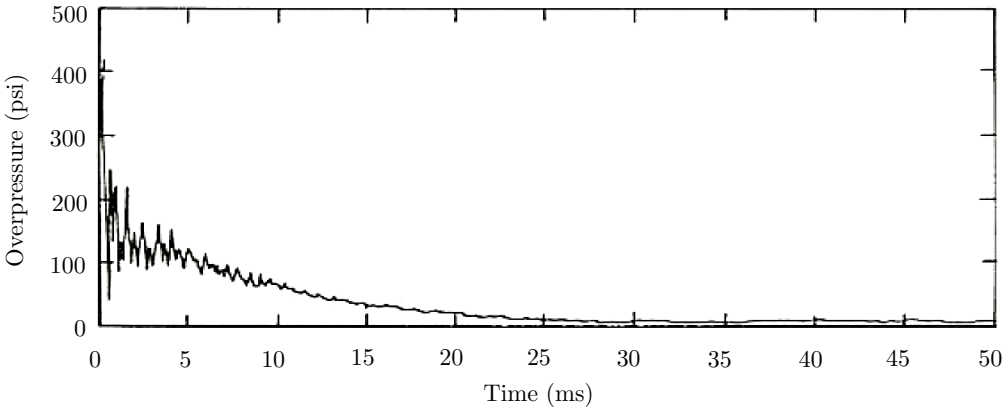

Figure 2.11: Graph of internal pressure vs time for a partially-confined cubicle ($\zeta = 0.0115$) [20].

The reflected blast pressures were only present shortly after detonation. Due to the presence of venting areas, some of the reflected shock waves escaped and the duration of the blast pressure loading was less than that of a fully-confined explosion of similar setup. The hot gas products also escaped, but slowly enough such that the loading duration of the gas pressures was longer than that of the blast pressures. The pressure within the partially-confined container gradually decayed to atmospheric pressure.

2.3.2.3 Fully-Vented Blasts

A fully-vented blast implies that the venting area of the container is large enough that the explosive products are very quickly released from the container. The duration of the gas pressure loading is less than the duration of the blast pressure. Since the magnitude of the gas pressure is much less than that of the blast pressure, the gas pressure does not provide any significant loading on the structure [19].

Keenan and Tancreto [19] analysed the loading within partially-confined and fully-vented containers, and idealised the pressure history for both conditions, as illustrated in Figure 2.12.

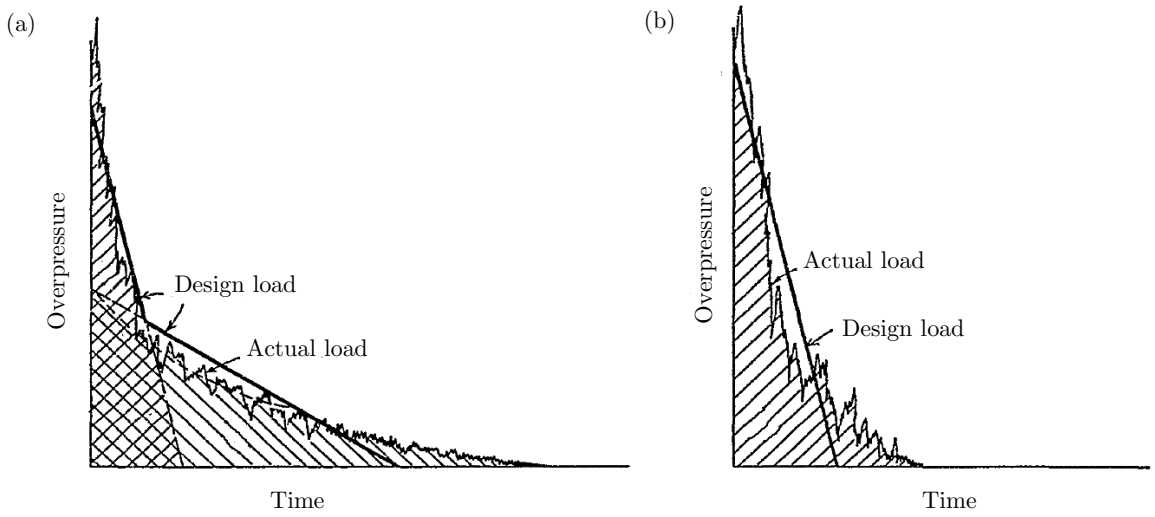

Figure 2.12: Graphs of internal pressure vs time for (a) partially-confined and (b) fully-vented cubicles [19].

The total duration of the loading within a fully-vented is less than that of a partially-confined cubicle. A partially-confined blast still comprises the two types of loads: a high magnitude, short duration blast pressure, and the low magnitude, long duration gas pressure. The loading within a fully-vented structure, however, is purely dominated by the blast pressure, and, once it decays completely, no further loading is imparted on the container [19].

2.4 Blast Testing of Unit Load Devices

The Aircraft Hardening Program was initiated by the Federal Aviation Administration (FAA) in 1990 to improve the survivability of commercial aircraft following an on-board explosion [21]. The program focused on three areas: blast characterisation, container hardening, and aircraft vulnerability. The container hardening program was introduced to assess the feasibility of manufacturing luggage containers which were blast resistant [21].

2.4.1 Hardened Unit Load Device Design

Gatto and Fleisher [21] conducted a survey of the research into the design of hardened luggage containers. The designs were limited by the specifications of the International Air Transport Association (IATA) in order for the new containers to be immediately integrated into the current aircraft fleet. The containers needed to adhere to criteria of the airline industry, which limited the container weight and cost, and required acceptable durability and operability. A total of eight hardening methods were investigated, and each was assessed against the calculated tare weight (which is the weight of an empty container) to contain a potential explosive of varied mass. The different methods attempted to improve the survivability of the ULD by utilising:

1. Thicker structural members.
2. Controlled venting with thicker structural members.
3. An increased gap between the luggage and thickened container walls.
4. The addition of stiffeners to the ULD frame.
5. Honeycomb-sandwich panels.
6. High-strength or highly ductile materials, such as high density polyethylene (HDPE), high strength fiberglass (HSFG), and high strength aluminium (HSAL).
7. A KEVLAR reinforced epoxy laminate, or KEVLAR fabric sheets.
8. A crushable foam liner.

The results of the calculations for each of the hardening methods are illustrated in Figure 2.13 (the material of the container tested for each method is listed in the legend). The first five methods showed limited potential as each resulted in excessive tare weights for a given explosive weight. The drawback of increasing the air gap (method three) and using a crushable foam liner (method eight) was that it significantly reduced the available volume within the container to store luggage. The best performing methods were the use of high-strength/highly ductile and KEVLAR materials. Although these methods could have resulted in a container

that would have fallen within the container weight specifications, the new manufacturing processes required to produce these types of containers would have both delayed the time of integration into the current fleet and increased the procurement cost of the containers [21].

Note: due to the sensitive nature of the results, no values for the explosive weight were provided.

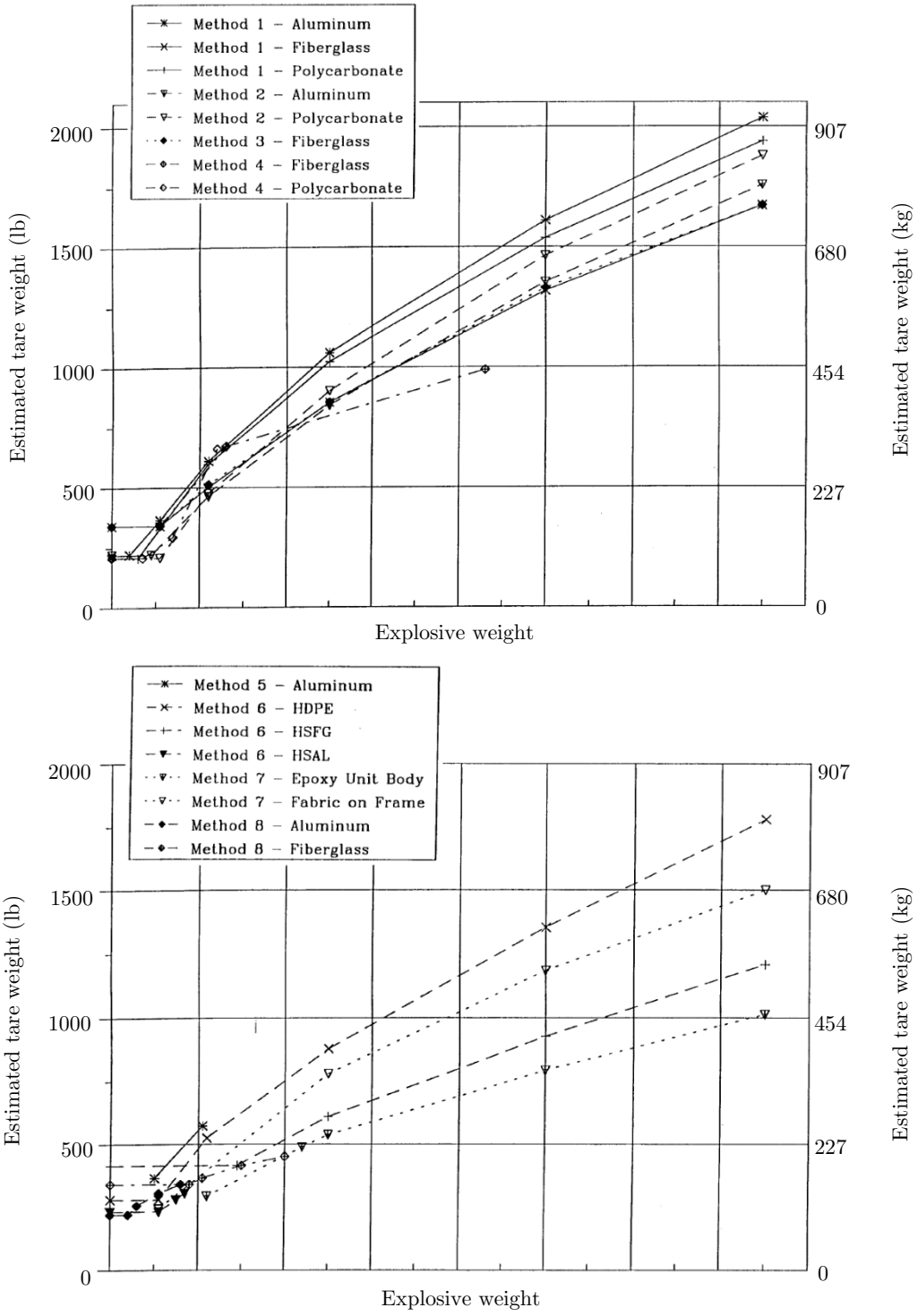

Figure 2.13: Graphs of the calculated container tare weight vs explosive weight for eight hardening methods [21].

2.4.2 Internal Blast Loading of Unit Load Devices

Gatto and Krznaric [22] determined the explosive loading within a ULD structure resulting from internal blast tests. Pressure transducers were used to measure the initial shock wave and the quasi-static pressure within the container. The container used for testing was a thick-walled steel structure with the internal dimensions of the LD-3 ULD. The side opposite the sloping panel was used as the door to the fixture. Ten different tests were performed to assess the loading on the container due to different charge locations, luggage capacities and types of venting. The same steel structure was used for all the tests. The charge mass and explosive type (C-4) also remained unchanged.

Three different luggage capacities were tested: 0% full (empty), 50% full and 75% full. Tests with the charge located in the centre of the structure were performed at the three different capacities. The initial shock and quasi-static pressures resulting from the blast load for these tests are shown in Figure 2.14.

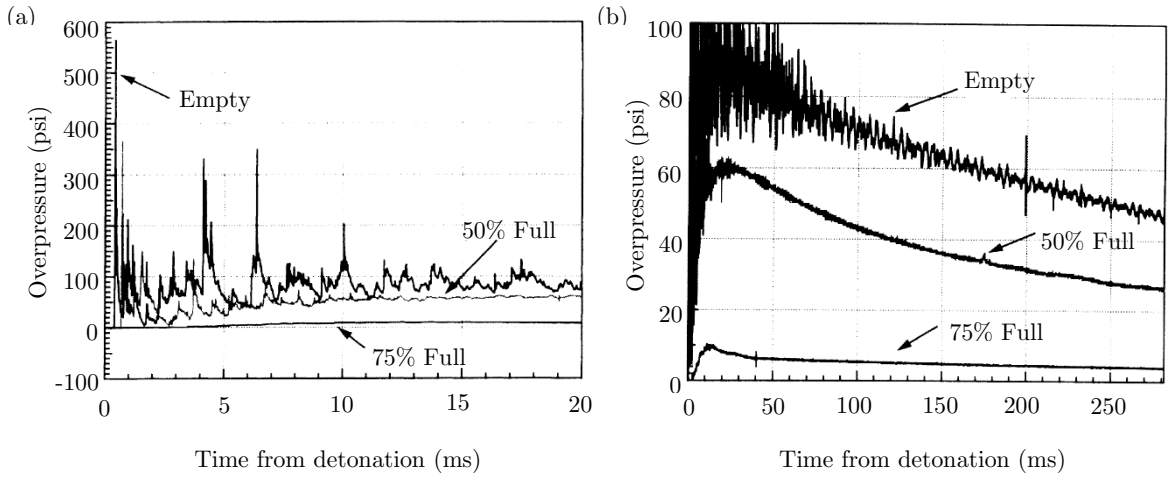

Figure 2.14: Graphs showing the effect of luggage capacity on the (a) initial shock pressure and (b) quasi-static pressure within a ULD [22].

The initial pressure and quasi-static pressure are reduced by increasing the capacity of luggage within the container. From Figure 2.14(a), the empty and 50% capacity tests showed distinct shock waves which were not present for the 75% capacity test. The initial pressure was reduced by approximately 35% and 99% when increasing the luggage capacity to 50% and 75%, respectively. From Figure 2.14(b), the quasi-static pressure was reduced by approximately 40% and 98% when the container was tested at 50% and 75% capacity, respectively.

Two types of venting were tested: The first was a door made from plywood which replaced the steel door used for the confined tests, to simulate venting after the container had failed. The second was a test with no door, simulating venting which was immediately available when the charge was detonated. The resulting loading condition due to the amount of venting was a fully-vented blast with a scaled venting area of $\zeta = 0.840$. The initial shock pressure of the two venting tests, and that of a test with the steel door in place (representing a fully-confined blast) are shown in Figure 2.15. No quasi-static pressure was measured for the two venting tests due to the fully-vented nature of the loading condition [22].

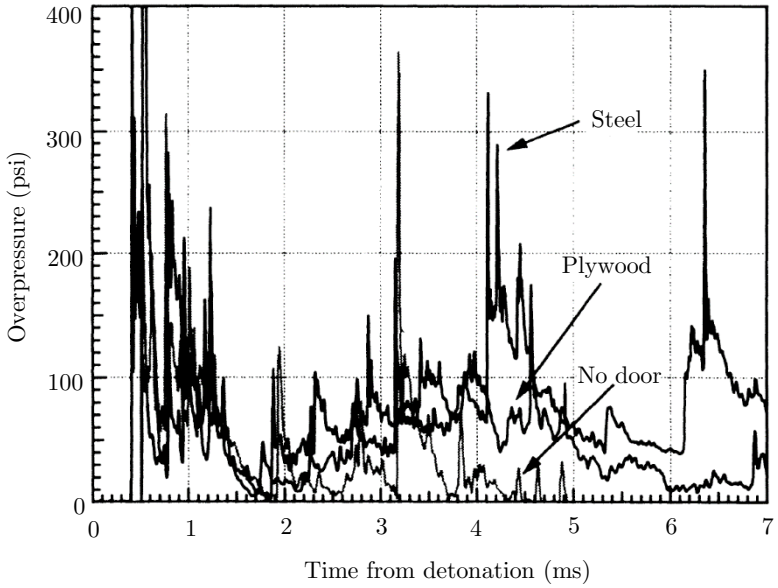

Figure 2.15: Graph showing the effect of different venting conditions, including no venting, on the initial shock pressure within a ULD [22].

The measured pressures during the first 2 ms following the detonation showed no significant difference amongst the three cases. After this time, however, the pressure histories differed. The test with the plywood door showed a decrease in reflected shock wave magnitude (compared to the fully-confined test case), and the test with no door showed a zero pressure reading after 5 ms. Although the overall loading on the container was reduced (since there was no quasi-static pressure loading during the vented tests and there was a reduction in the reflected shock pressures), any damage that would occur in the first 2 ms following the explosive detonation could not be avoided by venting [22].

2.4.3 Failure Modes of Unit Load Devices

Hargather et al. [23] employed optical measurement techniques to capture the failure of unit load devices subjected to internal blast loading. Three tests were performed on ULD-3 containers, which were filled to 75% capacity. The explosive charge was placed at two different locations, which for each test is illustrated in Figure 2.16.

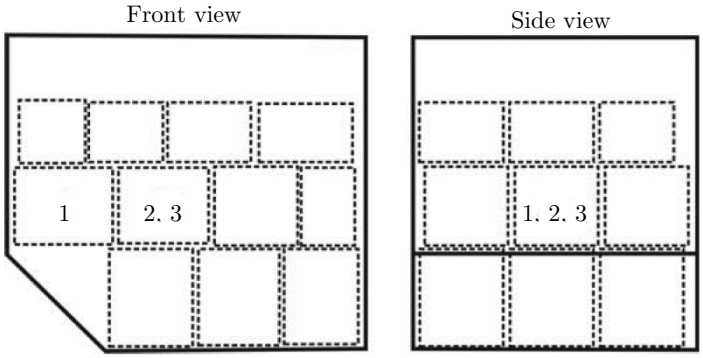

Figure 2.16: Schematic of the location of the explosive for three ULD-3 blasts performed by Hargather et al. [23].

The first test contained an explosive located nearest to the diagonal side of the ULD (the side closest to the aircraft fuselage). The consequent failure of the container in the first test is illustrated in Figure 2.17. The container ruptured when impinged by the shock wave. Accelerated material was ejected from the container after the shock wave emerged. The first mode of failure was therefore considered to be shock impact [23].

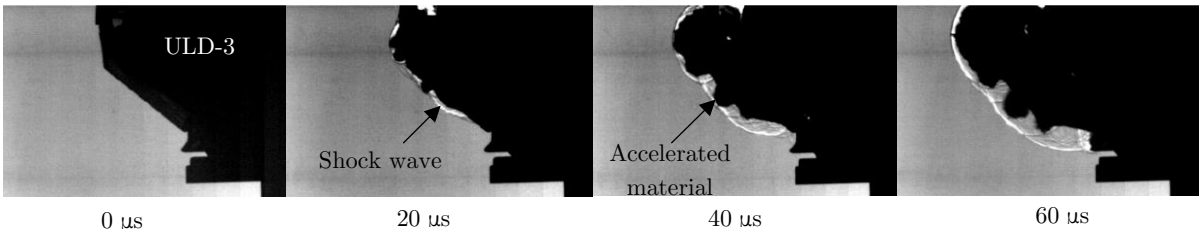

Figure 2.17: Photographs illustrating the strong shock wave emerging from bottom corner of ULD-3 followed by accelerated material ejection [23].

The remaining two tests also caused the container to fail, however, the shock wave emerging from the container was very weak. It was concluded that the luggage almost completely suppressed the shock wave. Accelerated material ruptured through the walls of the container about 100 µs after the shock wave emerged. The second failure mode was considered to be the damage resulting from blast-accelerated luggage material [23].

2.5 Blast Loading of Quadrangular Plates

The blast response of quadrangular plates has been extensively investigated. The failure of plates due to blast loading has been categorised into three modes, and the deformation of these plates has been widely studied using analytical, experimental and numerical approaches.

2.5.1 Failure Modes of Quadrangular Plates

Three modes of failure for fully clamped beams subjected to uniform explosive loads were identified by Menkes and Opat [24]. These modes described the type of permanent damage of the beams due to an impulsive load, as illustrated in Figure 2.18. In general, a greater impulse causes the failure to move into a higher mode. The modes of failure were classified as:

- Mode I: Large ductile deformation.
- Mode II: Tensile-tearing at the supports and deformation.
- Mode III: Transverse shear failure at the supports.

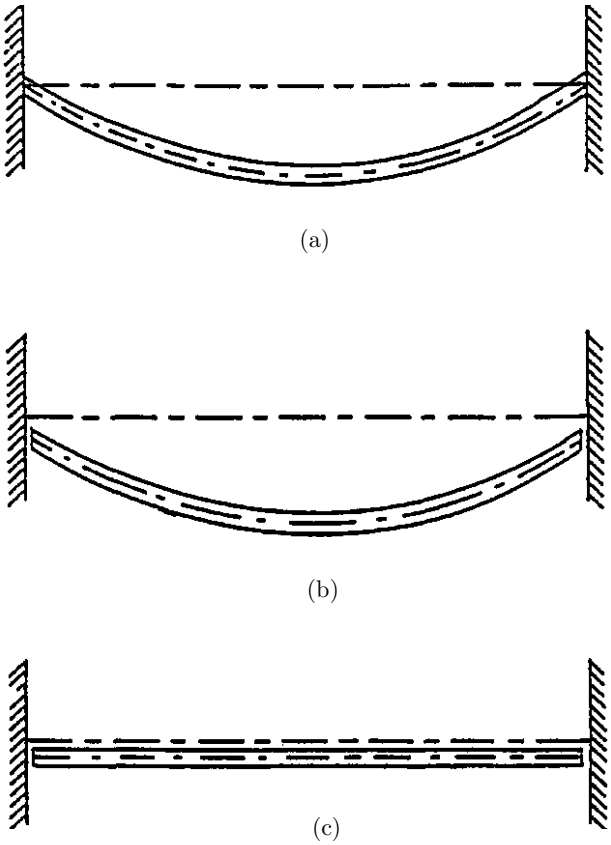

Figure 2.18: Schematics of the failure modes of fully-clamped beams (a) Mode I – large ductile deformation, (b) Mode II – tensile tearing and deformation, and (c) Mode III – transverse shear [25].

Olson et al. [26] performed experimental and numerical blast tests on clamped square plates and observed the same failure modes as those reported by Menkes and Opat [24]. Mode I and Mode II failure, and a trend towards Mode III failure, were observed from the tests. The progression towards higher modes was attributed to an increase in load intensity. Nurick and Shave [25] also conducted an experimental study on the failure of clamped square plates, with particular attention to the tearing failure at the boundary. Mode II failure was further divided into three phases:

- Mode II*: partial tearing at the supports.
- Mode IIa: complete tearing with increasing midpoint deformation.
- Mode IIb: complete tearing with decreasing midpoint deformation.

Nurick et al. [27] performed experimental tests on the blast loading of clamped circular plates, focusing on the onset of necking at the supports. From the results, Mode I failure was divided into three additional phases, each in addition to the large ductile deformation:

- Mode I: no visible necking at the boundary.
- Mode Ia: necking around part of the boundary.
- Mode Ib: necking around the entire boundary.

The results of the tests performed by Olson et al. [26] showed that the square plates exhibited the same modes of failure as circular plates.

2.5.2 Dimensionless Analysis

Various analytical models have been developed to predict and compare the behaviour of metal plates under high-impact loading. Johnson [28] put forward a non-dimensional damage number, as described by Equation 2.22.

$$\alpha = \frac{\rho v^2}{\sigma_d} \tag{2.22}$$

where: ρ is the material density, v is the impact velocity and σ_d is the damage stress.

This number is a ratio of the inertia of the loading to the resistance of the material to deformation [28]. Johnson's damage number is used as an indication of the damage regime of the plate, in terms of the permanent strain imposed during impact loading. Higher damage numbers indicate a higher magnitude of plate deformation. The main drawback of this damage number is that it does not take into account the type of impact, the target geometry and

dimensions, or the boundary conditions. In order to address these shortcomings, Nurick and Martin [29] extended the Johnson damage number to include the impulse, plate thickness and target area, as shown in Equation 2.23.

$$\alpha_o = \frac{I^2}{A_o^2 \rho \sigma_d H^2} \tag{2.23}$$

where: I is the total impulse which acts over an area A_o, and H is the plate thickness.

Jones [30] investigated the dynamic response of a fully-clamped rectangular plate subjected to a uniform pressure pulse. The plastic model allowed the plate to deform into a number of rigid regions which are separated by plastic hinges. Figure 2.19 illustrates the plastic hinges that develop within a rectangular plate and the plate dimensions, as defined by Jones [30].

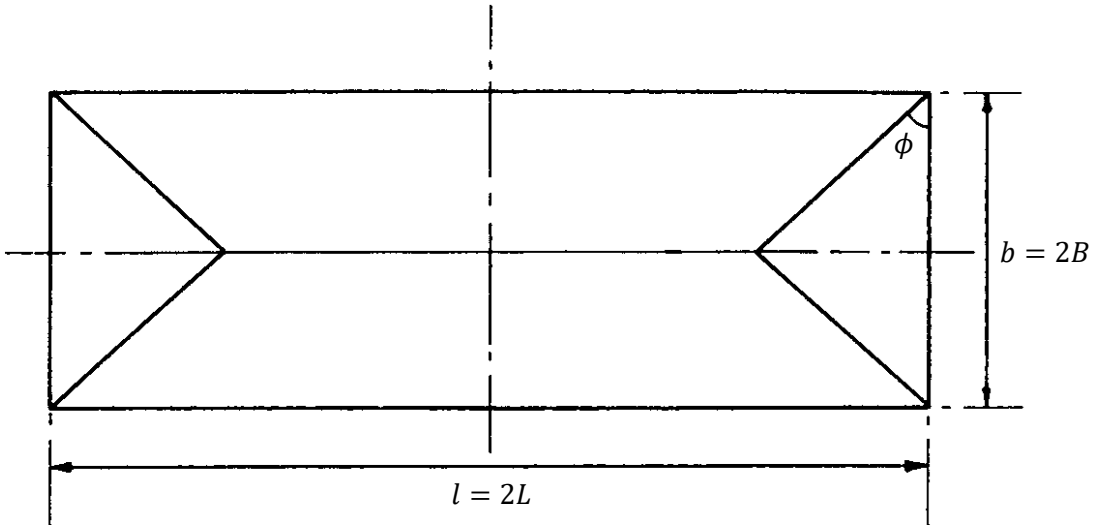

Figure 2.19: Schematic top view of a rectangular plate showing plastic hinge lines [30].

The aspect ratio of the plate was defined as Equation 2.24.

$$\beta = \frac{b}{l} = \frac{B}{L} \tag{2.24}$$

The angle defining the plastic hinge ϕ was related to the aspect ratio by Equation 2.25 [30].

$$\tan\phi = -\beta + \sqrt{3 + \beta^2} \tag{2.25}$$

A conservation of energy approach was used to develop the theoretical model, which included membrane forces and bending moments to predict the permanent ductile deformation (Mode I failure) and tensile tearing at the boundaries (Mode II failure). The model obeyed the Johansen yield condition and included the energy dissipation around the clamped boundaries. A dimensionless initial kinetic energy, shown in Equation 2.26, was introduced by Jones [30].

$$\lambda = \frac{\mu v^2 L^2}{M_0 H} \tag{2.26}$$

where: μ is the mass per unit surface area, M_o is the fully-plastic bending moment which, for a plate, is given by $M_o = \sigma_o H^2/4$, σ_o is the material yield stress, and L is the plate half length (as shown in Figure 2.19).

Similar to the modification of the Johnson damage number, Equation 2.26 can be modified to produce Equation 2.27.

$$\lambda = \frac{4I^2 L^2}{A_o^2 \rho \sigma_o H^4} = 4\alpha_o \left(\frac{L}{H}\right)^2 \tag{2.27}$$

Jones predicted the final midpoint deflection δ_f of a fully-clamped rectangular plate, which included the effect of strain-rate sensitivity.

$$\frac{\delta_f}{H} = \frac{(3-\xi_0)\left[\sqrt{1+\frac{\Gamma}{n}}-1\right]}{2[1+(\xi_0-1)(\xi_0-2)]} \tag{2.28}$$

where: ξ_0 is a geometry parameter given by $\xi_0 = \beta \tan\phi$,

Γ is the loading parameter given by $\Gamma = \frac{1}{6}\lambda\beta^2(3-2\xi_0)\left(1-\xi_0+\frac{1}{2-\xi_0}\right)$, and

n is the strain-rate parameter given by $n = 1 + \left(\frac{2v\delta_f}{3\sqrt{2}DB^2}\right)^{1/q}$

where: D and q are the Cowper-Symonds strain-rate coefficients.

An iterative solution process is required to determine the prediction for δ_f due to the presence of δ_f in the strain-rate parameter. Comparison of Equation 2.28 with experimental results of mild steel rectangular plates demonstrating Mode I failure showed reasonable agreement: the experimental results were bounded by the upper and lower limits of δ_f [30].

Zhao [31] suggested a new dimensionless number, which was referred to as the response number, to predict the response of beams and plates to dynamic loading. The derivation of the response number is based on the dimensional reduction of the governing equations for beams and plates. Equation 2.29 describes, in order, the response number as derived by Zhao, and the relation to the damage numbers reported by Johnson [28] and Jones [30].

$$R_n = \begin{cases} \dfrac{\rho v^2}{\sigma_o}\left(\dfrac{L}{H}\right)^2 \\ \alpha\left(\dfrac{L}{H}\right)^2 \\ \dfrac{\lambda}{4} \end{cases} \tag{2.29}$$

The prediction of the final midpoint deflection of a fully-clamped rectangular plate subjected to an impulsive load (and including strain-rate effects) using the response number was similar in form to that derived by Jones [30]. The prediction by Zhao is described by Equation 2.30.

$$\frac{\delta_f}{H} = \frac{(3-\xi_0)\left[\sqrt{1+\frac{2}{3n}R_n(3-2\xi_0)\left(1-\xi_0+\frac{1}{2-\xi_0}\right)}-1\right]}{2[1+(\xi_0-1)(\xi_0-2)]} \tag{2.30}$$

where: ξ_0 and n are as described in Equation 2.28.

Nurick and Martin [29] developed a damage number for quadrangular plates in the form of a dimensionless impulse (Φ_q), as described by Equation 2.31.

$$\Phi_q = \frac{I}{2H^2\sqrt{bl\rho\sigma_o}} \tag{2.31}$$

where: b and l are the plate width and length, respectively.

The dimensionless impulse was derived using the reworked Johnson damage number, as described by Equation 2.23, and additional geometrical dimensions of the target plate. This damage number is valid for plates exhibiting only Mode I failure. The dimensionless impulse for quadrangular plates is related to the dimensionless initial kinetic energy (λ) developed by Jones [30] according to Equation 2.32.

$$\Phi_q = \frac{1}{2}\sqrt{\lambda\beta} \tag{2.32}$$

Nurick and Martin [29] collected experimental test data of 156 uniformly loaded steel and aluminium rectangular plates. The final deflection to plate thickness ratio for each test was plotted against the dimensionless impulse, and a least-squares fit was determined, which resulted in a correlation coefficient of $R^2 = 0.984$. The empirical relationship for quadrangular plates is described by Equation 2.33 [29].

$$\frac{\delta_f}{H} = 0.471\Phi_q + 0.001 \tag{2.33}$$

Geretto et al. [32] performed three series of blast loading on square plates of varying thicknesses at different degrees of confinement: unconfined, fully-vented ($\zeta > 1$), and fully-confined blasts. By normalising the deflections to a nominal plate thickness, it was observed that the results across all the plate thicknesses and degrees of confinement correlated well with the dimensionless impulse formulated by Nurick and Martin [29], according to the relationship described by Equation 2.34 [32].

$$\frac{\delta}{H} = 0.48\Phi_q \tag{2.34}$$

The results from the tests performed by Geretto et al. [32], as shown in Figure 2.20, were compared against Equation 2.34, with upper and lower bounds equal to one plate thickness.

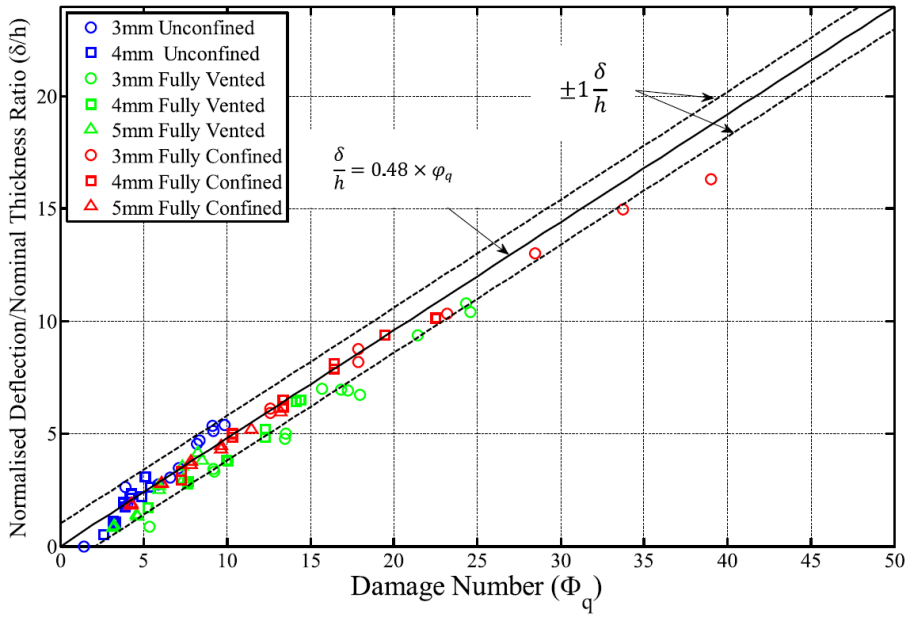

Figure 2.20: Graph of the relationship between midpoint deflection to thickness ratio and dimensionless damage number Φ_q [32].

The impulse used to calculate the damage number for the unconfined and fully-vented tests was determined experimentally. No impulse was measured from the fully-confined tests due to the equilibrium of the loading [32]. The impulse for the fully-confined tests could only be approximated by first deriving a relationship between the plate deflection and impulse and then establishing a fully-vented to unconfined impulse ratio [32]. In order to circumvent this, Yao et al. [33] reported a dimensionless number for the dynamic response of fully-confined box-shaped structures that did not require an impulse measurement. The work was based on the results of the fully-confined tests performed by Geretto et al. [32]. This new dimensionless number is described by Equation 2.35 [33].

$$D_{in} = \frac{Q}{4\sigma_o L^2 H} \tag{2.35}$$

where: Q is the total explosive energy calculated by $Q = E_0 \frac{m_{\exp}}{\rho_0}$,

where: E_0 is the detonation energy per unit volume, $m_{\exp}$ is the charge mass, and ρ_0 is the density of the explosive material.

An empirical relationship, described by Equation 2.36, was found to fit the data of the fully-confined test results, as shown in Figure 2.21. This relationship could be used to predict the dynamic response of fully-confined box structures of similar size to different blast loads [33].

$$\frac{\delta}{H} = 0.79 D_{in} \tag{2.36}$$

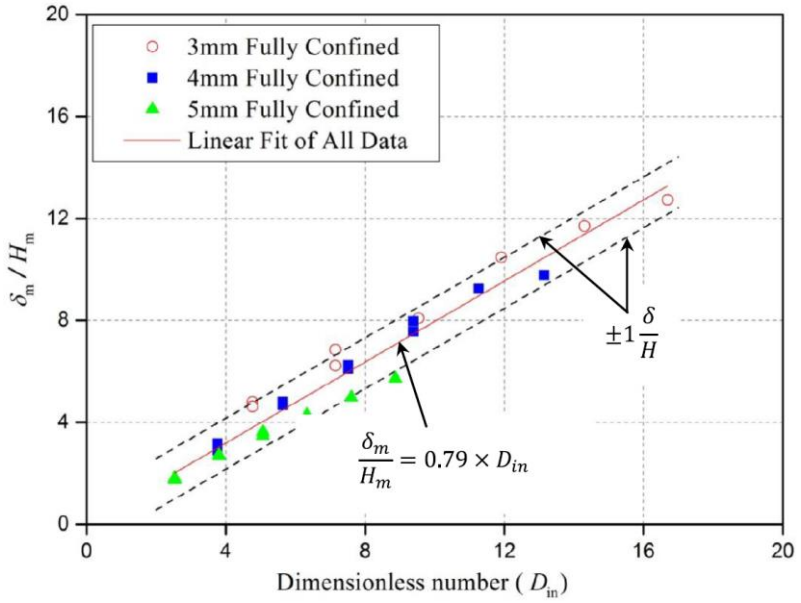

Figure 2.21: Graph of the relationship between midpoint deflection to thickness ratio and dimensionless number D_{in} for box structures [33].

2.5.3 Blast Testing of Aluminium Plates

Spranghers et al. [34, 35] investigated the response of aluminium plates to free-air blast loading. Experimental tests were performed and the transient response was measured using Digital Image Correlation (DIC) technology. The blast test was also simulated numerically using FEM software, LS DYNA. The explosive loading was produced by detonating spherical charges of Composition C4; each test was performed using 40 g of explosive located at a stand-off distance of 250 mm. The aluminium alloy used for the target plate was EN AW-1050A H24, the plate dimensions being 400 mm x 400 mm x 3 mm. The exposed target area was 300 mm x 300 mm.

Figure 2.22 illustrates the experimental results: the measured reflected pressure history at each of the corners of the target area for one of the blast tests (included is the numerically-determined reflected pressure), and the transient midpoint deflection for all the experimental tests. All the tests had the same loading configuration and exhibited similar responses.

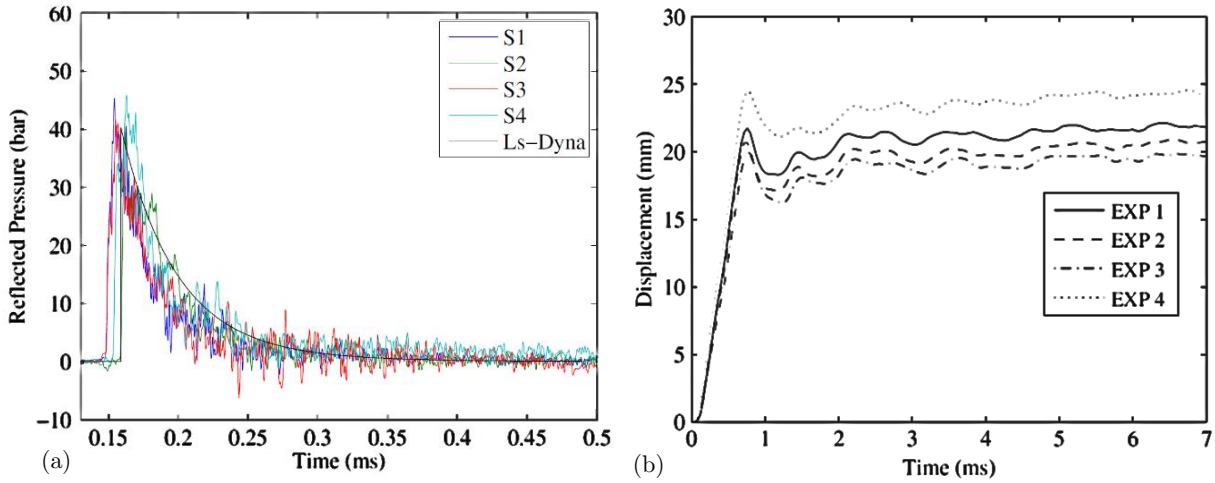

Figure 2.22: Results of free air blast tests showing the (a) reflected pressure history at the target area corners and (b) transient midpoint plate displacement [35].

The shock wave peaked just after 0.15 ms from the detonation, and induced a rapid material response in the target plate. Whilst the shock wave acted on the plate, a plastic response was observed: the target plate reached a peak displacement at approximately 0.8 ms. Once the shock wave disappeared, the plate exhibited damped elastic vibrations, evident from 1 ms onwards. The response was observed to diminish and started to settle after 5 ms.

Aune et al. [36] performed experimental blast tests on thin aluminium plates, investigating the effect of stand-off distance on the dynamic response. Aune et al. [37] performed a numerical study of the same tests. Square plates, with an exposed target area of 300 mm x 300 mm, were tested. The plates were cut from an EN AW-1050A H14 alloy and were 0.8 mm thick. Spherical

charges of Composition C4 explosive were used; the charge mass remained constant at 30 g and the stand-off distance varied amongst 250 mm, 375 mm, 500 mm and 625 mm.

From the experimental results it was observed that an increasing stand-off distance resulted in lower impulse transfers and therefore lower plate deflections [36]. The mode of failure for each test was observed to vary amongst the tests at different stand-off distances. Three different modes of failures are shown in Figure 2.23 for tests performed at 250 mm, 375 mm and 500 mm.

Figure 2.23: Photographs of plate failure showing (a) complete tearing at 250 mm SOD [37], (b) partial tearing at 375 mm SOD [37], and (c) large inelastic deformation at 500 mm SOD [36].

Testing at the nearest stand-off distance (250 mm) resulted in complete tearing of the target plate along the boundaries. Increasing the stand-off distance to 375 mm resulted in partial tearing of the target plate at the boundaries. These are classified as Mode IIa and Mode II* failures, respectively. At a 500 mm stand-off distance, only large inelastic deformation was observed – a Mode I failure. Boundary pull-in was observed to increase at higher blast loads.

2.5.4 Blast Testing of Box Structures

Geretto et al. [32] investigated the deformation of steel plates subjected to various degrees of confinement. The experiments comprised fully-confined and fully-vented cuboidal structures, and unconfined square plates. Spherical charges of PE4 explosive, and charge masses ranging from 10 g to 70 g, were detonated at a stand-off distance of 100 mm from all internal walls (during confined blast testing) and from the target plate (during unconfined blast testing). The exposed area of all the plates was 200 mm x 200 mm. The effect of confinement on the deformation of 3 mm thick plates is shown in Figure 2.24.

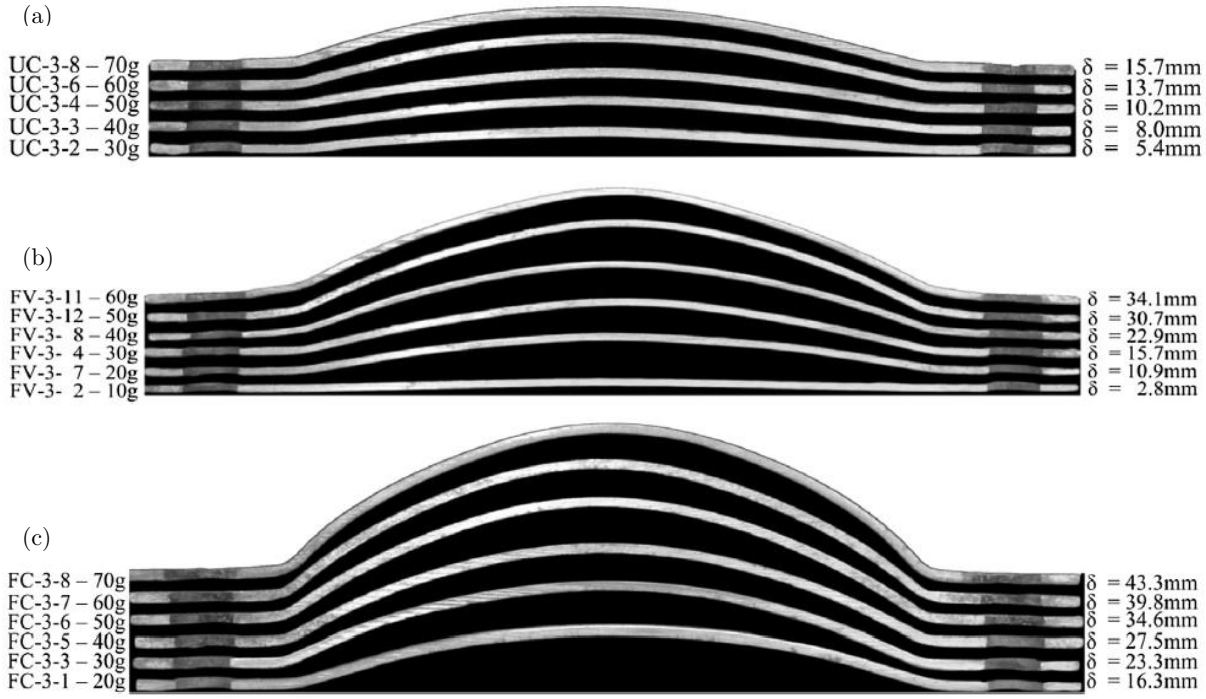

Figure 2.24: Photographs of midline cross-sections showing the deformation profile of 3 mm thick square plates subjected to (a) unconfined, (b) fully-vented and (c) fully-confined blast loading for various charge masses [32].

Irrespective of the degree of confinement, the midpoint displacement of the plate increased with an increasing charge mass. Furthermore, for the same charge mass, the midpoint displacement increased with an increasing degree of confinement. From the test results, fully-confined blast tests were observed to cause 4.0 times more damage than unconfined blast tests, while fully-vented blast tests caused 2.7 times more damage than unconfined blast tests [32].

Pickerd et al. [38] analysed the structural response and failure of 1 m^3 steel containers to internal blast loading. Cylindrical TNT explosives were detonated to produce the blast loading. DIC was used to capture the transient deformation profile of one side of the container soon after detonation, as shown in Figure 2.25.

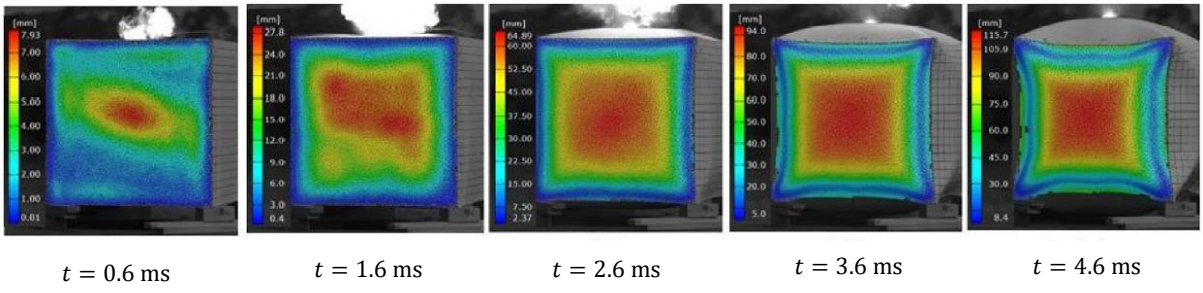

Figure 2.25: Transient deformation of steel container due to an internal blast load [38].

Internal blast loading of the containers initially caused uniform deformation in the central region of the container sides. The container would undergo expansion, and consequently the sides of the container would experience large deformations. The containers would undergo two expansive deformations; failure mostly occurred along the weld joints due to a weld tear initiation during the first container expansion. The following expansion would cause the weld tear to propagate along the weld joint [38].

Yao et al. [39] investigated the failure modes of steel cabin structures when subjected to internal explosions. Single cabin and three-cabin specimens were manufactured and blast tested. The single cabin structure had internal wall dimensions of 450 mm x 450 mm and was manufactured from 3 mm steel plates. The three-cabin structure had internal wall dimensions of 500 mm x 500 mm per cabin and was manufactured from 2 mm steel plates. The explosives were made from TNT and centrally located inside the cabins. The blast results of a single and three-cabin specimen are shown in Figure 2.26. Large inelastic deformations were evident in the single cabin, whereas two front panels were ejected from the three-cabin specimen, in addition to large permanent deformations.

(a) (b)

Figure 2.26: Photographs of the blast response and failure of (a) single cabin and (b) three-cabin specimens [39].

The observed failure modes exhibited Mode I (plastic deformation), Mode II (petalling or capping in the central region of the plate, and edge tearing) and Mode III (corner shear failure and shear failure over the entire plate/total plate ejection) failure [39]. An increasing charge mass resulted in more severe damage to the cabin structures, and plate ejection was suggested to cause damage to adjacent cabins (due to the high ejection velocity) [39].

2.6 Review Summary

Blast pressure: The simplified blast load generated by an explosion is represented by a large, instantaneous spike in pressure followed by an exponential decay in magnitude towards atmospheric pressure [8, 10]. The impulse generated during the positive phase of the loading is approximated as the total impulse generated by the blast [10]. A high peak overpressure, or extended blast duration increases the total blast impulse. Pressure reflections occur when the blast wave impinges on a surface. The magnitude of the reflected pressure wave is greater than the incident wave [9]. The reflected pressure is increased as the number of reflective surfaces increase: pressure reflections at the internal corners or vertices of structures are greater than the pressure reflection at a single surface.

Blast scaling: The laws of blast scaling are used to establish a scaled distance, from which the peak pressure of a blast is estimated, based on a number of empirical prediction models. One such model is proposed by Kinney and Graham [7] and provides an accurate, stable and continuous solution over a wide range of scaled distances.

Blast loading: Blast loading is broadly divided into two categories: unconfined and confined blasts. An unconfined blast is characterised by a single interaction with a blast wave (which has had no prior interaction with the structure) [8]. A confined blast produces additional blast loading: Reflected pressures are produced within the container which generate multiple high magnitude shock loads. Additionally, a rise in internal pressure is generated by the expansion of the explosive products, which produce a long duration, quasi-static load on the container [19,20]. The resultant damage to the structure increases as the degree of confinement increases [32].

ULD blast response: Blast testing of ULDs revealed that the presence of luggage and a single venting area reduced the overpressure within the container [22]. However, only one venting area was tested. In a different test, although the luggage suppressed the blast wave, blast-accelerated material caused rupture of the container [23].

Quadrangular plate blast response: Plate failure is observed by large inelastic deformation (Mode I failure) in the form of plastic hinges and boundary pull-in [24,30,37]. Plastic hinges develop along the clamped edges of the plate, and from each corner towards the plate midline [30]. Plate deformation is observed to increase as the blast loading increases. Particularly, a linear relationship between plate deflection and charge mass was observed for unconfined and confined blasts [32,33]. Partial or complete tensile tearing of the plate (Mode II failure) is observed when blast loading is further increased [36,37].

3 Experimental Design and Methodology

Experimental testing was performed to investigate the structural response of a unit load device (ULD) subjected to internal blast loading. The aim of the tests was to simulate representative loading of a ULD and determine the response of the diagonal face (that which would be closest to the aircraft fuselage) for different venting configurations. A scaled box was designed and manufactured based on a current ULD commonly used on most commercial aircraft and blast tested at various venting configurations.

3.1 ULD-3 Container

The ULD-3 is a popular unit load device as it is compatible with most wide-bodied commercial aircraft [5]. The ULD-3 is a half-width container with one diagonal side to accommodate the curvature of the aircraft body. The dimensions of the ULD-3 are shown in Figure 3.1 [40]. Two ULD-3 containers are installed alongside one another in the lower deck of the aircraft, as shown in Figure 3.2. Several pairs of containers are then loaded along the length of aircraft. This layout results in each ULD being immediately adjacent to at most three other containers. The front- and back-most pair of ULDs only have two adjacent containers.

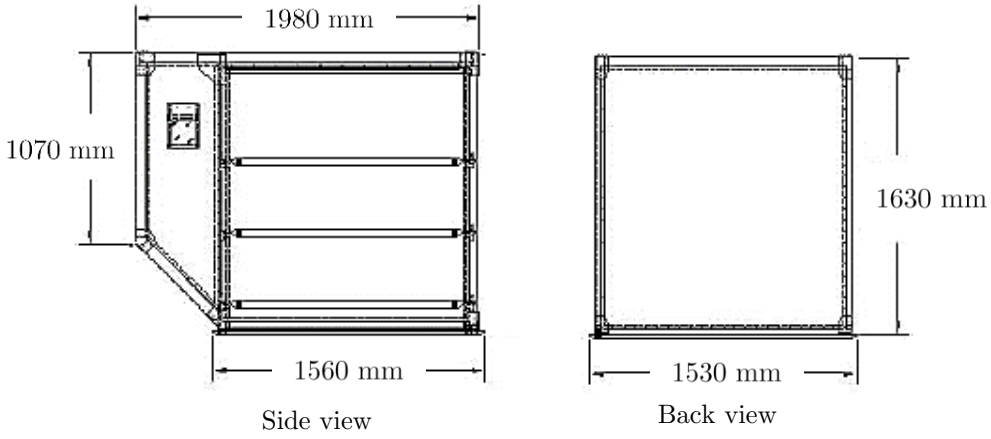

Figure 3.1: Schematic diagram of the dimensions of the ULD-3 container [40].

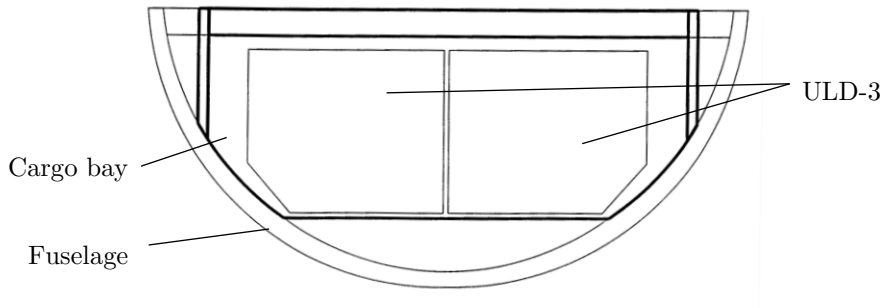

Figure 3.2: Schematic diagram of the positioning of two ULD-3s in the lower deck of an aircraft [21].

The diagonal side of the container lies closest to the fuselage. The failure of this face as a result of an internal explosion, and especially due to the close proximity of the fuselage, could result in catastrophic failure of the aircraft.

3.2 Venting Configurations

When an explosive detonation occurs on-board an aircraft and within a luggage container, the resulting shock waves and gas pressure built-up within the ULD can cause the container to rupture. The explosive products are able to escape which could consequently cause the fuselage skin to tear. The venting of an explosion from a fully-confined blast has been shown to reduce the loading within the structure [19,20,32]. The layout of ULDs in the lower deck of an aircraft would allow venting the explosive products from one container into another without altering the installation of the ULDs on-board the aircraft. The purpose of venting would be threefold:

- To allow the explosive products to be released from the container, reducing the quasistatic pressure within the container and the damage done by the blast [20].
- To direct the explosive products away from the fuselage and the passengers on the upper deck and into the (more expendable) adjacent containers.
- To allow the blast energy to be absorbed by more luggage in the adjacent containers as a useful blast mitigation technique [22].

The ULDs on-board the aircraft could be designed to vent into the adjacent containers. There would be three possible faces of each container from which venting areas could be made: the two side faces and the back face (that opposite the diagonal face). The possible venting configurations are shown in Table 3.1, ranging from no venting, to venting through a maximum of three faces. Due to the symmetry of the ULD geometry, venting out of either side face was considered to be a similar venting configuration.

Table 3.1: Possible configurations for venting into adjacent ULDs on-board an aircraft.

	Venting configuration	**Vented face(s)**
1	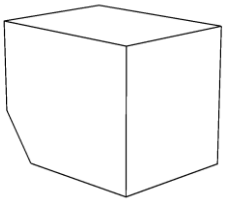	None.
2	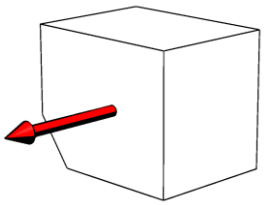 or 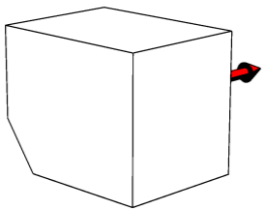	One side face.
3	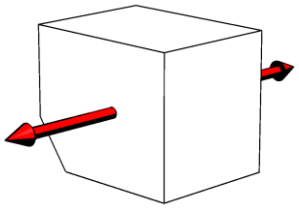	Both side faces.
4	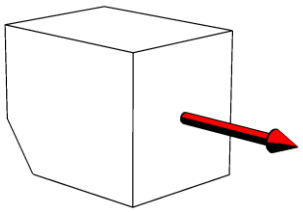	Back face only.
5	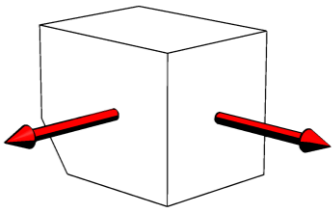 or 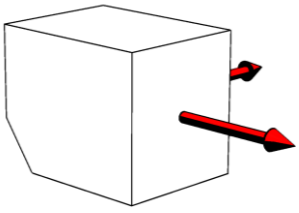	Back face and one side face.
6	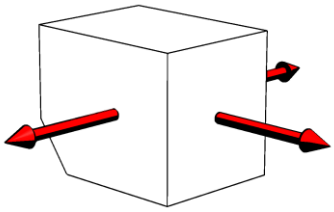	Back face and both side faces.

3.3 Confined Test Design

The box used for testing was a scaled version of the ULD-3 container. The diagonal face of the ULD (which lies closest to the fuselage of the aircraft) was chosen to be the face of interest for the experimental tests. The test box was designed to assess the blast response of the diagonal face only, which was represented by an aluminium target plate. All walls except the diagonal side were designed to remain rigid during the blast tests. The reasons for doing this were:

- A rigid-walled specimen would allow multiple blast tests to be performed within the single box. The box could be (irreversibly) modified to include venting areas in order to perform another set of repeatable tests with a different venting configuration, and ensure a quick turnover period between tests of the same venting configuration.
- A fully deformable box made from aluminium would be challenging to manufacture due to the difficulties with welding thin aluminium sheets, and scaling the connection techniques (such as the rivets and stiffeners).

3.3.1 Scale

To decide on a suitable scale, a number of ergonomic and technical factors were considered:

1. The box had to be big enough to allow a charge to be easily and accurately located inside it (particularly for the fully-confined tests).
2. The size and mass of the box was limited due to manual handling considerations. The maximum allowable mass of the box was set to 80 kg, which was deemed the heaviest mass to be handled by two people.
3. The box had to be big enough so that a large target area was created, allowing sufficient deformation (or modes of failure) to be analysed. The size of the target area was limited to having a minimum width of 100 mm.
4. A larger box (resulting in a larger stand-off distance) would allow larger charges to be used which would increase the accuracy of moulding, positioning and detonating the charge. For spherical charges, the lower limit was set to charges with a mass of 10 g.

To meet the above criteria, the dimensions of ULD-shaped boxes of varying scales were investigated, as shown in Table 3.2. The free (internal) volume of the box gave a measure of the space within which one could place the explosive charge at the correct location. The larger the scale, the easier it would be to operate within the box, however, the box would also become

Table 3.2: Ergonomic and technical specifications of various scaled boxes.

Scale	Free volume of box (10^6 mm^3)	Approximate mass of box (kg)	Exposed area of target plate (mm × mm)
1:10	4.80	13.5	153 × 70.0
1:8	9.37	26.4	191 × 87.5
1:6	22.2	62.6	255 × 117
1:5	38.4	108	306 × 140

heavier and more difficult to handle. The exposed area of the target plate, which had the same dimensions as the diagonal face, was used to predict the extent to which the target plate would deform: larger plates would exhibit deformations which would be easier to observe.

A 1:6 scale model was chosen as the most suitable option. The overall dimensions of a box at this scale are shown in Figure 3.3. A smaller box at a scale of 1:10, although very light, had a confining free volume which would make operating within the box (including mounting, positioning and activating the explosive charge) uncomfortable. The free volume provided by the 1:6 scale box had sufficient space to handle and accurately place the explosive within the box. Although a box at this scale was heavier than a box at a scale of 1:8, the larger target area was seen to be more beneficial than a decrease in required manpower. At a scale of 1:5, however, the box was deemed too heavy to be handled.

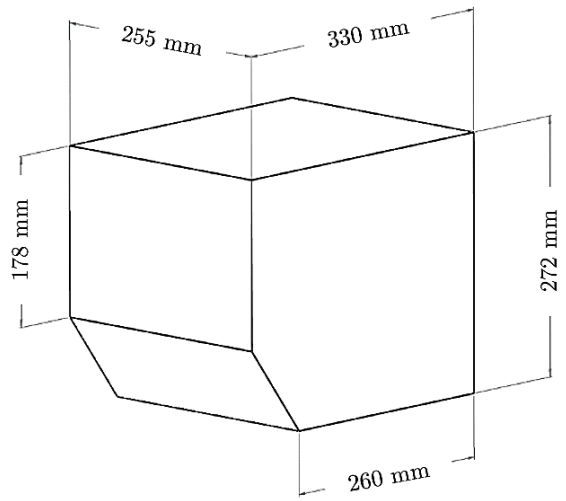

Figure 3.3: Schematic diagram of the dimensions of a 1:6 scaled ULD box.

3.3.2 Box Design

The experimental investigation comprised only internal blast tests, so only the internal dimensions and geometry of the box needed to be representative of a scaled ULD. The scaled dimensions of the ULD-3 were therefore used as the internal dimensions of the box, and the external geometry was modified to meet the requirements of the testing procedure. These requirements were:

1. All the sides except for the diagonal side were to remain rigid during the blast tests.
2. One of the rigid sides needed to be removable in order to place the explosive charge within the box during the fully-confined tests.
3. The diagonal face was to be an aluminium target plate which needed to be fully-clamped to the box.

The ULD box comprised five panels which were fillet welded together along both sides of the line of contact. These were two identical side panels, a bottom panel, a front panel and a back panel, as illustrated in Figure 3.4. These panels were cut from 20 mm thick mild steel to remain rigid during blast testing, to mitigate warping of the box when welding the panels and the flange, and to accommodate a total of twenty M10 holes, which were drilled and tapped into the panels at the top of the box. The top plate could then be bolted onto the box after the charge was placed for testing in the fully-confined blasts.

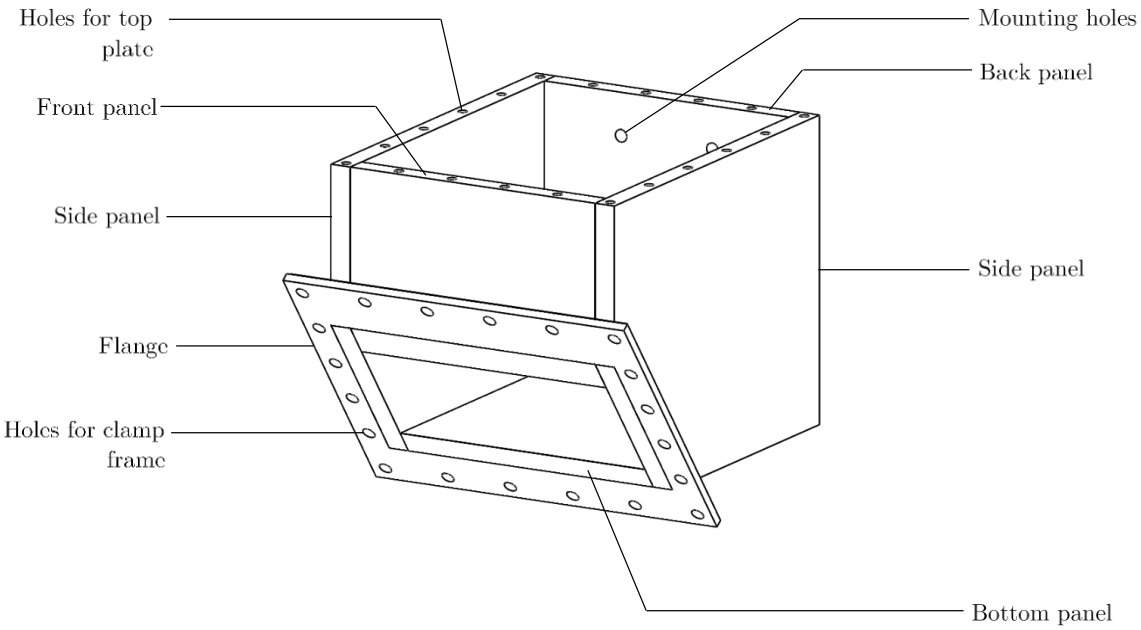

Figure 3.4: Diagram of ULD box (top panel removed) made up of five panels and a flange.

The top plate was chosen to be removable because it was not adjacent to the target plate on the diagonal side, and would not be used for mounting onto the pendulum. The top plate was cut from 10 mm mild steel, making it lighter than the other panels and easier to place and remove before and after testing, respectively. A 10 mm mild steel flange was included so that the target plate could be secured to the box using a clamp frame. The flange was placed and fillet welded to the box around the opening of the diagonal side. The exposed welds were grinded flush with the panels to ensure an even area between the flange and the target plate.

3.3.3 Clamp Frame Design

The top and bottom of the flange were extended to ensure the bolts used for clamping the target plate were not obstructed by the front and bottom panels, respectively. A total of 20 holes were cut through the flange for bolt fastening. A 20 mm mild steel clamp frame was designed to match the region of the flange, the location of the bolt holes, and the open area for the target plate. Likewise, the target plate was designed to match the dimensions of the flange and the location of the bolt holes. This design resulted in a 355 mm x 280 mm target plate with an exposed area of 255 mm x 117 mm. Figure 3.5 shows the clamped region and exposed area of the target plate. Due to the horizontal asymmetry of the clamping design, care was taken when mounting the clamp frame to ensure the open region matched the exposed area of the target plate from within the box.

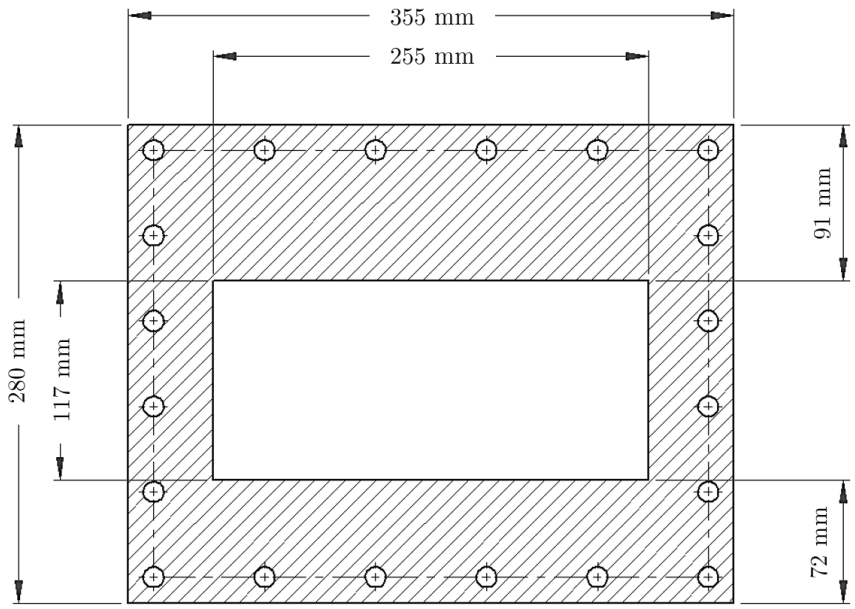

Figure 3.5: Diagram of target plate dimensions, showing clamped region (hatched) and exposed area (unhatched).

3.3.4 Venting and Mounting

The venting configuration had implications for the mounting orientation of the box on the test pendulum. The ULD box was mounted directly onto the loading end of the pendulum, which was kept level using balancing masses on the other end. Four bolts in a 200 mm x 95 mm rectangular arrangement were required to mount the box to the pendulum. The bolt holes used for mounting are shown in Figure 3.4. In order to prevent out-of-plane twisting of the pendulum, the box needed to be mounted such that the resultant impulse of the blast load was aligned with the longitudinal axis of the pendulum. In other words, the pendulum should only exhibit in-plane motion.

A summary of the venting and possible mounting configurations is given in Table 3.3. For reference, the different venting configurations are illustrated in Table 3.1. The first three venting configurations were able to be tested on the pendulum. Venting configuration 4 required venting out of the back panel only, which would require the front panel to be used for mounting. However, this panel was too small to be mounted onto the pendulum due to the presence of the flange. The fifth venting configuration required one side panel and the back panel to be used for venting areas. There was no panel from which to mount the box that would not cause twisting of the pendulum. The sixth venting configuration would also need to be mounted with the front panel. As a result, venting configurations 4, 5 and 6 could not be tested on the pendulum.

Table 3.3: Venting and corresponding mounting configurations of ULD box.

Venting configuration	**Panel(s) to be vented**	**Panel to be mounted**	**Note**
1	None	Back panel	Possible.
2	One side panel	Opposite side panel	Possible.
3	Both side panels	Back panel	Possible.
4	Back panel	Front panel	Panel too small to be mounted on pendulum.
5	Back panel and one side panel	None	Mounting on any panel would cause pendulum to twist.
6	Back panel and both side panels	Front panel	Panel too small to be mounted on pendulum.

Three configurations were therefore tested: configurations 1 to 3. The first configuration was fully-confined with no venting area. The second and third configurations both required venting areas, on one and both side panels, respectively. At the given model scale of 1:6, each venting area had dimensions 220 mm x 252 mm. These venting areas resulted in both the second and third configurations being classified as fully-vented tests because the scaled venting area was greater than 0.6. A summary of the types of blast loads resulting from the three configurations is shown in Table 3.4.

Table 3.4: Blast loading category for each tested venting configuration.

Venting configuration	**Scaled venting area**	**Loading category**
1	$\zeta = 0.0$	Fully-confined
2	$\zeta = 0.7$	Fully-vented
3	$\zeta = 1.4$	Fully-vented

3.4 Unconfined Test Design

Another set of tests for which a clamp frame needed to be designed was the unconfined blasts. This test series was considered to be blast testing of the target plate without the presence of the ULD box. The same clamping configuration was used so that the target plate had the same exposed area and clamped region as those tested using the ULD box. A second frame was designed to mount the clamped plate to the pendulum, and accommodate the existing clamp frame used for testing on the box.

3.5 Experimental Methodology

Four test series were conducted to experimentally determine the effect of venting configuration on the blast response of the aluminium target plate representing the diagonal side of a ULD. The tests included unconfined blasts (test series 1), fully-confined blasts (test series 2) and two configurations of fully-vented blasts (test series 3 with $\zeta = 0.7$ and test series 4 with $\zeta = 1.4$). All the blast tests were performed using a horizontal pendulum suspended from the ceiling of the blast chamber. The pendulum provided the necessary mounting for both the unconfined air blasts and confined blasting of the ULD box. A plastic explosive (PE4) charge was

detonated to produce the explosive loading on the target plates. The properties of this explosive are shown in Table 3.5. Bare, spherical charges of varying masses were detonated at a constant stand-off distance (SOD) of 163 mm for all the different test series. The SOD is measured as the distance from the centre of the charge to the target plate. The target plates were cut from the same sheet of a 2 mm thick aluminium alloy, grade 5754H22, to ensure consistent material properties across all the test series.

Table 3.5: Material and explosive properties of PE4

Density (kg/m^3) [41]	1.601
Detonation velocity (m/s) [41]	8193
TNT pressure equivalence (%) [10]	137

3.5.1 Unconfined Tests

The unconfined air blasts were performed on flat aluminium plates. The bare charge was detonated in air and the resulting pressure wave was impinged on the target plate. Due to the absence of any confinement, it was assumed there were no secondary shock waves or built-up pressure loads on the target plate [20].

3.5.1.1 Unconfined Load Description

The charge was located at the geometric centre of the target plate and at a stand-off distance of 163 mm by placing the charge within a polystyrene bridge. Figure 3.6 illustrates the placement of the polystyrene bridge before the charge was detonated. The polystyrene was assumed to burn quickly during the detonation of the charge and have insignificant effect on the blast response of the target plate [9].

3.5.1.2 Unconfined Test Description

The first set of unconfined air blasts was performed on the horizontal impulse pendulum. The purpose of this set was threefold:

1. To determine the rupture limit, in terms of charge mass, of the aluminium plate (above which no tests would be performed on the DIC pendulum).

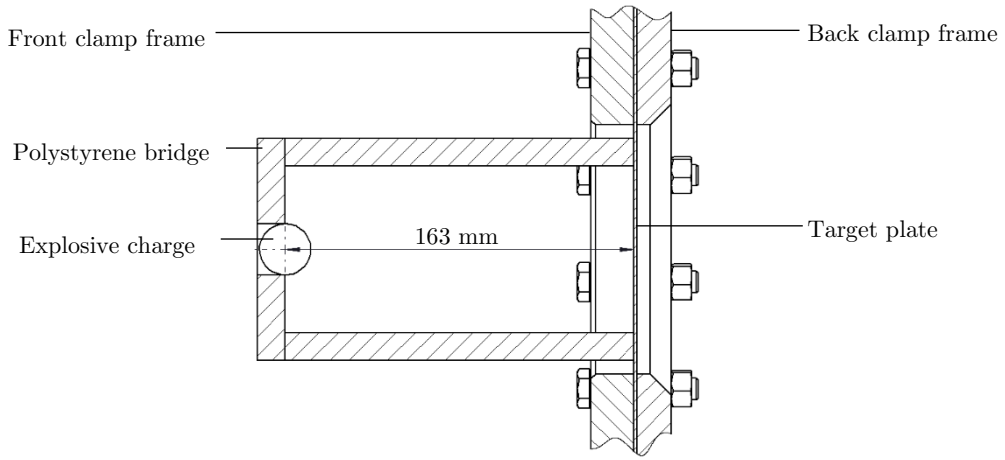

Figure 3.6: Diagram of the positioning of explosive charge for unconfined air blasts.

2. To assess the final deformation of the target plate in order to validate the numerical model simulating the tests.
3. To provide results of blast loading without any confinement to assess if the presence of the ULD itself affects the blast response of the target plate.

The test arrangement is shown in Figure 3.7. The target plate was secured between two clamp frames, resulting in an exposed area of 255 mm x 117 mm. A backing plate was used to mount the clamp frames onto the pendulum via four spacers, which would allow the target plate to deform without obstruction. Balancing masses were added to the rear of the pendulum to ensure the pendulum remained level during the tests.

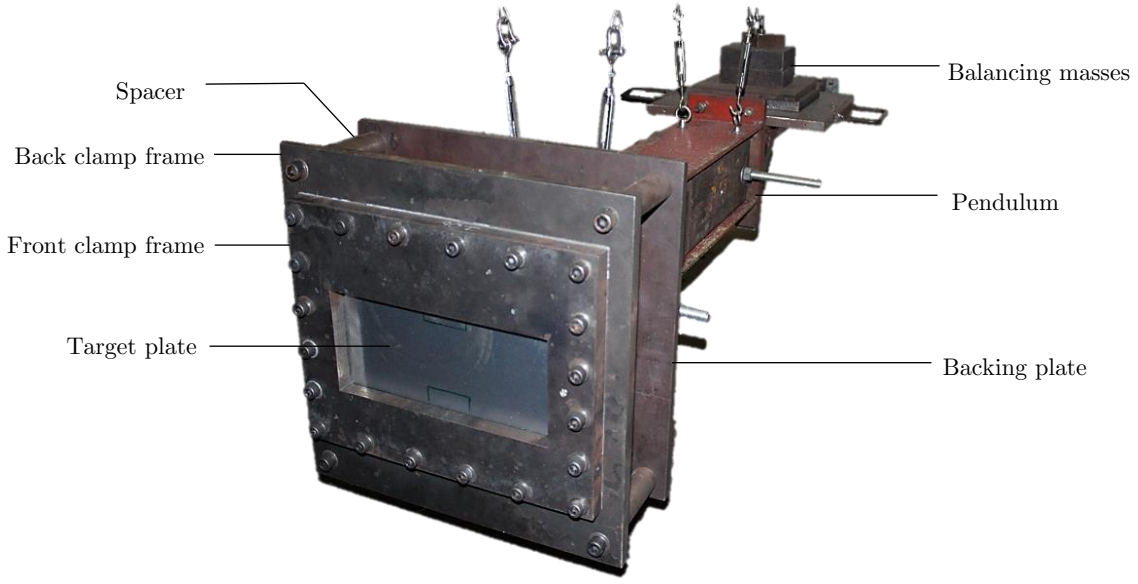

Figure 3.7: Photograph of the setup for unconfined air blasts.

3.5.1.3 Transient Deformation Measurements

Once the rupture threshold of the aluminium plates was established, additional tests were performed on a pendulum fitted with a pair IDT vision NR4 S3 high-speed cameras [42]. The cameras were used to film the out-of-plane displacement of the plates. The deformation of the target plate, when subjected to a blast load, was determined using the two sets of images by employing Digital Image Correlation (DIC). Further details about measuring the transient response are given in Section 3.6. A shroud was attached to either side of the pendulum to protect the equipment within the pendulum during the explosive testing: the shroud prevented the explosive products from interacting with the cameras and shielded the cameras from the intense light generated during the explosion. Low charge masses (up to 17 g) were detonated to ensure the plate did not rupture and eject high-speed fragments towards the camera system. The pendulum setup for the DIC tests is shown in Figure 3.8. The clamp frames and target plate were directly mounted onto the pendulum. Both shrouds were mounted to the sides of the pendulum and secured using a ratchet strap.

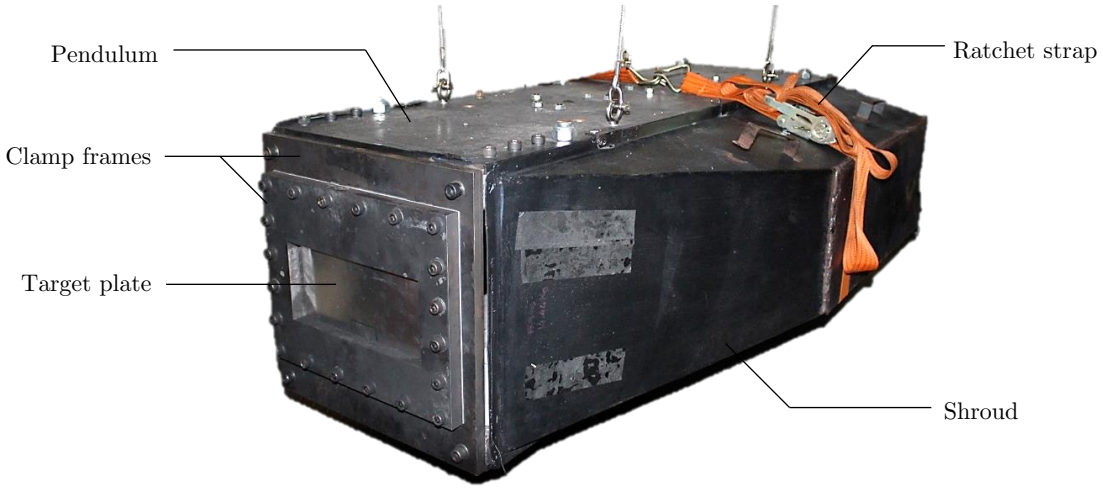

Figure 3.8: Photograph of pendulum arrangement using the high-speed camera system during unconfined air blast experiments.

Figure 3.9 illustrates the camera and lighting arrangement within the pendulum. The two high-speed cameras were positioned to the left and right end of the pendulum, and mounted on the same rail structure so that they could not move independently to one another. Two pairs of LED lights were used to provide the light required to illuminate the target area once the shrouds were attached to the pendulum.

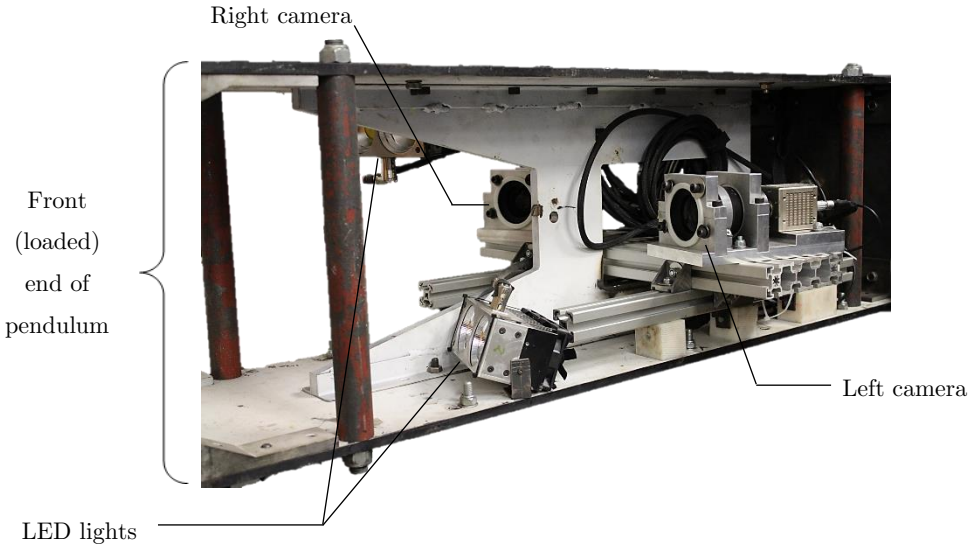

Figure 3.9: Photograph showing the internal layout of the camera and lighting systems (shrouds removed).

The two cameras formed an included angle of approximately 30°, and both were focussed on the central region of the target plate. The views of each camera were set to 1024 x 180 pixels, which provided a thin, full-width image of the target plate midline. The frame rate was set to 16000 fps (limited by the resolution of the camera views) and an exposure time of 31 μs was used during the blast tests (limited by the available light within the enclosed pendulum).

3.5.2 Confined Tests

Fully-confined and fully-vented blasts were performed on aluminium target plates representing the diagonal side of the manufactured ULD box. Bare charges were detonated within the empty container to produce a confined blast load on the plate. The effect of the degree of confinement was assessed by subsequently modifying the ULD box (by cutting out a venting area) to produce a different venting configuration for each confined test series.

3.5.2.1 Confined Load Description

The explosive charge was placed inside the ULD box and located using a polystyrene bridge identical to those used for the unconfined tests. The bridge ensured the charge was placed perpendicularly in line with the geometric centre of the target plate (which was the diagonal side of the box) and in the centre of the ULD box. Figure 3.10 shows the placement of the polystyrene bridge within the ULD box.

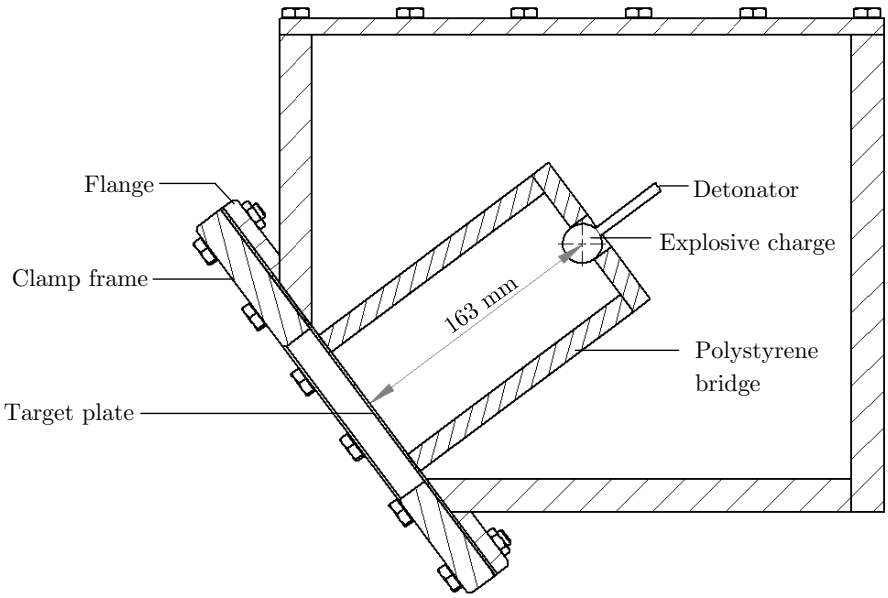

Figure 3.10: Diagram showing the positioning of a charge for internal explosive testing within the ULD box.

The stand-off distance of the fully-confined tests was kept at 163 mm – identical to that of the unconfined tests. The clamp frame securing the target plate to the box was also the same as the front clamp frame used in the unconfined tests. The target area and boundary conditions of the plates were therefore uniform across all the tests.

3.5.2.2 Fully-Confined Test Description

Fully-confined tests refer to the internal detonation of the sealed ULD box before any venting areas were introduced. Due to the lack of venting, the high-pressure explosive gases generated by the explosion were sealed within the structure and exerted a longer-term, quasi-static loading on the walls. The initial blast wave reverberated off the internal faces of the box which resulted in multiple shocks being exerted on the box [20].

The ULD box was directly mounted onto the horizontal pendulum using four M10 bolts through the back plate. The mounted box is shown in Figure 3.11. The target plate was secured to the flange of the box using a bolted clamp frame. The top plate of the box was removable to allow the charges to be placed inside the box, and bolted onto the box once the charge and detonator were in place. Two holes, each with a diameter of 2 mm, were drilled into the side of the box to allow the detonator cables to run out of the box and be connected to the trigger switch. The venting area created by these holes was considered negligible and the effect of the holes on the confinement of the test was assumed to be insignificant.

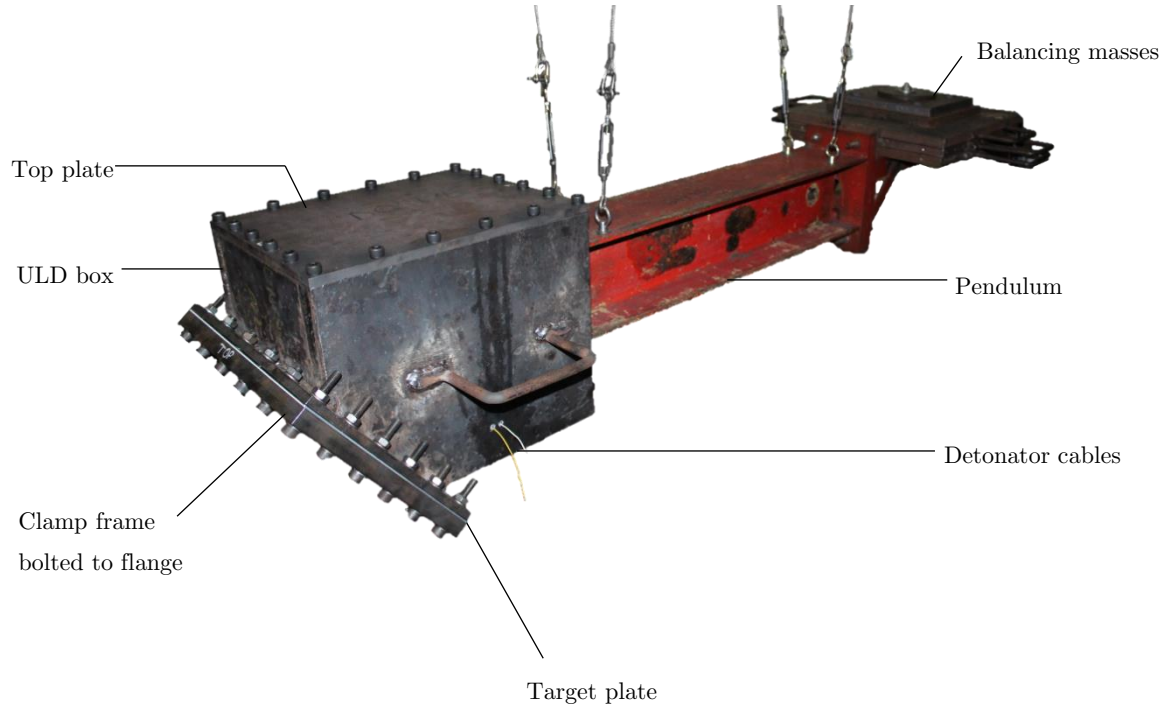

Figure 3.11: Photograph of fully-confined blast test arrangement.

3.5.2.3 Fully-Vented Test Description

The loading configuration used for the fully-vented tests was identical to the configuration used for the fully-confined tests, as shown in Figure 3.10. The fully-vented tests differed from the confined tests in that there was sufficient venting area for the explosive products to escape: it was assumed there was no pressure build-up within the structure [19]. However, due to the confinement of the structure, the initial blast wave was reflected off the internal walls and caused multiple shocks to be imposed on all the walls of the box and the target plate [19]. Two venting configurations were tested: the first configuration comprised of one venting area, resulting in a scaled venting area of $\zeta = 0.7$, and the second configuration had an additional, identically-sized venting area, which resulted in a scaled venting area of $\zeta = 1.4$.

The first fully-vented configuration was created by cutting a 220 mm x 252 mm venting area out of one of the side panels of the test box. Four holes were drilled into the opposite side panel from which to mount the box onto the pendulum, so that the venting area was aligned with the longitudinal axis of the pendulum to minimise the off-axis motion of the pendulum during the explosive testing. The existing four holes in the back plate were covered to prevent any venting through the holes. The setup of the first configuration of fully-vented tests is shown in Figure 3.12. Additional side masses were added to the pendulum to balance the off-axis weight of the clamp frame.

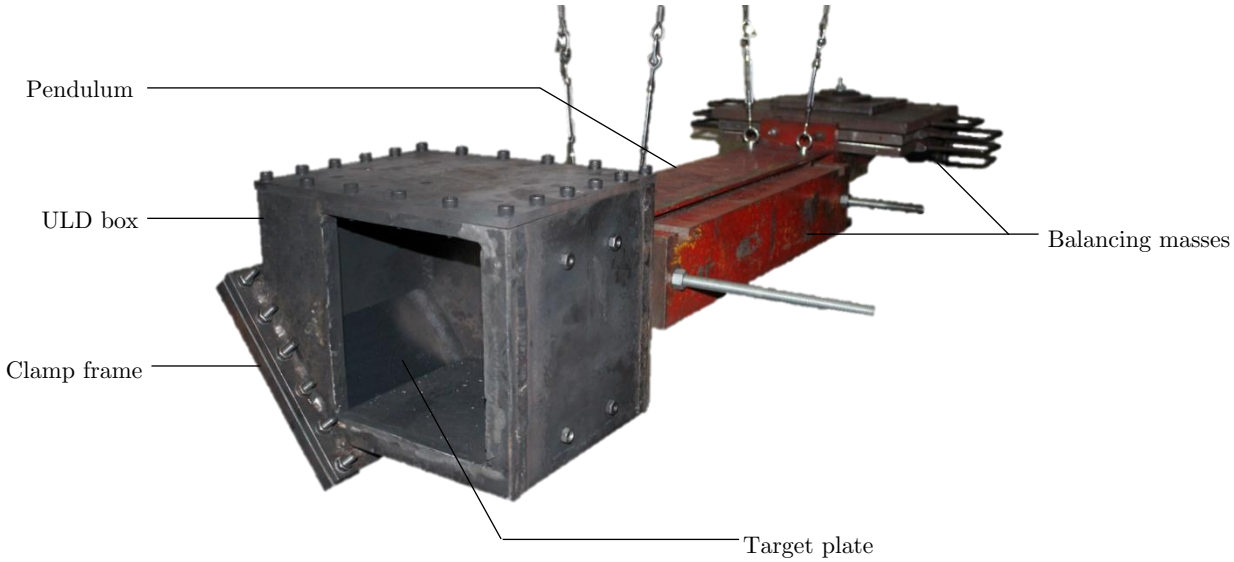

Figure 3.12: Photograph of fully-vented blast test arrangement for experiments with $\zeta = 0.7$.

A second venting area of 220 mm x 252 mm (identical to the first) was cut from the side panel opposite the existing venting area of the test box to create the second fully-vented test configuration. The symmetry of the test configuration enabled the box to be mounted onto the pendulum using the original mounting holes on the back plate (as mounted in the confined tests). The two identical venting areas would allow the explosive gases to be expelled through the sides simultaneously and not cause off-axis motion of the pendulum. The test setup is shown in Figure 3.13.

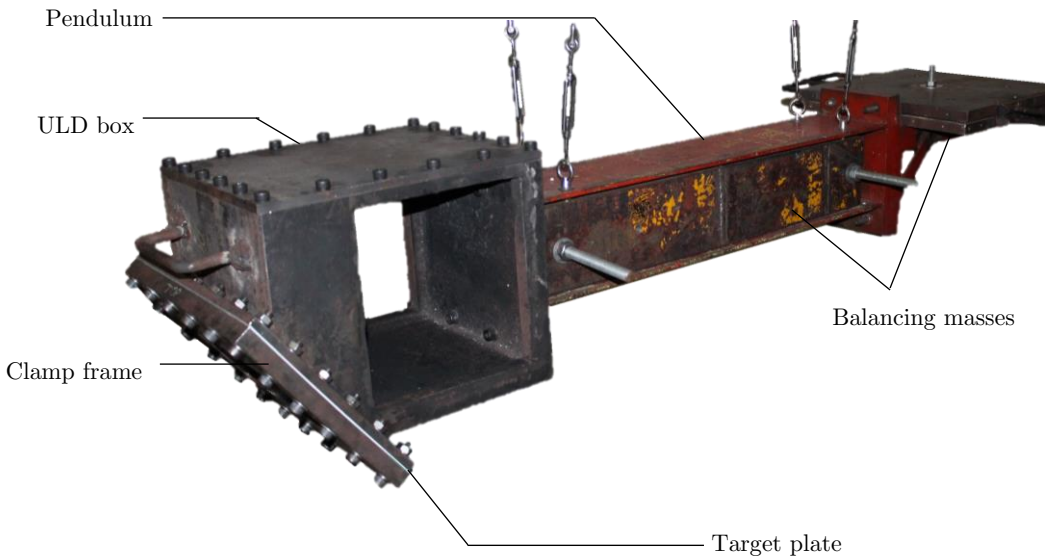

Figure 3.13: Photograph of fully-vented blast test arrangement for experiments with $\zeta = 1.4$.

3.6 Transient Response Measurement Methodology

Prior to blast testing using the DIC pendulum, both the target plate and high-speed cameras required preparation. The target plate had to be painted with a particular pattern to ensure the cameras were able to capture and track the deformation along the midline of the plate. The cameras subsequently needed to be calibrated to determine their relative positions to the target plate so that the captured deformation could be measured accurately. The images were processed and the deformation of the target plate determined using the Dantec Dynamics Istra 4D DIC software package.

3.6.1 Target Plate Preparation

The surface of the target plate exposed to the cameras was prepared using white primer and black paint. The region of application was only set to that which would be seen within the 1024 x 183 pixel band. The process is illustrated in Figure 3.14. First the plate was sand-blasted and degreased to roughen the surface and improve the adhesion of the primer to the plate (and mitigate the primer layer chipping off during testing). The primer was sprayed in a thin layer along the midline of the plate and allowed to dry completely before the black speckle pattern was applied. Care was taken to produce a pattern that had an acceptable variation in speckle size, shape and density distribution (avoiding speckled areas that were too sparse or too condensed).

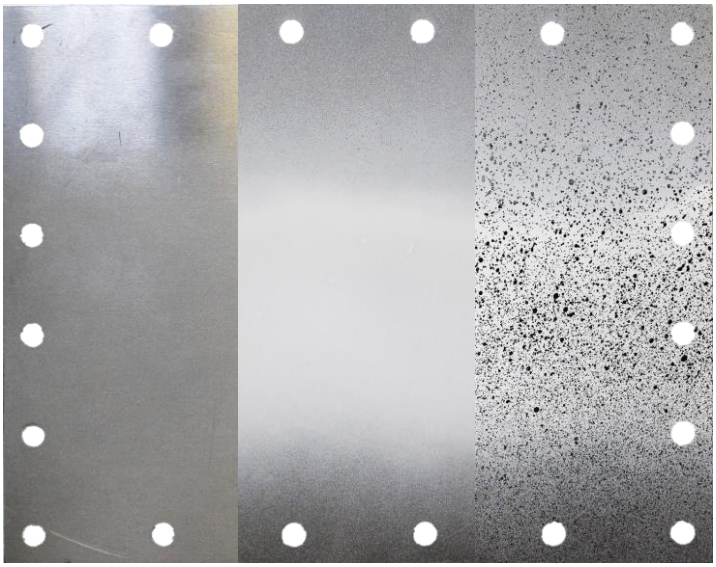

(a) (b) (c)

Figure 3.14: Photographs of target plate preparation showing (a) sandblasting, (b) priming and (c) speckling stages.

3.6.2 Camera Calibration

The calibration of the cameras was performed to establish certain projection parameters that would allow the deformation of the target plate to be accurately calculated. These parameters included the intrinsic properties of the camera imaging capability, such as the camera focal length, principal point location and orientation, and extrinsic properties of the software point-tracking capability, such as the translation vector and rotation matrix needed to measure distortions [42]. Images of a calibration target were recorded, with an accurate and known grid pattern, at various positions and orientations throughout the available scope of the cameras. The calibration target pattern contained 64 markers with a set of coordinate axes. The DIC software was used to track these markers from the recorded images, and determine a reference frame for both cameras that were compatible with one another. The calibration results were calculated and used as an input to the plate transient measurement process. Importantly, the calibration would ensure that the speckled pattern appearing in a pair of images recorded at the same time by both cameras was consistently tracked and could be analysed by the DIC software. In order to maintain accurate DIC results for every test, the cameras were recalibrated prior to each blast test because the intensity of the explosion could potentially have resulted in the cameras shifting and changing their relative positions. The previously calculated projection parameters would therefore not be valid for the slightly different camera orientations.

3.6.3 Trigger Switch

Because a single blast event, and the transient displacement of the target plate which followed, took place within 3 ms, it was important to ensure the cameras were recording and the images were being stored prior to the detonation of the explosive charge. To ensure no dynamic data was missed, a trigger switch was built into the polystyrene bridge using a sheet of tin foil which would allow an electric current to flow through it. Two connecting wires were attached to either side of the bridge (in contact with the foil) and connected to the camera image recording switch. Upon the detonation of the charge, and the almost-instantaneous destruction of the polystyrene bridge (and switch), the sudden break in current acted as the trigger to initiate the recording of the images. A buffer was set so that the cameras would store the ten images prior to the trigger being activated to account for any delays in the circuit response and ensure the transient response was captured.

4 Experimental Results

A total of twenty-six blast tests were performed on quadrangular aluminium plates to assess the blast response of a unit load device at four degrees of venting: unconfined, fully-vented (with scaled areas of $\zeta = 0.7$ and $\zeta = 1.4$), and fully-confined blasts. High-speed imaging and DIC methods were used to measure the transient blast response of the target plate in the unconfined tests. Final plate deformations were measured in all the test series, however, most of the plates exhibited warping once removed from the test rig. This permanent distortion was due to the residual stresses present in the plates following the blast loading. The deformed target plates were therefore bolted to the clamp frame, prior to being measured, to remove the influence of the distortions on the deflection measurements. Final midpoint and maximum deflections were measured using a height gauge and obtained from 3D scans of the plates. In all cases, the corresponding measurements were within 2% of one another. The 3D scans provided data to produce the target plate midline profile, as well as contour maps of the exposed area deformations.

4.1 Unconfined Blast Test Results

Thirteen unconfined blasts were successfully performed, with charge masses varying from 10 g to 25 g. A stand-off distance of 163 mm was used for all the tests. Three were performed prior to fitting the high-speed camera system, designated by the *UC* abbreviation. These tests were used to determine the charge masses which would not cause the plate to rupture and would therefore not damage the camera system. The remaining ten tests were performed on the DIC pendulum (with the camera system installed) to capture the transient response to the blast load, designated by the *DIC* abbreviation.

4.1.1 Permanent Plate Deflections

The permanent deflection of the unconfined tests is provided in Table 4.1. Slight asymmetry was evident in all the tests, so both the final midpoint deflection and final maximum deflection of each plate are listed. However, the difference is less than 1 mm in all the tests. The correlation between the difference in deflections (which was used as the measure of asymmetry) and the midpoint deflection of the target plate is shown in Figure 4.1. The observed trend was that a higher degree of asymmetry was present in plates with lower deflections. Significant asymmetry, in the context of these results, was a difference in deflection of more than 10%, and was observed in two cases: the DIC10–10 g and DIC5–12 g blast tests. The plates of these two tests exhibited the lowest deflections in the unconfined blast series.

The blast response of the unconfined test specimens was characteristic of the deformation of fully-clamped rectangular plates [26,29,30]. Mode I failure (large inelastic deformation) was observed in all the plates. The presence of plastic hinges was evident, especially in the plates which demonstrated higher deformations, and developed at an angle of approximately 54°. The theoretical value, described by Jones [30], for the aspect ratio of the exposed area of the target plate, was 53.1°. Boundary pull-in was observed in some of the tests; increasing boundary effects were exhibited, in order, in the UC2–20 g, UC3–25 g and DIC2–15 g blasts.

Table 4.1: Final deflection results of unconfined blast tests.

Test number	Charge mass (g)	Final midpoint deflection (mm)	Final maximum deflection (mm)	Difference in deflection (%)
DIC3	10	7.22	7.88	8.4
DIC10	10	5.73	6.58	13
UC1	12	7.61	7.81	2.6
DIC1	12	7.11	7.63	6.8
DIC4	12	8.50	9.16	7.2
DIC5	12	6.32	7.14	11
DIC2	15	12.36	12.61	2.0
DIC6	15	12.89	13.06	1.3
DIC7	17	10.67	11.13	4.1
DIC8	17	13.85	13.92	0.5
DIC9	17	10.65	11.58	8.0
UC2	20	11.10	11.86	6.4
UC3	25	14.89	14.92	0.2

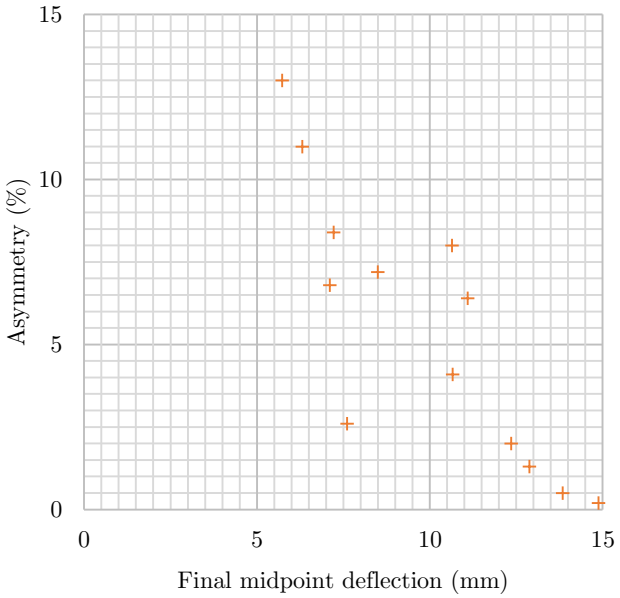

Figure 4.1: Graph of the correlation between plate asymmetry and final midpoint deflection in unconfined blasts.

The final midpoint deflections for the unconfined blasts are shown in Figure 4.2. Three tests were observed to produce anomalous results: both 15 g tests and DIC8–17 g produced irregularly high deflections. Inspection of the target plates revealed large boundary pull-in of the top and bottom edges of DIC2–15 g (which exhibited a greater boundary effect than in all

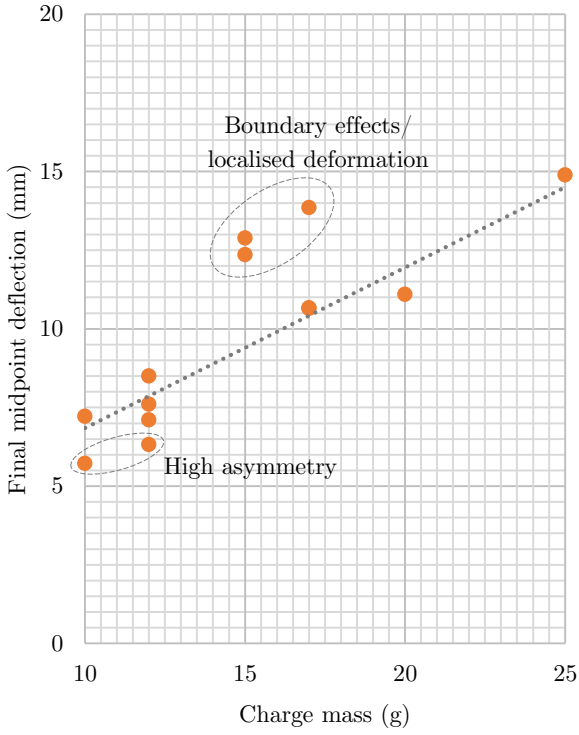

Figure 4.2: Graph of final midpoint deflection vs charge mass for the unconfined blast tests.

Figure 4.3: Final long-side midline profiles of selected unconfined blast tests.

the unconfined blast tests). Localised deformations were present in the other two blast tests. The irregularities of these unconfined tests and the effect on the test results are further discussed in Section 8.1.1. Also identified in Figure 4.2 are the 10 g and 12 g tests displaying high asymmetry. The deflections of the remaining blasts correlated well with a linear regression line, demonstrating a coefficient of determination of $R^2 = 0.96$.

An increase in charge mass resulted in an increase in plate deformation. This trend was true for both the midpoint and midline deflection of the target plate. Figure 4.3 illustrates the final plate profile of selected unconfined blasts from each of the tested charge masses. Although slight asymmetry was exhibited, two deformation zones were observed in all the profiles: a short, steady rise in deflection from either edge of the clamp frame and a longer, central plateau with little change in height. At increasing charge masses, the edge displacements became steeper, resulting in higher midline deflections, however, the length of the central region remained unchanged. Shown in Figure 4.4 are the contour plots of the target plates corresponding to the midline profiles of Figure 4.3. The height difference between two contour lines was set to 1 mm. The contour plots further demonstrate the development of the plastic hinges and slightly asymmetric deformation. At higher charge masses, such as in Figure 4.4(c)–(d), the plastic hinges of the deformed plates were more clearly exhibited. The plates exhibited plastic deformation along the clamped edges and two pairs of plastic hinges were observed to develop from each corner and meet at the plate midline. These two intersections were joined by a longitudinal plastic hinge.

Slight asymmetric deformation was observed in most of the plates and is accentuated by the contour lines in Figure 4.4. The difference in profile height in the central region of the plates was consistently less than 2 mm. Higher deflections were observed to occur closer to the right edge of the plate, indicating that the asymmetry was likely due to a consistent factor – such as the charge location or a non-uniform clamping (boundary) condition – instead of being due

Note: Consecutive contour lines indicate a difference in height of 1 mm.

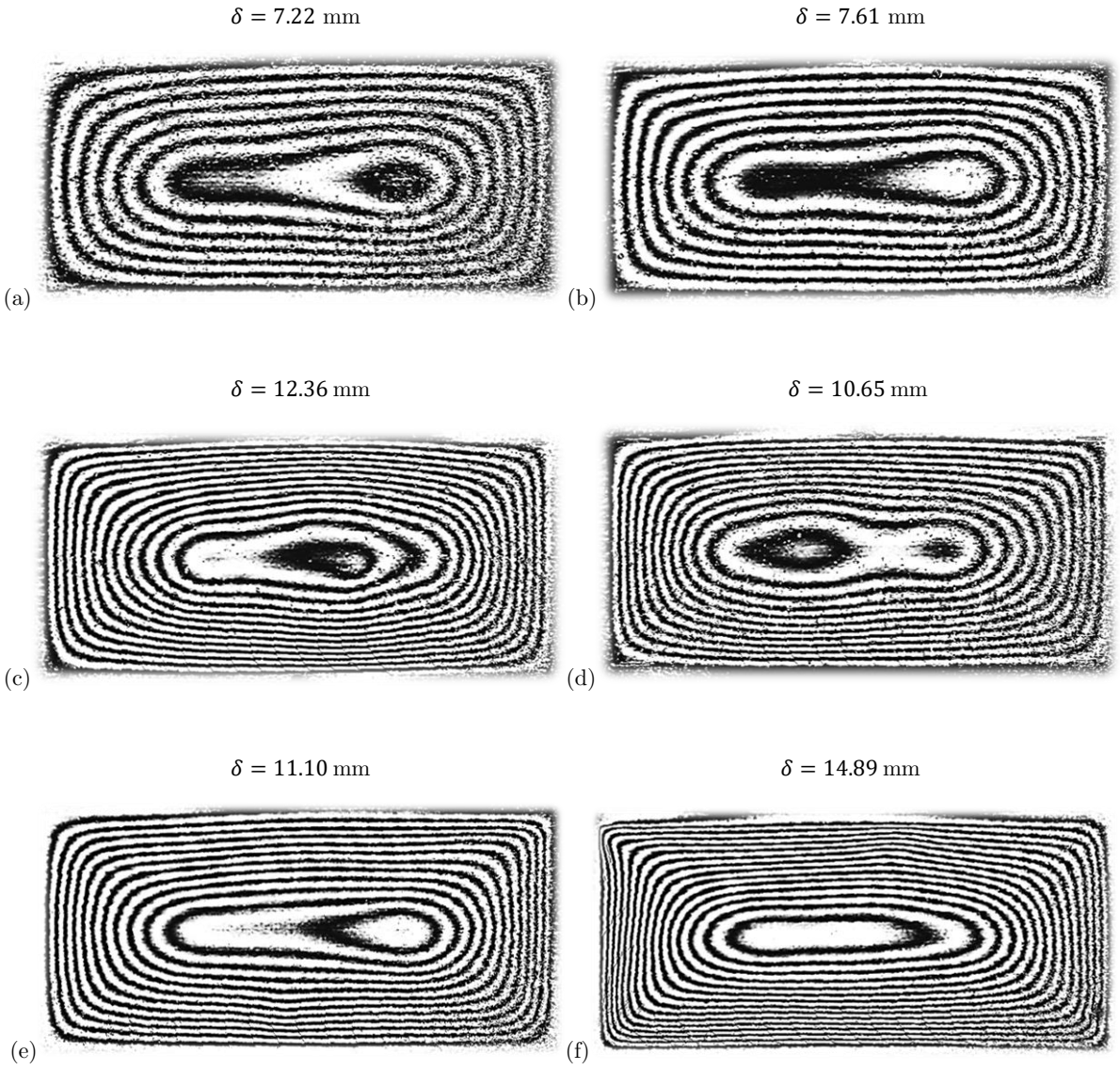

Figure 4.4: Contour plots of exposed target plate area for unconfined blasts performed with charge masses of (a) 10 g, (b) 12 g, (c) 15 g, (d) 17 g, (e) 20 g and (f) 25 g.

to irregularities in charge shape, plate material or charge detonation. However, the unconfined blast results were considered valid since the target plates (except for those with localised deflections or irregular boundary effects) exhibited only slight asymmetry and the final midpoint deflections demonstrated a linear dependency on charge mass.

4.1.2 Transient Plate Deflections

DIC was applied to the images captured during the unconfined blasts tests to determine the transient target plate deformation. The initial response of the plate to the blast load was a sudden rise to a peak deflection which attenuated to a final deformed state. The results for the peak midpoint deflections of the unconfined blasts are presented in Table 4.2.

Table 4.2: DIC results for the peak midpoint deflection of unconfined tests.

Test number	Charge mass (g)	DIC status	Peak midpoint deflection (mm)	Final midpoint deflection (mm)	Reason for no data
DIC3	10	Successful.	9.84	7.22	-
DIC10	10	Successful.	9.34	5.73	-
DIC4	12	Successful.	11.19	8.50	-
DIC5	12	Successful.	9.43	6.32	-
DIC6	15	Successful.	15.41	12.89	-
DIC9	17	Successful.	13.67	10.65	-
DIC1	12	No data.	-	7.11	Irregular speckling.
DIC2	15	No data.	-	12.36	Sparse speckling.
DIC7	17	No data.	-	10.67	Trigger failure.
DIC8	17	No data.	-	13.85	Paint flaking off.

In some cases, no DIC data was captured. In two cases, no data was captured due to improper speckling of the target plate. In one case, the camera trigger was not activated by the detonation of the charge and the blast response was not recorded. In one 17 g detonation, the sudden, large deformation caused the paint on the plate to flake off, exposing the reflective surface of the aluminium and causing the DIC software to be unable to continue the analysis.

The transient midpoint deflections of the successful DIC tests are shown in Figure 4.5. The plates were observed to begin moving at approximately 100 µs and the peak midpoint deflection was reached before 400 µs for almost every test. Thereafter, the plates exhibited elastic oscillations which converged towards a final deformation. A greater elastic vibration was observed in the tests with lower charge masses, as evidenced by the 3 mm – 5 mm difference between the initial peak and subsequent trough in deflection of the 10 g and 12 g tests. The 15 g and 17 g tests displayed a difference of approximately 2.5 mm and 3 mm, respectively.

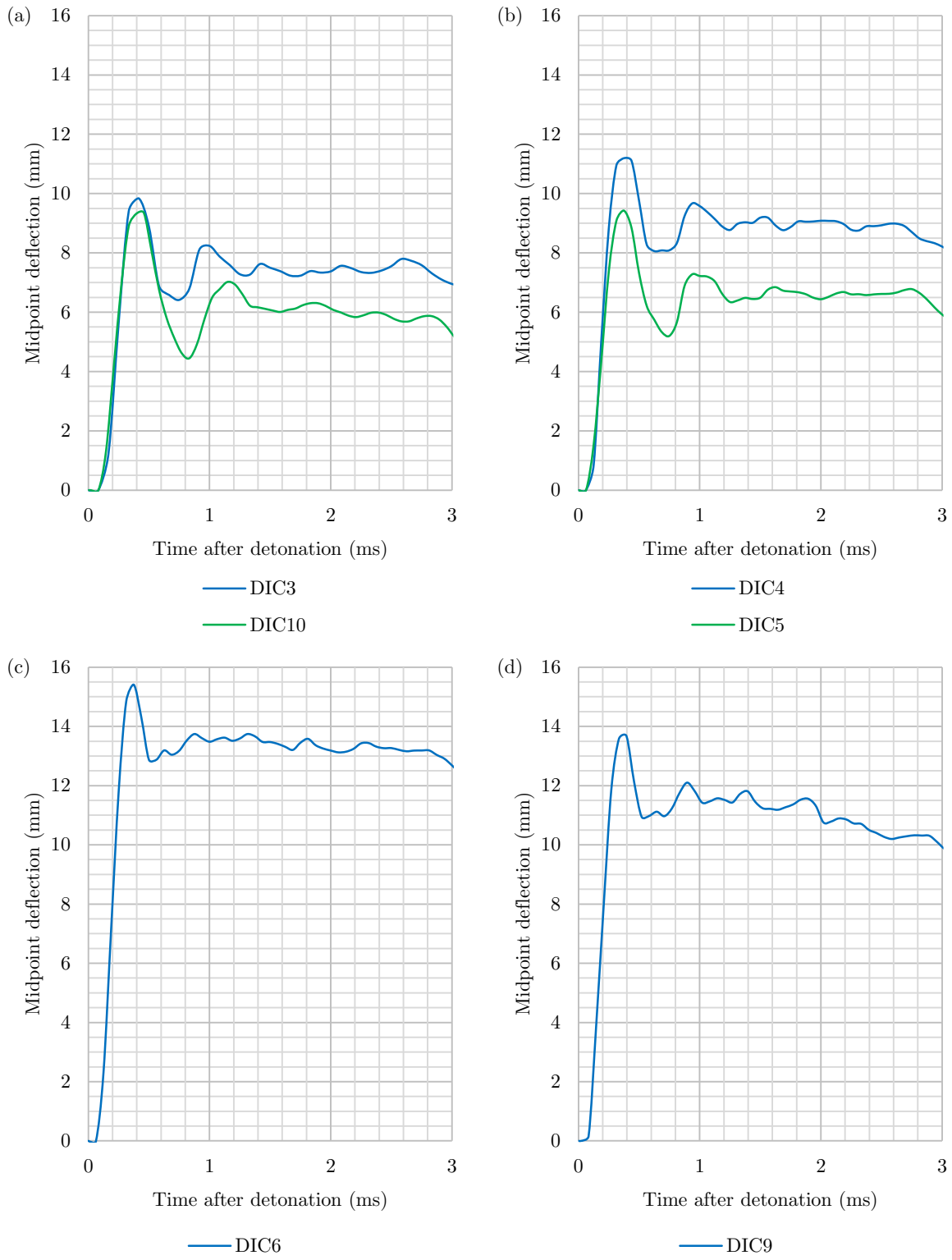

Figure 4.5: Transient midpoint deflections of unconfined blasts tested with charge masses of (a) 10 g, (b) 12 g, (c) 15 g, and (d) 17 g.

The transient midline profile deflection due to unconfined blast loading is shown in Figure 4.6 to Figure 4.11. In some cases, the DIC results produced regions of spurious deformations, usually in the form of an upward or downward deflection spike. This anomaly was due to dust specks, or other fragments, moving past the camera lenses during the blast and obscuring the plate deformation. These regions were removed, consequently creating blank regions in the data, as seen in Figure 4.6 and Figure 4.11.

The plate profile progression from an initial, single peak to that with two peaks was observed to occur before the maximum deformed state was reached. The initial peak exhibited an off-centre development in all the tests, which increased in eccentricity – particularly at higher charge masses – and resulted in asymmetric profile development. The same template was used to locate the polystyrene bridge – used to hold the charge in place before detonation – for all the tests, suggesting that the off-centre deformation was not due to charge location. Furthermore, a test setup with a 25 mm off-centre charge placement (as suggested by the DIC9–17 g results of Figure 4.11) would be noticeable prior to blasting and consequently unlikely to be performed. A non-uniform clamping condition, resulting in less contact forces on one side of the clamp, was a plausible explanation for the off-centre deformation being biased to one side of the plate, and the eccentricity increasing at higher charge masses. However, no boundary pull-in was observed at either plate sides, suggesting the initial off-centre deformation was elastic but resulted in stronger plastic hinges, and greater permanent deformation, on the right side of the target plate.

Data for test DIC3–10 g was captured at a sampling frequency of 12 000 Hz, resulting in a new data point every 83.33 μs. The maximum plate profile was observed 416.7 μs after detonation in this test. In all the following DIC tests, the sampling frequency was increased to 16 000 Hz to obtain additional data points and improve the accuracy of the peak deformation result. The period between data was 62.5 μs for these tests, and the peak deformed state for these tests was observed to occur at approximately 375 μs after the detonation of the explosive, which would be a slightly more accurate representation of the peak displacement.

Following the peak deformation, the midline deflection reduced and converged towards the final plate profile. The shape of the peak midline profile did not change significantly as the final profile was reached. In the 10 g and 12 g tests, the transient response demonstrated a slower convergence towards the final profile compared to the 15 g and 17 g tests. A large elastic response at smaller charge masses was evidenced by greater oscillations about the final profile; at higher charge masses the elastic response was observed to converge quickly with fewer oscillations.

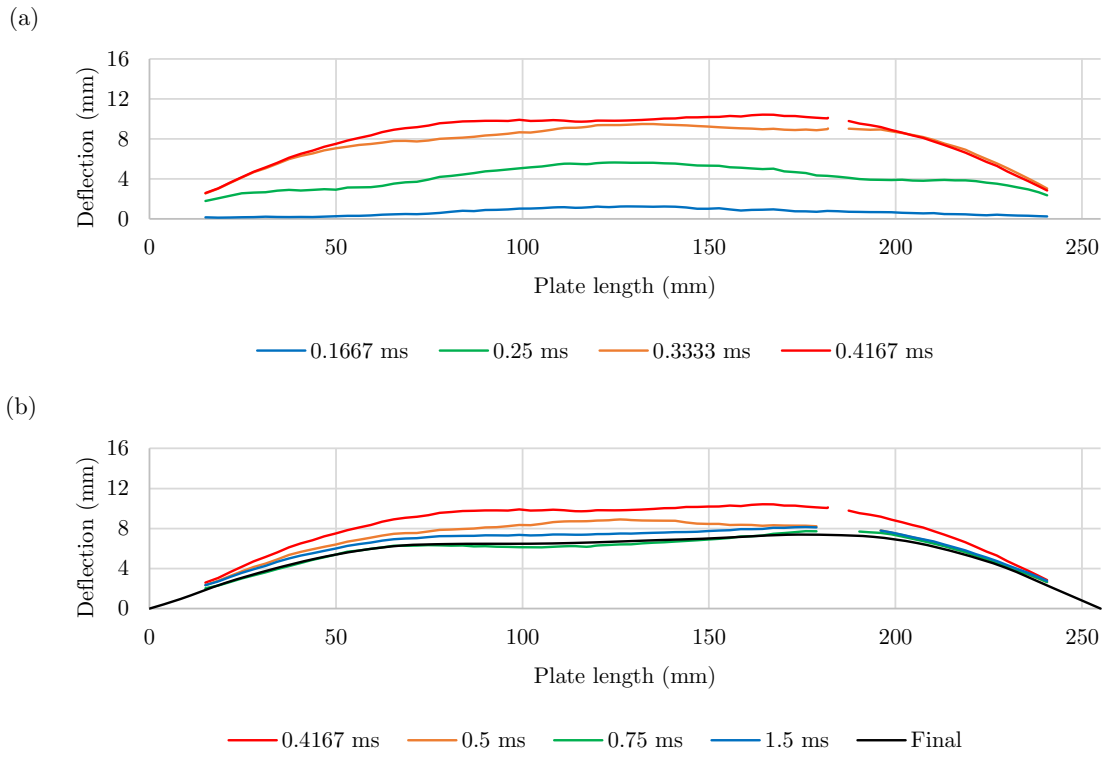

Figure 4.6: Graphs of the transient midline profile for test DIC3–10 g illustrating the development from (a) undeformed to peak deformation and (b) peak to final deformation.

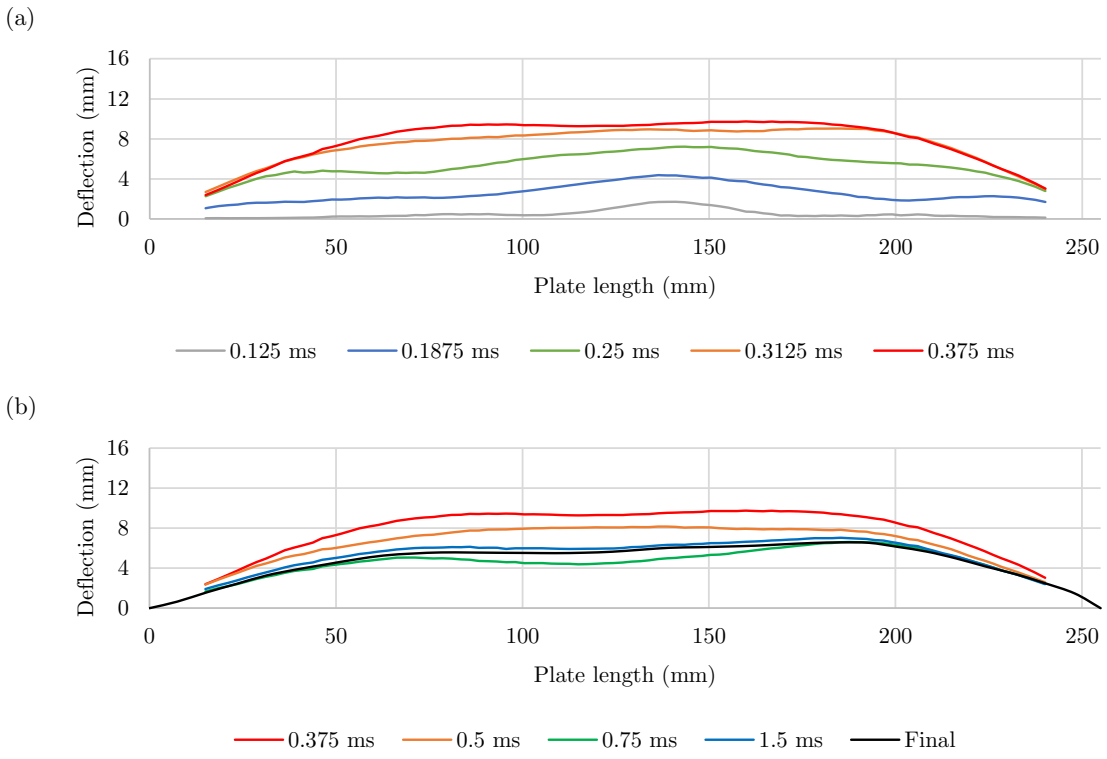

Figure 4.7: Graphs of the transient midline profile for test DIC10–10 g illustrating the development from (a) undeformed to peak deformation and (b) peak to final deformation.

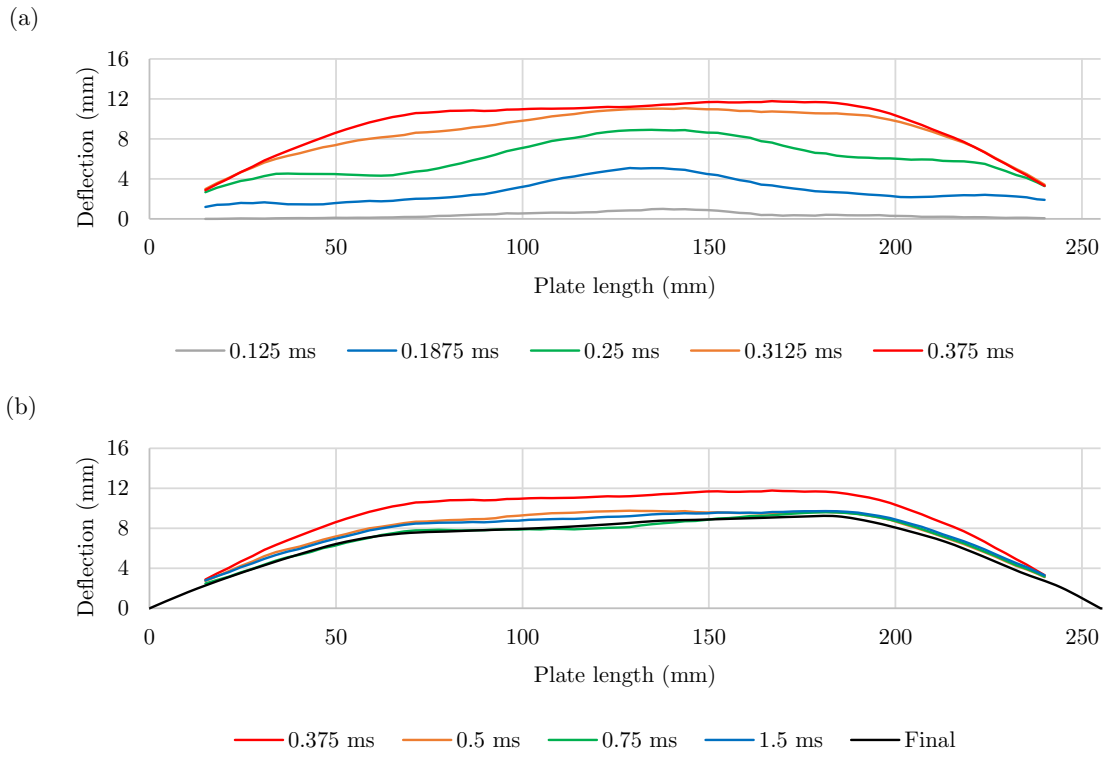

Figure 4.8: Graphs of the transient midline profile for test DIC4–12 g illustrating the development from (a) undeformed to peak deformation and (b) peak to final deformation.

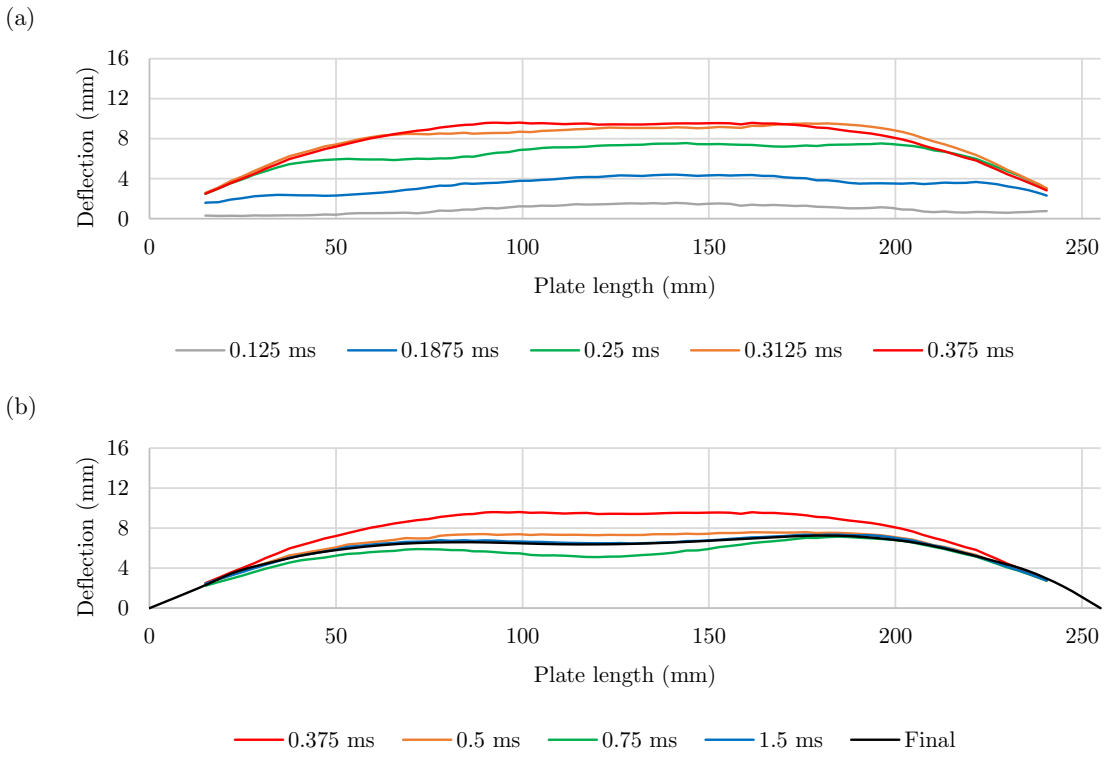

Figure 4.9: Graphs of the transient midline profile for test DIC5–12 g illustrating the development from (a) undeformed to peak deformation and (b) peak to final deformation.

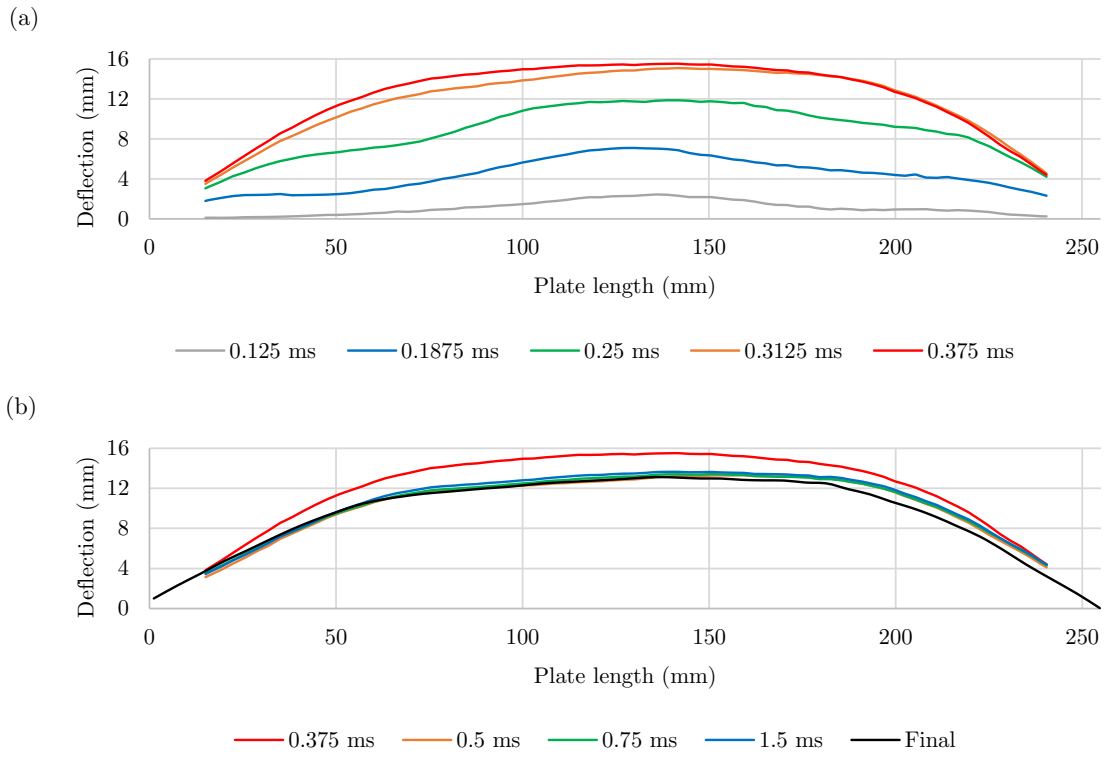

Figure 4.10: Graphs of the transient midline profile for test DIC6–15 g illustrating the development from (a) undeformed to peak deformation and (b) peak to final deformation.

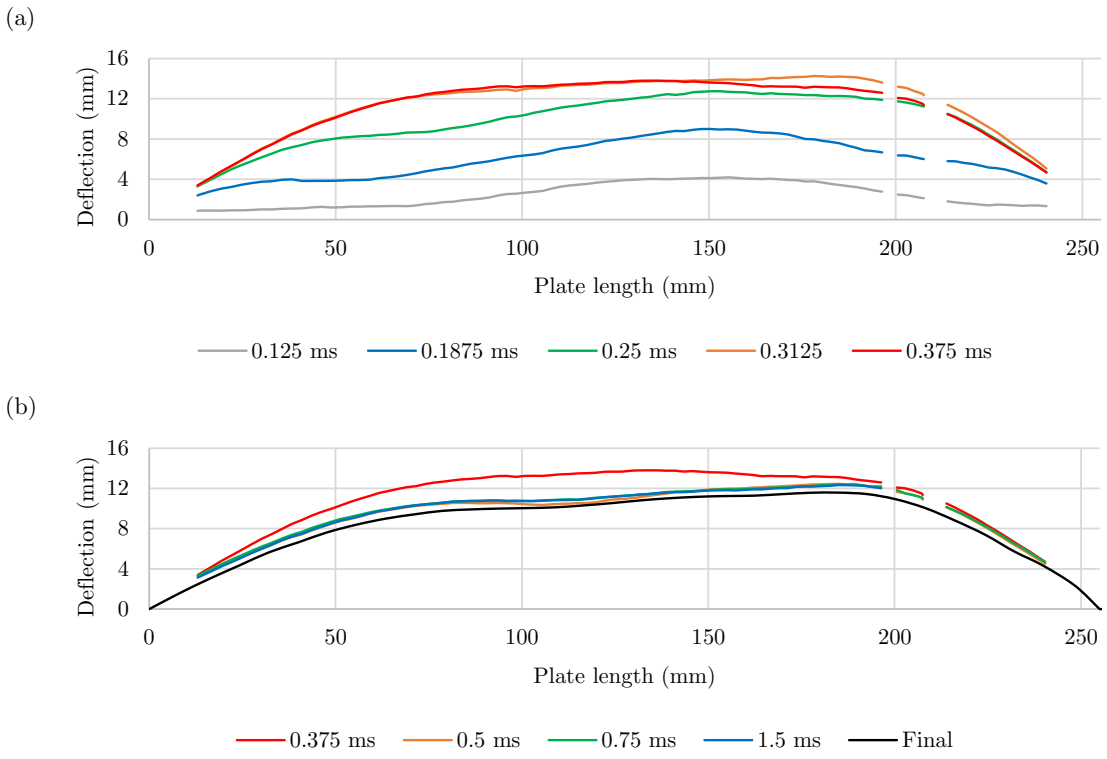

Figure 4.11: Graphs of the transient midline profile for test DIC9–17 g illustrating the development from (a) undeformed to peak deformation and (b) peak to final deformation.

4.2 Fully-Confined Blast Test Results

Five fully-confined blast tests, at charge masses varying from 10 g to 20 g, were performed using the ULD box without any venting areas. These tests were designated by the *FC* abbreviation. The transient response was not measured, and only final plate deformations were available for analysis. The midpoint deflections of the target plates are listed in Table 4.3. Complete rupture of the target plate was observed in the 20 g test. The remaining tests exhibited symmetric deformation with the midpoint deflection being the maximum deflection.

Table 4.3: Midpoint deflections of fully-confined tests.

Test number	**Charge mass (g)**	**Final midpoint deflection (mm)**
FC3	10	13.67
FC2	12	16.34
FC4	15	17.01
FC5	17	17.25
FC1	20	Rupture

An increase in deflection was evident when the charge mass of the tests was increased. However, the relationship between deflection and charge mass was not linear, as shown in Figure 4.12. Instead, a non-linear, concave relationship was demonstrated by the plates tested with charge masses greater than 12 g. Over this range, the gradient decreased as the charge mass increased, indicating a deflection limit was approached before complete rupture (at 20 g) occurred. For tests with charge masses below 12 g – where the effects of a rupture threshold were absent – a linear trend in deflection was assumed, as suggested in literature [29,32,33] and by the other blast tests performed in this project.

For the tests with charge masses ranging from 10 g to 17 g, the target plates deformed as a uniform dome. In each of these tests, mode I failure was evidenced by the development of characteristic plastic hinges and boundary pull-in at all the clamped edges. Increased deformation, in terms of both greater deflection and greater boundary pull-in, was observed at higher charge masses. The final midline profiles of the fully-confined target plates are shown in Figure 4.13. The profiles exhibited a steady rise in deflection from either clamped edge and a slightly-bulging central region. Each of the plates displayed symmetrical profiles, with similar profile shapes being produced by the 12 g, 15 g and 17 g blasts: these three tests exhibited midline deformations within 1 mm of each other. The contour plots of the unruptured plates,

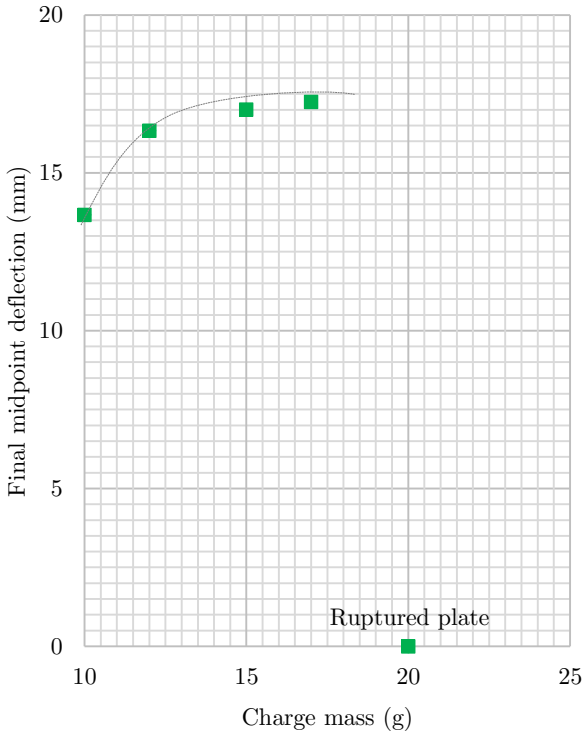

Figure 4.12: Graph of final midpoint deflection vs charge mass for fully-confined tests.

shown in Figure 4.14, further demonstrated the symmetrical deformation of the target plates. The plastic hinge development from each corner towards the midline was also observed. The bottom corners of the target plate were not adequately captured by the 3D scanner, resulting in greyed-out patches in these regions.

The fully-confined test at 20 g exhibited mode II failure (complete tensile-tearing at the clamped supports). The ruptured target plate of test FC1 is shown in Figure 4.15. Tearing first occurred along the top edge of the exposed target area, as evidenced by the scorch mark of leaked explosive products in this region. Tearing continued along the side edges of the target area, causing the plate to hinge along the bottom edge (most of this hinge remained on the target plate). However, tearing along the bottom edge soon commenced, resulting in complete rupture of the exposed target plate area. Additionally, boundary pull-in was observed at both

Figure 4.13: Final long-side midline profiles of fully-confined tests.

Note: Consecutive contour lines indicate a difference in height of 1 mm.

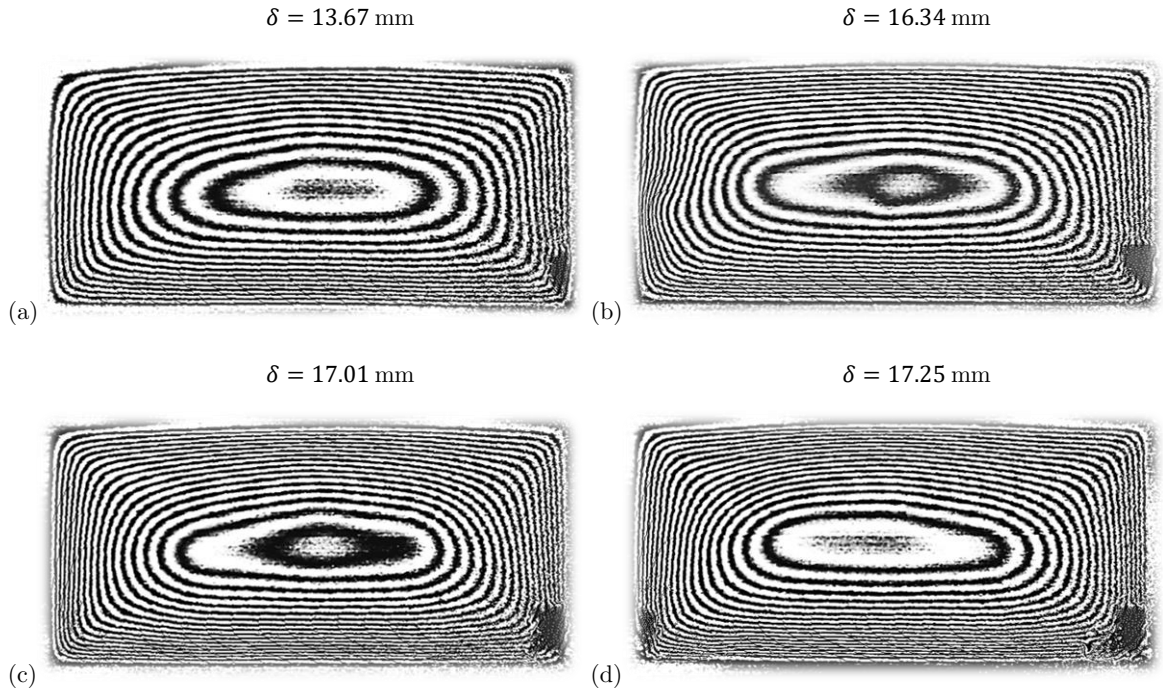

Figure 4.14: Contour plots of exposed target plate area for fully-confined blasts performed with charge masses of (a) 10 g, (b) 12 g, (c) 15 g and (d) 17 g.

the bottom and side edges, causing distortion of the bolt holes along those edges. The failure of the FC1–20 g target plate indicated the severity of a fully-confined blast compared to configurations with less confinement: the 20 g fully-confined blast was the only test – out of those performed with other venting configurations – to cause complete plate rupture.

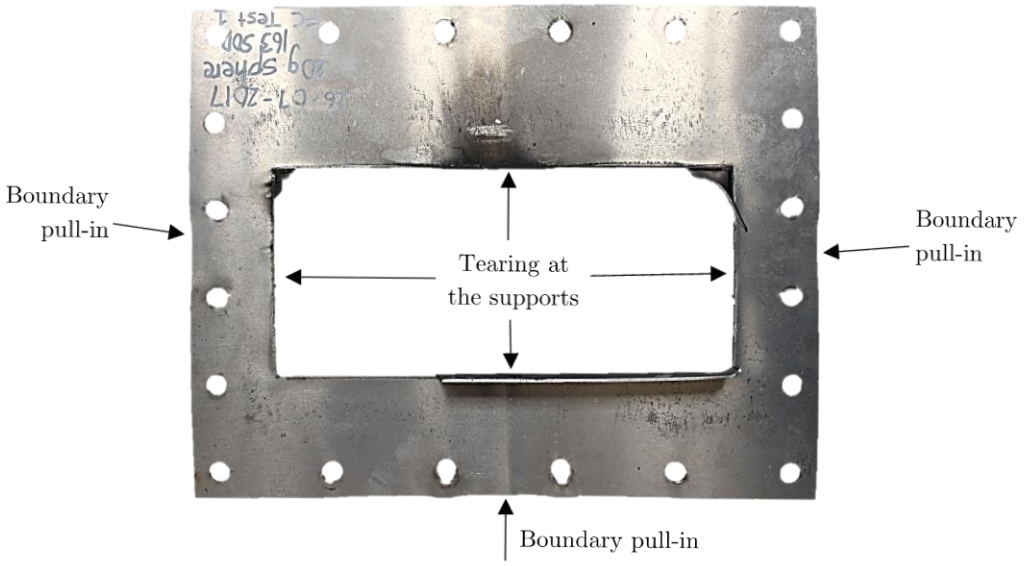

Figure 4.15: Photograph of ruptured target plate from FC1 – 20 g test.

4.3 Fully-Vented ($\zeta = 0.7$) Blast Test Results

The first series of fully-vented blast tests was tested with the box having a 220 mm x 252 mm venting area cut from one side panel, resulting in a scaled venting area of $\zeta = 0.7$. The tests were therefore designated by the *FV(0.7)* abbreviation. Four different charge masses, ranging from 10 g to 25 g, were tested. Table 4.4 lists the midpoint and maximum deflection of the first series of fully-vented tests. Although asymmetric deformation was observed in two of the tests, the difference in deflection was less than 10% and the asymmetry was consequently considered negligible.

Table 4.4: Deflection results of fully-vented ($\zeta = 0.7$) blast tests.

Test number	Charge mass (g)	Final midpoint deflection (mm)	Final maximum deflection (mm)	Difference in deflection (%)
FV(0.7)2	10	11.51	11.66	1.3
FV(0.7)1	15	15.89	15.89	0.0
FV(0.7)3	20	17.84	18.77	4.9
FV(0.7)4	25	23.24	23.24	0.0

Mode I failure of the target plates was observed in each of tests. All the plates developed plastic hinges characteristic of quadrangular plate blast loading and the tests at 15 g and higher exhibited boundary pull-in along the top and bottom plate edges. An increase in plate deformation was observed at higher charge masses, however, no transition to mode II failure (plate tearing) was present in any of the results. The final midpoint deflection results are shown in Figure 4.16. A linear regression line was fitted to the data, resulting in a coefficient of determination of $R^2 = 0.97$. The strong linear relationship suggested that a rupture threshold was not approached in these blast tests – even at 25 g, the highest tested charge mass in the experiments.

The final midline profile of the plates is shown in Figure 4.17. The plates demonstrated similar profile development: a sudden, steady rise in deflection from both clamped edges which transitioned to a slightly-bulging plateau in the central region of the plate. The gradient of the edge deflections increased as the charge mass increased, resulting in higher midline deflections. The length of the central plateau remained similar across all the tests. Despite the asymmetric venting configuration of the ULD box, most of the plate profiles did not display significantly asymmetric deformations. The venting area was located to the right of the target plates shown in Figure 4.17. Higher deflections were expected to occur in the plate region closer to the side

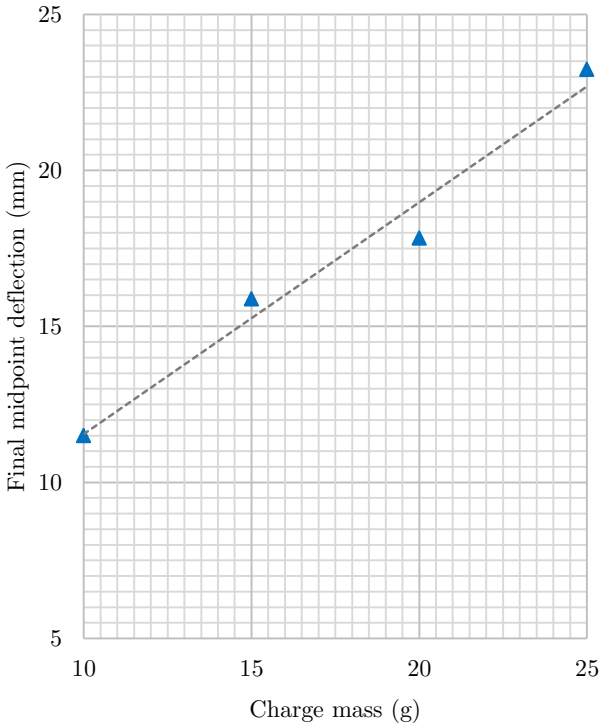

Figure 4.16: Graph of final midpoint deflection vs charge mass for the fully-vented ($\zeta = 0.7$) blast tests.

of the ULD box without any vents, since more pressure would accumulate in this region compared to the vented (opposite) side of the box. Contour plots are shown in Figure 4.18 to further evaluate the deformation of the target plates. The contour plots corresponded with the orientation of the midline profiles; the vented side of the box was therefore located on the right side of the plots. The test performed at 20 g displayed slight asymmetry consistent with the venting configuration: a maximum deflection was observed toward the sealed (unvented) side of the plate due to the additional pressure accumulation in this region. The remaining tests, however, exhibited symmetric deformations, with the peak deflection occurring at, or near, the midpoint of the plate.

Figure 4.17: Final long-side midline profiles of fully-vented ($\zeta = 0.7$) tests.

Note: Consecutive contour lines indicate a difference in height of 1 mm.

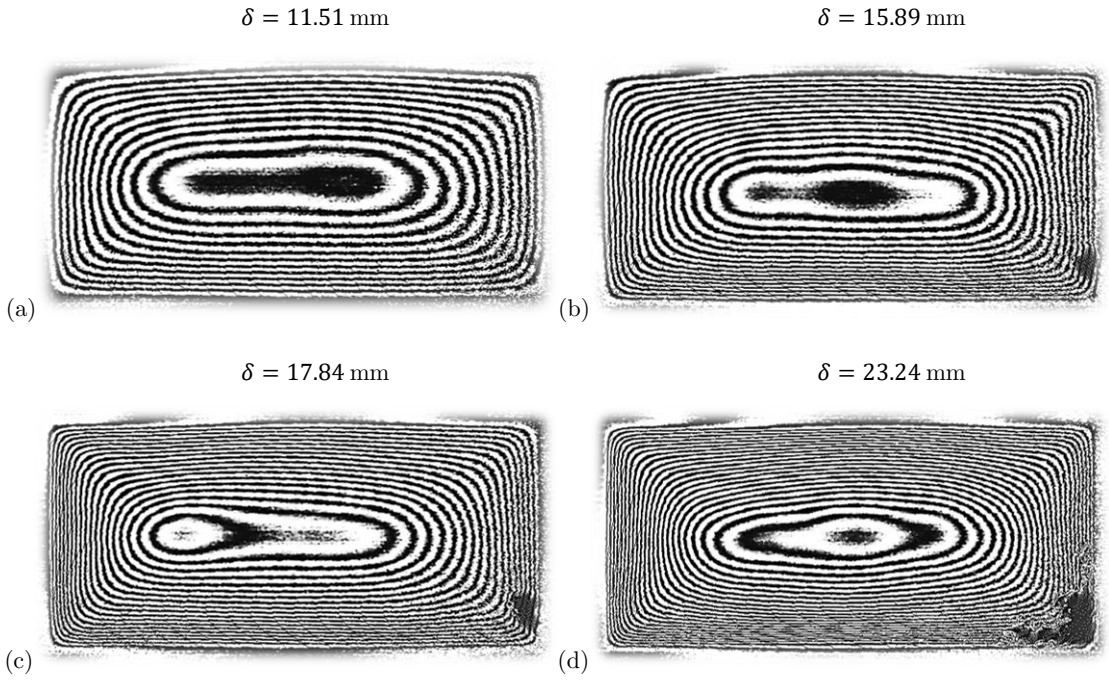

Figure 4.18: Contour plots of exposed target plate area for fully-vented ($\zeta = 0.7$) blasts performed with charge masses of (a) 10 g, (b) 15 g, (c) 20 g and (d) 25 g.

4.4 Fully-Vented ($\zeta = 1.4$) Blast Test Results

The second series of fully-vented blasts was tested with the box having a second venting area of 220 mm x 252 mm cut from the side panel opposite the existing vented panel. This configuration resulted in a scaled venting area of $\zeta = 1.4$, hence the second set of fully-vented tests was designated by the *FV(1.4)* abbreviation. The test procedure was identical to the first series of fully-vented tests, with charge masses ranging from 10 g to 25 g being tested. The final plate response was measured, and slight asymmetry in the deformation was observed. However, the difference between the maximum and midpoint deflections was less than 10% in all cases. Both the final midpoint and maximum plate deflections are listed in Table 4.5.

Table 4.5: Deflection results of fully-vented ($\zeta = 1.4$) blast tests.

Test number	Charge mass (g)	Final midpoint deflection (mm)	Final maximum deflection (mm)	Difference in deflection (%)
FV(1.4)1	10	11.09	11.13	0.4
FV(1.4)2	15	15.42	16.06	3.9
FV(1.4)3	20	19.03	19.25	1.2
FV(1.4)4	25	19.67	20.08	2.1

Mode I failure was observed in all the plates. Characteristic plastic hinges were established in all but the 15 g test, and boundary pull-in was observed at the top and bottom edges of the plates in the 20 g and 25 g tests. Increased deformation was observed in the plates blasted with higher charge masses, however, as in the first fully-vented test series, no mode II failure was exhibited by any of the plates.

The final midpoint deflection is shown in Figure 4.19. The midpoint deflection was observed to increase as the charge mass increased. No rupture threshold was approached in the first series of fully-vented tests and, since this series provided more venting opportunity, the same was assumed for this series. Consequently, a linear regression line was fitted to the data, which resulted in a coefficient of determination of $R^2 = 0.92$.

The final midline deformation was also observed to increase with an increasing charge mass. The final midline profiles of the target plates are shown in Figure 4.20. In all the tests, except that tested at 15 g, the midline profile demonstrated two distinct zones: a steady increase in height from the clamped sides and a central region with a slightly-bulging plateau. The 15 g test, however, produced a left-skewed, dome-like profile with no distinct zones. The 25 g test also exhibited deformation that was skewed to the left side of the plate, whereas the 10 g and 20 g displayed symmetric deformations. The contour plots in Figure 4.21 highlight the deformations of the target plates. The formation of plastic hinges was observed in each corner

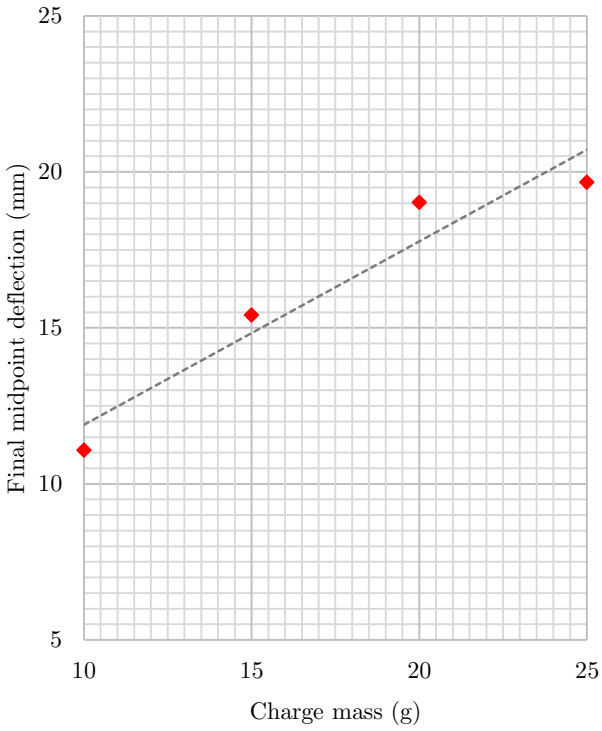

Figure 4.19: Graph of final midpoint deflection vs charge mass for the fully-vented ($\zeta = 1.4$) blast tests.

Figure 4.20: Final long-side midline profiles of fully-vented ($\zeta = 1.4$) tests.

of all the tests. Unlike the other plates, that of the 15 g test displayed no plateau region, indicating uncharacteristic plastic hinge formation. Since the 25 g test also displayed a left-biased deformation, one plausible explanation for the asymmetric profiles was a non-uniform clamping boundary condition. Furthermore, the 10 g and 15 g tests, indicated in Figure 4.21(a) and (b), respectively, displayed localised deformations in similar regions near the bottom edge of the plate. The asymmetry in deformation, particularly in the 15 g test, was therefore likely to be due to irregular boundary effects. The remaining tests were considered valid, despite exhibiting some inconsistency in deformation, since the overall deformations exhibited only minor asymmetry and consistent final midpoint deflection magnitudes.

Note: Consecutive contour lines indicate a difference in height of 1 mm.

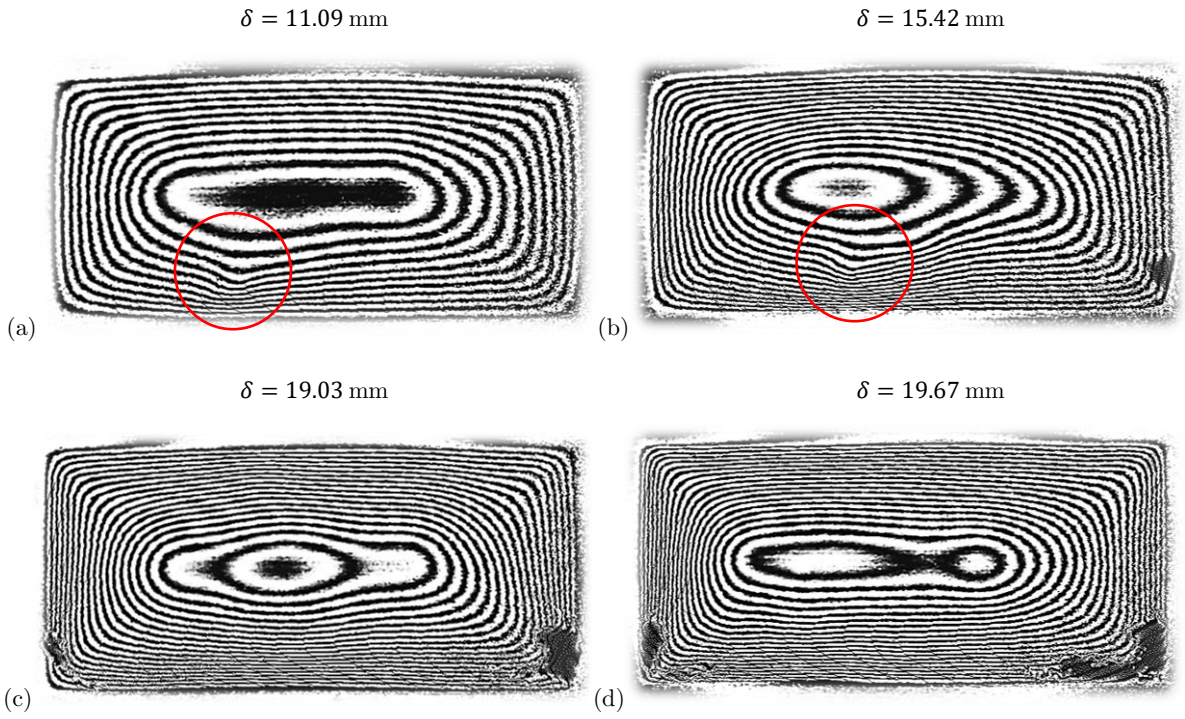

Figure 4.21: Contour plots of exposed target plate area for fully-vented ($\zeta = 1.4$) blasts performed with charge masses of (a) 10 g, (b) 15 g, (c) 20 g and (d) 25 g.

4.5 Results Summary

The final midpoint deflections of all the blast tests is shown in Figure 4.22. Evident in all tests was an increasing midpoint deflection as charge mass was increased. An envelope was placed around the results of each confinement case, displaying distinct deformation regions. Since there was no clear distinction between the results of the two fully-vented blast series, a single envelope contained both sets of midpoint deflections. The only other overlap in deformation envelopes was with the 17 g fully-confined blast. The blast response of the fully-confined target plates exhibited a deflection limit as the rupture threshold was approached; complete plate tearing (Mode II failure) occurred in the 20 g fully-confined test. All the other target plates exhibited only large inelastic deformation (Mode I failure) – including those tested above 20 g at lower degrees of confinement – and all the other blast series displayed a linear relationship between the final midpoint deflection and charge mass.

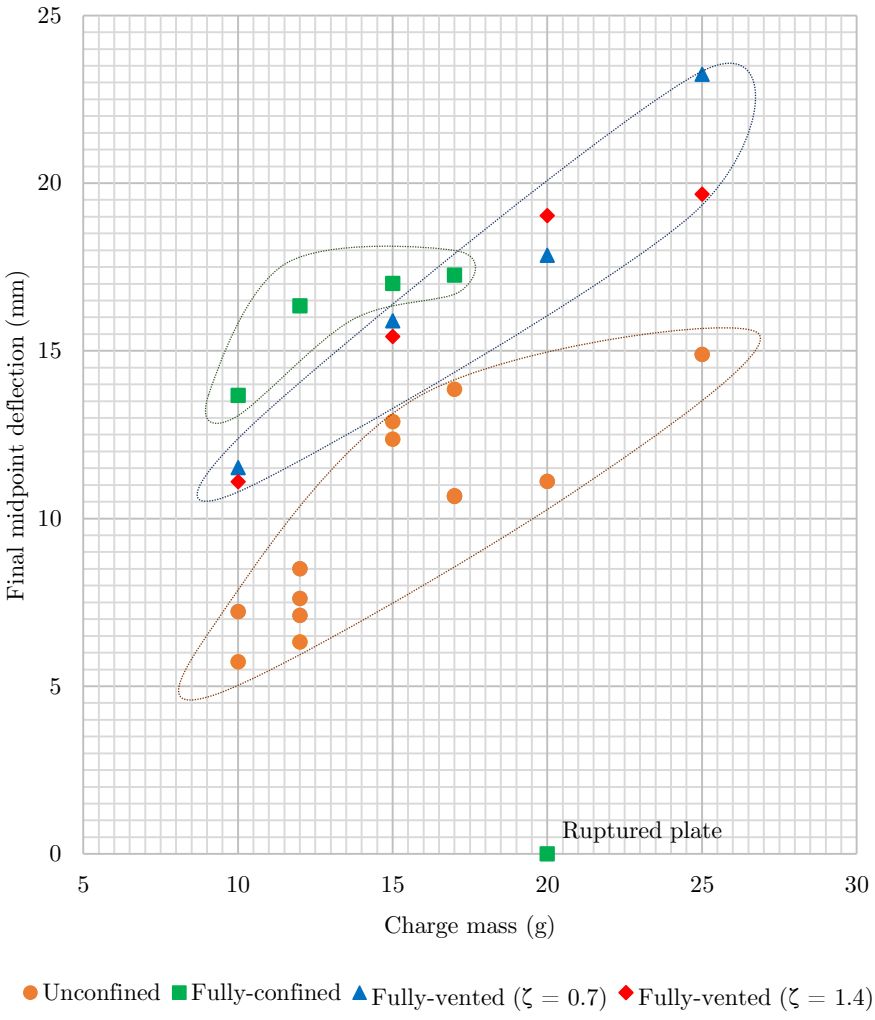

Figure 4.22: Graph of final midpoint deflection vs charge mass for all experimental blast tests.

5 Material Characterisation

In order to produce accurate numerical simulations of the blast experiments, a representative material model for the aluminium target plate needed to be developed. The model needed to be easily implemented into finite element packages, and capable of describing the material behaviour at large strains, and high strain-rate and temperature loadings (such as those resulting from an explosive detonation). One such model is that proposed by Johnson and Cook [43]. In order to assess the strain-hardening effects of the material, a series of tensile tests were performed. The effect of roll direction on the mechanical properties of the material was investigated during the tensile tests. The strain-rate and thermal sensitivity of the material was assessed through a review of literature.

5.1 Aluminium Specimens

The target plates used in all the blast experiments were cut from a single 1250 mm x 2700 mm sheet of 2 mm flat rolled Aluminium alloy, grade AA5754-h22. This particular grade was chosen because of the high yield stress and elongation at failure. The chemical composition for the grade is detailed in Table 5.1. In particular, this material has a relatively high magnesium content which is responsible for increasing the strength of the aluminium alloy [44].

Table 5.1: Chemical composition of AA 5754-h22 [45].

Chemical	Si	Fe	Cu	Mn	Mg	Cr	Zn	Others	A*l*
Composition (%)	0.22	0.24	0.02	0.08	2.74	0.03	0.05	0.03	96.59

To assess the quasi-static response of the material due to large strains, a series of uniaxial tensile tests were performed. The dog-bone specimens for these tests were cut from the same sheet as the target plates to ensure the material properties were representative of the target plates. The aluminium sheet was manufactured using a rolling process causing the mechanical properties to become anisotropic. In order to assess the influence of roll direction, two sets of dog-bone specimens were used: one set aligned at 0° (parallel) and the other at 90° (perpendicular) to the roll direction. The cutting layout of the aluminium sheet is illustrated in Figure 5.1. A total of 28 plates and 66 dog-bone specimens (36 parallel and 30 perpendicular) were cut from the aluminium parent sheet.

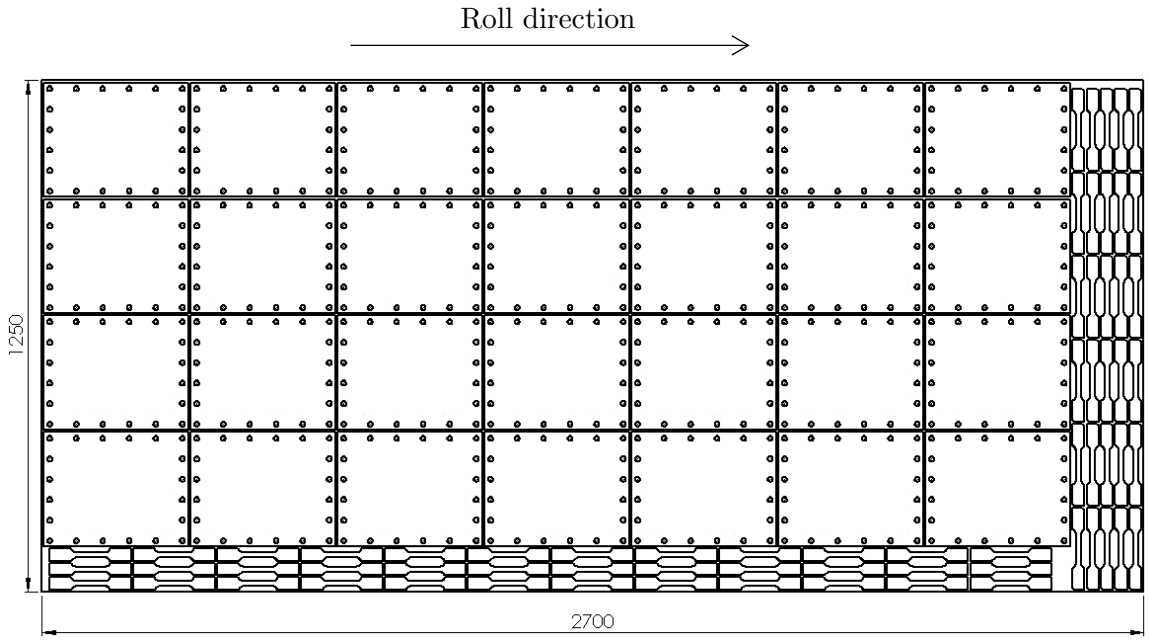

Figure 5.1: Cutting layout of aluminium parent sheet.

5.2 Tension Test

The tensile tests were performed according to the ASTM E8 test standard [46] for tensile testing of metallic materials. This standard allows, for a rectangular tension test specimen, a gauge length of 50.0 ± 0.1 mm and a specimen width of 12.5 ± 0.2 mm. The thickness of the material was 2 mm and all other dimensions adhered to the minimum limit outlined by the standard [46]. Figure 5.2 shows a schematic of the dog-bone specimen used for tensile testing.

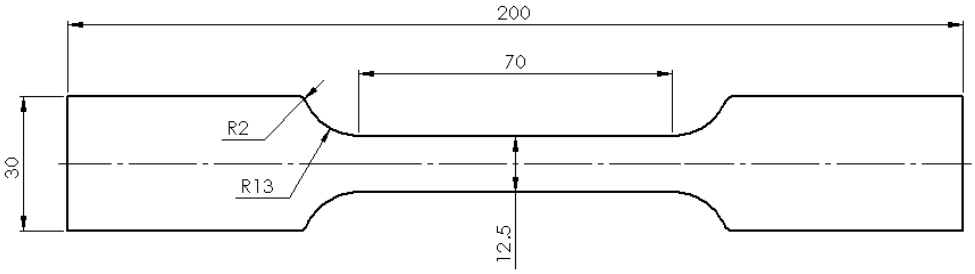

Figure 5.2: Schematic diagram showing the dimensions of a flat, rectangular dog-bone specimen used for uniaxial tension tests.

The uniaxial tension tests were performed on a Zwick 1484 universal testing machine. A load cell measured the force history of the test and an extensometer (with an initial separation distance matching the specimen gauge length of 50 mm) was used to measure the corresponding displacement of the specimen. From this data the engineering stress (σ_{eng}) vs engineering strain (ε_{eng}) results were determined using Equations 5.1 and 5.2, respectively.

$$\sigma_{eng} = \frac{F}{A_o} \tag{5.1}$$

$$\varepsilon_{eng} = \frac{\delta}{L_o} \tag{5.2}$$

where: F is the force causing a change in length δ of a specimen with initial cross-sectional area A_o and gauge length L_o.

The tensile tests were performed by controlling a constant crosshead speed in accordance with Control Method C of ASTM E8. A crosshead speed of 1 mm/min was used, which corresponded to a strain rate of $3.33 \times 10^{-4}\ s^{-1}$. Five specimens from both the 0° and 90° tensile test specimens were tested. A typical engineering stress-strain curve for each orientation is shown in Figure 5.3. A difference in mechanical properties was observed between the two sets, with the 0° specimens exhibiting a higher yield and tensile strength, but a lower elongation at failure than the 90° specimens. The serrated flow which was present once the specimen begins yielding was determined to be a physical phenomenon arising from the presence of magnesium atoms in the microstructure of the material [47,48]. The grain boundaries surrounding these solutes hindered the motion of dislocations, and increased the load-bearing capacity of the material until the resistance was overcome and a new grain boundary was encountered, causing another spike [47].

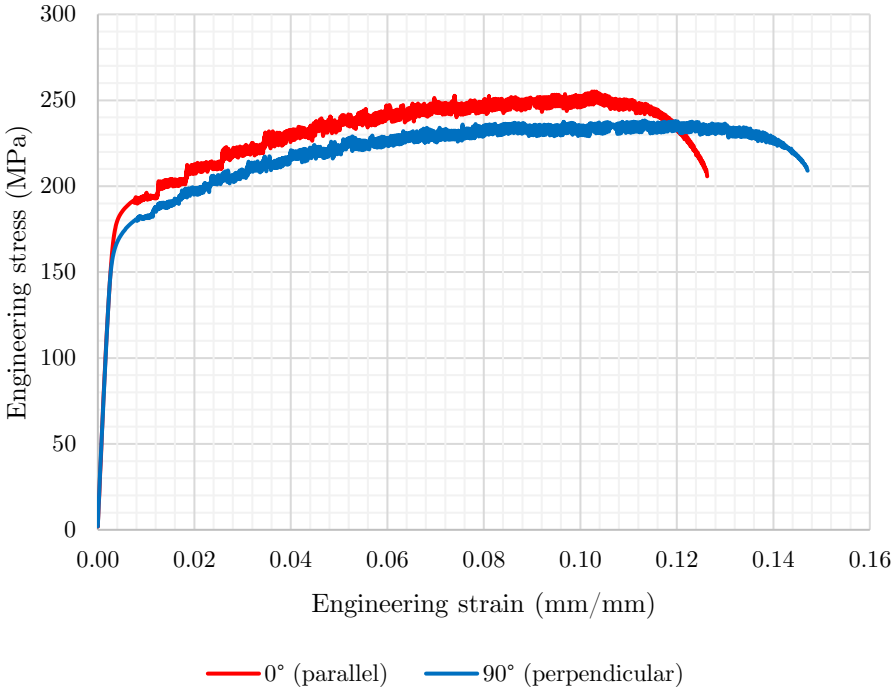

Figure 5.3: Graph of engineering stress vs engineering strain for tensile tests performed at 1 mm/min.

The engineering stress-strain curve was to identify certain mechanical properties of the tested material, such as the yield stress, ultimate tensile strength (UTS) and modulus of elasticity. It did not, however, provide a true indication of the material behaviour because it was assumed that the cross-sectional area and gauge length remained constant during the tension test. The true stress (σ_T) is the axial load acting across the instantaneous cross-sectional area and the true strain (ε_T) is the increase in the instantaneous gauge length. The value of these are found using Equations 5.3 and 5.4, respectively.

$$\sigma_T = \sigma_{eng}(1 + \varepsilon_{eng}) \tag{5.3}$$

$$\varepsilon_T = \ln(1 + \varepsilon_{eng}) \tag{5.4}$$

Equations 5.3 and 5.4 are only valid until the UTS is reached. The UTS was identified by the maximum stress on the engineering stress-strain curve. Once this stress was surpassed, the specimen underwent necking (a form of damage where the cross-sectional area rapidly decreased and became non-uniform) and Equation 5.3 began to overstate the actual stress in the specimen. The true stress-strain curves for the engineering stress-strain curves from Figure 5.3 are shown, up to the UTS.

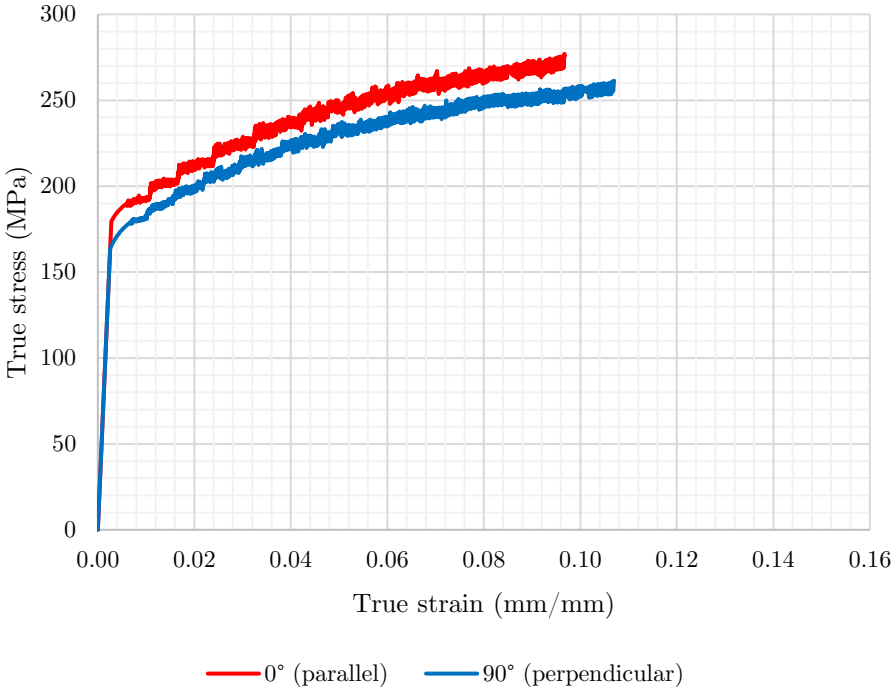

Figure 5.4: Graph of true stress vs true strain determined from engineering stress vs engineering strain curves.

5.3 Johnson-Cook Material Model

The material model proposed by Johnson and Cook [43] constitutively defines the von Mises equivalent flow stress (σ_f) of the material in terms of plastic strain (ε_P), strain rate ($\dot{\varepsilon}$) and temperature (T):

$$\sigma_f = [A + B(\varepsilon_P)^n] \times [1 + C \ln(\dot{\varepsilon}^*)] \times [1 - (T^*)^m] \tag{5.5}$$

where: the homologous strain rate and temperature are defined as:

$$\dot{\varepsilon}^* = \frac{\dot{\varepsilon}}{\dot{\varepsilon}_o} \quad \text{and} \quad T^* = \frac{T - T_r}{T_m - T_r}, \text{ respectively,}$$

where: $\dot{\varepsilon}_o$ is the reference strain rate, T_r is the reference temperature, and T_m is the melt temperature of the material.

The first term of Equation 5.5, governed by constants A, B and n, describes the effect of strain hardening; the second term, governed by constant C, describes the strain-rate; and the third term, governed by constant m, describes the material behaviour due to thermal effects. The

quasi-static tensile test results were used to determine constants A, B and n. Taking the reference strain rate and reference temperature as those of the tensile tests (i.e. $\dot{\varepsilon}_o = \dot{\varepsilon}$ and $T_r = T$), the homologous strain rate and homologous temperature became $\dot{\varepsilon}^* = 1$ and $T^* = 0$, respectively, and Equation 5.5 was consequently reduced to:

$$\sigma_f = A + B(\varepsilon_P)^n \tag{5.6}$$

Equation 5.6 was used to describe the relationship between the true stress and the true plastic strain of the tension test results. The plastic strain was calculated by removing the elastic strain from the results:

$$\varepsilon_P = \varepsilon - \frac{\sigma}{E} \tag{5.7}$$

where: E is the modulus of elasticity, defined as the gradient of the linear (elastic) region of the engineering stress-strain curve.

Equation 5.7 was applied to the true stress-strain data to produce a true stress vs true plastic strain curve for each tension test. Once again, representative curves of the two tensile tests were plotted, as shown in Figure 5.5.

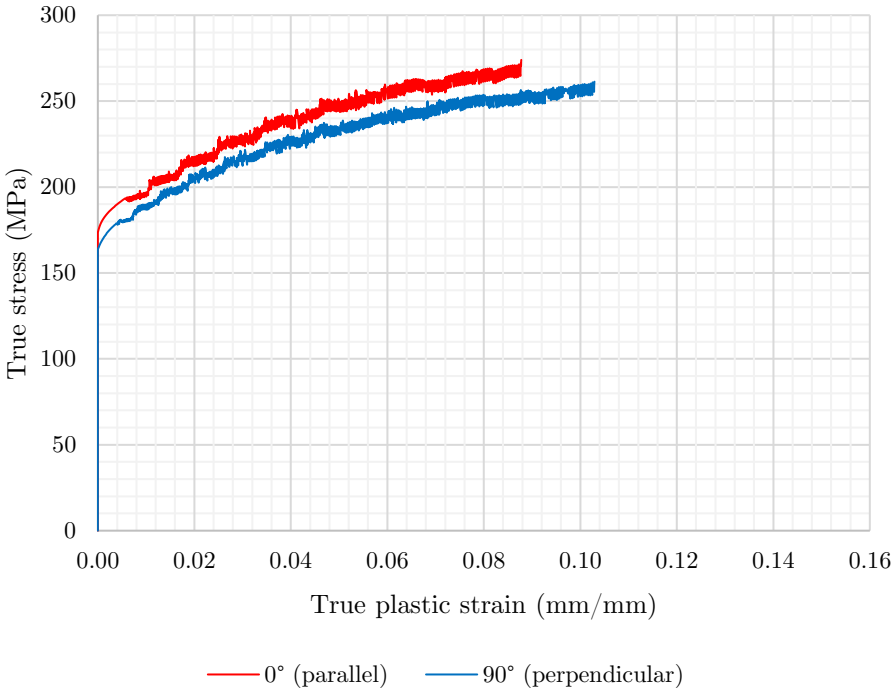

Figure 5.5: Graph of true stress vs true plastic strain.

In order to fit the strain hardening component of the Johnson-Cook equation to the tension test data, Equation 5.6 was linearised to produce Equation 5.8.

$$\ln(\sigma_f - A) = n \ln(\varepsilon_P) + \ln(B) \tag{5.8}$$

The first constant, A, was identified as the y-intercept of the true stress-plastic strain curve in Figure 5.5, which was the point at which the material started to yield and develop plastic strain. This value was taken to be the average yield stress of the test data to which the model was being fitted. A linear function was then fitted to the $\ln(\sigma_T - A)$ vs $\ln(\varepsilon_P)$ data using least-squares regression and, from this, the gradient n and intercept $\ln(B)$ were found. The strain-hardening constants are stated in Table 5.2. Since there was no consideration of damage evolution when determining the constants from the tension tests, the Johnson-Cook material model implemented numerically would not predict any damage, in terms of material necking or rupture, either. Since the majority of the experimental tests did not exhibit rupture of the target plate, this limitation was considered acceptable.

Table 5.2: Constants for the strain-hardening component of the Johnson-Cook constitutive model.

Test series	A **(MPa)**	B **(MPa)**	n	R^2
0°	177.6	495.8	0.6627	0.9740
90°	164.1	430.8	0.6195	0.9643
0° and 90°	170.9	431.5	0.6252	0.8387

Note: no damage evolution was considered when determining the Johnson-Cook constants.

The Johnson-Cook fits were plotted against all the experimental data of both sets of tensile tests, illustrated in Figure 5.6. Although the fit at low strains was representative of the test data, the correlation diverged at larger strains. Each of tensile tests reached the UTS at slightly different strain values, which meant that there were fewer data points with which to fit the Johnson-Cook model at larger strains. In order to develop a representative fit at both low and high strains, and to establish the performance of the Johnson-Cook material model, numerical simulations of the tensile tests were performed.

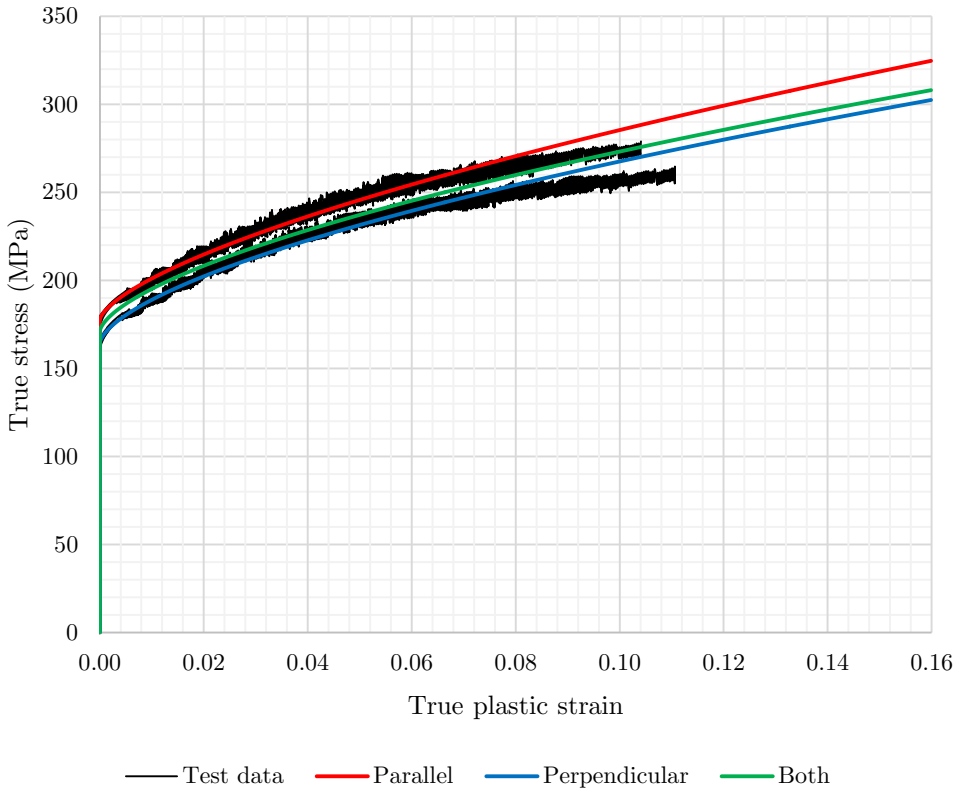

Figure 5.6: Graph of the Johnson-Cook model fitted to test data.

5.4 Tension Test Simulations

The tensile test was simulated in LS DYNA®. Due to the long duration of a quasistatic tensile test, an implicit solver was used to develop the simulation. The implicit method allowed a user-defined time step size to be implemented which was advantageous in reducing the computational time of the simulation [50]. To further reduce the computational time of the analysis a quarter-symmetry model was used. Additionally, the majority of the clamped area, which was assumed to not deform during the tensile tests, was not modelled. Figure 5.7 illustrates the modelled region with respect to the full dog-bone specimen.

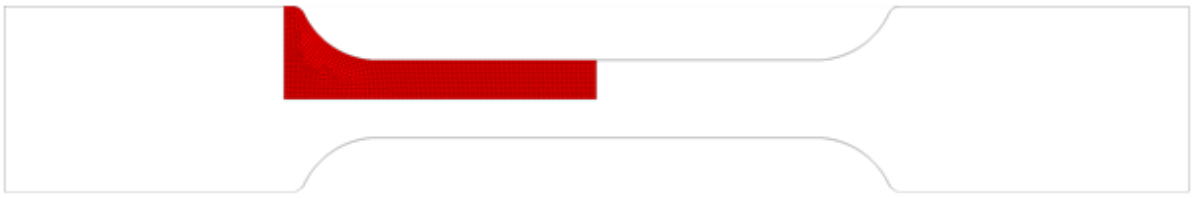

Figure 5.7: Schematic showing the modelled region of tensile test specimen using quarter symmetry.

The specimen was modelled using quadrilateral shell elements with a thickness of 2 mm. The aspect ratio of most of the elements were kept close to unity when meshing the domain. All the dimensions of the simulated specimen matched those of the dog-bone specimens used for experimental testing. The experimental crosshead speed was enforced in the simulation by prescribing a velocity of 0.5 mm/min to the wide end of the simulated specimen: the symmetry of the model would ensure the correct crosshead speed of 1 mm/min was achieved. The meshing of the specimen, the symmetry boundaries and the prescribed velocity are shown in Figure 5.8.

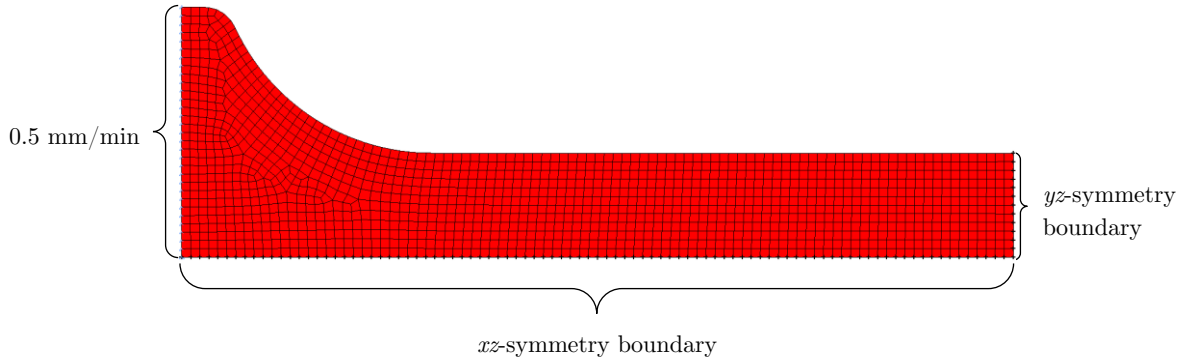

Figure 5.8: Diagram of the mesh and boundary conditions of tensile test simulation.

The implicit analysis was implemented using the various control cards available in LS DYNA®. The CONTROL_IMPLICIT_GENERAL card was used to initiate the implicit analysis and the initial time step size. A non-linear solution method was selected using the CONTROL_IMPLICIT_SOLUTION card; this method allowed iterations within a time step to be performed until equilibrium of the solution was reached. The default solver was selected in the CONTROL_IMPLICIT_SOLVER card, which performed the necessary calculations to reach convergence of the solution. The CONTROL_IMPLICIT_AUTO card was used to activate an automatically-adjusted time step size and, consequently, to set the minimum and maximum limits of the time step size (DTMIN and DTMAX, respectively). The maximum time step size was varied to investigate the convergence of the implicit solution. An optimum time step size was determined by performing a convergence study of the tensile test simulations with the maximum timestep set to 100 s, 10 s, 5 s, 2 s and 1 s. The CPU time required for each case to reach convergence was determined and the accuracy of the solution was assessed. Small time step sizes resulted in severe CPU time requirements and large time step sizes reduced the accuracy of the solution. Figure 5.9 illustrates the total CPU time taken to complete an implicit analysis of the tensile test for varying DTMAX values.

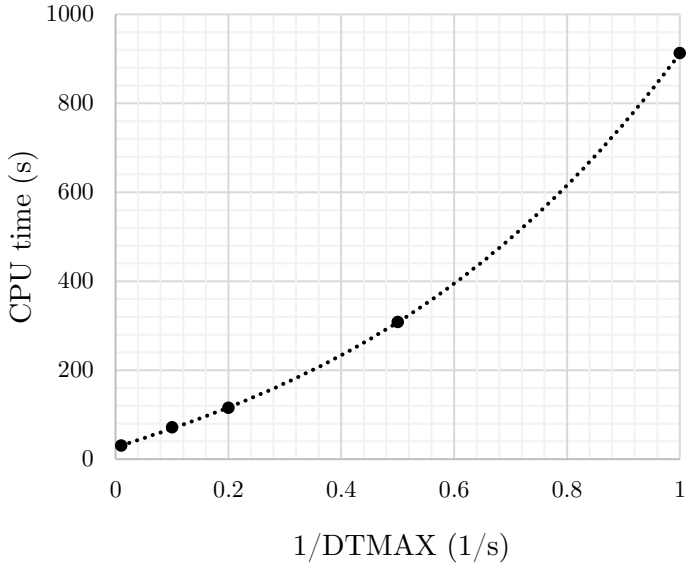

Figure 5.9: Graph of CPU time required to run the implicit analysis at different maximum time step sizes.

A steep increase in CPU time was observed for DTMAX values smaller than 5 s. Figure 5.10 illustrates the stress-strain response of the simulated specimen for the same DTMAX values and the convergence of the solution towards the analytical Johnson-Cook fit, highlighting the yield response for each case. The overall behaviour, particularly at plastic strains greater than 2%, was simulated accurately for all the tested time steps. With DTMAX set to 100 s, the solution converged to the analytical solution after plastic strains of 8%. The behaviour at yielding, however, varied amongst the tested cases. The two smaller time steps (with a DTMAX value of 2 s and 1 s) exhibited early yielding at stresses approximately 45 MPa less than the yield stress of the material. The two larger time steps (with a DTMAX value of 10 s and 100 s) exhibited the largest overshoot at yielding. The closest fit to the analytical solution was achieved using a DTMAX of 5 s and this time step was implemented for all the subsequent tensile test simulations. The Johnson-Cook parameters were manually iterated to produce a stress response with representative fit to the experimental data at both low strain (yielding) and high strain values. The final Johnson-Cook parameters are listed in Table 5.3.

Table 5.3: Final Johnson-Cook constants for AA5754h22.

Orientation	***A*** **(MPa)**	***B*** **(MPa)**	***n***	***C*** [49]	***m*** [49]
0°	172.2	370.2	0.5410	0.002979	2.519
90°	160.5	339.8	0.5206	0.002979	2.519

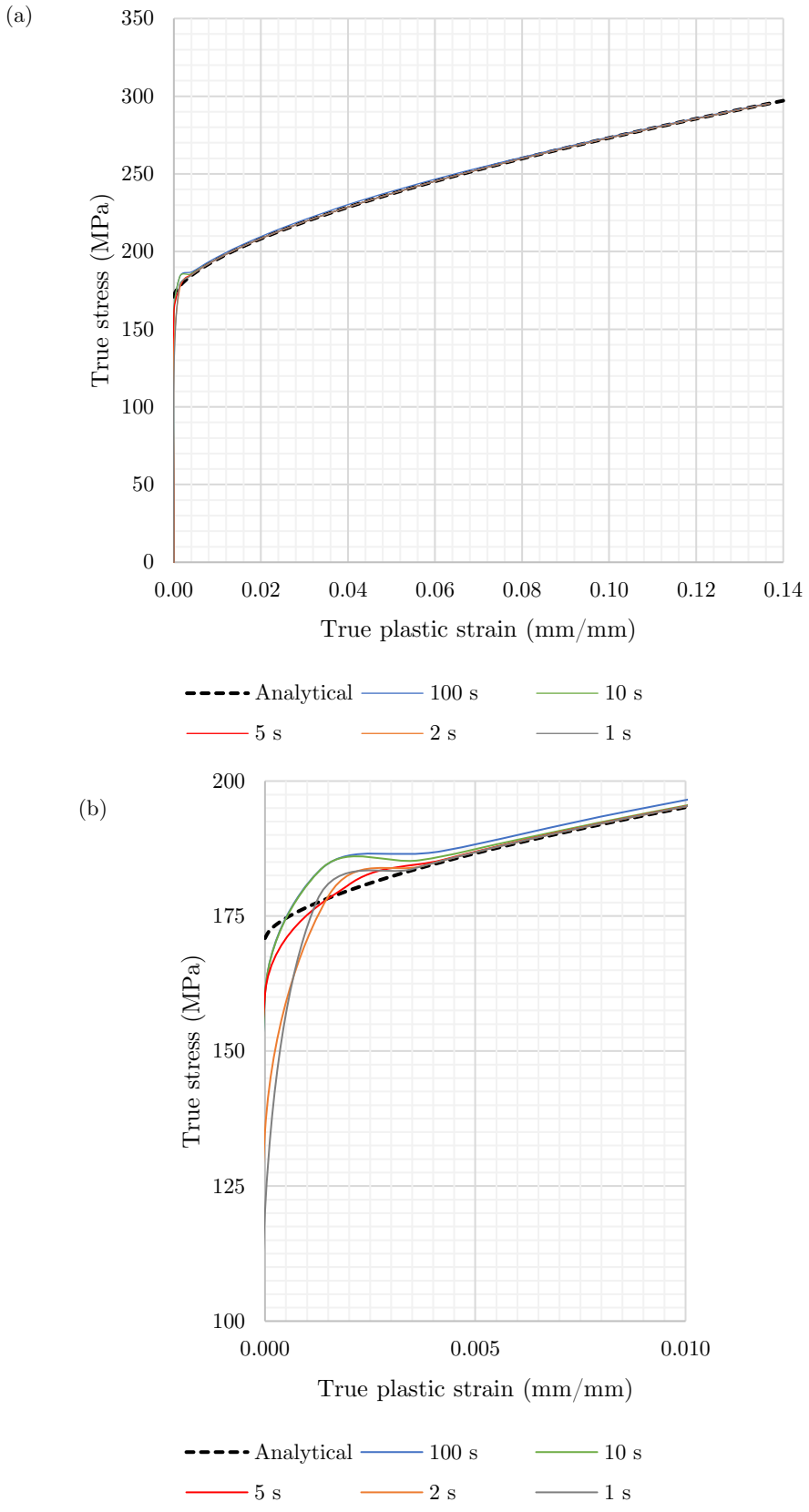

Figure 5.10: Graphs showing the effect of DTMAX on the convergence of the non-linear implicit solver at capturing (a) the overall response and (b) the point of yielding of the tensile test specimen.

The final optimised true stress vs true plastic strain curves for both sets of tensile tests (parallel and perpendicular to the roll direction) are shown in Figure 5.11. The experimental results of all the tension tests within each set are plotted. The analytical and simulation results show good agreement with the experimental data, and each other.

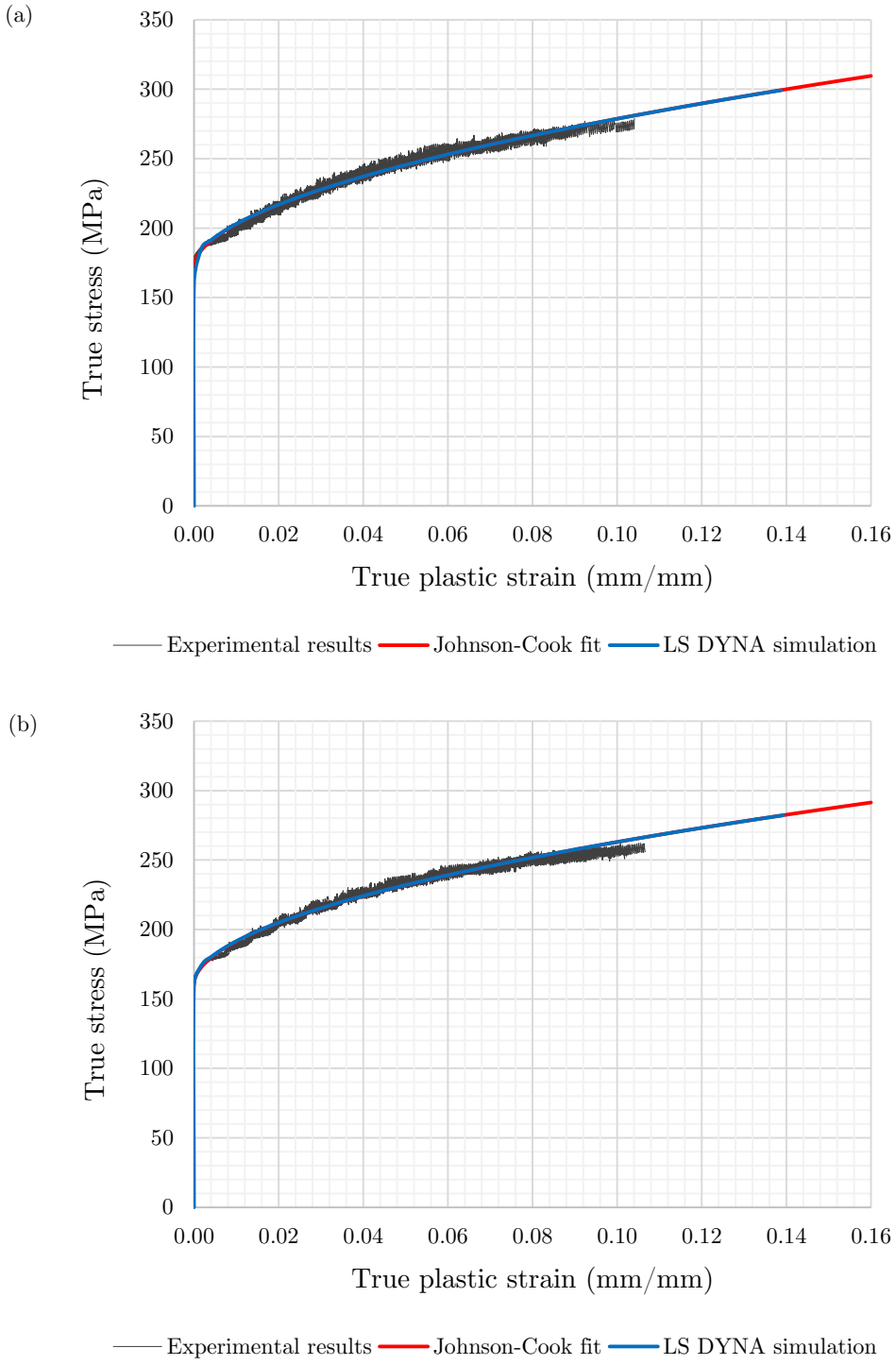

Figure 5.11: Graphs showing the comparisons of experimental, analytical and numerical results of tension tests for specimens aligned (a) parallel and (b) perpendicular to the roll direction of the parent sheet.

6 Blast Model Development

This chapter describes the formulation of the meshes for the air, explosive, target plate and additional structural components (clamp frame and ULD box) used to simulate the experimental blast tests. The material properties and equations of state (EOS), where applicable, for the different materials are described. A mesh independence study is detailed, which discusses the approach used to determine the optimum element size for both the air and plate meshes. Finally, the four blast models used to simulate the experimental tests are presented.

The numerical simulations were performed using LS-DYNA®, a computational software package used to analyse structures subjected to static and/or dynamic loads. LS-DYNA is capable of simulating highly transient phenomena, such as the highly dynamic loads produced by explosions and high-velocity impact [50]. Complex models can be generated which contain both Lagrangian and Eulerian formulations. Lagrangian meshes deform with the material, allowing the mesh to be used to measure the deformation of continuum structures. The Eulerian mesh is fixed in space and allows materials to deform independently of the mesh [50].

6.1 Fluid Properties

The air domain was modelled using three-dimensional, eight-node solid elements. A one-point integration, multi-material arbitrary Lagrangian-Eulerian (MMALE) element formulation was implemented, which allowed the explosive to occupy and propagate through the same mesh as the air. The spherical charge was included in the air domain using the initial volume fraction geometry keyword, which designated the initial shape, size and position of the explosive.

6.1.1 Air

The air was modelled as a medium through which the explosive could propagate. Therefore the air was considered to be a null material which did not react with the explosive products. The air was assumed to obey the ideal-gas EOS described by Equation 6.1 [51].

$$P = \rho RT = (\gamma - 1)\frac{\rho}{\rho_0}E_0 \tag{6.1}$$

where: P is the gas pressure

ρ and T are the current density and temperature of the gas, respectively,

R is the gas constant given by $R = C_p - C_v$,

where: C_p and C_v are the specific heats of the gas at constant pressure and volume, respectively,

γ is the specific heat ratio given by $\gamma = \frac{C_p}{C_v}$,

ρ_0 is the initial density of the gas, and

E_0 is the initial internal energy per unit volume, given by $E_0 = \rho_0 C_v T$.

The properties of air at standard pressure (101.325 kPa) and room temperature (298.15 K) were calculated using Equation 6.1 and constants from [51]. These properties are listed in Table 6.1 and agree with values obtained by Kinney and Graham [7].

Table 6.1: Properties of air at standard pressure and room temperature [51].

R ($\mathbf{kJ/kg \cdot K}$)	γ	ρ_0 ($\mathbf{kg/m^3}$)	E_0 ($\mathbf{kJ/m^3}$)
0.2870	1.400	1.184	253.3

The ideal-gas EOS was implemented using a linear polynomial function available in LS-DYNA, which is described by Equation 6.2 [50].

$$P = C_0 + C_1\mu + C_2\mu^2 + C_3\mu^3 + (C_4 + C_5\mu + C_6\mu^2)E_0 \tag{6.2}$$

where: C_0 – C_6 are user-defined constants, and

μ is a volumetric parameter given by $\mu = \frac{\rho}{\rho_0} - 1$.

The ideal gas EOS of Equation 6.1 was achieved by substituting the following constants into Equation 6.2.

$$\begin{gathered} C_0 = C_1 = C_2 = C_3 = C_6 = 0 \\ C_4 = C_5 = \gamma - 1 \end{gathered} \tag{6.3}$$

6.1.2 Explosive

The explosive was modelled using the Jones-Wilkins-Lee (JWL) EOS and the high explosive burn material available in LS-DYNA. The pressure of the detonation products was controlled by the JWL equation, described by Equation 6.4 [41].

$$P_{JWL} = A\left(1 - \frac{\omega}{R_1 V}\right)e^{-R_1 V} + B\left(1 - \frac{\omega}{R_2 V}\right)e^{-R_2 V} + \frac{\omega E}{V} \tag{6.4}$$

where: A, B, ω, R_1 and R_2 are material-specific parameters,

V is the relative volume of the explosive, and

E is the detonation energy per unit volume of the explosive.

The detonation of the explosive was simulated using burn fractions, which controlled the resulting energy release. The high explosive pressure was a function of the EOS pressure and the burn fraction (F), as described by Equation 6.5 [50]. The explosive pressure was equal to the EOS pressure once the burn fraction reached or exceeded unity, indicating the completion of the detonation (burn) process.

$$P = P_{JWL} \cdot \min(1, F) \tag{6.5}$$

The burn fraction is described by Equation 6.6 [50].

$$F = \max(F_p, \beta) \tag{6.6}$$

where: F_p is the programmed burn model, and

β is the beta burn model.

Both the programmed burn and beta burn models were activated during the explosive detonation simulation. The programmed burn option controlled the detonation of the explosive by computing the lighting time for each explosive material element. At any current time, the programmed burn model is described by Equation 6.7 [50].

$$F_p = \begin{cases} \dfrac{2(t - t_l)DA_{e\max}}{3V_e} & \text{if } t > t_l \\ 0 & \text{if } t \leq t_l \end{cases} \tag{6.7}$$

where: t_l is the lighting time of the element, given by $t_l = \frac{l_d}{D}$,

where: l_d is the distance from the centre of the element to the detonation point,

D is the detonation velocity of the explosive,

$A_{e_{\max}}$ is the maximum surface area of the element, and

V_e is the element volume.

The beta burn option was used to initiate the detonation of an explosive element undergoing volumetric compression. The beta burn model is described by Equation 6.8 [50].

$$\beta = \frac{1 - V}{1 - V_{CJ}} \tag{6.8}$$

where: V is the relative volume, and

V_{CJ} is the Chapman-Jouguet relative volume, given by $V_{CJ} = 1 - \frac{P_{CJ}}{\rho_0 D^2}$ [50],

where: P_{CJ} is the Chapman-Jouguet pressure, and

ρ_0 is the material density of the explosive.

The parameters, specific to PE4, which were used to describe the JWL equation of state and the detonation process are listed in Table 6.2.

Table 6.2: Equation of state and detonation parameters for PE4 [41].

Equation of State Parameters					Detonation Parameters			
A (MPa)	B (MPa)	R_1	R_2	ω	E_0 (MJ/m^3)	D (m/s)	P_{CJ} (MPa)	ρ_0 (kg/m^3)
609770	12950	4.5	1.4	0.25	9000	8193	28000	1601

6.2 Structure Properties

The target plate was modelled using four-node quadrilateral shell elements. The shell elements were assigned a constant thickness of 2 mm to match the actual target plate. The Belytschko-Tsay element formulation was used, and through-thickness integration was performed using two-point Gauss quadrature. Although the main limitation of using shell elements is the underestimation of the element through thickness [50], the thinning of the target plate was not used as a measure in the experimental results. The clamp frame and ULD box were modelled using three-dimensional, eight-node solid elements with a constant stress element formulation.

6.2.1 Target Plate

The Johnson-Cook material model was used for the aluminium target plate. The model includes the hardening effects at high strain-rate loading and the softening effects of adiabatic temperature increases due to plastic work in the material. The Johnson-Cook definition of the material flow stress is given by Equation 5.5 in Section 5.3.

The aluminium alloy used for the target plate during the experimental tests was of grade 5754h22, and the Johnson-Cook constants for this material were determined through material characterisation process, as discussed in Chapter 5. Table 6.3 lists the Johnson-Cook constants and some of the material properties for the aluminium grade used. The material properties listed are: the density (ρ), shear modulus (G), elastic modulus (E), Poisson's ratio (ν), melt temperature (T_m), and specific heat (C_p) of the aluminium.

Table 6.3: Johnson-Cook constants and material properties of AA5754h22.

Johnson-Cook Parameters					Material Properties [51,52]					
A (MPa)	B (MPa)	n	C	m	ρ (kg/m^3)	G (GPa)	E (GPa)	ν	T_m (K)	C_p (kJ/kg · K)
160.5	339.8	0.5206	0.003	2.52	2700	27.0	68.0	0.3	600	0.900

6.2.2 Clamp Frame and ULD Box

An elastic material model was used for the mild steel clamp frame and ULD box. These components were assumed to not deform plastically during the experimental blasts, which could be affirmed numerically, especially for the thinner 10 mm top plate and flange. The simple material model was therefore chosen instead of a rigid material model. The material properties of mild steel are listed in Table 6.4. The properties required for the material model were: the density (ρ), elastic modulus (E) and Poisson's ratio (ν).

Table 6.4: Material properties of mild steel [53].

Material Properties		
ρ (kg/m^3)	E (GPa)	ν
7850	210.0	0.3

6.3 Mesh Independence Study

A mesh independence study was performed to determine an acceptable mesh size combination for both the air domain and target plate. The peak and final midpoint displacements of the target plate were used as the measure for acceptable mesh sizes, as well as the CPU time required to complete the simulation. However, before the mesh independence study was performed, a preliminary test was completed to assess the accuracy of the blast pressure produced in the air domain.

6.3.1 Blast Pressure

A quarter-symmetry model was developed to test the blast pressure formulation within the air domain. The air domain was set to dimensions of 50 mm × 50 mm × 200 mm. Air meshes with element sizes ranging from 1 mm to 8 mm were used, while the detonation of explosives with charge masses ranging from 10 g to 25 g was simulated. The peak pressure was measured using a tracer point located at a stand-off distance of 163 mm. The tracer was located off the boundary surfaces to mitigate any errors that accumulate along the domain boundaries. The peak pressure was compared to the empirical solution obtained by Kinney and Graham [7]. Shown in Figure 6.1 is the effect of the air mesh size on the peak pressure produced by the blast simulation and the CPU time required to complete the simulations.

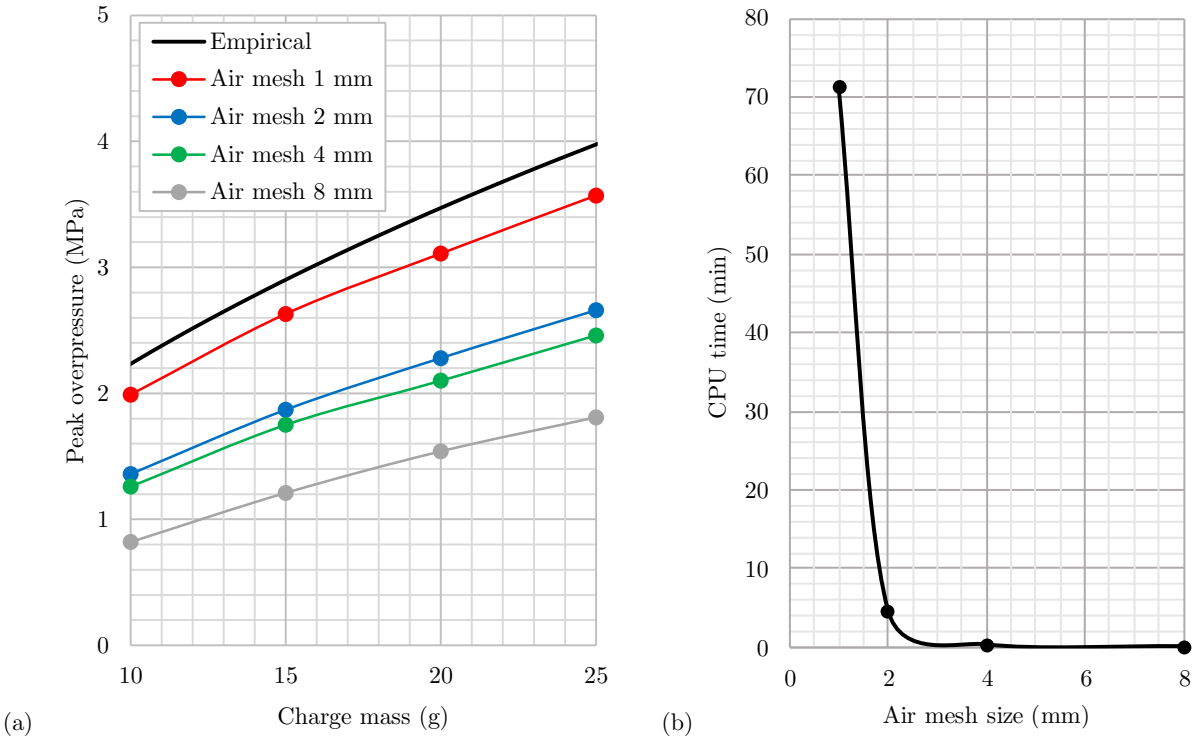

Figure 6.1: Graph showing the effect of the air mesh size on (a) the peak pressure at a 163 mm stand-off for varying charge masses and (b) the required CPU time to complete the air blast simulation.

The explosive model was deemed suitable for simulating a blast wave since the simulated peak pressures were observed to approach the empirical solution as the air mesh became more refined. The 1 mm air mesh captured the most representative peak pressure, approximately 25% greater than that captured by the 2 mm air mesh for the same charge mass. Although a representative explosive model is necessary to produce an accurate target plate response, it is the numerical interaction between the explosive and target plate which results in the blast response of the target plate. The deformation of the plate should therefore be used as the measure for selecting an appropriate mesh resolution, and not only the capability of the air mesh to accurately capture the blast pressure. The latter is, however, useful as an indication of the accuracy of the simulated plate deformation.

6.3.2 Plate Deflection

The mesh independence study was performed, using the blast model shown in Figure 6.2. Only the exposed area of the target plate was simulated, making it possible to use a quarter-symmetry model for the study. A 128 mm × 58 mm × 210 mm air domain was used, within which the 128 mm × 58 mm target plate was placed. All the nodes along the *xz*– and *yz*–planes of both the air and plate meshes were assigned corresponding symmetry boundary conditions.

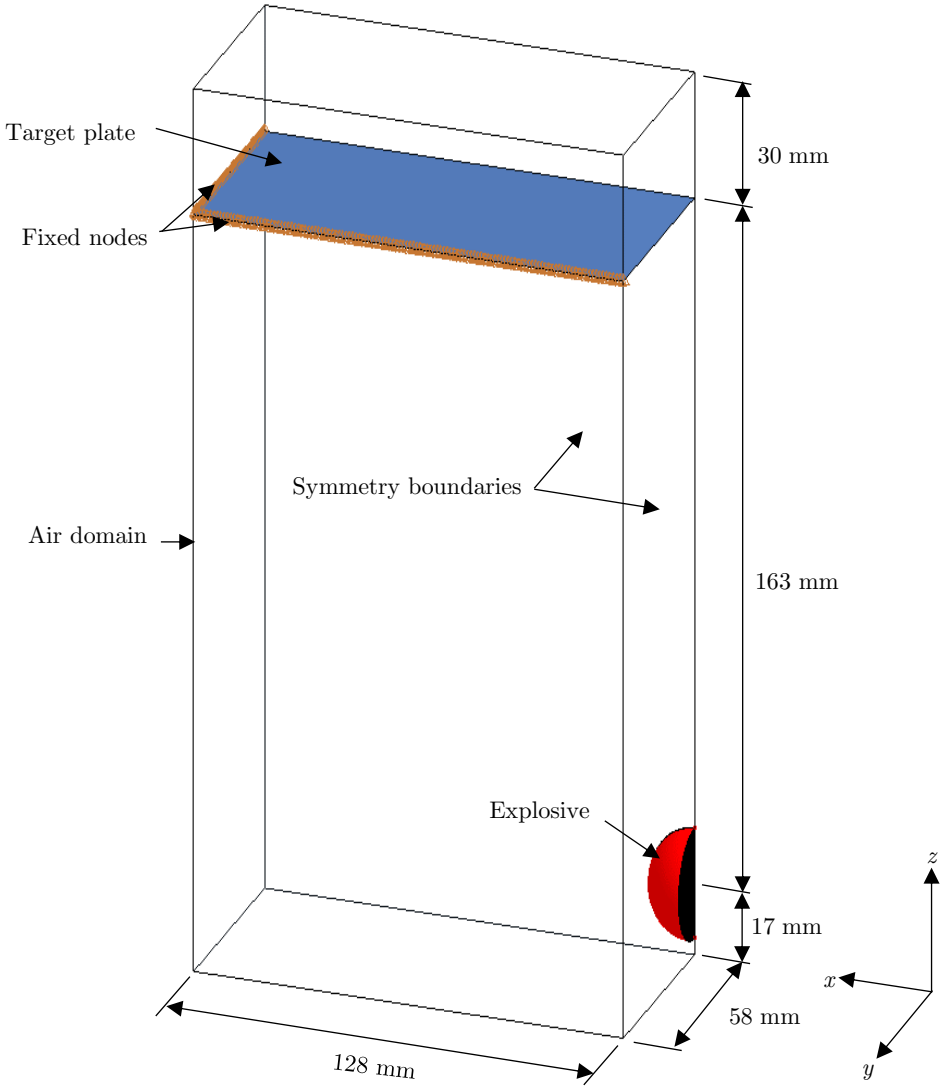

Figure 6.2: Numerical blast model for mesh independence study.

The elements on the remaining faces of the air mesh were assigned pressure-outflow boundary conditions, while the nodes on the remaining two edges of the target plate were assigned fixed boundary conditions, in both translation and rotation (to represent the fully-clamped edges of the target plate). For the purposes of the mesh independence study, this simplistic boundary condition was considered sufficient. The mass of the explosive was kept constant at 25 g for each of the plate deflection tests.

The air mesh element size was varied from 1 mm to 4 mm. The target plate element size was varied from 0.25 mm to 2 mm. The maximum value of the plate element size did not exceed the air mesh element size (a requirement necessary for ensuring proper interaction between the air and plate meshes, and preventing leakage of explosive material passing through the plate [50]). The results of the study are shown in Figure 6.3.

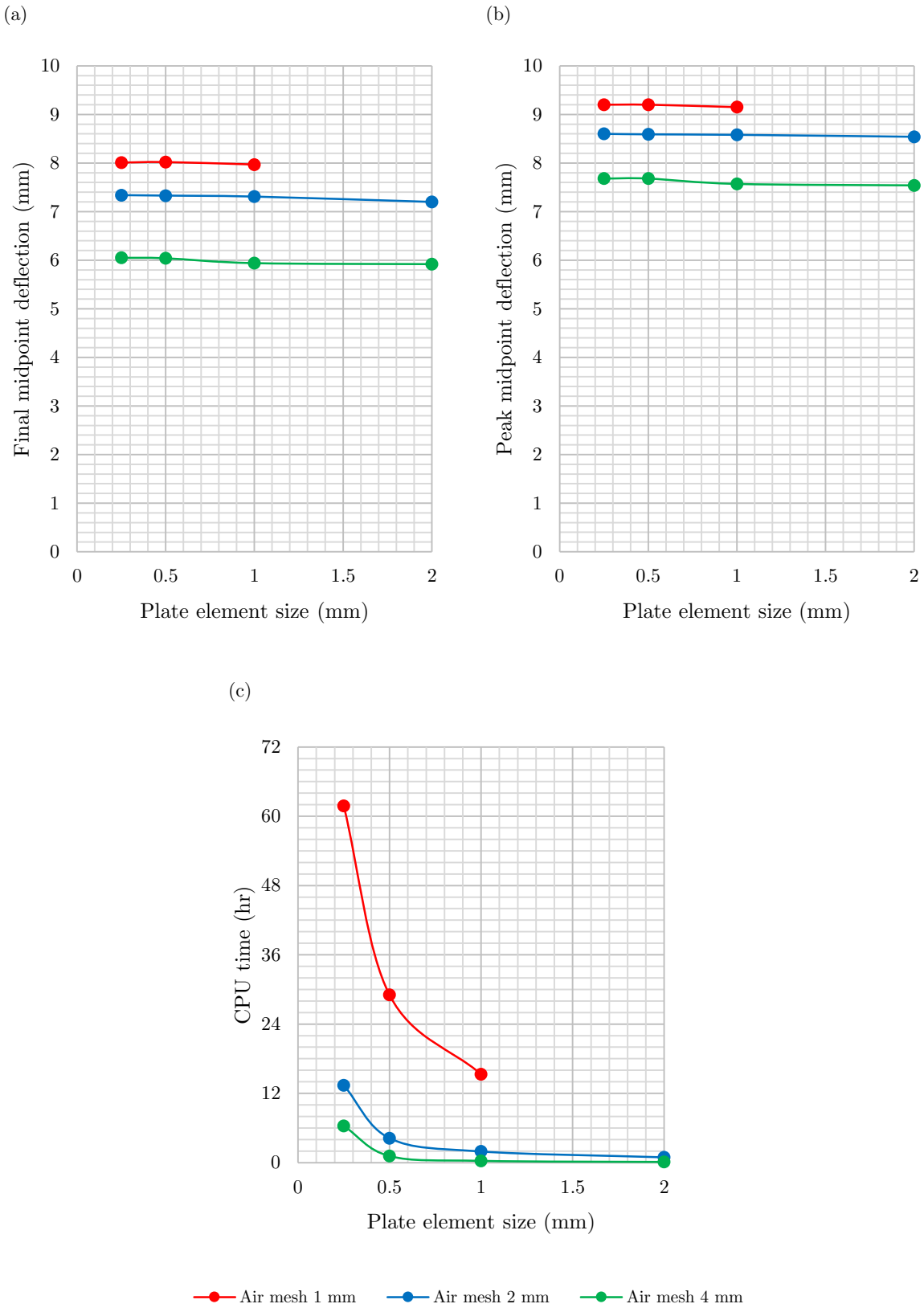

Figure 6.3: Graphs of the mesh independence study results for numerical simulations of plate blasting showing the effect of mesh size on the (a) final midpoint deflection of the target plate, (b) peak midpoint deflection of the target plate, and (c) required CPU time to run the simulation.

The study revealed that the solution was independent of the tested target plate mesh resolutions, particularly when using an air mesh size of 2 mm and less, for both final and peak midpoint deflections. For a 4 mm air mesh, the solution was independent of plate element sizes of 0.5 mm and less. This outcome was evidenced by the deflection results for the same air mesh size being within a 2% difference. However, the air mesh size had a greater influence on the results, indicating a very fine mesh resolution (less than 1 mm) would be required to obtain a mesh independent solution. Due to CPU time practicalities, mesh resolutions finer than 1 mm were not tested. The CPU time required to complete the simulations with a 1 mm air mesh size (and the same plate element size) was at least 8 times greater than simulations run with larger air mesh sizes. Since the model used in this study was a relatively simple, quarter-symmetry model, it was expected that the numerical models developed to simulate the experimental tests would require significantly more CPU time to complete. The main reasons for this assumption were that the final blast test models would require the inclusion of additional structural components (a clamp frame and ULD box) and have less symmetry options available (to reduce the simulated domain).

It was decided to use a 2 mm element size for both the air mesh and target plate. Reducing the target plate element size (for the same air mesh size) produced negligibly different results, and reducing the air mesh size increased the required CPU time to beyond that which was deemed practical. The simulation with this mesh resolution combination produced final and peak midpoint deflections that were 9.7% and 7.2% lower, respectively, than those predicted in the simulation with a 1 mm resolution for both the air mesh and target plate, and only required 6% of the CPU time to complete. This compromise was considered acceptable and necessary to successfully complete all the final blast test simulations.

6.4 Development of Structural Components

The structural components of the numerical models included the target plate, the clamp frame and the ULD box. All the simulations required a target plate and clamp frame, whereas the confined blast simulations also required the ULD box. For each of the structural components, a full and half-symmetry version was required: half-symmetry could be utilised for all the simulations except for the first series of fully-vented blast tests, for which there was no plane of symmetry. Additionally, contact between the structural components, particularly between the target plate and clamp frame/ULD box, needed to be controlled to ensure an accurate boundary condition across the clamped region was simulated.

6.4.1 Target Plate

The target plate had total dimensions of 355 mm × 280 mm with an off-centre exposed area of 255 mm × 117 mm. The length of the target plate was halved when modelling the half-symmetry version. The surface of the plate was meshed with 2 mm × 2 mm shell elements. The clamped region of the plate was selected by means of a segment set, which allowed a series of element surfaces to be grouped together and collectively assigned contact properties. Figure 6.4 illustrates the clamped region surrounding the exposed area of the target plate, for both the full and half-symmetry models.

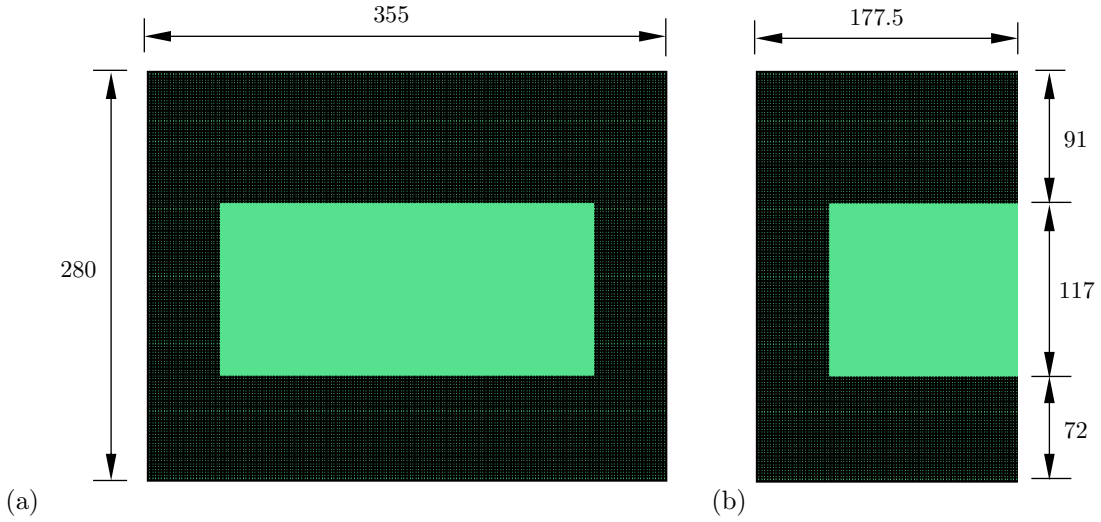

Figure 6.4: Numerical model of target plate, showing exposed area and shaded clamped region for (a) full and (b) half-symmetry models.

6.4.2 Clamp Frame

The geometry of the clamp frame was identical to that of the clamped region of target plate. When developing the clamp frame, the surface was first divided into sections, as illustrated by the surface layout diagram in Figure 6.5, to ensure a structured mesh was created. The sections were modelled and meshed with 2 mm shell elements. The duplicate nodes along the shared edges were merged, and the shells were used to generate the solid elements for the clamp frame. From the surface layout, both the full and half-symmetry versions could be created be selecting the appropriate shells to extrude. The total thickness was set to 20 mm and 10 sections were created, ensuring the aspect ratio of the solid elements was close to unity (approximately 2 mm × 2 mm × 2 mm). The solid clamp frame structure, for a half-symmetry model, is shown in Figure 6.6. The top and bottom surfaces of the clamp frame were assigned a segment set to ensure contact with the target plate could be controlled.

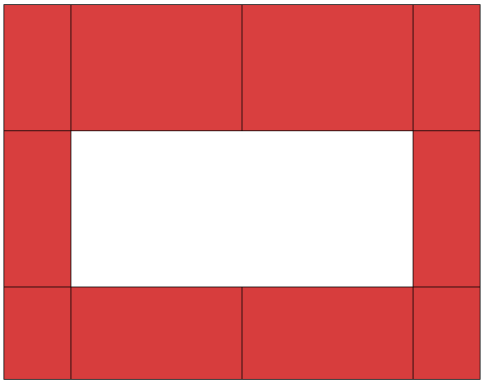

Figure 6.5: Surface layout diagram for generating the solid clamp frame structure.

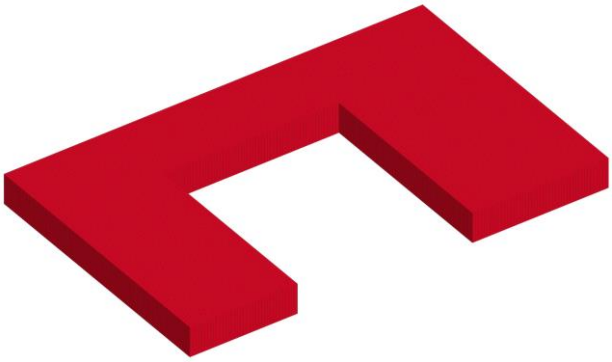

Figure 6.6: Half-symmetry model of clamp frame.

6.4.3 ULD Box

Three versions of the test box were created, one for each series of confined blast tests. A single surface layout was created, as illustrated in Figure 6.7, from which all three test boxes could be produced. Each surface was meshed with 2 mm shell elements and the duplicate nodes appearing on the shared edges were merged to form an interconnected surface layout. This layout included the geometry of all the components of the box – each of the panels, the flange and the venting area of the side panel – which could be created individually by selecting and extruding the appropriate surfaces to produce the solid elements representing the structure. The solid elements were set to 2 mm in height to maintain an aspect ratio close to unity. Using the same layout to produce all the box components ensured that the nodes on all the adjacent surfaces, following the extrusion of the shells, aligned correctly so that the nodes could be properly merged, resulting in a cohesive box structure. The fully-confined box was generated for a half-symmetry model, as illustrated in Figure 6.8(a). The first series of fully-vented blast tests used a ULD box with only one vented side, requiring a full model to be simulated due to

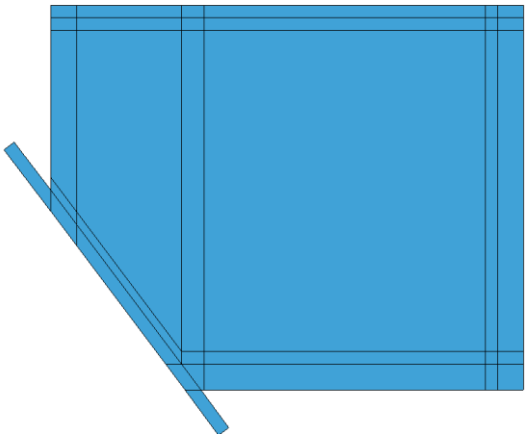

Figure 6.7: Surface layout diagram for generating the solid ULD box structure.

the absence of any symmetry planes. The box for this series of simulations is shown in Figure 6.8(b). The second series of fully-vented blast tests used a ULD box with two vented sides, which was simulated using a half-symmetry model, as shown in Figure 6.8(c). The flange surface on all three box models was assigned a segment set to control the contact between the flange and the target plate.

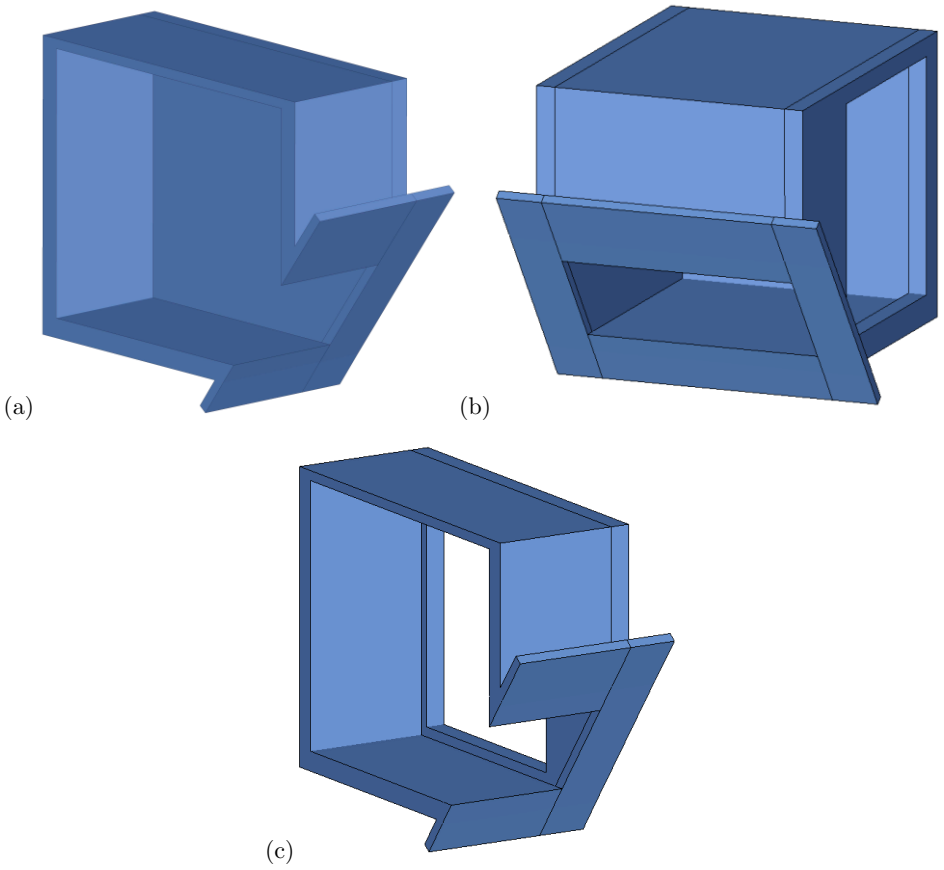

Figure 6.8: Solid element model of ULD box for the (a) fully-confined, (b) first series of fully-vented and (c) second series of fully-vented blast tests.

6.4.4 Contact

The clamped condition of the target plate was simulated by enforcing contact between the target plate and, in the case of the unconfined blast tests, two clamp frames. For the confined blast tests, the contact was enforced between the target plate and both the clamp frame and the flange of the ULD box. To create these contact conditions, an automatic surface-to-surface contact card is created. The segment sets of the two contact surfaces are specified, one in the master (clamp frame/flange) and the other in the slave (target plate) capacity. Checks are performed to ensure the slave segments only transverse tangentially to the master segments, allowing them to slide without moving/pulling away from the surface. The *automatic* contact card performs these checks from both the master and slave segments, resulting in the distinction being inconsequential to the contact condition [50]. To ensure realistic movement of the target plate between the clamping surfaces, a static and dynamic friction coefficient must be specified. The inclusion of friction would replicate the boundary pull-in of the plate should the forces be high enough. The coefficient of friction for aluminium-steel contact was specified as 0.61 for both static and dynamic resistance [54].

6.5 Blast Models

Four blast models were developed to simulate each series of experimental tests: the unconfined blasts, fully-confined blasts and two series of fully-vented blasts with different venting areas. Use of the symmetry of each test configuration (where applicable) was made to improve the computation time for each simulation. For each simulation the peak midpoint deflection, the final (average) midpoint deflection and the final (average) plate profile was recorded. The simulations were run to capture the first 3 ms of the plate response following the detonation of the explosive charge.

The air domain was modelled using three-dimensional, eight-node solid brick elements with a unity aspect ratio (1:1:1) and an element length of 2 mm. An MMALE element formulation was used to model the air and explosive. Hourglass control of the solid elements was implemented using the Flanagan-Belytschko viscous form with exact volume integration. The air was modelled to obey the ideal-gas relation, and the explosive was modelled using the Jones-Wilkins-Lee equation of state and the high explosive burn material model.

The target plate was modelled using two-dimensional, four-node quadrilateral shell elements with an element length of 2 mm. The plate had a thickness of 2 mm. The full dimensions of the target plate were 355 mm × 280 mm with an exposed area of 255 mm × 116 mm. The

Belytschko-Tsay element formulation was used to model the plate. Flanagan-Belytschko viscous form hourglass control was also implemented for the shell elements. The Johnson-Cook material model was used to define the material behaviour during high strain and high strain-rate loadings, and elevated temperatures.

6.5.1 Unconfined Blast Model

The unconfined blast tests were modelled using a half-symmetry model. The model comprised the air domain (including explosive), target plate and two clamp frames. The charge was located at a stand-off distance of 163 mm. Charge masses ranging from 10 g to 25 g were tested, which corresponded to charge radii of 11.4 mm to 15.5 mm, respectively. The height of the air domain was set to 220 mm to accommodate the maximum charge size, the stand-off distance and the deformation of the plate. The dimensions of the air domain were set to 280 mm × 178 mm × 220 mm to include the entirety of the clamp frames. The unconfined blast model is shown in Figure 6.9. The nodes of the air mesh and target plate located on the yz–plane were assigned symmetry boundary conditions. Those of the clamp frames were assigned fixed boundary conditions to ground the simulation and prevent any rigid body motions. The resultant displacement of the nodes on the target plate would therefore be equal to the absolute deflection of the plate itself.

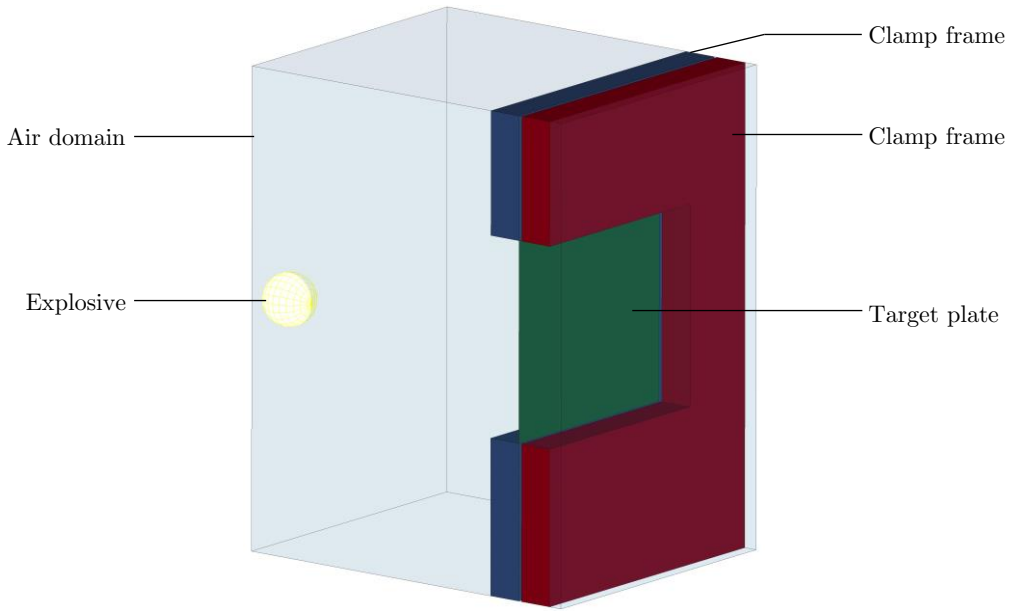

Figure 6.9: Numerical blast model for unconfined tests.

6.5.2 Fully-Confined Blast Model

The fully-confined blast tests were modelled using the half-symmetry model shown in Figure 6.10. The model comprised the air domain, the ULD box, the clamp frame and the target plate. The nodes in the *xy*-plane were assigned symmetry boundary conditions. The air domain was developed to include the ULD box, excluding the flange, and consequently had dimensions of 370 mm x 302 mm x 148 mm. This air domain size ensured the fluid-structure interaction between the air/explosive and ULD walls was maintained (modelling the air domain to match the internal dimensions of the box would result in pressure leaving the air mesh once the ULD walls begin to deform slightly). The target plate remained within the air mesh during deformation by moving into the space available between the bottom corner of the air domain and the diagonal side of the ULD box, ensuring there was no loss in interaction between the air/explosive and target plate. The explosive was located within the air domain at a stand-off distance of 163 mm and charge masses ranging from 10 g to 20 g were simulated.

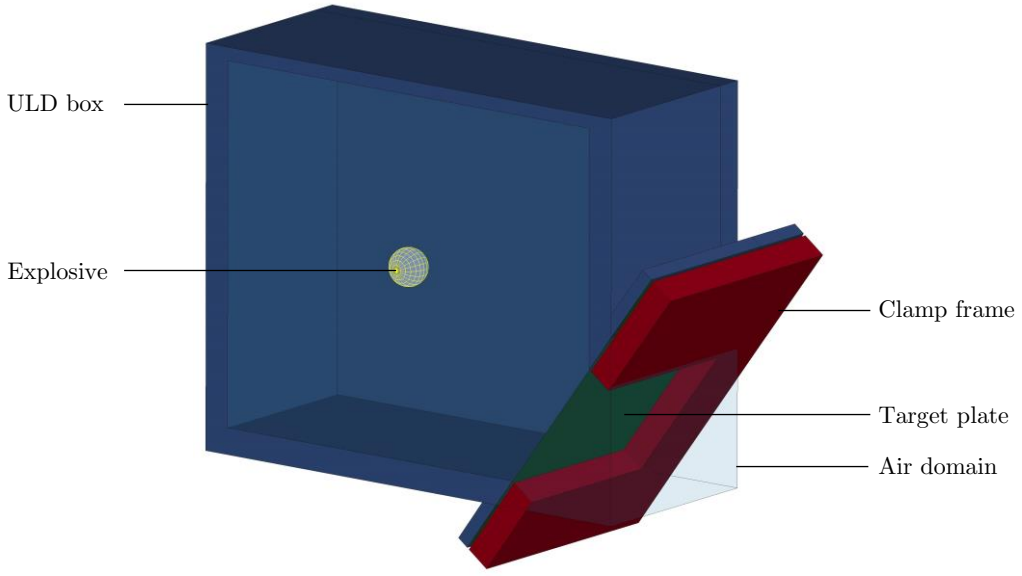

Figure 6.10: Half-symmetry numerical blast model for fully-confined tests.

6.5.3 Fully-Vented Blast Models

The fully-vented tests each required a vented area to be present during testing. The first series had one venting area present, resulting in a scaled-venting area of $\zeta = 0.7$. Since there was no symmetry present with this configuration, the entire test rig was modelled: the full structure

of the ULD box with one venting area (as shown in Figure 6.8(b)), the clamp frame and the target plate, as well as an air domain with dimensions 370 mm x 302 mm x 295 mm. The second series of fully-vented tests had a second venting area, resulting in a scaled-venting area of $\zeta = 1.4$. The symmetry of this setup allowed a half-symmetry model to be simulated, requiring half model of the vented ULD box, as shown in Figure 6.8(c). The clamp frame, target plate and air domain were the same as used in the fully-confined model. The Cartesian system used in the fully-confined and fully-vented models was identical, requiring no change in the explosive location, target plate and clamp frame placement, or the symmetry boundary conditions. The blast models for both fully-vented tests are shown in Figure 6.11.

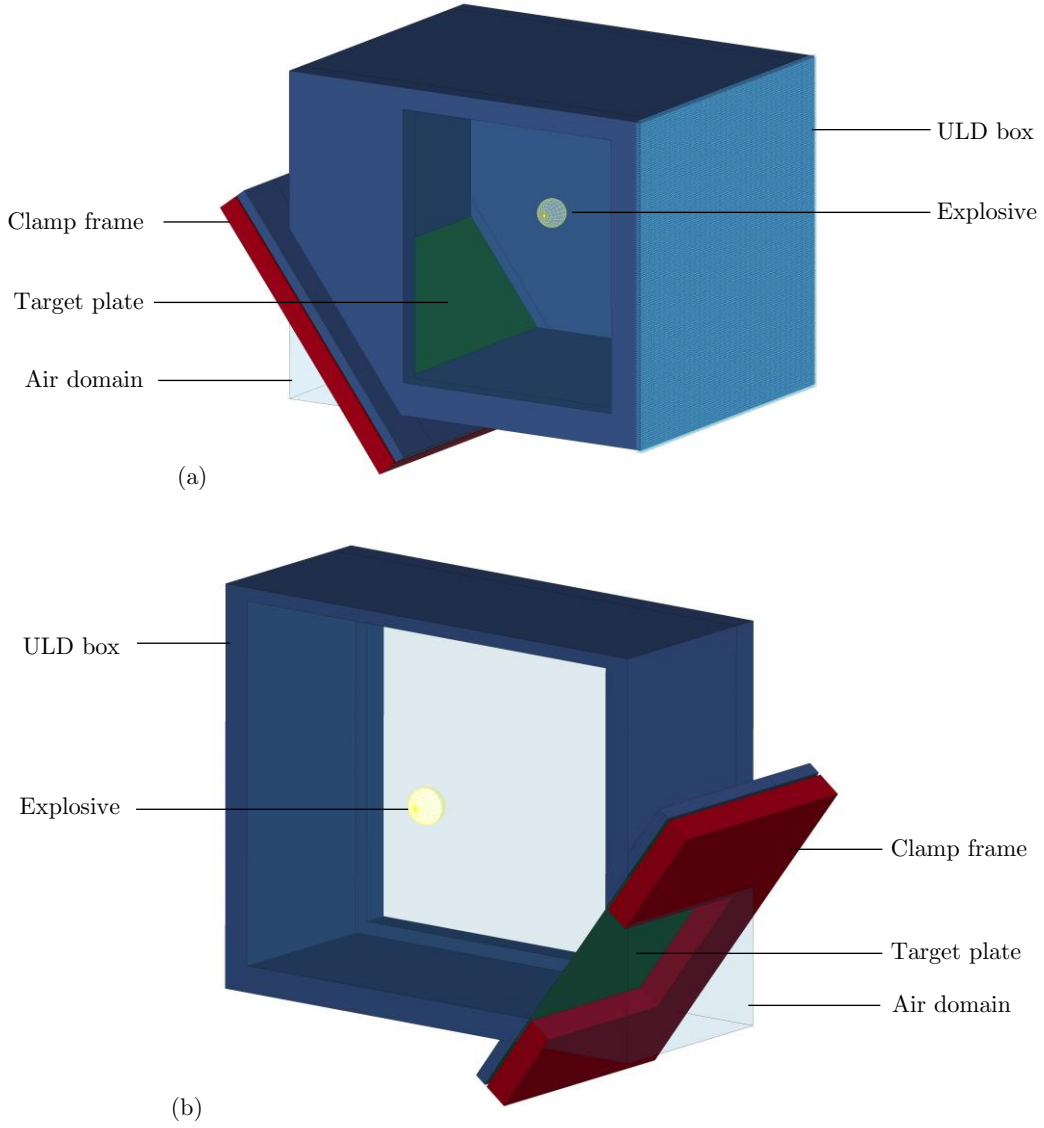

Figure 6.11: Numerical blast models for fully-vented tests simulated using a (a) full model with $\zeta = 0.7$ and (b) half-symmetry model with $\zeta = 1.4$.

6.6 Fluid-Structure Interaction

All the structural components were modelled using a Lagrangian mesh and placed within the MMALE air mesh. A penalty method was used to couple the plate with the air and explosive so that the fluid-structure interaction could be modelled, and the pressure loading on the plate enforced. The required duration of active pressure loading – and the consequent effect on the plate deformation – was investigated to establish the loading phases for the simulations.

6.6.1 Coupling

A penalty coupling technique was implemented to enforce the fluid-structure interaction between the Lagrangian/slave (structural components) and solid/master (air and explosive) meshes. The constraint was introduced in the numerical model using the constrained-Lagrange-in-solid card. Two cards were required for each simulation: one to maintain interaction between the target plate and explosive, and another for the interaction between the clamp frame/ULD box and explosive. A 2×2 coupling-point distribution was defined across each Lagrangian element to enforce the coupling and prevent leakage (explosive material passing through and not physically interacting with the Lagrangian mesh).

6.6.2 Loading Phases

Most of the simulation time was due to the convergence of a solution for the air mesh at each time step. The fundamental purpose of the air mesh was to produce and propagate the explosive blast wave to create the high-pressure loading on the target plate. However, once the blast pressure diminished to a magnitude small enough not to transfer any significant impulse to the target plate, the air mesh was removed from the simulation. This pressure cut-off was instrumental in improving the simulation time because it removed the need to calculate a converged solution at every time step for a large mesh which no longer affected the response of the target plate. Additionally, the fluid-structure interaction, which was also a computationally-expensive constraint to implement, did not need to be enforced.

Determination of a pressure cut-off time was particularly important for the fully-confined model. As shown in Figure 6.12(a), there were several pressure reflections taking place within the ULD box following the detonation of the explosive. Furthermore, the pressure within the ULD did not diminish to atmospheric conditions. Three pressure cut-off times were evaluated: the first at 0.5 ms (capturing the first two pressure reflections), the second at 0.7 ms (capturing

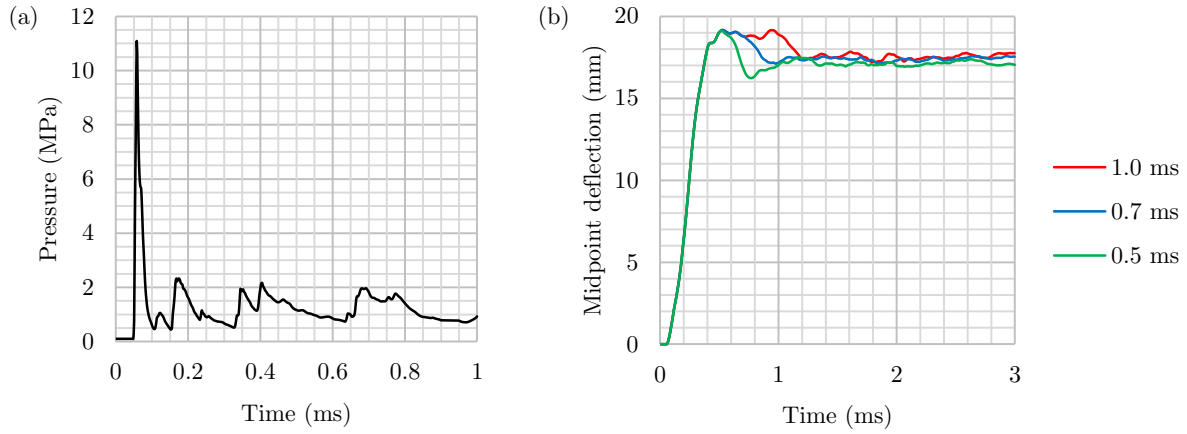

Figure 6.12: Fully-confined 17 g simulation result showing (a) pressure and (b) midpoint deflection histories.

the first three pressure reflections) and the third at 1 ms, after which simulation run-times became impractical. The transient midpoint displacement for the three pressure cut-off times is shown in Figure 6.12(b). The initial response of the plate was identical, however, the plate response differed from approximately 0.6 ms. Unloading the plate (switching off the air mesh) caused the displacement to drop from a peak position and converge towards a final deflection. A later pressure cut-off time resulted in a longer duration at the peak displacement position. However, despite being unloaded at different times, the final midpoint displacements were similar for the three cases; later pressure cut-off times resulted in slightly higher final deflections. Consequently, a pressure cut-off time of 0.7 ms was chosen for the fully-confined blasts. The peaks of the first three pressure reflections were captured, the deflection difference (compared to the 1 ms case) was 0.7%, and the CPU time was reduced by 33%.

Pressure cut-off times for the unconfined and fully-vented blasts were established by identifying the time at which the pressure diminished to atmospheric conditions. Table 6.5 lists the pressure cut-off times for each of the blast models. Each simulation was run in two stages: The first was the loading stage, where all components were simulated and the termination time was set to the pressure cut-off time. The second was an unloading phase, where a restart analysis was performed by inputting the loading conditions from the first stage and deleting the air mesh and FSI constraints. The second stage termination time was set to 3 ms, which was the time by which the plate vibrations of all the simulated blast configurations converged.

Table 6.5: Pressure cut-off times for numerical simulations.

Blast model	**Unconfined**	**Fully-vented**	**Fully-confined**
Pressure cut-off time (ms)	0.2	0.4	0.7

This page is intentionally left blank.

7 Numerical Results

The previous chapter reported on the development and validation of numerical simulations of the physical blast experiments. This chapter presents the results from the simulations of the fully-confined tests, the two fully-vented tests (with different venting areas), and the unconfined tests. Charge masses ranging from 10 g to 20 g were tested in the fully-confined simulations, whereas charge masses up to 25 g were tested in all three of the other cases. The first 3 ms of the blast response of the target plate was of interest in each simulation and comprised a loading phase, where the explosive was detonated and the resulting blast pressure imparted impulse to the target plate, and an unloading phase, where the target plate vibrated elastically in the absence of the blast pressure to reach a final deformed shape.

The results presented herein focus on the blast load evolution for each of the confinement cases, the resulting transient deformation of the long-side midline (which included the plate midpoint) and the blast pressure history at the midpoint and corners of the exposed target plate. The goal was to provide additional insight into the loading (which could not be experimentally measured) and how the blast pressure wave influenced the structural response of the target plate.

7.1 Blast Load Evolution

The loading phase included the detonation of the explosive and the subsequent propagation of the pressure wave through the air. The fluid-structure interaction was properly maintained and ensured that the pressure waves were reflected off of – and that impulse was transferred to – the structural components. The propagation of the blast wave throughout the loading phase was captured in each of the simulations. The results of a 15 g charge detonation in each of the simulations is shown in Figure 7.1 through to Figure 7.4.

The fully-confined blast load evolution is shown in Figure 7.1. Following detonation, the blast wave propagated radially outwards and towards the walls of the ULD box and the target plate. After 60 μs the blast wave had reflected off the top and bottom panels, and the target plate, as indicated by zones of high pressure in these regions. At approximately 80 μs, reflections between the target plate and ULD box walls created high pressure zones along the target plate edges. By 100 μs, the pressure wave started propagating back towards the centre of box. The target plate started deforming after 100 μs. From 200 μs onwards, the blast wave underwent several complicated interactions resulting in a quasi-static pressure accumulation within the structure.

The blast load evolutions for the fully-vented simulations, with $\zeta = 0.7$ and $\zeta = 1.4$, are shown in Figure 7.2 and Figure 7.3, respectively. The blast load development up to 60 μs was identical to that of the fully-confined case. However, at after 60 μs, the blast wave began to vent through holes of the structure and leave the air domain. The venting of the blast pressure resulted in the absence of wave reflections at the venting regions. Consequently, at approximately 200 μs, when the blast wave had propagated back towards the centre of the box, the internal blast wave exhibited a lower magnitude and fewer interactions than in the fully-confined simulation at the same time.

The blast load evolution for an unconfined blast is illustrated in Figure 7.4. The blast pressure impinged on the target plate by 60 μs and accumulated along the target plate edges after approximately 80 μs. The target plate began to move after approximately 100 μs, as observed in the other simulations. After 100 μs, however, the blast wave propagated out of the air domain and had almost entirely diminished after 180 μs.

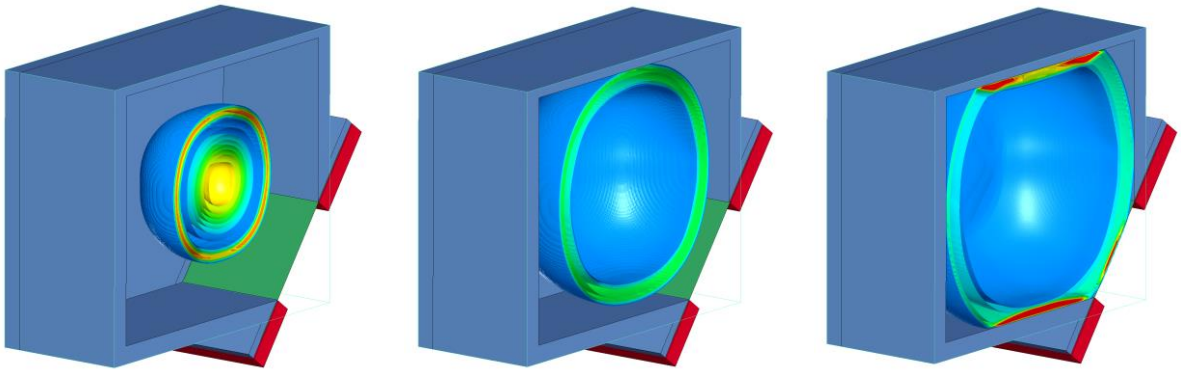

20 µs
Blast wave propagates radially.

40 µs

60 µs
Blast wave reflects off target plate and ULD walls.

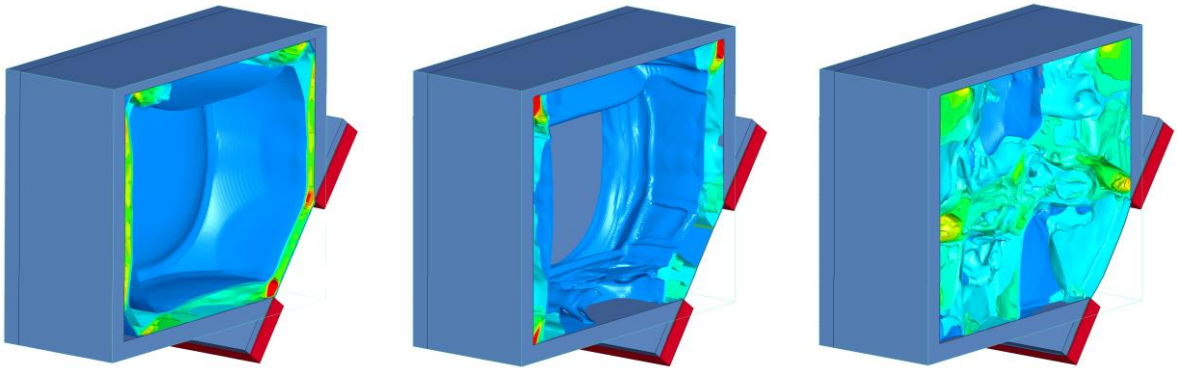

80 µs
High pressure accumulation along target plate edges.

100 µs
High pressure accumulation along ULD box edges.

200 µs
Reflected pressure waves return to centre of ULD box.

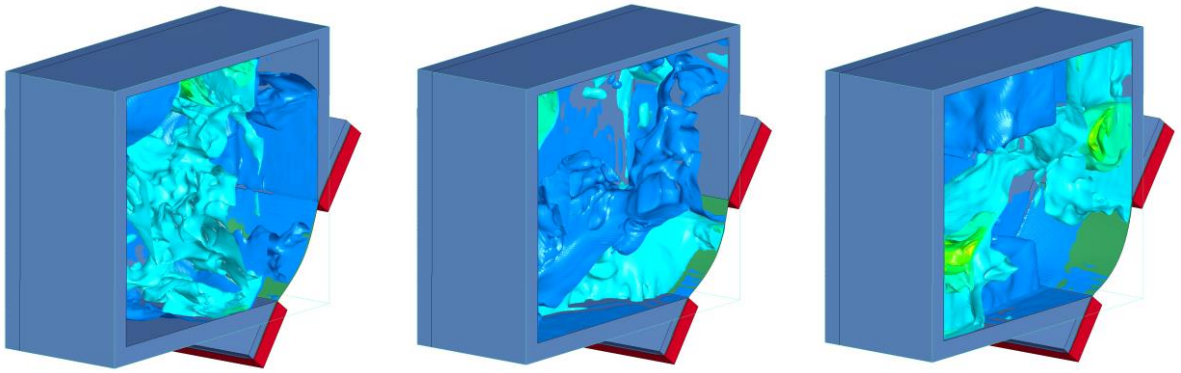

300 µs

400 µs

500 µs
Complicated internal pressure reflections and quasi-static internal pressure build-up.

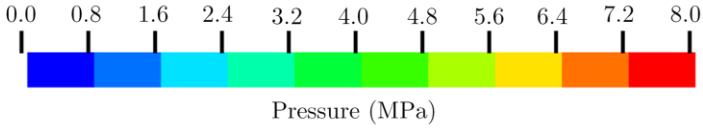

Figure 7.1: Blast load evolution for a 15 g charge detonation in the fully-confined blast model.

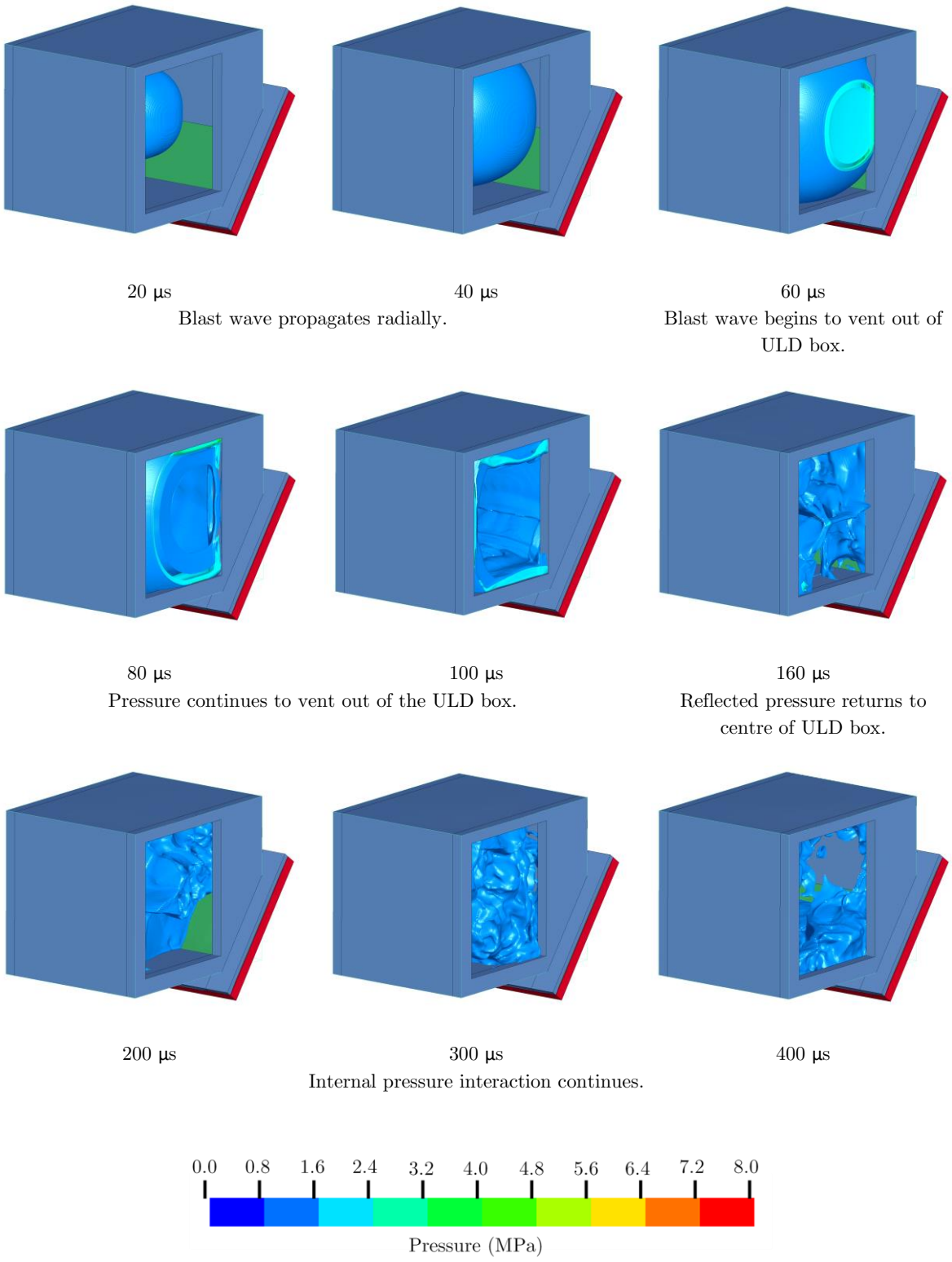

Figure 7.2: Blast load evolution for a 15 g charge in the fully-vented ($\zeta = 0.7$) blast model.

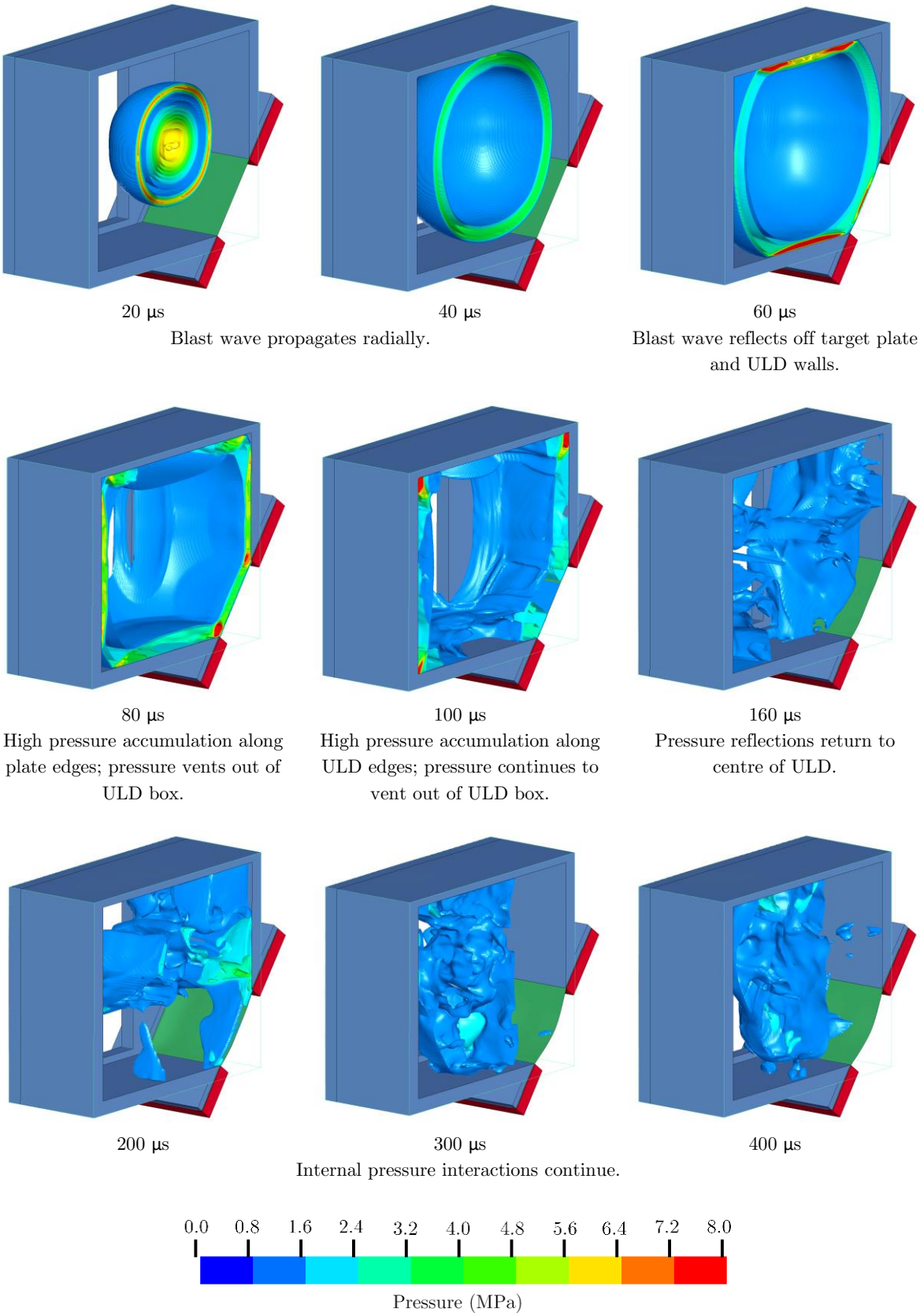

Figure 7.3: Blast load evolution for a 15 g charge in the fully-vented ($\zeta = 1.4$) blast model.

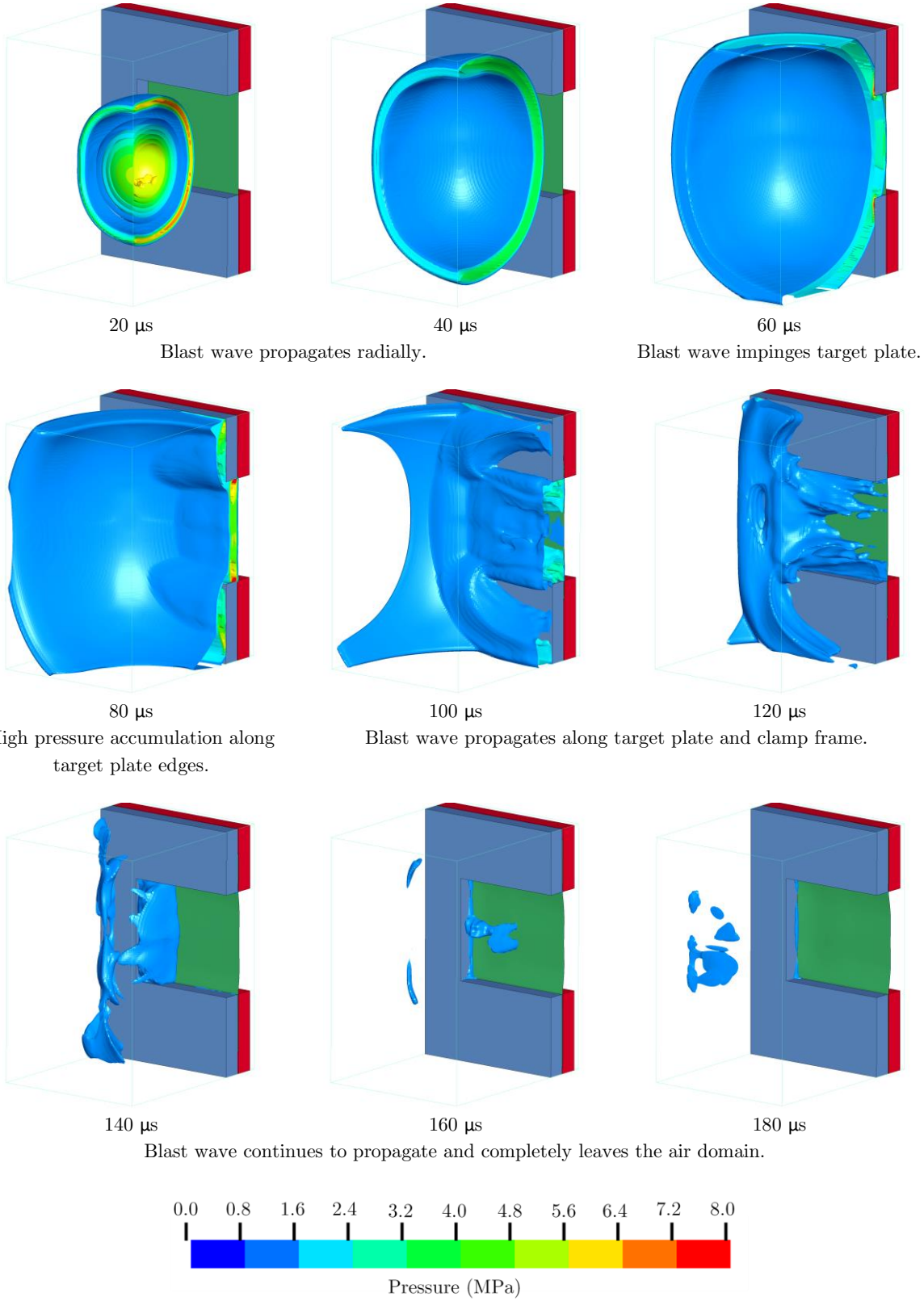

Figure 7.4: Blast load evolution for a 15 g charge in the unconfined blast model.

7.2 Target Plate Deflection

The response of the target plate was recorded for the first 3 ms following the detonation of the explosive. The blast response of the target plate was measured by the deformation of the long-side midline. Two phases of the deformation were captured in the simulations: a peak deflection of the plate due to the blast pressure was reached, and thereafter a damped vibratory response of the plate was exhibited from which the final midline profile was approximated.

7.2.1 Transient Midpoint Deflection

The deflection of the midpoint was used as a comparison of the blast response of the target plate across all the simulated test cases. The peak midpoint deflection for each simulation is listed in Table 7.1. The peak midpoint deflection increased with an increase in the charge mass and an increase in the degree of confinement (or decrease in venting area).

Table 7.1: Numerical peak midpoint deflection for varying charge masses and degrees of confinement.

Charge mass (g)	**Peak midpoint deflection (mm)**			
	Fully-confined	**Fully-vented ($\zeta = 0.7$)**	**Fully-vented ($\zeta = 1.4$)**	**Unconfined**
10	14.02	12.90	11.47	8.48
12	15.60	14.17	12.75	9.38
15	17.95	16.47	14.80	10.99
17	19.17	17.55	15.93	11.71
20	21.54	19.69	17.90	12.93
25	-	22.82	20.46	14.96

The overall transient midpoint deflection for each simulation showed a similar proportionality to the charge mass and degree of confinement as that of the peak midpoint deflection. The transient midpoint deflection of the target plate for each simulation (and for all the tested confinement cases) is shown in Figure 7.5.

Note: no fully-confined blast simulation was performed at 25 g.

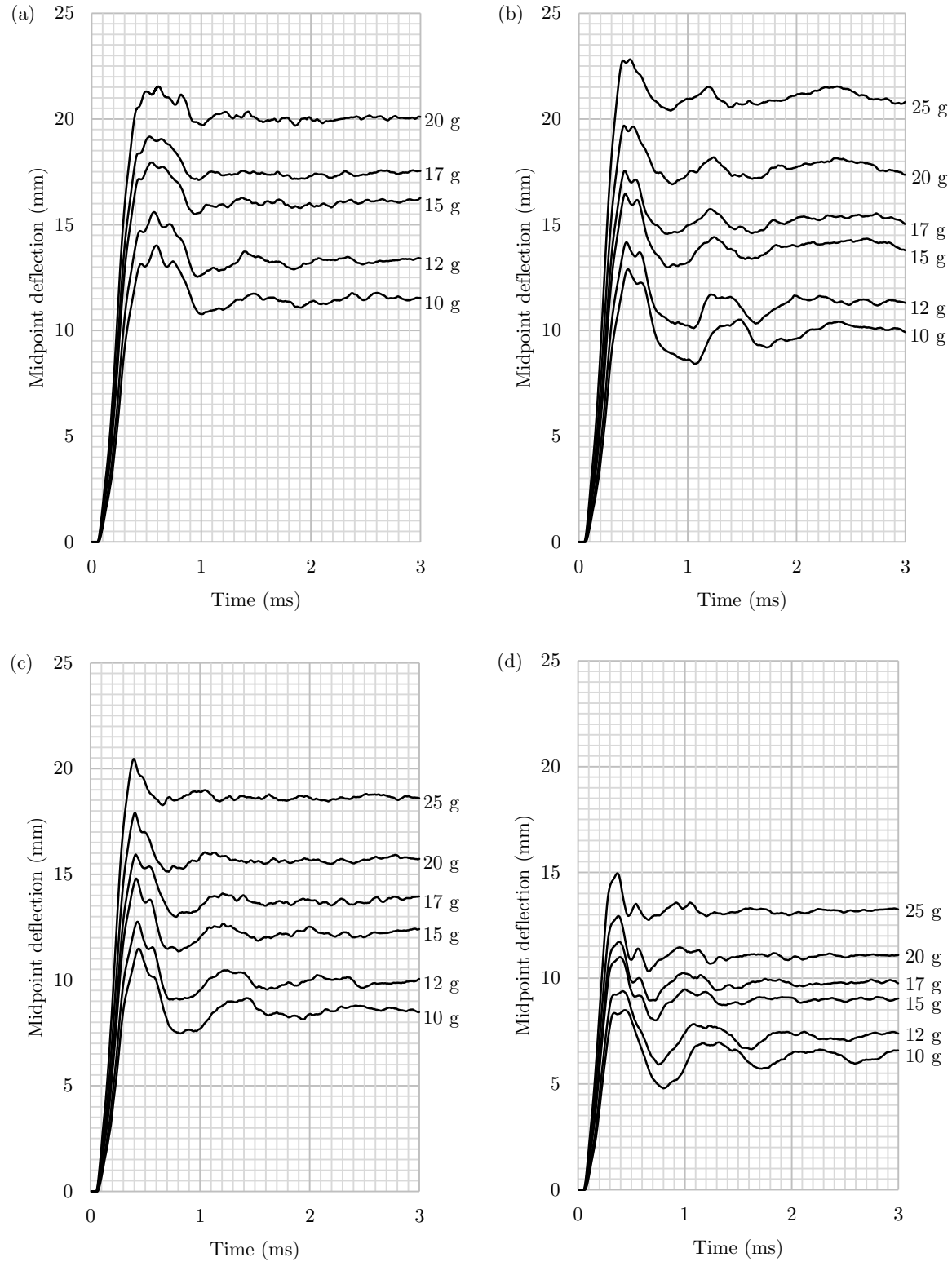

Figure 7.5: Graphs of the transient midpoint deflection of the target plate for (a) fully-confined, (b) fully-vented ($\zeta = 0.7$), (c) fully-vented ($\zeta = 1.4$) and (d) unconfined blast simulations.

The peak midpoint deflection for the fully-confined blast simulations was observed to occur at approximately 0.6 ms after the detonation of the explosive. For the two fully-vented blast simulations, the peak midpoint deflection occurred at approximately 0.45 ms and 0.40 ms for the cases with venting area ratios of $\zeta = 0.7$ and $\zeta = 1.4$, respectively. The peak midpoint deflection for the unconfined blast simulations occurred at approximately 0.38 ms. The initial velocity with which the plate begins to move increased with an increase in charge mass, as evidenced by the steeper gradients at higher charge masses. However, similar initial velocities were observed for the different degrees of confinement; the higher peak deflections (at higher degrees of confinement) resulted in the arrival of the peak deformation at later times.

7.2.2 Final Midpoint Deflection

The final midpoint deflection of the target plate was calculated as the average midpoint deflection over the time range of 2 ms and 3 ms after the detonation of the explosive. In most of the simulations there was a steady vibratory response of the target plate during this period. The final midpoint deflection for all the simulated tests is listed in Table 7.2 and plotted in Figure 7.6. These deflections exhibited a trend consistent with the transient midpoint response: the deflection increased with both an increase in charge mass, and an increase in the degree of confinement.

Table 7.2: Numerical final midpoint deflection for varying charge masses and degrees of confinement.

Charge mass (g)	**Final midpoint deflection (mm)**			
	Fully-confined	**Fully-vented ($\zeta = 0.7$)**	**Fully-vented ($\zeta = 1.4$)**	**Unconfined**
10	11.51	10.13	8.60	6.36
12	13.32	11.40	9.93	7.26
15	16.07	14.14	12.23	8.99
17	17.42	15.35	13.75	9.76
20	20.03	17.84	15.70	11.05
25	-	21.17	18.63	13.19

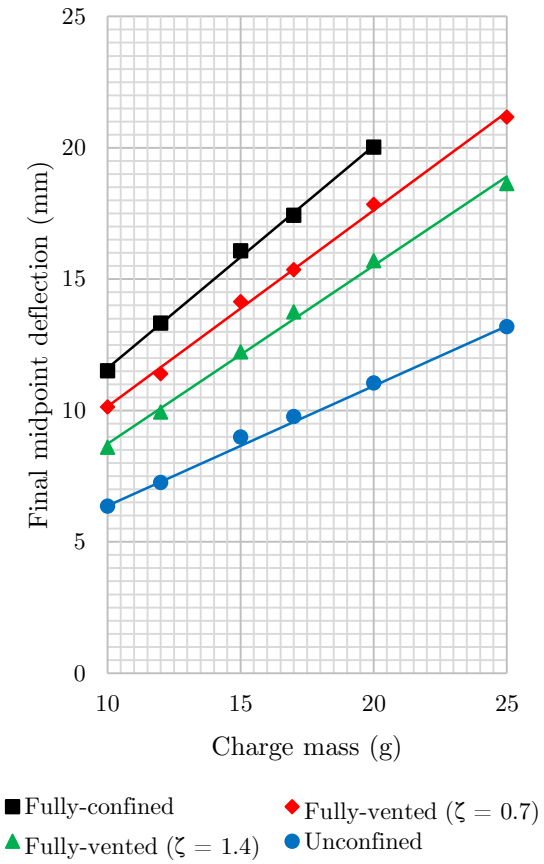

Figure 7.6: Graph of the final midpoint deflection vs charge mass for all blast simulations.

Two observations were made of Figure 7.6. Firstly, a linear relationship between the final midpoint deflection and charge mass was exhibited by each of the degrees of confinement. Secondly, as evidenced by the steepening gradient from the unconfined to the fully-confined blast simulations, the rate at which the midpoint deflection increased (with respect to charge mass) increased with an increasing degree of confinement.

7.2.3 Transient Midline Deflection

The deflection of the long-side midline was measured to assess the overall deformation profile of the target plate. This deformation provided an indication of the blast pressure distribution across the plate as well as the mode shapes exhibited during the transient deformation of the plate. The former is particularly relevant for the asymmetric configuration of the first (single-sided) fully-vented blast model. The latter provided an insightful result for all the blast tests since the final midline profile was often not the same shape as those developed during the transient deformation phase. The transient midline profiles for the smallest and biggest charge mass for all of the confinement cases are shown in Figure 7.7 through to Figure 7.14.

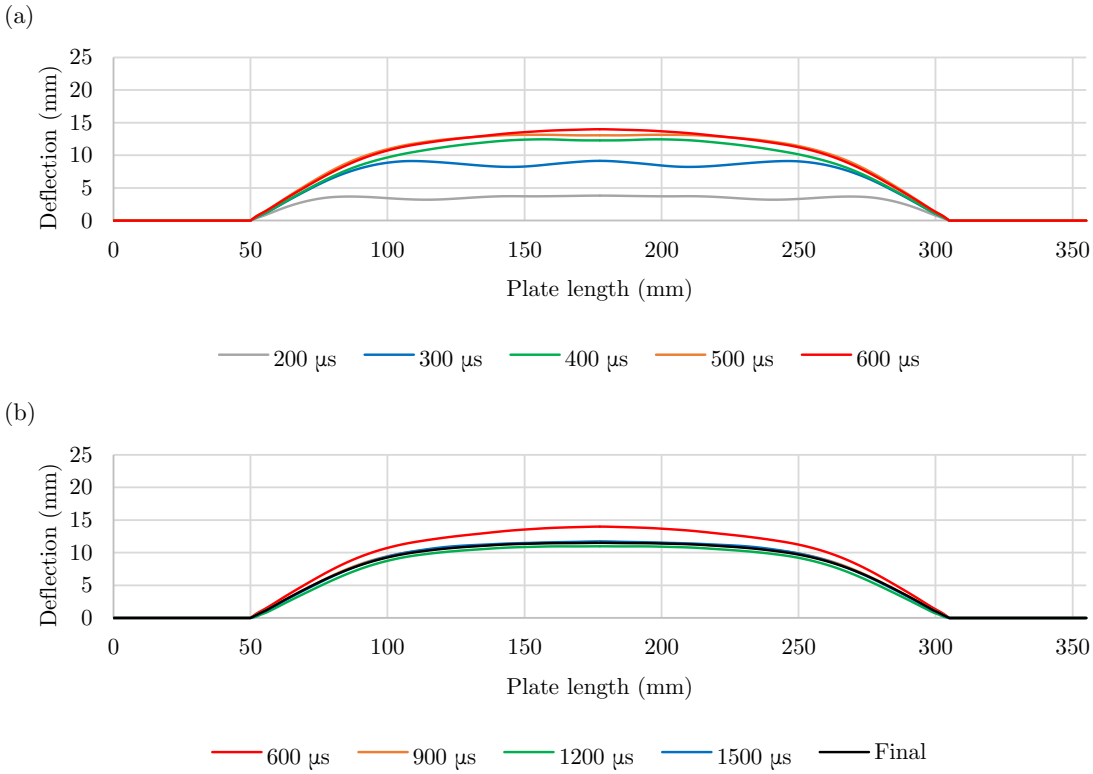

Figure 7.7: Graphs of the transient midline profile for a fully-confined blast simulation with a 10 g charge, deforming from (a) undeformed to peak deformation and (b) peak to final deformation.

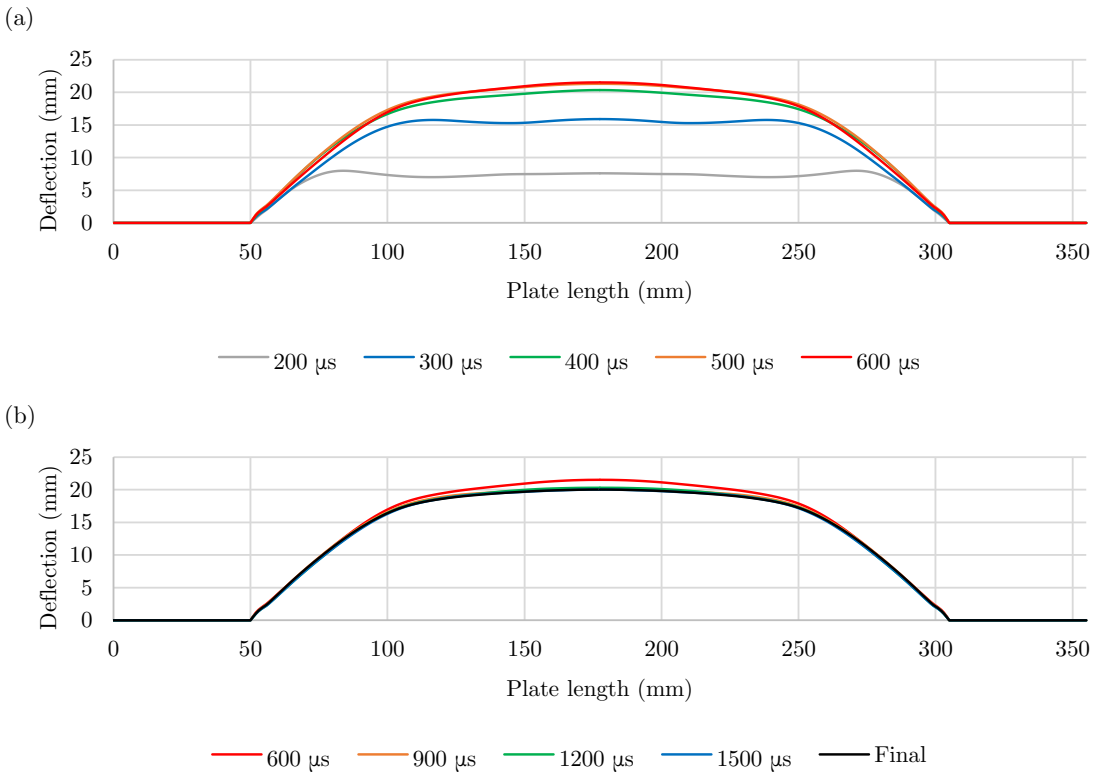

Figure 7.8: Graphs of the transient midline profile for a fully-confined blast simulation with a 20 g charge, deforming from (a) undeformed to peak deformation and (b) peak to final deformation.

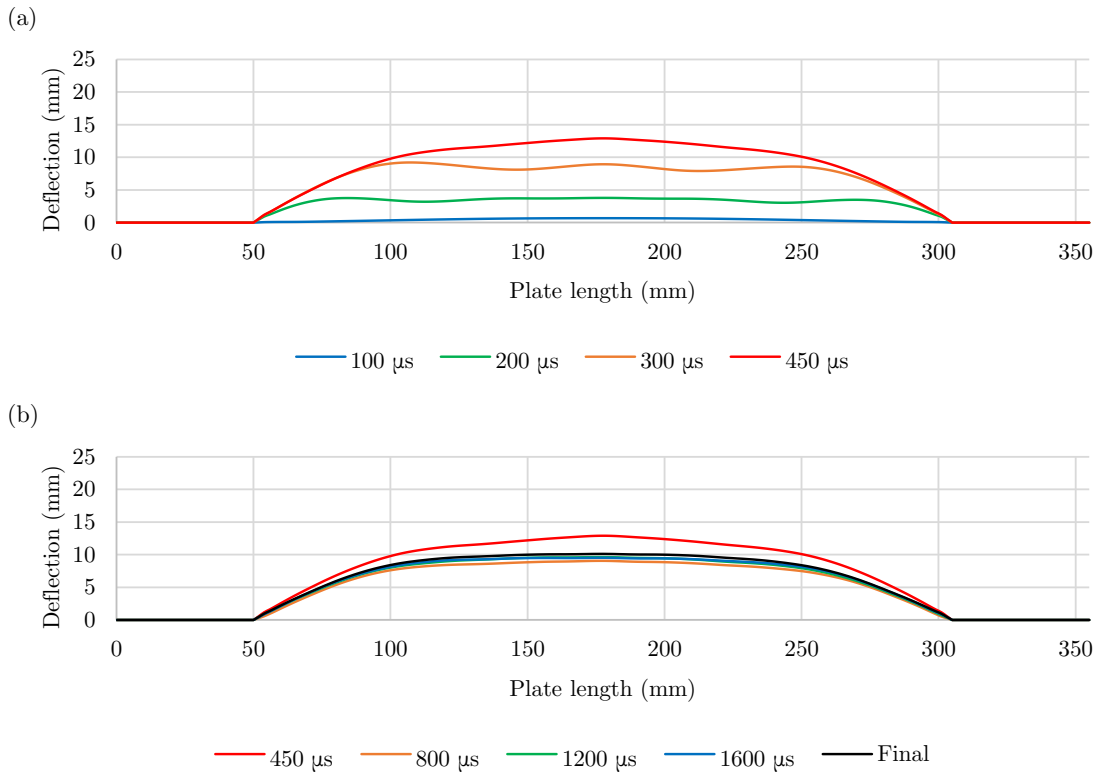

Figure 7.9: Graphs of the transient midline profile for a fully-vented ($\zeta = 0.7$) blast simulation with a 10 g charge, deforming from (a) undeformed to peak deformation and (b) peak to final deformation.

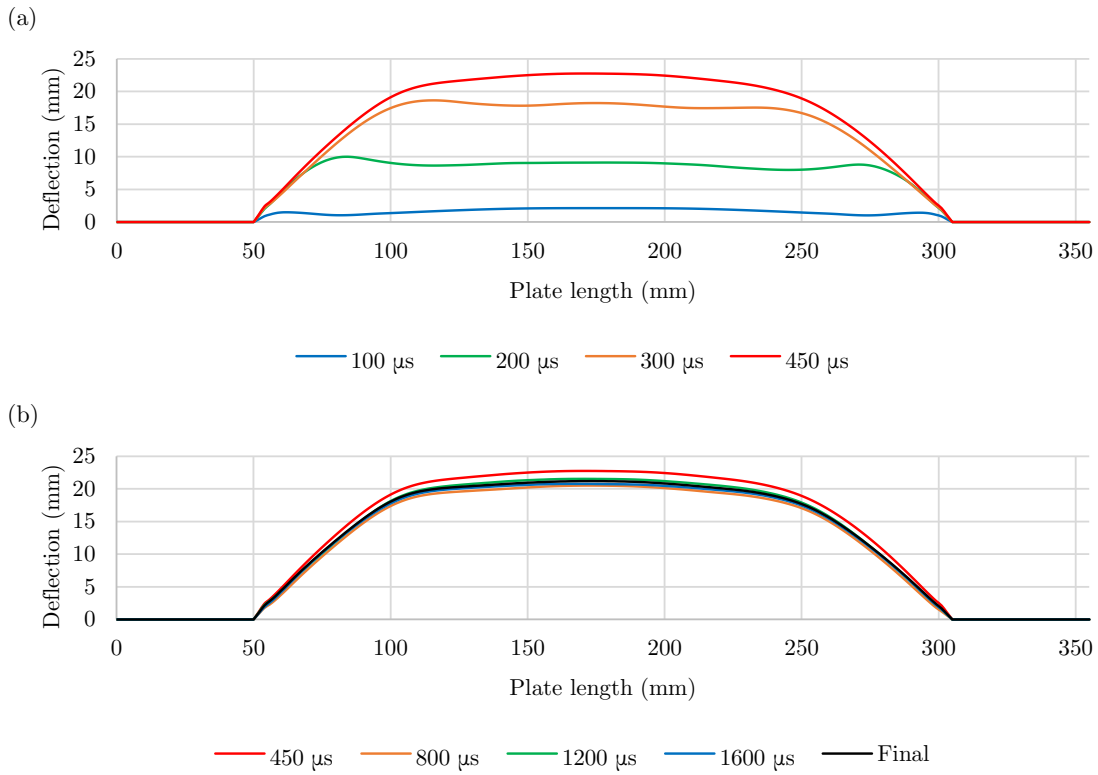

Figure 7.10: Graphs of the transient midline profile for a fully-vented ($\zeta = 0.7$) blast simulation with a 25 g charge, deforming from (a) undeformed to peak deformation and (b) peak to final deformation.

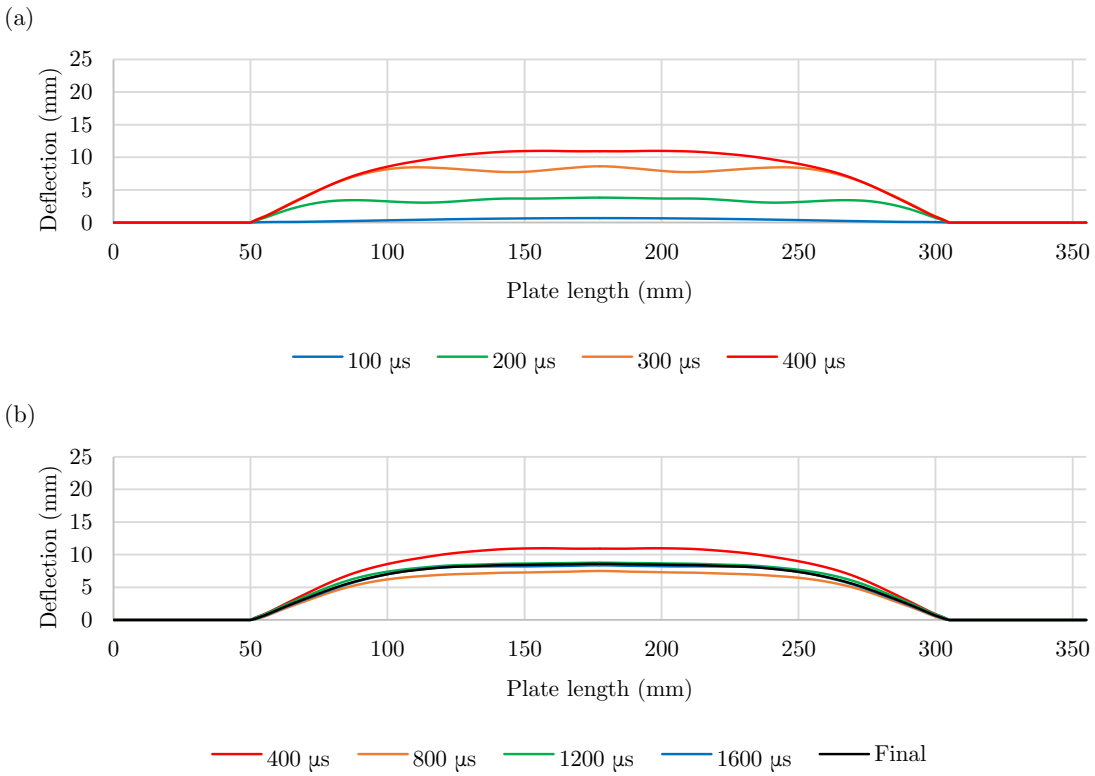

Figure 7.11: Graphs of the transient midline profile for a fully-vented ($\zeta = 1.4$) blast simulation with a 10 g charge, deforming from (a) undeformed to peak deformation and (b) peak to final deformation.

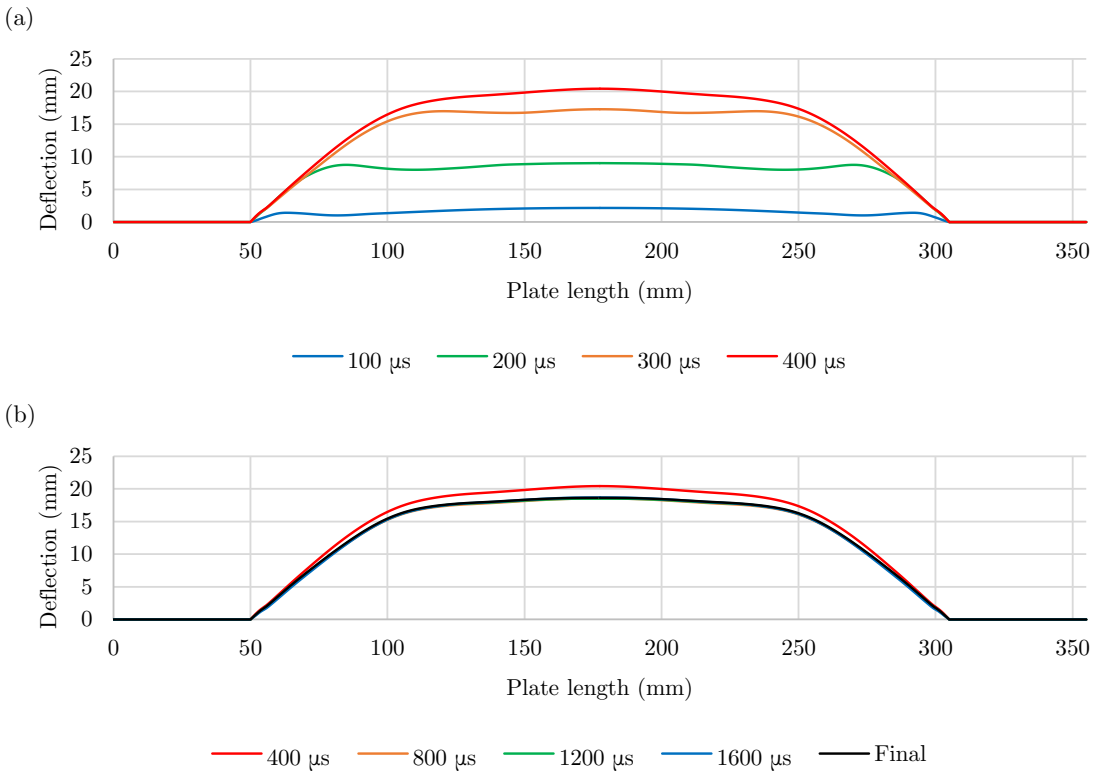

Figure 7.12: Graphs of the transient midline profile for a fully-vented ($\zeta = 1.4$) blast simulation with a 25 g charge, deforming from (a) undeformed to peak deformation and (b) peak to final deformation.

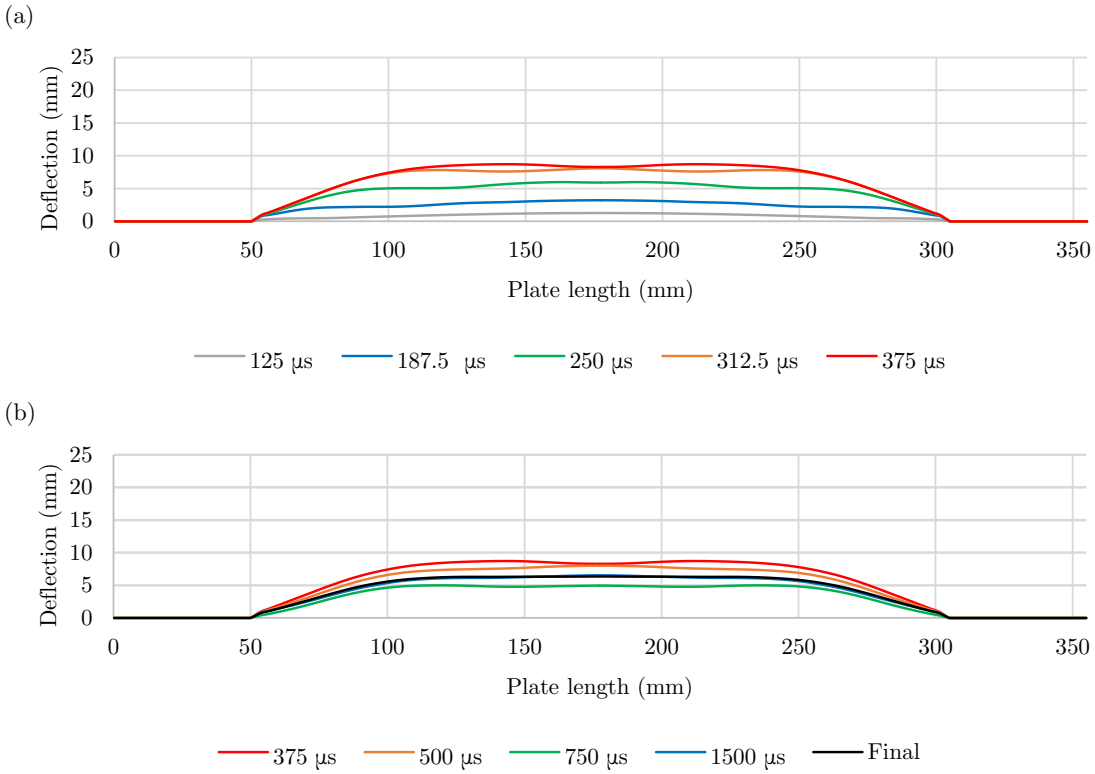

Figure 7.13: Graphs of the transient midline profile for an unconfined blast simulation with a 10 g charge, deforming from (a) undeformed to peak deformation and (b) peak to final deformation.

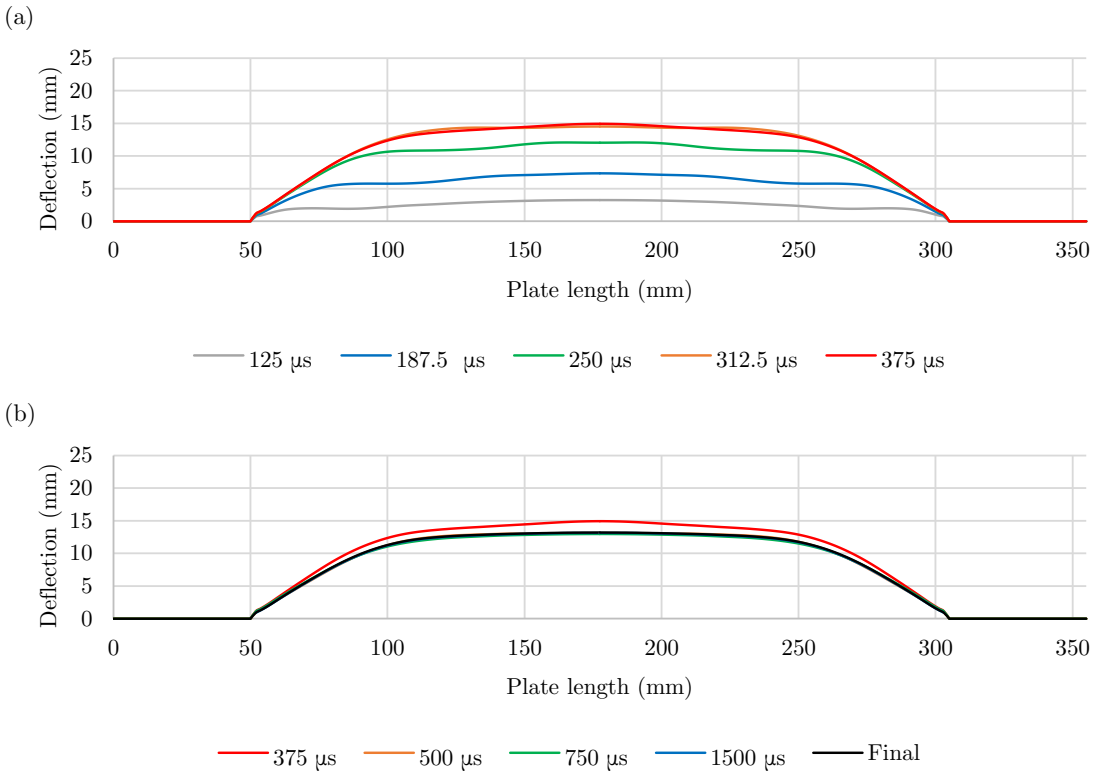

Figure 7.14: Graphs of the transient midline profile for an unconfined blast simulation with a 25 g charge, deforming from (a) undeformed to peak deformation and (b) peak to final deformation.

As observed in Figure 7.7 through to Figure 7.14, the transient response of the plate midline exhibited two phases: a steady rise to the peak deformed shape, and a damped elastic vibration converging towards the final midline profile. At higher charge masses, the elastic response converged more quickly towards the final deformed profile. This trend was evidenced by the lack of oscillations following the peak deformation (for all the confinement cases) at the highest tested charge mass. At the lowest charge mass, especially in the simulations with lower degrees of confinement, the midline profile was seen to undergo a slower convergence towards, and greater oscillations about, the final profile.

The transient profile shapes leading up to the peak midline profile exhibited three peaks: one at the midpoint and one at each end of the developing profile plateau. An asymmetric profile was observed to develop in the fully-vented ($\zeta = 0.7$) blast simulations, as seen in Figure 7.9 and Figure 7.10, with one side deforming more than the other. The side with the lesser deformation corresponded to the side with the venting area. In some cases, the peak midpoint deflection was not the greatest transient deflection in the plate. The two outer peaks deflected more than the peak at the midpoint in the 10 g fully-vented ($\zeta = 1.4$) and 10 g unconfined simulations, shown in Figure 7.11(a) and Figure 7.13(a), respectively. However, in all the simulations, the midline profile following the peak deformation tended towards only a single peak at or, in the case of the asymmetric fully-vented configuration, near the plate midpoint.

7.2.4 Final Midline Profile

The final midline profile was determined by the average midline deflection from 2 ms to 3 ms after the detonation of the explosive. Figure 7.15 illustrates the final midline profile of each simulation for all the confinement cases. In general, the final midline profile comprised two distinct zones: a sudden, steady increase in height from either edge of the clamp frame and a central region which developed into a flat plateau or a slightly bulging, dome-like profile.

Within each confinement case, the final profile of the target plates exhibited greater deflection at higher charge masses. For the same charge mass, the profile also deflected more as the degree of confinement was increased. Increasing the degree of confinement and, to a lesser degree, the charge mass caused the central region of the final midline profile shape to transition from a flat plateau – as exhibited by the unconfined blast simulations in Figure 7.15(d) – to a concave bulge – as exhibited by the confined blast simulations in Figure 7.15(a) – (c). The final profiles of the plates in the fully-vented ($\zeta = 0.7$) blast simulation were asymmetric, with the vented side of the plate exhibiting slightly lower deflections.

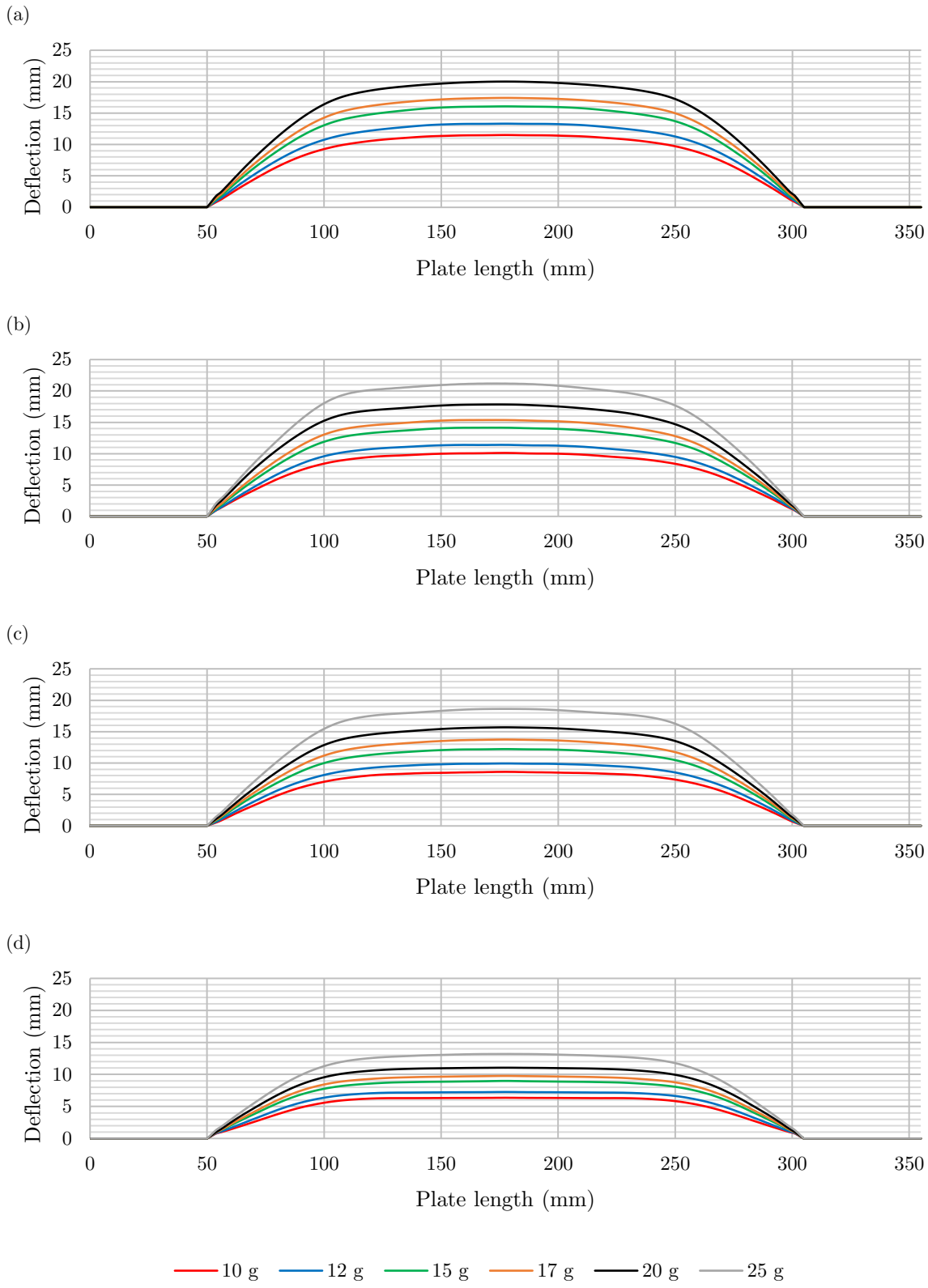

Figure 7.15: Graphs of the final midline profiles of the target plate at various charge masses for (a) fully-confined, (b) fully-vented ($\zeta = 0.7$), (c) fully-vented ($\zeta = 1.4$) and (d) unconfined blast simulations.

7.3 Blast Pressure History

The loading phase of the simulation was created by detonating an explosive charge to produce a blast pressure wave which impinged on and transferred an impulsive load to the target plate. Pressure tracers were located at the target plate centre point and each of the corners of the exposed area, as shown in Figure 7.16. The midpoint tracer was present in all the blast simulations and measured the pressure reflected against the target plate only. The corner tracers were only included in the confined blast models and provided an indication of the pressure accumulation at the corners of the target plate due to the reflection of three surfaces: the target plate, the side panel and front/bottom panel of the ULD box.

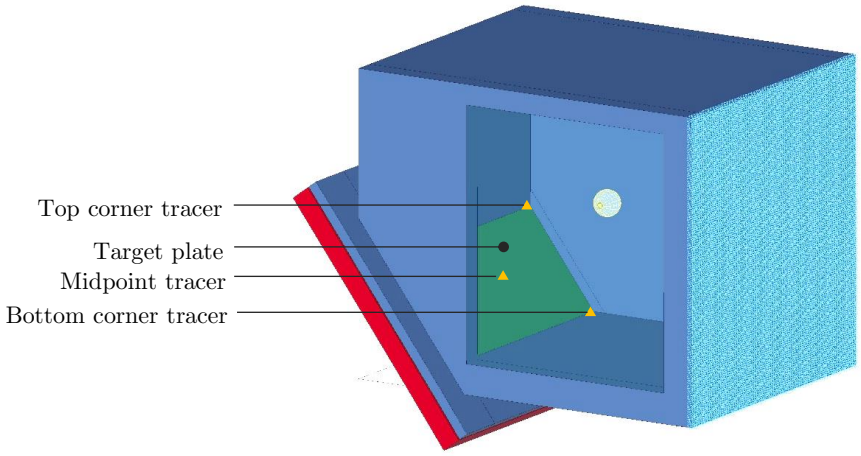

Figure 7.16: Location of pressure tracers on the target plate in the confined blast models.

7.3.1 Midpoint Pressure

The midpoint pressure history for each simulation is shown in Figure 7.17. The arrival time of the blast wave decreased with an increasing charge mass. The magnitude of the peak pressures for the confined blast simulations (and for the same charge mass) were near-identical. However, the fully-confined pressure history exhibited a number of additional significant pressure peaks which were indicative of the occurrence of several blast wave reflections. There was also a build-up of internal pressure within the ULD box. The blast wave reflections, albeit fewer in number, were also present in both fully-vented pressure histories, although the additional peak pressures had lower magnitudes – a consequence of the venting areas reducing the number of blast wave reflections and preventing internal pressure build-up. The pressure history for the unconfined simulation exhibited no reflections and no pressure build-up: only one significant peak pressure was present which diminished back to atmospheric conditions.

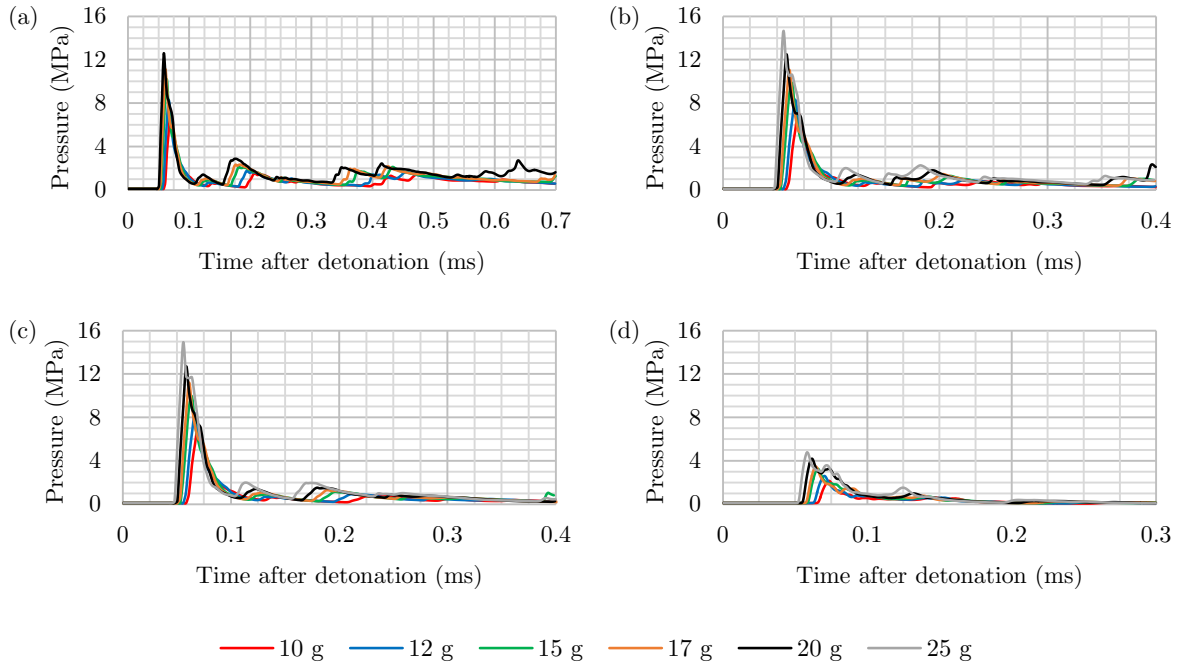

Figure 7.17: Graphs of midpoint pressure history for (a) fully-confined, (b) fully-vented ($\zeta = 0.7$), (c) fully-vented ($\zeta = 1.4$) and (d) unconfined blast simulations.

7.3.2 Corner Pressure

A pressure tracer was placed at each of the top and bottom corners present in the simulation. As a result of using half-symmetry to develop the fully-confined and fully-vented ($\zeta = 1.4$) models, only one pair of tracers was present. Two pairs of tracers were present in the fully-vented ($\zeta = 0.7$) model: one pair corresponded to corners near a closed side panel, while the other to those near a vented side panel. Figure 7.18 to Figure 7.20 illustrate the corner pressure histories of each of the confined blast simulations.

The arrival time of the pressure wave decreased as the charge mass increased. The pressure at the top corner was consistently lower than the pressure at the bottom corner. The pressures at the corners near a vented side were also lower than those of corresponding corners near a closed side. The pressure histories at the closed-side corners of the fully-vented ($\zeta = 0.7$) simulations were near-identical to those of the fully-confined simulations. Furthermore, the pressure histories at the vented-side corners of the fully-vented ($\zeta = 0.7$) simulations and the corners of the fully-vented ($\zeta = 1.4$) simulations were also near-identical. The blast loads in the confined blast models were therefore consistently produced despite the use of symmetry to reduce the simulated domain of the fully-confined and fully-vented ($\zeta = 1.4$) models.

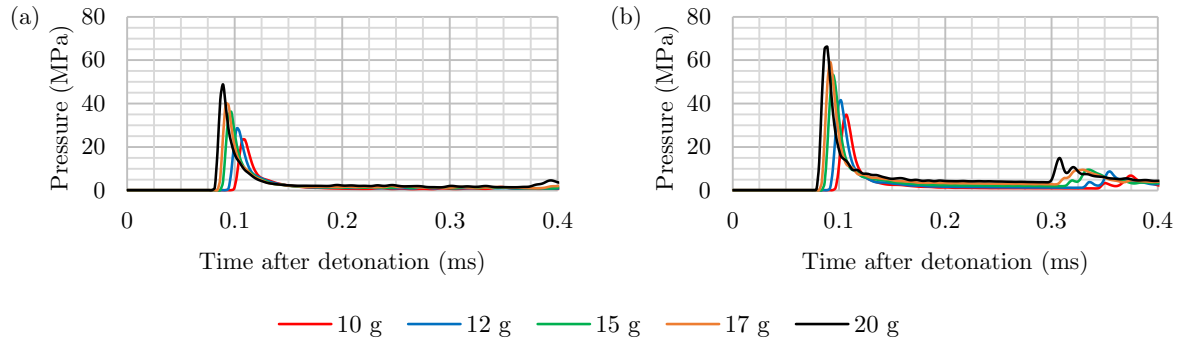

Figure 7.18: Graphs of pressure history for fully-confined simulations at the (a) top and (b) bottom corners of the target plate.

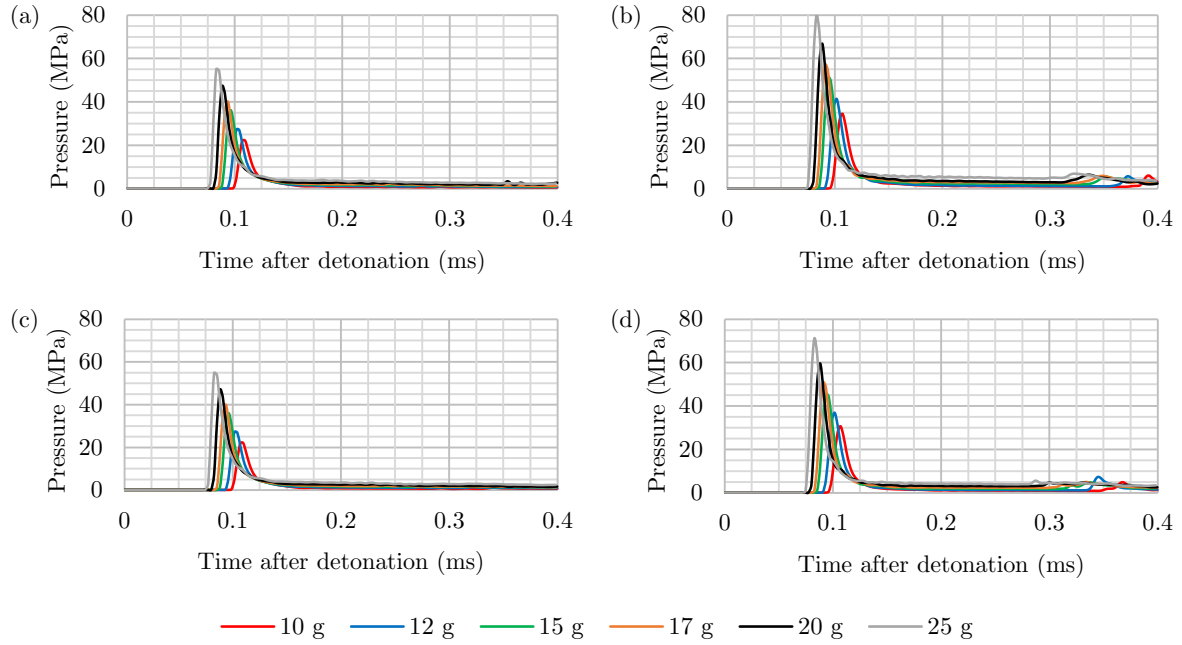

Figure 7.19: Graphs of pressure history for fully-vented ($\zeta = 0.7$) simulations at the (a) top and (b) bottom corners near the closed side and the (c) top and (d) bottom corners near the vented side of the target plate.

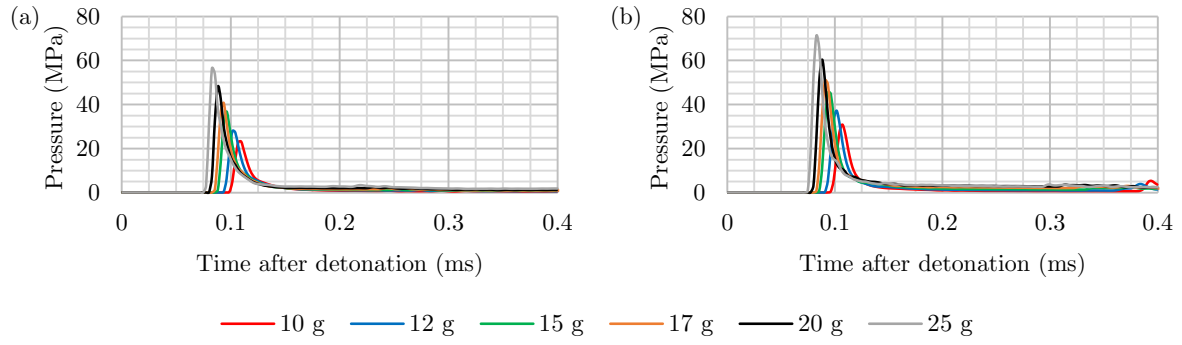

Figure 7.20: Graphs of pressure history for fully-vented ($\zeta = 1.4$) simulations at the (a) top and (b) bottom corners of the target plate.

This page is intentionally left blank.

8 Discussion

This chapter assesses the deformations of all the blasts tests, the consistency with which the outcomes adhere to published work, and the comparisons between the experimental and numerical results. The experimental results are assessed for compliance with the established response of quadrangular plates subjected to uniform blast loading. The capability of the numerical model – in particular, the target plate mesh – at capturing the expected quadrangular plate deformation is also analysed. The experimental and numerical results, particularly the target plate midpoint and midline deflections, are compared and evaluated for consistency. The effect of the venting configuration on the blast response of the target plate is assessed, and the practical application of the project outcomes are discussed. Finally, the limitations of the present work are presented.

8.1 Quadrangular Plate Blast Response

The response of the target plate to uniform blast loading was assessed to determine the compliance with theoretical predictions and existing experimental results found in literature. The assessment included the experimental results obtained from blast testing and the simulated results obtained from the numerical blast models. The experimental deflection results were assessed according to established work, and the inconsistencies (present in the fully-confined and unconfined blast tests) were addressed. The numerical model was assessed to determine the capability of the target plate mesh at capturing the expected blast response by undergoing representative deformations without excessive warping of the shell elements.

8.1.1 Deflection and Charge Mass

The deflection of a fully-clamped quadrangular plate subjected to blast loading usually exhibits a linear dependency on the charge mass [32,33]. This trend was evident in each of the simulated blast tests, as well as in both the experimental fully-vented blast tests. The fully-confined blast

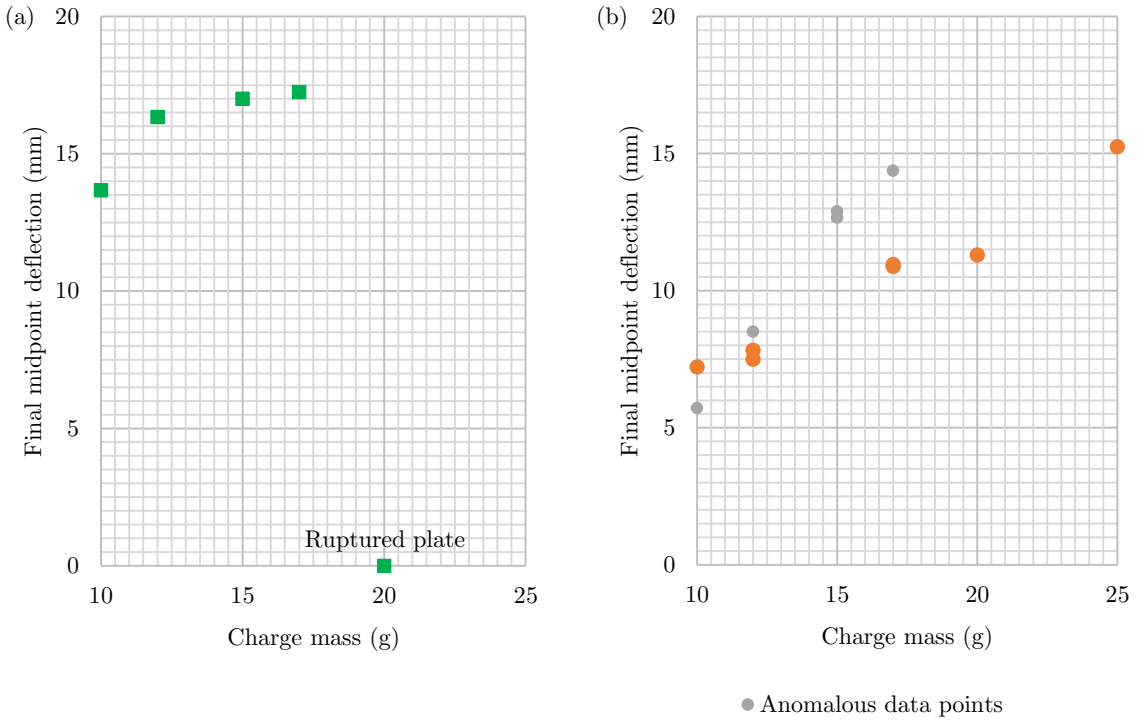

Figure 8.1: Graphs of experimental final midpoint deflections for (a) fully-confined and (b) unconfined blast tests.

tests performed experimentally, however, demonstrated a non-linear, concave relationship which decreased in gradient as the rupture threshold (occurring at a 20 g blast) was reached. The unconfined midpoint results exhibited a region of inconsistently high deflections at 15 g and 17 g. The final midpoint results of both the fully-confined and unconfined blast tests are shown in Figure 8.1.

The non-linear gradient of the fully-confined tests was attributed to the deformation limit being reached as the rupture threshold of the plate was approached, and not experimental error. This effect was observed in the plates tested with charge masses greater than 12 g.

From the unconfined blast results, three tests exhibited inconsistent midpoint deflections: both 15 g tests and one 17 g test. Inspection of the 17 g target plate revealed localised deformation near the centre of the plate, resulting in a midpoint deflection 30% greater than the 17 g tests exhibiting uniform deformation. Further investigation revealed central localised deformation in a 10 g and 12 g test plate. The contour plots of the plates are shown in Figure 8.2. One of the 15 g tests exhibited localised deformation near the clamped edge of the plate, as shown in Figure 8.2(c). A similar localised deformation was also visible in the 17 g case. The other 15 g test exhibited significant boundary pull-in – more than that exhibited by the unconfined 25 g

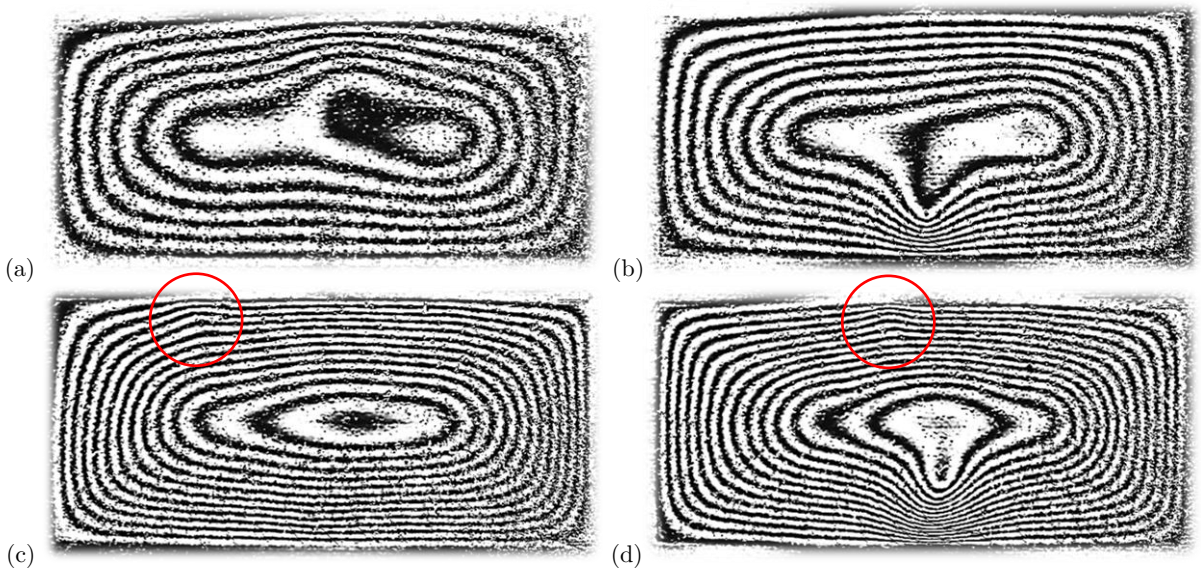

Figure 8.2: Contour plots showing the presence of localised deformation in unconfined blasts with charge masses of (a) 10 g, (b) 12 g, (c) 15 g and (d) 17 g.

test – which contributed to the inconsistently high deflection. These five tests, which can be identified in Figure 8.1(b), were consequently excluded from the comparison with the numerical results in Section 8.2.2.

8.1.2 Target Plate Mesh Deformation

The entire mesh used to model the target plate was inspected to ensure that reasonable deformations were achieved and that the shell elements did not warp excessively. Mesh deformations occurred along the top and bottom edges of the plate in the form of boundary pull-in, and – to a much greater extent – along the edges of the exposed area in the form of plastic hinges. Two plate models were used in the numerical simulations: a half-symmetry model for the fully-confined, fully-vented ($\zeta = 1.4$) and unconfined blasts, and a full (no symmetry) model for the fully-vented ($\zeta = 0.7$) blasts. The simulations resulting in the greatest deformation of the half-symmetry and full plate models were the 20 g fully-confined and 25 g fully-vented ($\zeta = 0.7$) blasts, respectively. The overall, final deformation and the deformation of the exposed area of the meshes for both these blast simulations are shown in Figure 8.3. The exposed area of the target plates exhibited the formation of plastic hinges consistent with the theoretical prediction proposed by Jones [30]. The target plate was observed to deform plastically along all the clamped edges. Two pairs of plastic hinges developed from each of the corners towards the midline of the plate. A longitudinal plastic hinge developed along the plate midline, joining the intersection of the two pairs of corner plastic hinges. Similar deformations

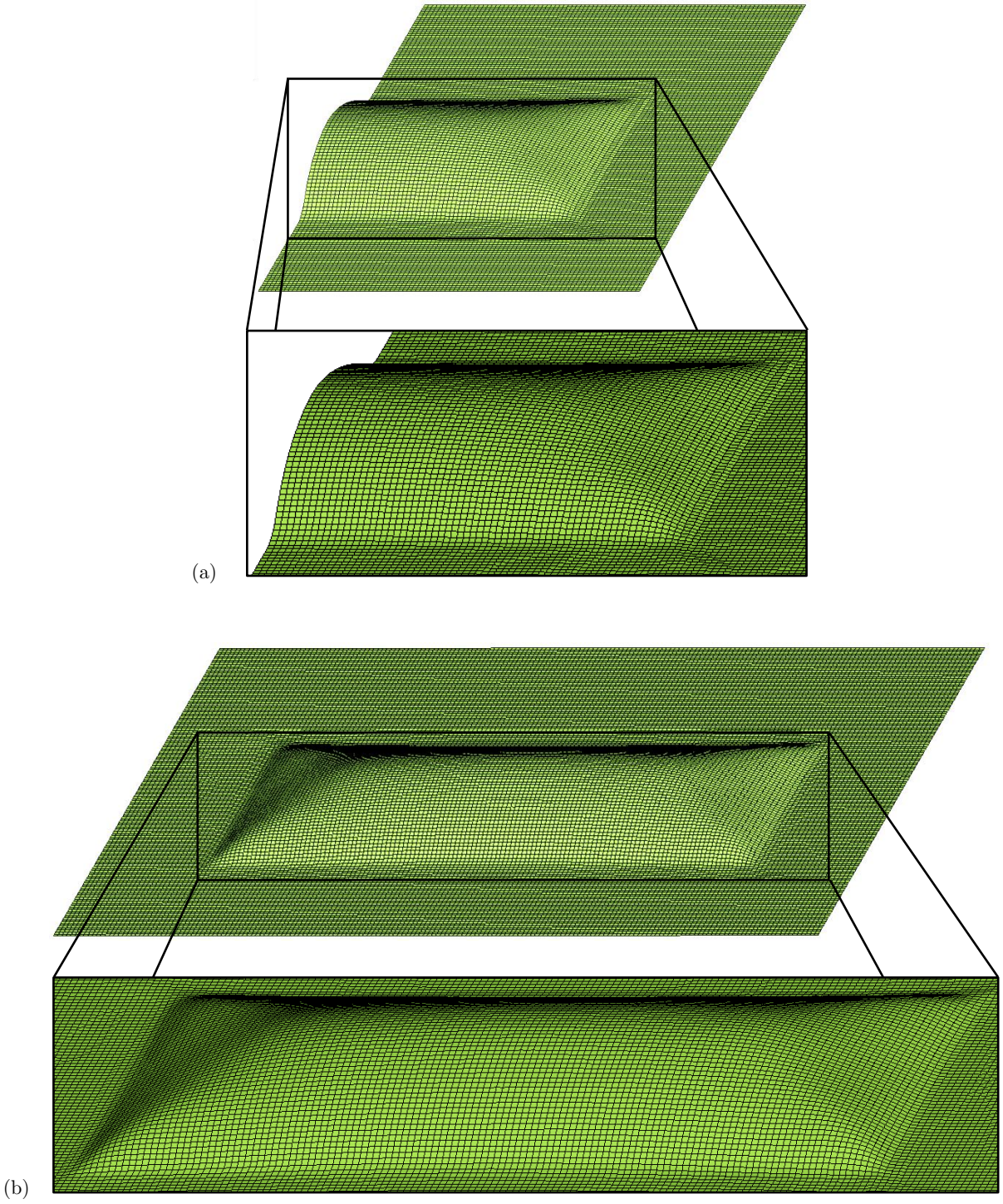

Figure 8.3: Images of the overall and exposed area mesh deformations for (a) 20 g fully-confined and (b) 25 g fully-vented ($\zeta = 0.7$) blast simulations.

were observed in all the target plates in each of the blast models. The shell elements along the clamped edges of the target plate (as well as throughout the entire plate) were observed to be sufficiently-sized to not undergo extreme warping, resulting in well-captured and representative simulated target plate deformations.

8.2 Comparison of Experimental and Numerical Results

Comparisons between the experimental and simulated blast response of the target plate were performed to assess how representative the numerical blast simulations were of the experimental results. This comparison comprised the transient and final deformation of the target plate. A comparison of the transient response was only possible for the unconfined tests since no DIC was used (and no transient deflection data was recorded) during the confined blast testing. Final midpoint deflection and midline profile comparisons were performed for all the confinement cases.

8.2.1 Transient Midpoint Deflections

The transient deflection of both the experimental and numerical tests exhibited the expected response of a clamped plate subjected to blast loading: a peak deformation was reached, and thereafter damped elastic vibrations converged towards the final deflection. The experimental and numerical transient midpoint deflection results for the unconfined blasts are shown in Figure 8.4.

The transient midpoint deflection for the 10 g and 12 g unconfined blasts, as illustrated in Figure 8.4(a) and Figure 8.4(b), respectively, showed good correlation with the experimental DIC outputs. Both the initial ramp-up in deflection and elastic response were well-captured in the simulations. The peak deflection of the 12 g DIC 5 test and the minimum deflection of the 10 g DIC 10 test were accurately captured numerically. Additionally, the elastic vibrations were bounded by the experimental results of both cases. The general trend of the elastic response – in terms of the period and number of oscillations – was also similar, demonstrating that the numerical damping of the elastic response was representative of the experimental data. As a result, the simulated and experimental elastic vibrations showed similar settling times and final deflections.

The comparison of the 15 g experimental and numerical results is shown in Figure 8.4(c). The experimental result of the 15 g unconfined blast was significantly greater than that obtained numerically, however, the initial ramp-up in deflection was captured. As discussed in Section 8.1.1, the experimental results of the 15 g tests were considered unrepresentative of the general trend of the unconfined blast results. The main irregularity was that the deformation was greater than the deformation due to the blast load of a 17 g charge. The numerical result, however, demonstrated a blast response consistent with all the unconfined blast simulations.

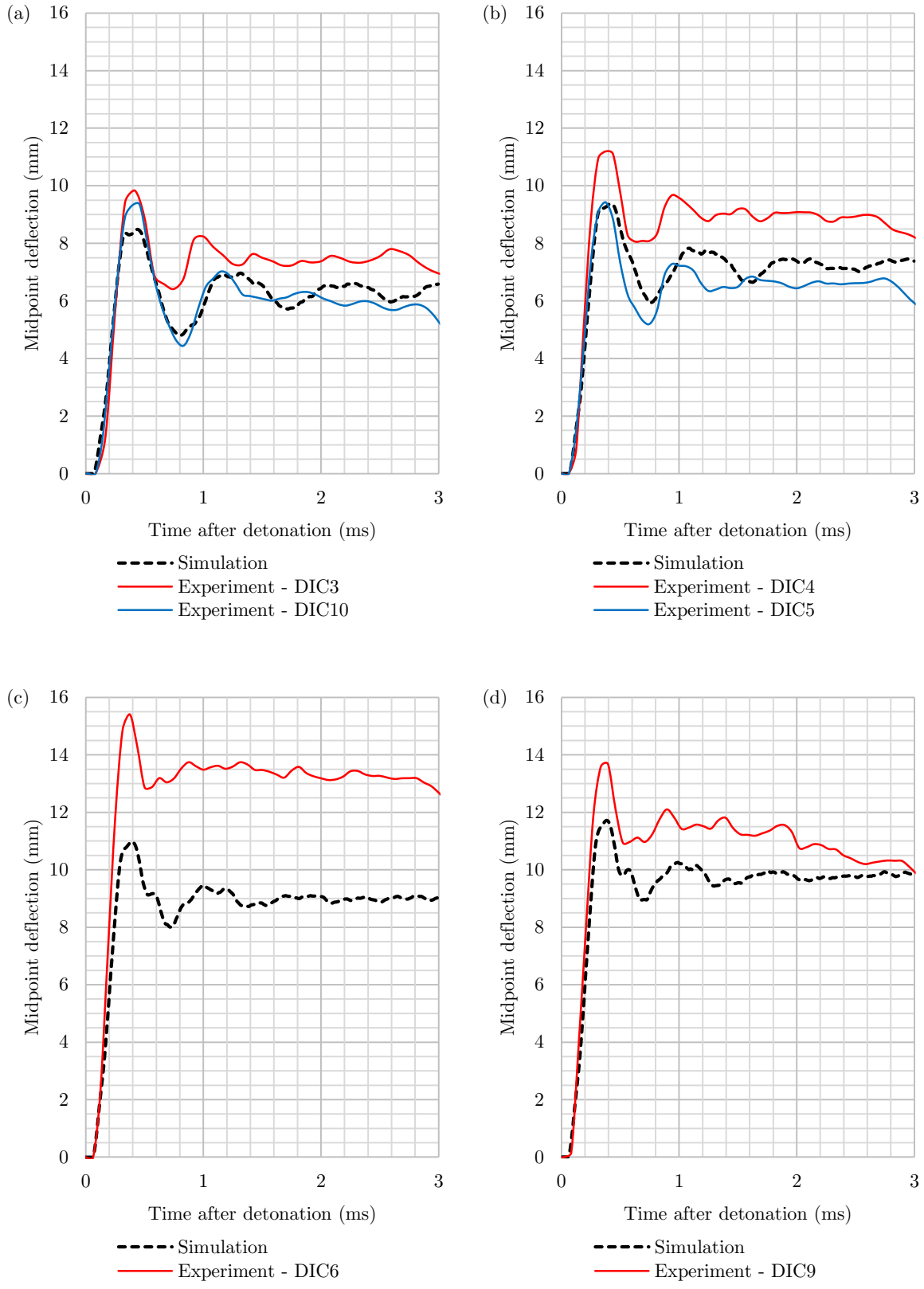

Figure 8.4: Graphs comparing the simulated and experimental results of the transient target plate midpoint deflection due to unconfined blasts with charge masses of (a) 10 g, (b) 12 g, (c) 15 g and (d) 17 g.

Comparison of the numerical and experimental results of the 17 g unconfined blast results showed a similar correlation as those of the tests at 10 g and 12 g (particularly when comparing the upper bound of the experimental results). The transient response was under-predicted by the simulation, with the numerical peak midpoint deflection being approximately 14% less than the experimental value. However, this under-prediction of the peak midpoint deflection was also present in both the 10 g and 12 g cases. Despite exhibiting higher deflections throughout the period shown, after 2 ms the experimental transient deflection started to settle towards a deflection closer to the final simulated midpoint deflection.

The comparison between the numerical and experimental transient midpoint deflection of the 10 g, 12 g and 17 g unconfined blasts showed consistent results, especially when compared to the upper bound of the 10g and 12 g cases. The average difference between the peak and final midpoint deflections of these tests were 14.8% and 11.7%, respectively. However, in each case, the difference is less than 2 mm (the thickness of the target plate).

8.2.2 Final Midpoint Deflection

The final midpoint deflection of the target plate from the experimental and simulated blasts were compared for all the confinement cases. These comparisons are shown in Figure 8.5. In each case, the simulated and experimental tests resulted in final midpoint deflections which increased as the charge mass increased. The experimental results are plotted within a $\pm$ 2 mm (one plate thickness) envelope which was considered an acceptable variance in the experimental results [29,32].

The unconfined final midpoint deflections shown in Figure 8.5(a) demonstrated a good correlation between the numerical and experimental results. The deflection of both exhibited a linear proportionality with charge mass. The simulated final midpoint deflection was consistently less than that of the experimental target plates, but the difference was within one plate thickness. Since none of the actual target plates tested at charge masses of 10 g, 12 g and 17 g exhibited significant boundary pull-in, and no rupture threshold was approached in the unconfined tests, the difference in test results was considered largely due to the mesh dependency of the numerical solution, as discussed in Section 6.3.2.

A comparison of the fully-confined blast results is shown in Figure 8.5(b). The experimental results converged towards a maximum final midpoint deflection as the rupture limit of the plate was reached (at 20 g charge mass). This non-linearity was not captured by the simulated blasts because no damage model was included in the simulations. The numerical results were

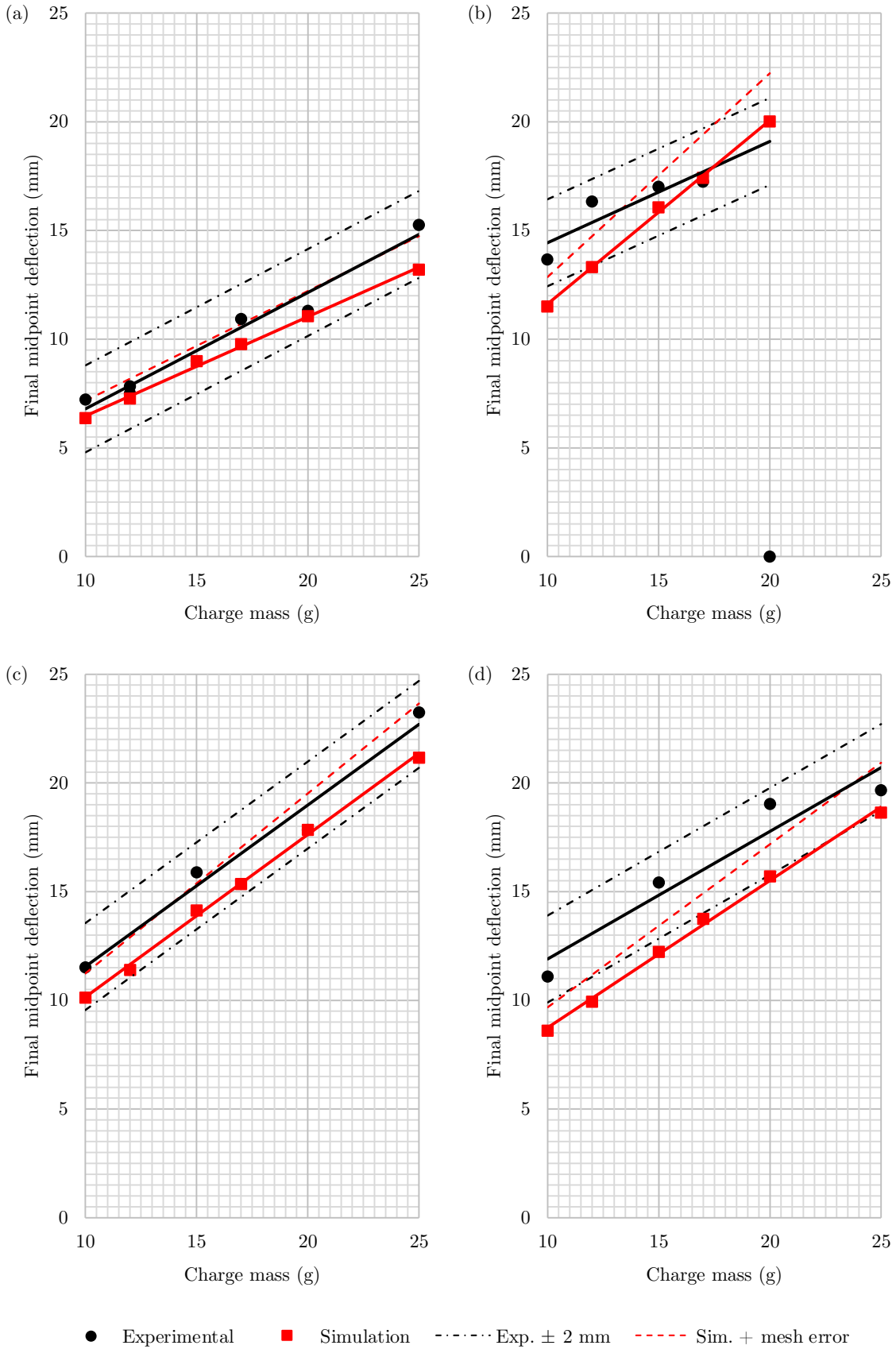

Figure 8.5: Graphs comparing the experimental and numerical final midpoint deflections of the target plate for (a) unconfined, (b) fully-confined, (c) fully-vented ($\zeta = 0.7$) and (d) fully-vented ($\zeta = 1.4$) blasts.

observed to continue along a linear trend as the charge mass was increased. Consequently, there was poor correlation between the experimental and numerical results. The experimental results were, however, fitted with a linear trend to compare to the numerical results. Only the simulated blasts at 15 g and 17 g predicted final midpoint deflections that were within one plate thickness of the corresponding experimental results. The absence of a damage model in the simulations was considered the main reason for the discrepancy between the two results. The simulations were unable to capture the decreasing gradient in the final midpoint deflections between 12 g and 17 g, or the rupture of the target plate at 20 g.

The experimental and numerical results of the first set of fully-vented blasts, with a venting area ratio of $\zeta = 0.7$, are compared in Figure 8.5(c). There was good correlation between the results: the numerical results were within one plate thickness of the experimental deflections and the linear trends of the two results exhibited similar gradients. The numerical deflections were generally lower than those of the experiments (the 20 g blast resulted in identical final midpoint deflections) and was attributed largely to the mesh resolution of the simulations.

The final midpoint deflections of the second series of fully-vented blasts ($\zeta = 1.4$) are shown in Figure 8.5(d). The numerical deflections, except that of the 25 g charge, were observed to fall below the 2 mm tolerance of the experimental results. The mesh resolution of the simulations was not the only factor responsible for the dissimilarity between the numerical and experimental results. As discussed further in Section 8.3.3, the main difference between the two fully-vented blast tests was that, in the experimental tests little significance between the fully-vented blasts was observed, whereas in the numerical tests there was a clear distinction between the two fully-vented blast results. This disparity was considered a contributing factor to the difference in numerical and experimental results of the second fully-vented blast series.

To address the dependency of the numerical solution on the mesh resolution, the simulation results were increased by 9.7% (the difference in final deflections between the meshes tested in Section 6.3.2) to approximately account for the mesh error and provide an indication of a mesh independent solution. The resultant curves were included in Figure 8.5 and showed excellent correlation with the experimental results for the unconfined and fully-vented ($\zeta = 0.7$) tests. In the fully-confined and fully-vented ($\zeta = 1.4$) tests, including the mesh error produced numerical results that were within the acceptable tolerance envelope, however, the deflection trends did not compare favourably with the experimental outcomes. Therefore the mesh dependency of the solution, although resulting in lower predicted deflections for all the simulations, was not the only factor affecting the disparity in the experimental and numerical results of the fully-confined and fully-vented ($\zeta = 1.4$) cases, as discussed above.

8.2.3 Final Midline Profiles

The final midline profiles of the target plate for both the numerical and experimental blast tests are shown in Figure 8.6. There was generally a good agreement between the experimental and numerical midline profiles of the unconfined and fully-vented ($\zeta = 0.7$) blast tests, and a poorer agreement between all the fully-vented ($\zeta = 1.4$) blast tests and the fully-confined blast tests at lower charge masses, as suggested by the comparison of the final midpoint deflections of the same test series in the previous section.

As shown in Figure 8.6(a), only the unconfined 15 g target plate exhibited a higher experimental deformation profile than the simulated result. Each of the remaining numerical unconfined tests accurately captured the final midline profile of the experimental target plates, including the deformation of the sides of the target area and the plateau in the central region. The slight asymmetry of the experimental results was observed to be inconsequential since the entire midline profile showed good agreement with the symmetric, numerical results.

The fully-confined final midline profiles are shown in Figure 8.6(b). The experimental and numerical profiles for the 15 g and 17 g blast tests showed good agreement. The profiles for the 12 g blast showed poorer agreement between the numerical and experimental tests, with the former producing a significantly lower deformed profile. The 10 g blast results, although better than those of the 12 g blast, also exhibited a lower numerical deformation profile. The two main contributing factors towards the discrepancy in results between the experimental and numerical fully-confined tests were the mesh resolution used in the simulations and the absence of a damage model for the plate material. The mesh effect consistently produced lower deflections in all the simulated tests (as discussed in the previous section). The absence of a damage model resulted in an over-prediction of the fully-confined deformation trend at charge masses greater than 12 g. The combination of these two confounding factors resulted in agreeable numerical and experimental results in the 15 g and 17 g tests, however, it would be misleading to conclude that the fully-confined numerical model was accurate in these cases since the simulated deformation trend was misrepresentative of the experimental results, as seen in Figure 8.5(b).

The midline profiles of the fully-vented ($\zeta = 0.7$) blasts are shown in Figure 8.6(c). Although exhibiting slightly under-predicted deformations, the numerical results showed good agreement with all the experimental profiles and captured the asymmetrical deflections well.

Shown in Figure 8.6(d) are the final profiles of the fully-vented ($\zeta = 1.4$) blasts. The experimental tests exhibited higher plate deflections than the numerical results and asymmetric

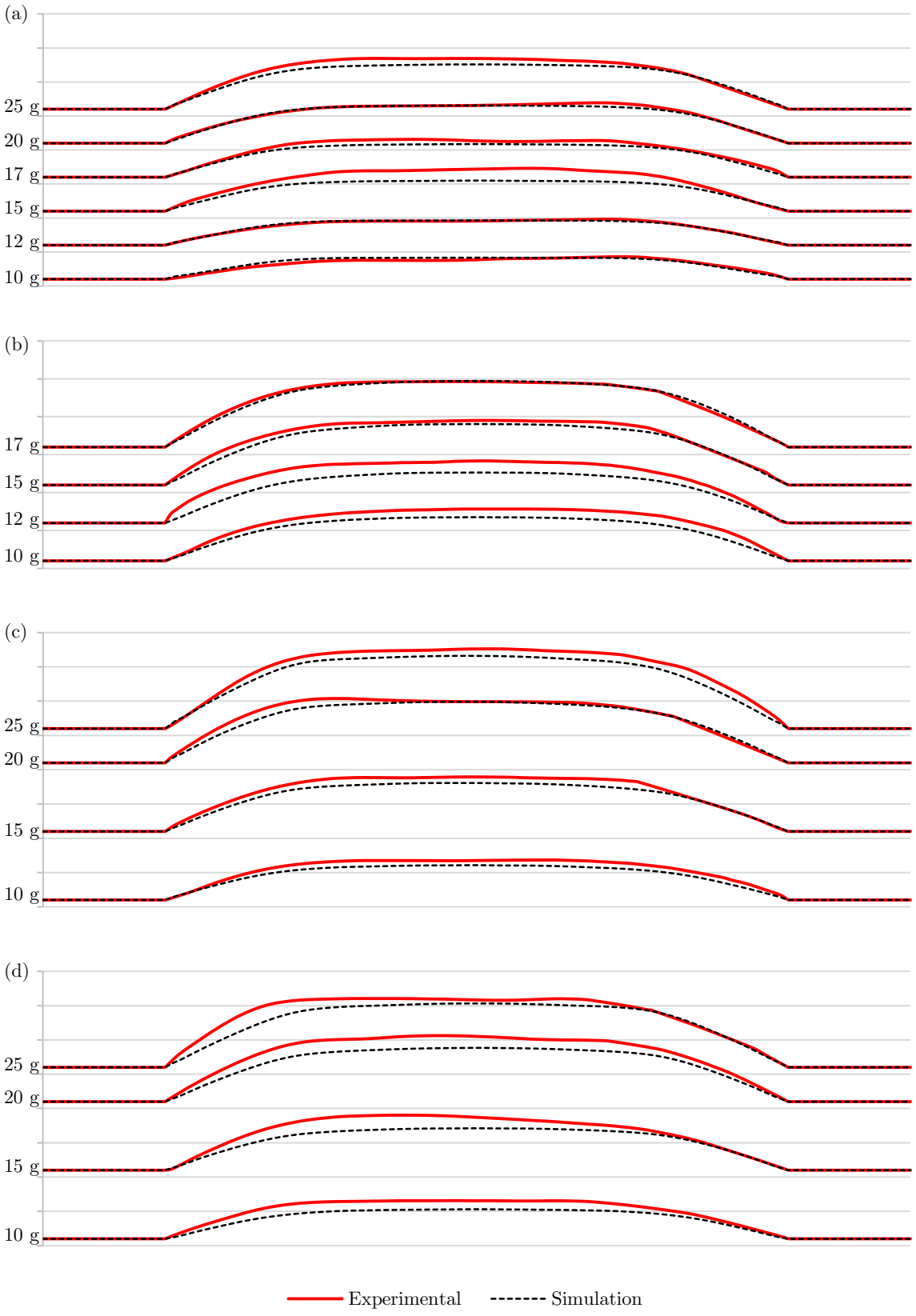

Figure 8.6: Graphs comparing the experimental and numerical final midline profiles of the target plate for (a) unconfined, (b) fully-confined, (c) fully-vented ($\zeta = 0.7$) and (d) fully-vented ($\zeta = 1.4$) blasts.

plate profiles, instead of symmetric midlines as produced in the simulations. As discussed further in Section 8.3.3, both the experimental fully-vented blasts, for the same charge mass, exhibited similar midline profiles, whereas the numerical results produced distinct blast responses between the two. The numerical results exhibited a disparity in the fully-vented ($\zeta = 1.4$) tests because the simulated plate deformations were influenced more by the increase in available venting area than the experimental tests (which exhibited almost no difference).

8.3 Effect of Venting Configuration

Three series of confined blast testing were performed, experimentally and numerically, to assess the effect of the venting configuration on the blast response of the target plate clamped to the diagonal side of a ULD box. The three configurations were the fully-confined (no venting) blasts, and two series of fully-vented blasts (one with a single venting area on the side panel of the ULD, and the other with a second venting area on the opposite side panel). The effect of the venting configuration was assessed in terms of the blast pressure within the container, the transient and final deflections of the target plate, and the failure modes of the tested plates.

8.3.1 Internal Pressure

The pressure resulting from the detonation of an explosive within the ULD box was predicted numerically. The actual pressures produced during the experimental tests were not measured. The pressure history at the midpoint of the target plate resulting from a 17 g charge for the three different confinement cases is shown in Figure 8.7. The initial peak pressure was identical – in terms of magnitude, arrival time and duration – for all three cases. The fully-confined blast produced three more reflected pressure pulses during the first 1 ms following detonation. The fully-vented blasts, however, produced fewer reflected pressure pulses which were lesser in magnitude than the corresponding fully-confined blast. Each subsequent pressure reflection had a lower magnitude and longer duration than the previous. The first significant reflection of each confinement case occurred between 0.17 ms and 0.18 ms. Thereafter, the fully-vented ($\zeta = 1.4$) blast pressure diminished towards atmospheric pressure. At approximately 0.37 ms, a second pressure reflection occurred in the fully-confined and fully-vented ($\zeta = 0.7$) blasts; the pressure in the latter subsequently diminished towards atmospheric pressure. The third pressure reflection of the fully-confined blast occurred just before 0.7 ms. The pressure subsequently diminished towards a value greater than atmospheric pressure.

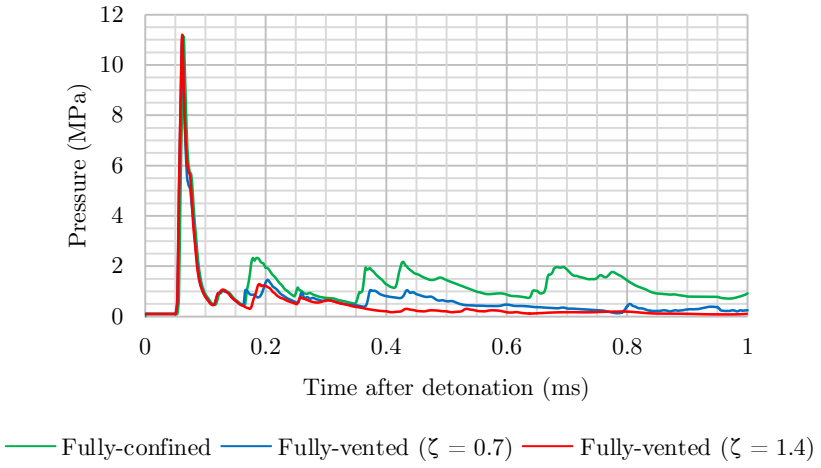

Figure 8.7: Graph of midpoint pressure history of a 17 g charge for confined blast loadings.

The three pressure histories displayed responses consistent with results obtained in literature. The fully-confined blast exhibited several internal reflections of the blast pressure wave and a quasi-static build-up of pressure greater than atmospheric pressure, as described by Kingery et al. [20]. The fully-vented blasts displayed fewer internal pressure reflections and a quickly diminishing internal pressure towards atmospheric conditions, consistent with the findings of Keenan and Tancreto [19]. The initial peak pressure was unaffected by the degree of confinement. The number of blast reflections was greatest at no venting and decreased as the available venting area increased. The fully-confined configuration exhibited an elevated, non-atmospheric quasi-static pressure load resulting from the absence of venting areas. The fully-vented configurations, on the other hand, exhibited a diminishing internal quasi-static load towards atmospheric conditions. The rate at which atmospheric pressure was reached increased as the venting area increased.

8.3.2 Transient Response of Target Plate

The transient midpoint deflection of the target plate for the confined blast tests was only captured numerically since no DIC was used for the corresponding experimental tests. The transient response of the target plate midpoint for each of the confined blasts subjected to the explosive loading of a 17 g charge is shown in Figure 8.8. The initial gradient of the deflection curve was identical in each case, indicating the initial velocity of the plate was the same for each degree of confinement, at a constant charge mass.

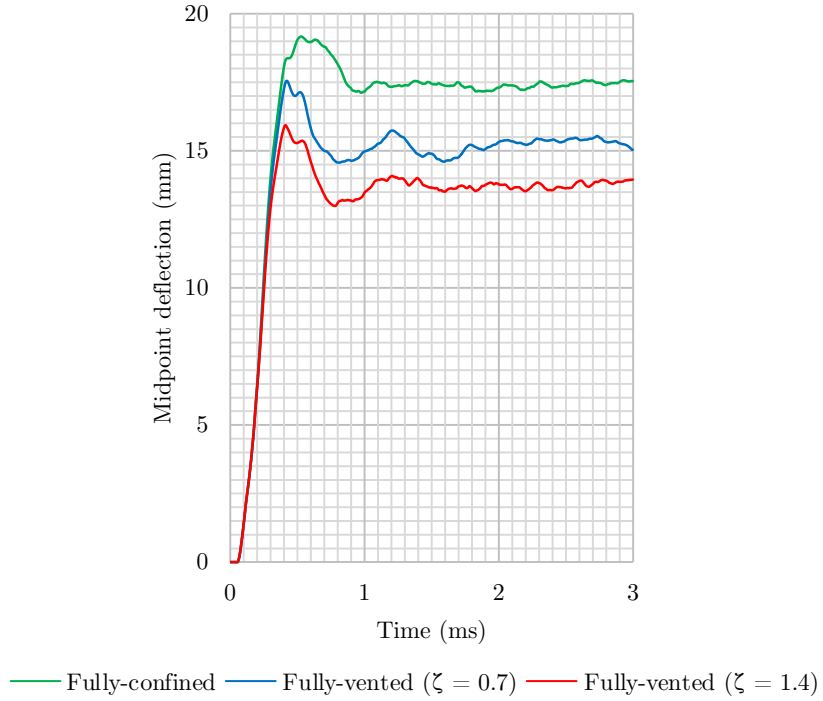

Figure 8.8: Graph of the transient midpoint deflection due to a 17 g charge for confined blast loading.

The midpoint of the fully-vented ($\zeta = 1.4$) test exhibited the earliest and smallest peak deflection. The fully-vented ($\zeta = 0.7$) test produced a peak midpoint at a similar time, but with a 9.2% higher deflection. The fully-confined test produced the highest peak midpoint deflection, which occurred approximately 1.5 ms after the peak midpoint of the fully-vented tests was reached. All three cases exhibited a drop from the peak position, after which a damped elastic vibratory response was observed which converged towards a final midpoint deflection.

The fully-vented tests displayed peak deflections occurring at similar times, as well as similar elastic responses following the peak midpoint deflection. All three confinement cases, however, displayed a distinct transient response in terms of the peak and final deflections reached during the blast tests: the midpoint deflection increased as the degree of confinement increased. This trend was consistent with the findings by Geretto [32] of the blast loading of cuboidal structures at varying degrees of confinement.

On average, the peak midpoint deflection of the fully-confined blasts was 65% higher than an unconfined blast with the same charge mass. The fully-vented blasts, with $\zeta = 0.7$ and $\zeta = 1.4$, exhibited average peak midpoint deflections which were 51% and 36% higher, respectively, than the corresponding unconfined blasts.

8.3.3 Final Deformation of Target Plate

The final midline profiles of the target plates were obtained from both the experimental and numerical blast tests. The midline profiles of the target plates at the different venting configurations (but for the same charge mass) were compared. Shown in Figure 8.9 are the experimental final midline profiles for each of the confined blasts at charge masses of 10 g and 15 g. The target plate of the fully-confined blast tests exhibited higher deflections than the fully-vented blast tests at the same charge mass. The target plates of the two fully-vented blasts showed an insignificant difference in the final midline profile in the 10 g tests. The plate from the fully-vented ($\zeta = 1.4$) blast test with a 15 g charge mass showed asymmetric deformation despite being a symmetric venting configuration. However, the region of maximum deformation showed little difference in deflection when compared to the fully-vented ($\zeta = 0.7$) midline profile at the same charge mass. At lower charge masses, the venting configuration for

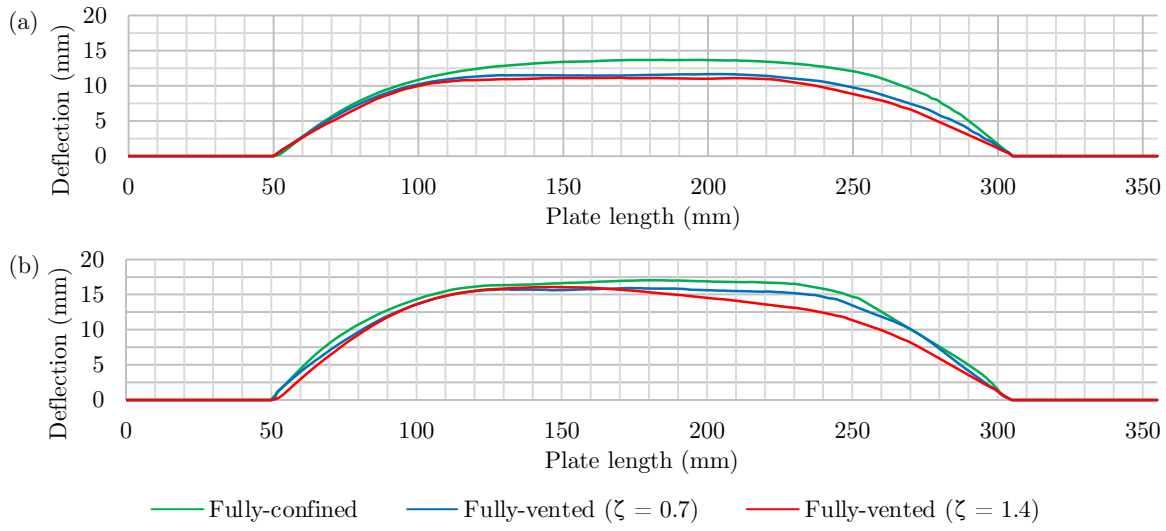

Figure 8.9: Graphs of experimental final midline profiles for confined blasts subjected to loadings from (a) 10 g and (b) 15 g charge masses.

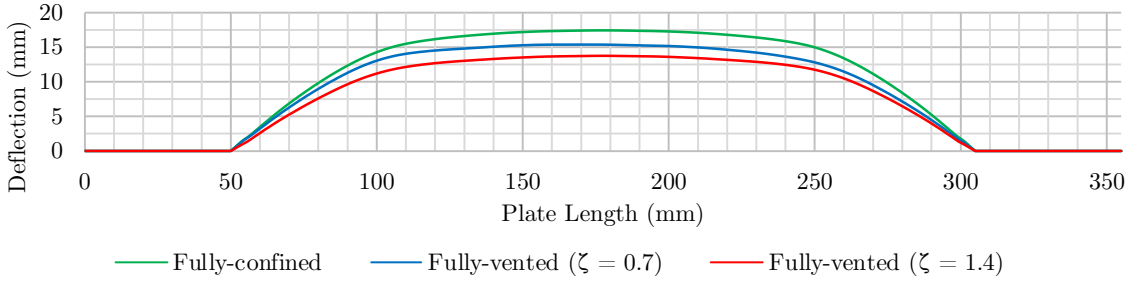

Figure 8.10: Graph of numerical final midline profiles for confined tests due to loadings from a 17 g charge mass.

the fully-vented tests did not influence the deformation of the target plate significantly. However, in the numerical results, the target plates of the two fully-vented blasts displayed distinct deformation profiles. The numerical midline profiles for the confined blasts due to a 17 g charge mass are shown in Figure 8.10. The deformation is seen to increase as the available venting area decreases, with the fully-confined test exhibiting the greatest deformation.

The average increase in the experimental and numerical final midpoint deflection is listed in Table 8.1 for each of the venting configurations. The increase is based on the final midpoint deflection of a target plate subjected to a corresponding experimental or numerical unconfined blast with the same charge mass. In both the experimental and numerical tests, the fully-confined blast produced the greatest plate deformation. The fully-vented blast results from the experimental tests demonstrated similar final midline profiles, indicating there was little effect due to the venting configuration between the fully-vented blast tests. However, the numerical midline profiles indicated that there was a significant venting effect on the deformation of the target plate, since the two different venting configurations resulted in two distinctly different final midline profiles and midpoint deflections. This distinction in deformation between the fully-vented test results was consistent across all the other simulated tests.

Table 8.1: Average increase in experimental and numerical target plate deflections due to venting configuration.

Degree of confinement	**Increase in final midpoint deflection (%)**	
	Experimental	**Numerical**
Fully-confined	82	81
Fully-vented ($\zeta = 0.7$)	57	59
Fully-vented ($\zeta = 1.4$)	51	39

Note: Percentage increase in deflection is based on the corresponding unconfined blast results.

8.3.4 Modes of Failure

The blast response of the ULD box was indicated by the deformation (or other failure) of the target plate. In most cases, the mode of failure remained the same, with almost all the target plates from the experimental and simulated blasts exhibiting large permanent deflections. The deformation of the target plate exposed area, in terms of plastic hinge development, and the amount of boundary pull-in was observed to increase as both the charge mass and the degree of confinement increased, however, these remained instances of Mode I failure.

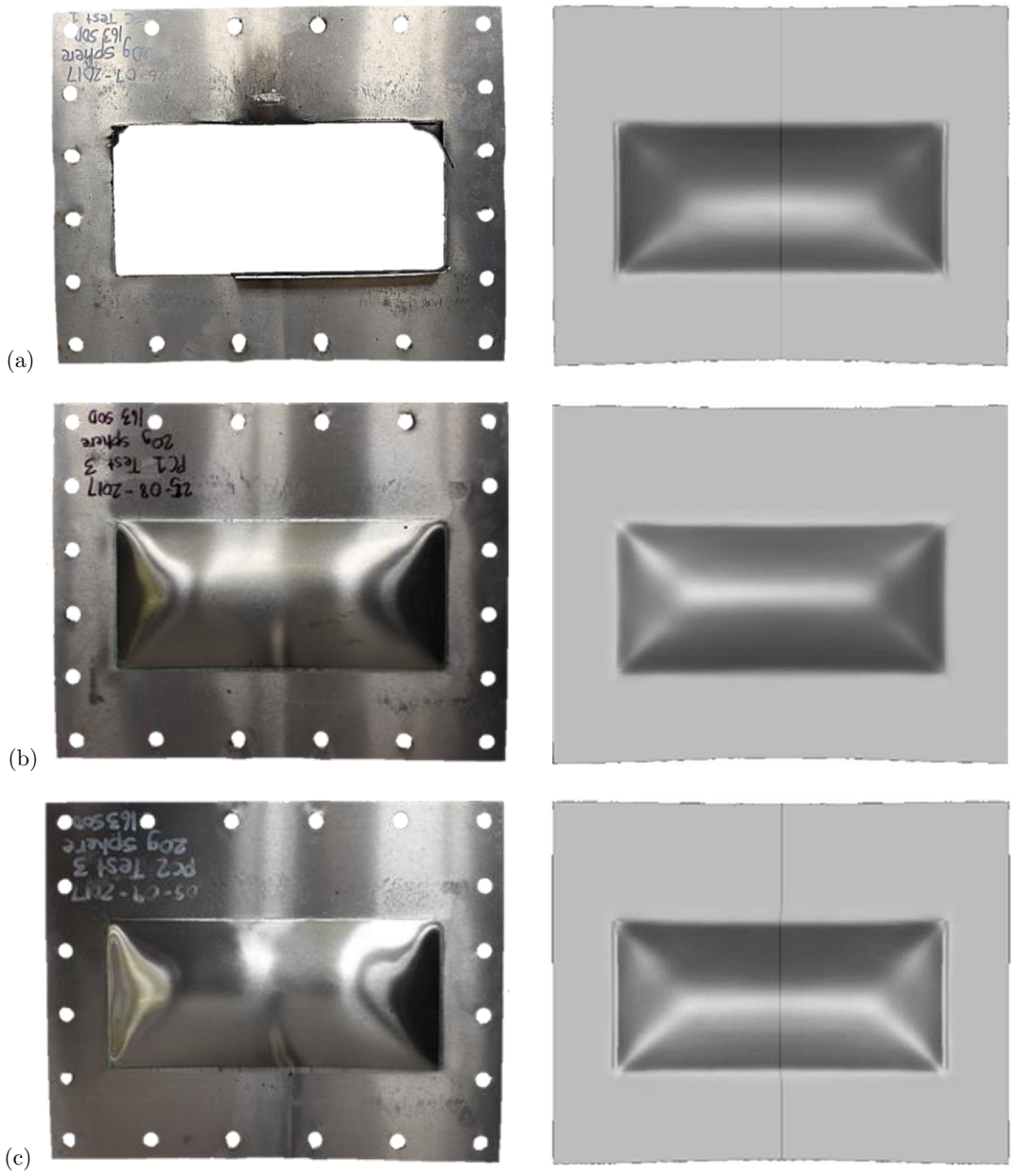

Figure 8.11: Photographs of the experimental (left) and images of the simulated (right) target plates showing final deformations of 20 g (a) fully-confined, (b) fully-vented ($\zeta = 0.7$) and (c) fully-vented ($\zeta = 1.4$) blasts.

In some cases, the mode of failure differed between tests performed at different venting configurations, but at the same charge mass, as evidenced in the confined blasts when tested with a 20 g charge. The deformed target plates of the experimental and simulated fully-confined and fully-vented blasts at 20 g are shown in Figure 8.11, displaying different modes of failure in the experimental tests. In the fully-confined experimental blast test, the target plate exhibited Mode II failure: tearing of the plate along the boundary supports. Significant boundary pull-in was observed along the top and bottom clamped edges (highlighted by the distortion of the bolt holes in these regions), as well as slight pull-in along the other two sides.

The target plates from the two fully-vented experimental blast tests, also at a 20 g charge, remained intact and only exhibited Mode I failure: large ductile deformations. Boundary pull-in was observed along the top and bottom clamped edges only, but less severe than that in the corresponding regions of the fully-confined blast test. Furthermore, the fully-vented blasts at 25 g did not exhibit tearing (partial or complete) of the target plate either. The venting configuration was therefore considered the main contributing factor for the transition from Mode I to Mode II failure for the range of charge masses tested experimentally.

The simulated target plates only exhibited Mode I failure in the form of plastic hinge development and boundary pull-in. The latter was noticeable at the top and bottom edges of the target plates; only minor boundary pull-in occurred along the shorter plate sides. Although the models were able to capture boundary pull-in, the absence of the clamping bolts in the simulations resulted in a more uniform boundary failure than that observed experimentally.

Overall, the simulated deformation of the target plate in each of the blast models captured representative plastic deformation of the plate due to the blast load: plastic hinge development consistent with theoretical predictions and boundary pull-in, as observed in the experimental tests, were present in the numerical results. The simulations did not exhibit Mode II failure since no damage model was included. This absence did not affect the results where plate rupture was not expected, such as the unconfined and fully-vented blasts. However, in the fully-confined blasts – where a rupture threshold was present – the numerical deflections were seen to diverge from the experimental results, as discussed in Section 8.2.2.

8.4 Application to Aircraft ULDs

The Lockerbie bombing disaster is an example of the catastrophic failure of an aircraft in the event of an explosive detonation within a luggage container. The primary cause of the aircraft destruction was the rupture of the aircraft skin which, due to the large difference in internal and atmospheric pressures, resulted in total decompression of the fuselage. Preventing rupture, or extreme deformation, of the ULD during blast loading would prevent damage to the aircraft skin and increase the probability of aircraft survival.

The detonation of an explosive within a sealed ULD container produces a fully-confined blast load on the structure. This configuration has been shown in literature [20,32] – and by the results obtained in this project – to result in the greatest damage to the structure when compared to configurations with less confinement. For this reason, the effect of venting was investigated to assess the possibility of reducing the damage and improving the survivability

of a ULD container. To achieve this, a scaled ULD model was blast tested with different venting configurations and the response of the diagonal side (that which would be positioned closest to the fuselage of the aircraft) was measured. Three of the allowable, practical venting configurations of a ULD onboard an aircraft (as illustrated in Table 3.1) were investigated experimentally: no venting, venting out one side panel, and venting out both side panels. Although not tested experimentally, configurations including a venting area on of the back panel remain viable options in practice.

The initial peak pressure of the blast wave was observed to be similar in each of the confined blast tests. The fully-confined blast exhibited a number of blast wave reflections and the generation of a quasi-static internal pressure greater than atmospheric pressure. The fully-vented configurations, however, reduced the number of blast wave reflections and the internal pressure returned to atmospheric conditions. Introducing venting areas to the structure reduced the loading within the ULD following the initial pressure wave. This difference in loading was observed to affect the failure mode of the target plate: the fully-confined blast caused complete plate rupture during the 20 g blast, whereas the other confined blast configurations did not cause rupture, even when tested at charge masses greater than 20 g.

Evidenced by the work performed in this project, introducing a venting area on one side panel resulted in an average reduction in target plate deflection of 11.1% compared to the fully-confined results. Introducing two venting areas resulted in a reduction of 16.7% and 22.2% in the experimental and simulated deflections, respectively, compared to the fully-confined deflections. Furthermore, the unconfined blast tests produced deflections which were 44.4% less than the fully-confined tests. Despite the discrepancy in experimental and numerical results for the double vent configuration, there remained a clear trend: an increase in venting area resulted in less deflection of the target plate. Although the unconfined blast tests represent the absence of the ULD itself – an impractical application given the current need for unit load devices – the results represent the maximum reduction in damage to which an increasing venting area would tend. Therefore, introducing additional venting areas (such as on the back panel of the ULD) would reduce the deflection of the target plate by between 16.7% and 44.4%.

By extrapolating these outcomes to aircraft ULDs currently in use, the practical application of introducing venting areas is considered beneficial in ULDs. The potential explosion would transition from producing a fully-confined to a fully-vented blast load and, as a result, the damage endured by the container would be reduced which, in addition to the explosive products being vented into the adjacent containers, would potentially shield the aircraft skin from rupturing and prevent destruction of the aircraft. Implementation of the venting

configurations tested in this project is possible: each container would vent into the two longitudinally adjacent containers, through the two side panels (represented by the test configuration with $\zeta = 1.4$), whilst the containers located at the front- and back-most ends of the lower deck would only vent into the one longitudinally adjacent container through one side panel (represented by the test configuration with $\zeta = 0.7$). These configurations were satisfactory blast mitigation techniques, since both reduced the probability of plate rupture and resulted in deflection reductions of more than 10%. Venting into the opposite container through the back panel, although not tested, remains a viable configuration for aircraft ULDs and was predicted to further improve the blast response of the structure when used in conjunction with the venting configurations tested in this project.

8.5 Limitations of the Project

Experimental blast testing was performed within the BISRU blast chamber. The blast tests were therefore limited to the available testing apparatus of the blast chamber:

- The experimental tests were limited to a total of three venting configurations: no venting, single-sided venting and double-sided venting. At least two ULD boxes were required to replicate each of the six venting configurations that would normally be possible to implement in practice. However, not all of the configurations could be tested on the available blast pendulum, either due to loading or mounting considerations. Therefore, only a single ULD box was manufactured, from which two venting areas were sequentially introduced to produce the fully-vented configurations.
- The experimental results of the confined blast tests were limited to only final plate deformations, with no transient deformations being captured. The target plate on the diagonal face of the ULD box could not be safely mounted onto, and tested using, the DIC pendulum. Therefore, no transient experimental results of the target plate could be obtained for any of the confined blast test series. Successful DIC data was, however, obtained for the unconfined blast tests.

The numerical model was developed without the inclusion of a damage or failure model. Although this exclusion did not affect the tests which did not exhibit plate tearing, the simulation was unable to capture the failure of the fully-confined tests. Furthermore, performing predictive simulations at higher charge masses, particularly for the fully-vented configurations, would yield unreliable results when the actual rupture threshold (determined experimentally) is approached.

9 Conclusions

The effect of the venting configuration on the blast response of a ULD box was evaluated by measuring the deformation of a target plate attached to the ULD diagonal side. The ULD was subjected to blast loads of varying magnitudes and tested at various degrees of confinement. The influence of the venting configuration and charge mass on the plate response is presented, the meeting of the objectives stated at the beginning of the project is assessed and the practical application of the project findings is discussed.

9.1 Influence of Venting Configuration

The effect of venting configuration on the blast response of the ULD box was observed to influence the deformation of the target plate, in terms of final deflections and boundary pull-in, as well as the mode of failure. An increasing venting area resulted in less plate deformation, whereas reducing the venting area increased the probability of plate tearing. Overall, more damage was observed in the tests at higher degrees of confinement.

The final midpoint deflections of the fully-confined blasts and the fully-vented blasts ($\zeta = 0.7$) were approximately 80% and 60% higher, respectively, than the corresponding unconfined blasts. This increase in deflection was evident in both the experimental and numerical blast tests for both venting configurations. However, the final midpoint deflections of the fully-vented blasts ($\zeta = 1.4$) from the experimental and numerical tests were approximately 50% and 40% higher, respectively, than the corresponding unconfined tests. The numerical results displayed a greater effect of the venting configuration between the two fully-vented tests than the experimental results. Overall, the target plate deflection increased as the degree of confinement increased (or the available venting area decreased).

The venting configuration was observed to influence the mode of failure of the target plate. The experimental fully-confined blast test exhibited Mode II failure – complete rupture of the target plate – when tested at 20 g. This failure was indicated by the entire exposed area tearing

away from the target plate. The fully-vented blast tests only exhibited Mode I failure – large inelastic deformation – when tested at 20 g and higher. The probability of Mode II failure increased as the degree of confinement was increased.

9.2 Influence of Charge Mass

The deflection of the target plate was observed to increase with an increasing charge mass. A higher charge mass produced a blast wave with greater peak pressure, and consequently transferred greater impulse to the target plate. The influence of charge mass was observed to be greater in the tests at higher degrees of confinement. The experimental fully-confined blast tests exhibited a decreasing deflection gradient as the rupture threshold (of 20 g) was approached. This effect was noticeable in the fully-confined blasts tested with charge masses greater than 12 g. Each of the other blast tests (experimental and numerical) exhibited a linear relationship between midpoint deflection and charge mass.

9.3 Meeting the Project Objectives

A 1:6 scaled ULD box was manufactured which allowed three subsequent venting configurations to be tested. A fully-confined configuration was made possible by making the top panel of the box removable. The charge was placed within the box and thereafter the top panel was bolted to the box. Two small holes were drilled into the side panel to allow the detonator cables to be connected to the trigger switch. The first fully-vented test configuration was created by cutting a 252 mm x 220 mm venting area in one side panel. This configuration resulted in a venting area ratio of $\zeta = 0.7$. The second fully-vented configuration was created by cutting a second venting area (with dimensions identical to the first) in the opposite side panel. As a result, the second fully-vented test series had a venting area ratio of $\zeta = 1.4$.

Experimental blast testing was successfully performed at four different degrees of confinement. Unconfined blast tests provided dynamic deformation results of the target plate midpoint and midline with the aid of high-speed cameras and DIC processing technology. Confined blast tests using the ULD box were performed, and final plate deformations were obtained for the fully-confined and two fully-vented test series. The effect of the venting configuration was determined by modes of failure of the target plate: large inelastic deformations (Mode I) were observed in most of the target plates, with complete tearing (Mode II) observed in the 20 g fully-confined test plate.

Tension tests were performed to determine the work hardening coefficients of the Johnson-Cook constitutive material model to represent the aluminium, grade 5754h22, used for the target plate. The strain-rate sensitivity coefficient and thermal sensitivity exponent were acquired from published literature [49]. The Johnson-Cook constants used to represent the material behaviour are listed in Table 9.1. The tension tests were simulated in LS DYNA® using an implicit solver and produced stress-strain results which demonstrated excellent correlation with the analytical Johnson-Cook fit of the experimental tension test results.

Table 9.1: Johnson-Cook constants used to model aluminium target plate.

A (MPa)	**B (MPa)**	**n**	**C**	**m**
160.5	339.8	0.5206	0.003	2.519

Four numerical blast models were successfully developed to simulate each of the four experimental test series. The models exhibited effective fluid-structure interaction and the resultant transient deformation (midpoint and midline) of the target plate was captured. Contact between the target plate, clamp frame and ULD flange (in the case of confined tests) ensured a representative clamped boundary condition of the plate. The pressure history at the target plate midpoint and corners was recorded and displayed results which were consistent across the three confined blast models.

Both the experimental and numerical results displayed deformation patterns, in terms of plastic hinge development and boundary pull-in, which were consistent with theoretical and existing experimental work. Strong correlations of the final midpoint and midline deflections for the experimental and numerical results were observed in the unconfined and fully-vented ($\zeta = 0.7$) blast results. The fully-confined results did not compare favourably, due to the absence of a damage model in the simulations, and resulted in the numerical results not capturing the same blast response as the experimental deflections as the rupture threshold (at 20 g) was approached. The experimental results of the second fully-vented test series, with $\zeta = 1.4$, exhibited little distinction from those of the first fully-vented test series. In the numerical results, however, there was a clear distinction between the two sets of results. Consequently, the numerical and experimental target plate deflections for the second fully-vented test series did not compare favourably either.

9.4 Application of Project Findings

The application of the results obtained in this project is considered beneficial to aircraft ULDs used in practice. Introducing venting areas has been shown to reduce the blast loading within the structure. A fully-confined structure experiences several reflected shock loads and a quasi-static rise in internal pressure. Although the magnitude and duration of the initial blast load is unaffected, an increase in venting area reduces the number and magnitude of the subsequent blast reflections, and increases the rate at which the internal pressure diminishes to atmospheric conditions. Consequently, tests of the single and double venting configurations of the ULD box showed a reduction in the plate deflections by up to 11.1% and 22.2%, respectively. Furthermore, both the fully-vented configurations prevented rupture of the target plate when tested at the same, or a higher, charge mass than that which caused rupture in the fully-confined blast.

These results present the introduction of venting in ULDs as a favourable blast mitigation technique. The venting configurations tested in this project are based on the current positioning of ULDs onboard an aircraft and are therefore possible to implement. The single venting configuration is representative of ULDs positioned at the front and rear ends of the aircraft lower deck, in which case venting out only one side panel is possible. The double venting configuration is representative of the remaining ULDs, where venting out both side panels is possible. Venting into the opposite ULD (through the back panel) is possible for all the containers, but was not tested in this project.

The single venting configuration was observed to adequately prevent plate rupture and, despite exhibiting a lower reduction in deflection compared to the double venting configuration, was considered sufficient in reducing the blast damage of the ULD. Therefore, each of the containers (including those positioned at the ends) will be capable of mitigating damage to and preventing rupture of the ULD structure. By implementing the tested venting configurations in practice, the blast response of the ULD container, in the event of an explosion therein, can be improved.

10 Recommendations

Recommendations for further work are listed in this chapter. The work performed in this project was divided into three main sections: the experimental blast testing, aluminium material characterisation and numerical modelling. The work should be extended to include investigations into the other parameters affecting the blast response of the target plate, improve the results of the experimental and numerical tests, address the limitations present in the work, and expand the simulations to predict the outcomes of the blast configurations not tested experimentally.

10.1 Experimental Testing

Further experimental work should include the following:

- The rupture limit of the fully-vented tests should be established. Identifying this threshold would provide further understanding of the effect of the venting configuration on the failure of the target plate.
- The effects of luggage capacity should be investigated. As reported by Gatto and Krznaric [22] and Hargather et al. [23], the presence of luggage affects the blast loading within a ULD. Tests should be performed to determine the significance of luggage capacity at different venting configurations.
- The effect of charge location within the ULD should be investigated. Due to the random nature of the position of a potential explosive within the luggage container, blast testing should be performed at various charge locations, similar to work presented by Hargather et al. [23].
- The blast response of a ULD of different material should be assessed. The same test setup should be used to investigate the deformation of target plates of various materials used in practice, as proposed by Gatto and Fleisher [21]. Potential materials to be tested include, but are not limited to: high strength (aircraft grade) aluminium, high

strength fibreglass, GLARE panels, KEVLAR® reinforced composites, and honey-comb sandwich panels.

- The pressure history at points of interest within the ULD box should be measured by including pressure transducers in the test setup.
- The transient response of the confined blast tests should be measured. Modification should be made to the design of the ULD box or the current DIC pendulum (else the development of a new testing rig should be implemented) to allow for the dynamic deformation of the target plate during confined blast testing to be recorded.

10.2 Material Characterisation

To verify the material constants obtained from literature, the following should be performed on the material of the target plate:

- The strain-rate sensitivity of the plate material should be determined by performing tests at high strain-rates using a Split Hopkinson Pressure Bar.
- The thermal sensitivity (or thermal softening effects) of the aluminium should be determined by performing tests at elevated temperatures.

10.3 Numerical Modelling

The following modifications to the numerical models are suggested:

- The other venting configurations not tested experimentally should be simulated.
- Further analysis should be made into the investigation of the effects of the reflected pressure waves during confined blast loading.
- The walls of the ULD box should be modified (in terms of material and thickness) to simulate a ULD with multiple deformable panels.
- The influence of thermal effects on the numerical results should be investigated by performing a thermal-structural analysis in the simulations.
- A damage and failure model should be included to produce representative simulation results for tests which exhibit tearing.

References

[1] Aerospaceweb.org, *Commercial Airline Bombing History*, accessed on 2 September 2017 at: http://www.aerospaceweb.org/question/planes/q0283.shtml

[2] L. Dearden, *Isis plane attack: Egypt admits 'terrorists' downed Russian Metrojet flight from Sharam el Sheikh for first* time, Independent Web Article, accessed on 2 September 2017 at: http://www.independent.co.uk/news/world/africa/isis-plane-attack-egypt-terrorists-downed-russian-metrojet-flight-from-sharm-el-sheikh-islamic-state-a6893181.html

[3] R. Kriel & P. Cruickshank, *Source: 'Sophisticated' laptop bomb on Somali plane got through X-ray machine*, CNN Web Article, accessed on 2 September 2017 at: http://edition.cnn.com/2016/02/11/africa/somalia-plane-bomb/index.html

[4] S. Emerson & B. Duffy, *The Fall of Pan-Am 103: Inside the Lockerbie Investigation*, G.P. Putnam's Sons, New York, U.S.A (1990).

[5] Airlog Group, *Air Freight ULD (Unit Load Device) Specifications* (2011).

[6] Photograph of Airbus A300 fuselage cross-section, obtained on 12 April 2017 at: https://commons.wikimedia.org/wiki/File:Airbus_A300_cross_section.jpg

[7] G.F. Kinney & K.J. Graham, *Explosive Shocks in Air*, 2nd edition, The Macmillan Company, New York, U.S.A (1985).

[8] U.S. Army Corps of Engineers, Naval Facilities Engineering Command and Air Force Civil Engineer Support Agency, *Structures to Resist the Effects of Accidental Explosions*, Report UFC 3-340-02, US Department of the Army and Defense Special Weapons Agency, Washington, D.C., U.S.A (2008).

[9] P.D. Smith & J.G. Hetherington, *Blast and Ballistic Loading on Structures*, Butterworth-Heinemann (1994).

[10] V. Karlos & G. Solomos, *Calculation of Blast Loads for Application to Structural Components*, European Laboratory for Structural Assessment, Joint Research Centre, Institute for the Protection and Security of the Citizen, JRC Technical Report EUR 26456 EN, European Union (2013).

[11] B. Hopkinson, *British Ordnance Board Minutes 13565* (1915).

[12] C. Cranz, *Lehrbuch der Ballistik*, Springer-Verlag, Berlin, Germany (1926).

[13] W.E. Baker, P.A. Cox, P.S. Westine, J.J. Kulez & R.A. Strehlow, *Explosion Hazards and Evaluation*, Elsevier Scientific Publishing Company (1983).

[14] International Ammunition Technical Guideline, *Formulae for Ammunition Management*, IATG 01.80:2015, 2nd edition (2015).

[15] H.L. Brode, *Numerical Solution of Spherical Blast Waves*, Journal of Applied Physics, **29**(6), American Institute of Physics, New York, U.S.A (1955).

[16] N.M. Newmark & R.J. Hansen, *Design of Blast Resistant Structures*, Shock and Vibration Handbook Volume 3, McGraw-Hill, New York, U.S.A (1961).

[17] J. Henrych, *The Dynamics of Explosion and Its Use (Developments in Civil Engineering)*, Elsevier Science Ltd (1979).

[18] C.A. Mills, *The Design of Concrete Structures to Resist Explosions and Weapon Effects*, 1st Int. Conference on Concrete for Hazard Protections, Edinburgh, U.K (1987).

[19] W.A. Keenan & J.E. Tancreto, *Blast Environment from Fully and Partially Vented Explosions in Cubicles*, Technical Report R 828, Civil Engineering Laboratory, Naval Construction Battalion Center, California, U.S.A (1975).

[20] C. Kingery, R. Schumacher & W. Ewing Jr, *Internal Pressure from Explosions in Suppressive Structures*, Memorandum Report ARBRL-MR-02848, US Army Armament Research and Development Command, Ballistic Research Laboratory, Aberdeen Proving Ground, Maryland, U.S.A (1978).

[21] J.A. Gatto & H.J. Fleisher, *Hardened Luggage Container Design Survey*, Federal Aviation Administration Technical Center, Aviation Security Research and Development Service, Atlantic City International Airport, New Jersey, U.S.A (1993).

[22] J.A. Gatto & S. Krznaric, *Pressure Loading on a Luggage Container due to an Internal Explosion*, Structures Under Shock and Impact, pp. 61–77 (1996).

[23] M. J. Hargather, G.S. Settles & G.A. Gatto, *Full-Scale Optical Experiments on the Explosive Failure of a ULD-3 Air Cargo Container*, The 4th International Aviation Security Technology Symposium, Washington, D.C., U.S.A (2006).

[24] S.B. Menkes & H.J. Opat, *Tearing and Shear Failures in Explosively Loaded Clamped Beams*, Experimental Mechanics, **13**(11), pp. 480–486 (1973).

[25] G.N. Nurick & G.C. Shave, *The Deformation and Tearing of Thin Square Plates Subjected to Impulsive Loads – An Experimental Study*, International Journal of Impact Engineering, **18**(1), pp. 99–116 (1996).

[26] M.D. Olson, G.N. Nurick & J.R. Fagnan, *Deformation and Rupture of Blast Loaded Square Plates – Predictions and Experiments*, International Journal of Impact Engineering, **13**(2), pp. 279–291 (1993).

[27] G.N. Nurick, M.E. Gelman & N.S. Marshall, *Tearing of Blast Loaded Plates with Clamped Boundary Conditions*, International Journal of Impact Engineering, **18**(7–8), pp. 803–827 (1996).

[28] W. Johnson, *Impact Strength of Materials*, Edward Arnold (1975).

[29] G.N. Nurick & J.B. Martin, *Deformation of Thin Plates Subjected to Impulsive Loading – A Review – Part II: Experimental Studies*, International Journal of Impact Engineering, **8**(2), pp. 171–186 (1989).

[30] N. Jones, *Structural Impact*, 2nd edition, Cambridge University Press (2012).

[31] Y.P. Zhao, *Suggestion of a New Dimensionless Number for Dynamic Plastic Response of Beams and Plates*, Archive of Applied Mechanics, **68**, pp. 524–538 (1998).

[32] C. Geretto, S. Chung Kim Yuen & G.N. Nurick, *An Experimental Study of the Effects of Degrees of Confinement on the Response of Square Mild Steel Plates Subjected to Blast Loading*, International Journal of Impact Engineering, **79**, pp. 32–44 (2015).

[33] S. Yao, D. Zhang & F. Lu, *Dimensionless Number for Dynamic Response Analysis of Box-Shaped Structures Under Internal Blast Loading*, International Journal of Impact Engineering, **98**, pp. 13–16 (2016).

[34] K. Spranghers, I. Vasilakos, D. Lecompte, H. Sol & J. Vantomme, *Full-Field Deformation Measurements of Aluminium Plates Under Free Air Blast Loading*, Experimental Mechanics, **52**, pp. 1371–1384 (2012).

[35] K. Spranghers, I. Vasilakos, D. Lecompte, H. Sol & J. Vantomme, *Numerical Simulation and Experimental Validation of the Dynamic Response of Aluminium Plates Under Free Air Explosions*, International Journal of Impact Engineering, **54**, pp. 83–95 (2013).

[36] V. Aune, E. Fagerholt, K.O. Hauge, M. Langseth & T. Børvik, *Experimental Study on the Response of Thin Aluminium and Steel Plates Subjected to Airblast Loading*, International Journal of Impact Engineering, **90**, pp. 106–121 (2016).

[37] V. Aune, G. Valsamos, F. Casadei, M. Larcher, M. Langseth & T. Børvik, *Numerical Study on the Structural Response of Blast-Loaded Thin Aluminium and Steel Plates*, International Journal of Impact Engineering, **99**, pp. 131–144 (2017).

[38] V. Pickerd, H. Bornstein, P. McCarthy & M. Buckland, *Analysis of the Structural Response and Failure of Containers Subjected to Internal Blast Loading*, International Journal of Impact Engineering, **95**, pp. 40–53 (2016).

[39] S. Yao, D. Zhang, F. Lu & X. Li, *Experimental and Numerical Studies on the Failure Modes of Steel Cabin Structure Subjected to Internal Blast Loading*, International Journal of Impact Engineering, **110**, pp. 279–287 (2017).

[40] Brinkley, *ULD – Unit Load Devices and Contours: AKE*, accessed on 20 November 2016 at: http://brinkley.cc/ULD/ake.htm

[41] B.M. Dobratz & P.C. Crawford. *LLNL handbook of explosives: Properties of chemical explosives and explosive simulants*, Technical Report UCRL-52997, Lawrence Livermore National Laboratory, University of California, California, U.S.A (1985).

[42] R. Curry, *Response of plates subjected to air-blast and buried explosions*, PhD Thesis, University of Cape Town, Cape Town, South Africa (2017).

[43] G.R. Johnson & W.H. Cook, *A constitutive model and data for metals subjected to large strains, high strain rates and high temperatures*, Proceedings of the 7th International Symposium on Ballistics, pp. 541–547, Netherlands (1983).

[44] J.R. Davis, *Alloying: Understanding the Basics – Light Metals and Alloys: Aluminium and Aluminium Alloys*, ASM International, pp. 351–461 (2013).

[45] Henan Yongyang Import and Export Company Ltd., Mills Test Certificate of Aluminium Sheet 5754/H22, Technique Standard GB/ZT3880-2006, China (2017).

[46] ASTM E8/E8M-16a, *Standard Test Methods for Tension Testing of Metallic Materials*, ASTM International (2013).

[47] S.S. Panicker et al., *Characterization of Tensile Properties, Limiting Strains, and Deep Drawing Behaviour of AA5754-H22 Sheet, at Elevated Temperature*, Journal of Materials Engineering and Performance, **24**(11), pp. 4267–4282 (2015).

[48] M. Türköz, H.S. Halkaci & M. Koç, *The Effect of Temperature and Strain-Rate Sensitivity on Formability of AA 5754*, Applied Mechanics and Materials, **217**–**219**, pp. 1596–1601 (2012).

[49] R. Smerd, S. Winkler, C. Salisbury, M. Worswick, D. Lloyd & M. Finn, *High strain rate tensile testing of automotive aluminium alloy sheet*, International Journal of Impact Engineering, **32**, pp. 541–560 (2005).

[50] LS DYNA®, *Keyword User's Manual Volume I,* Livermore Software Technology (LSTC) (2016).

[51] Y.A. Çengel & M.A. Boules, *Thermodynamics: An Engineering Approach, Seventh Edition in SI Units*, McGraw Hill, New York, U.S.A (2011).

[52] ASM Handbook, *Volume 2: Properties and Selection: Nonferrous Alloys and Special-Purpose Materials,* 10th Edition Metals Handbook, ASM International (1993).

[53] ASM Handbook, *Volume 1: Properties and Selection: Irons Steels and High Performance Alloys,* 10th Edition Metals Handbook, ASM International (1993).

[54] The Engineering Toolbox, *Friction and Friction Coefficients*, accessed on 20 October 2018 at: https://www.engineeringtoolbox.com/friction-coefficients-d_778.html

This page is intentionally left blank.

Appendix A Simulated Transient Midline Deflections

Introduction

The transient midline deflections of all the blast simulations are presented in this appendix, including those presented in Section 7.2.3, for completeness. The fully-confined results (presented first) comprise tests from 10 g to 20 g charge masses, whereas the fully-vented and unconfined tests further include a 25 g blast. Each set of results is divided into two phases: the first is the development of the profile up to a peak deformed position and the second is the convergence towards the final midline profile. Peak positions were reached at 600 µs for the fully-confined tests, 450 µs for the fully-vented ($\zeta = 0.7$) tests, 400 µs for the fully-vented ($\zeta = 1.4$) tests and 375 µs for the unconfined tests. The final midline profile was determined as the average midline profile over the 2 ms and 3 ms period.

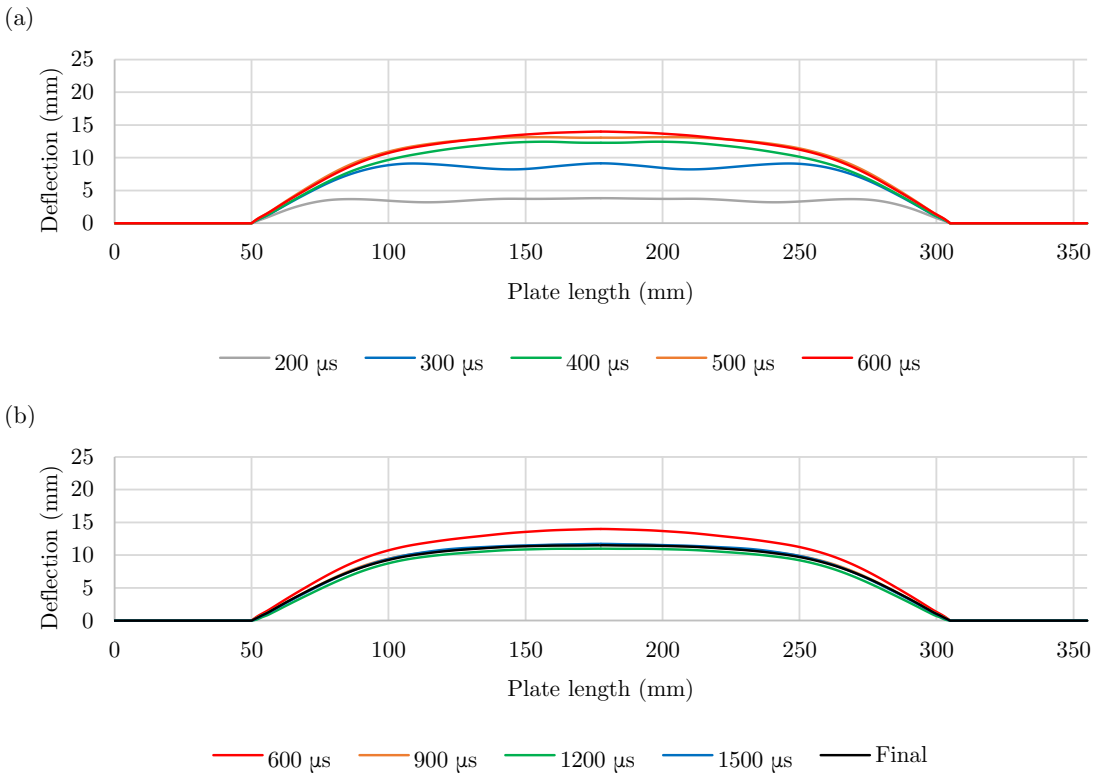

Figure A.1: Graphs of the transient midline profile for a fully-confined blast simulation with a 10 g charge, deforming from (a) undeformed to peak deformation and (b) peak to final deformation.

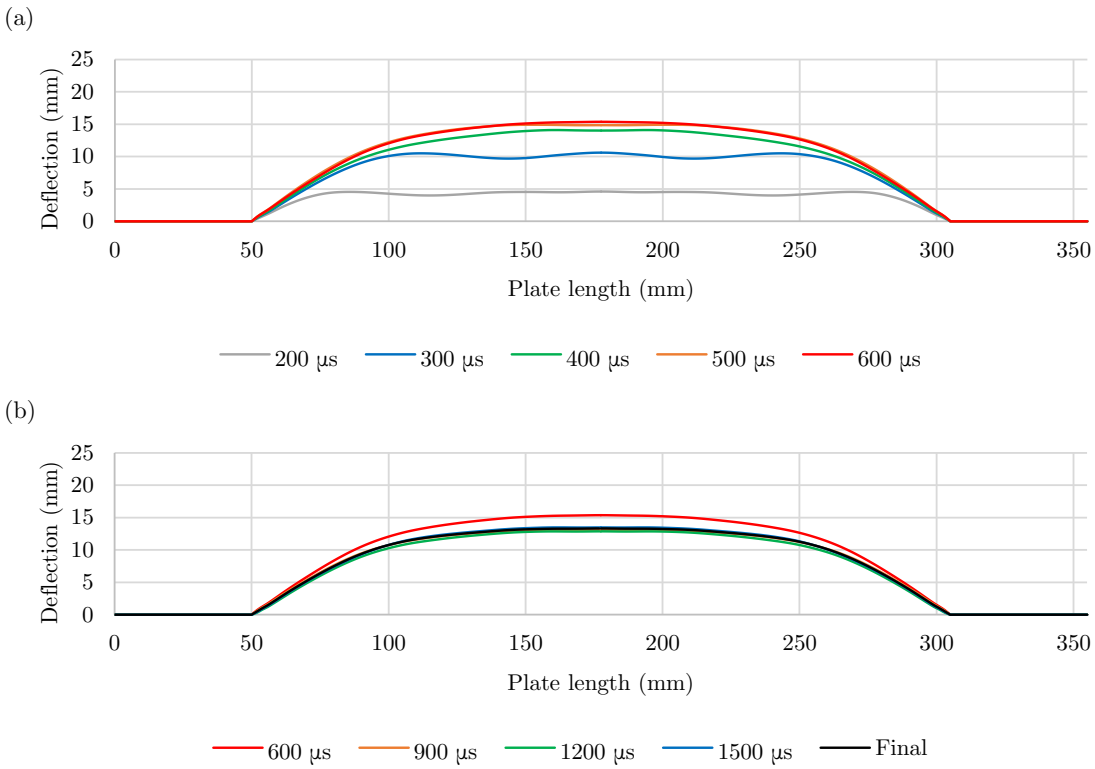

Figure A.2: Graphs of the transient midline profile for a fully-confined blast simulation with a 12 g charge, deforming from (a) undeformed to peak deformation and (b) peak to final deformation.

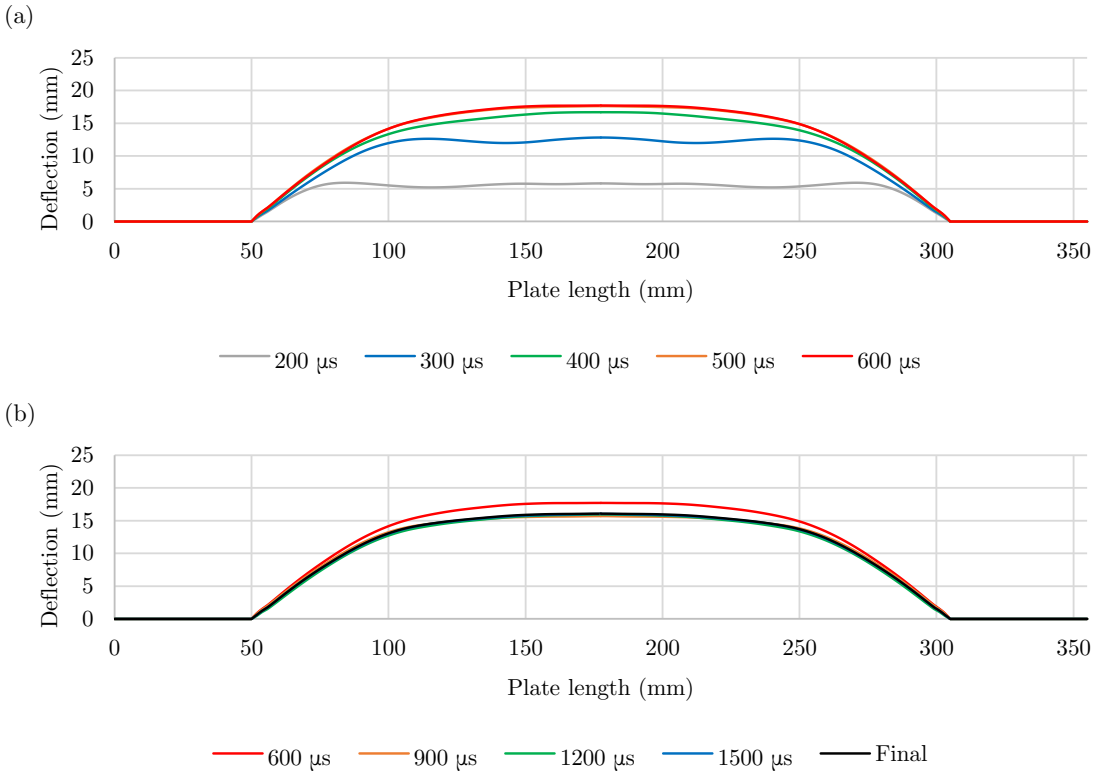

Figure A.3: Graphs of the transient midline profile for a fully-confined blast simulation with a 15 g charge, deforming from (a) undeformed to peak deformation and (b) peak to final deformation.

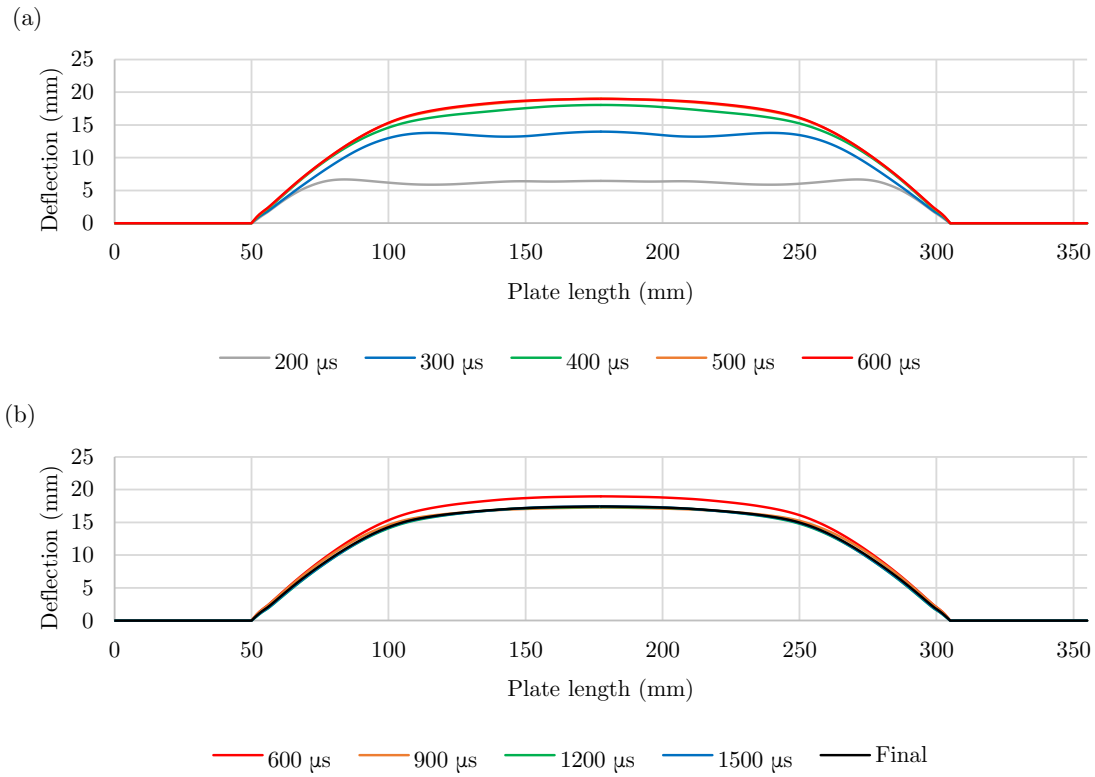

Figure A.4: Graphs of the transient midline profile for a fully-confined blast simulation with a 17 g charge, deforming from (a) undeformed to peak deformation and (b) peak to final deformation.

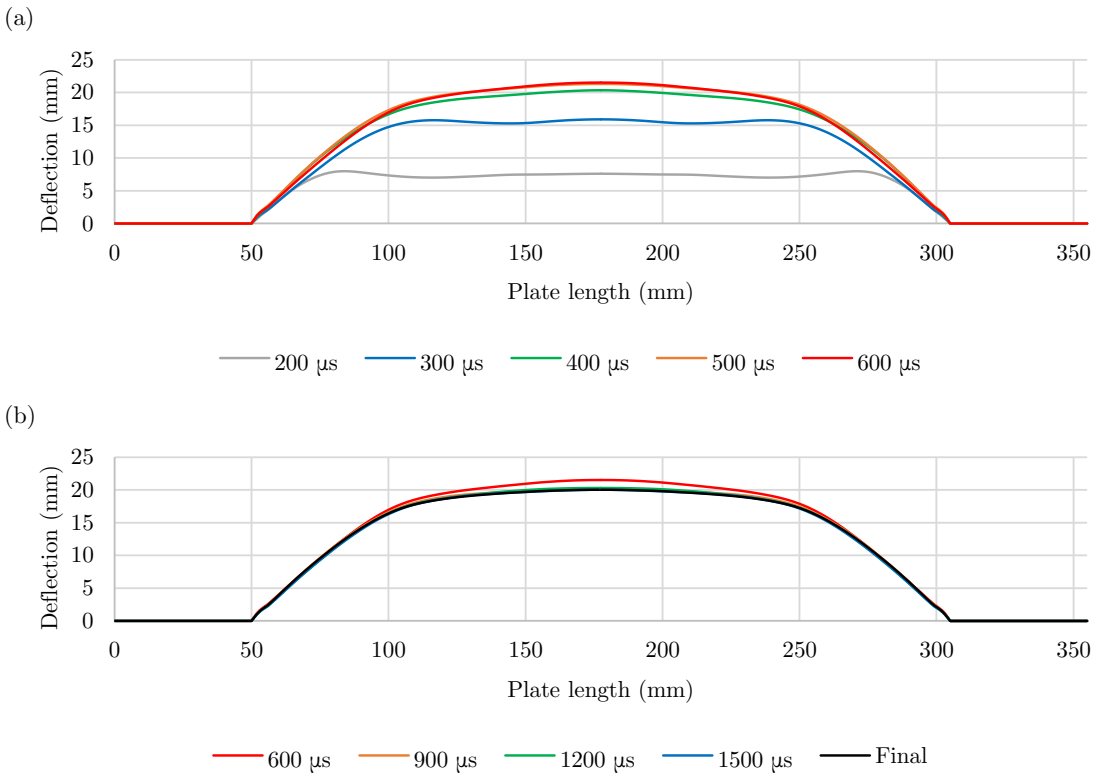

Figure A.5: Graphs of the transient midline profile for a fully-confined blast simulation with a 20 g charge, deforming from (a) undeformed to peak deformation and (b) peak to final deformation.

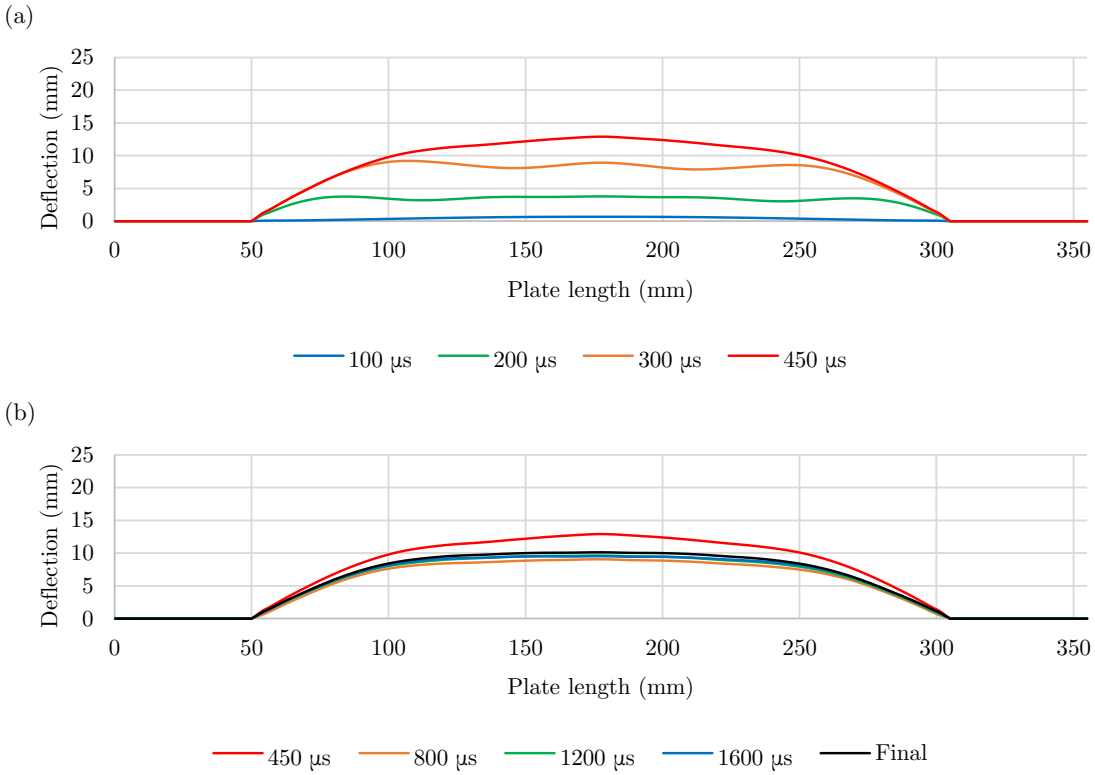

Figure A.6: Graphs of the transient midline profile for a fully-vented ($\zeta = 0.7$) blast simulation with a 10 g charge, deforming from (a) undeformed to peak deformation and (b) peak to final deformation.

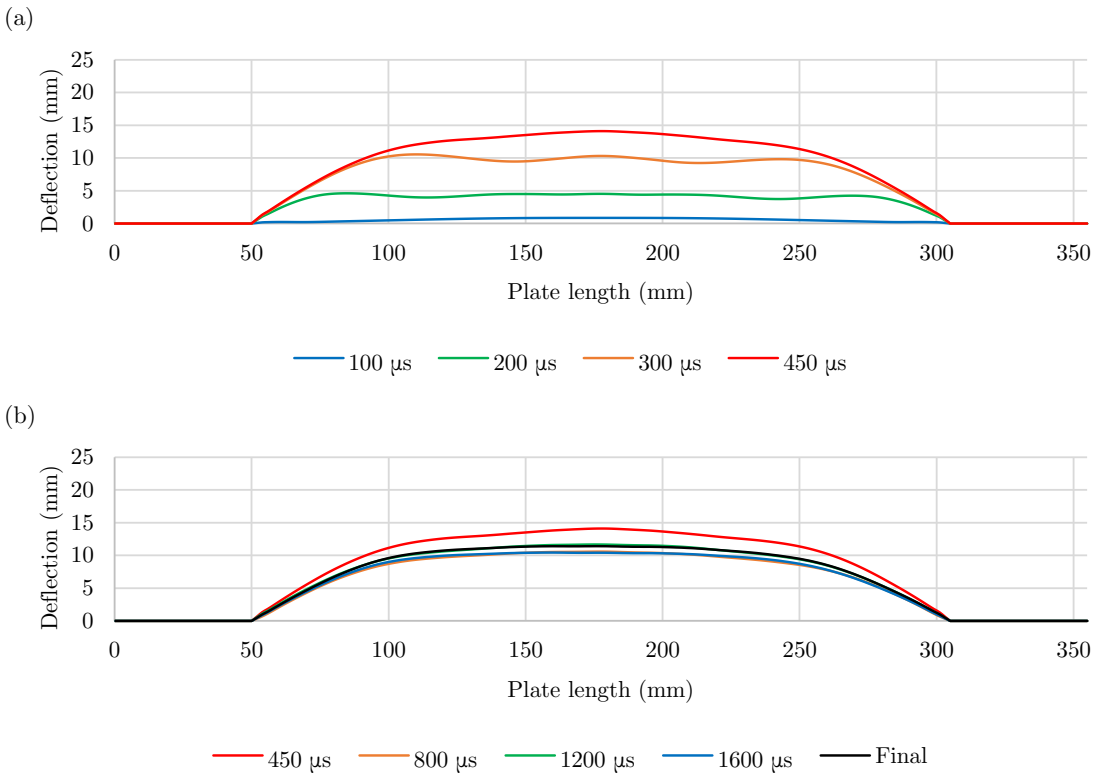

Figure A.7: Graphs of the transient midline profile for a fully-vented ($\zeta = 0.7$) blast simulation with a 12 g charge, deforming from (a) undeformed to peak deformation and (b) peak to final deformation.

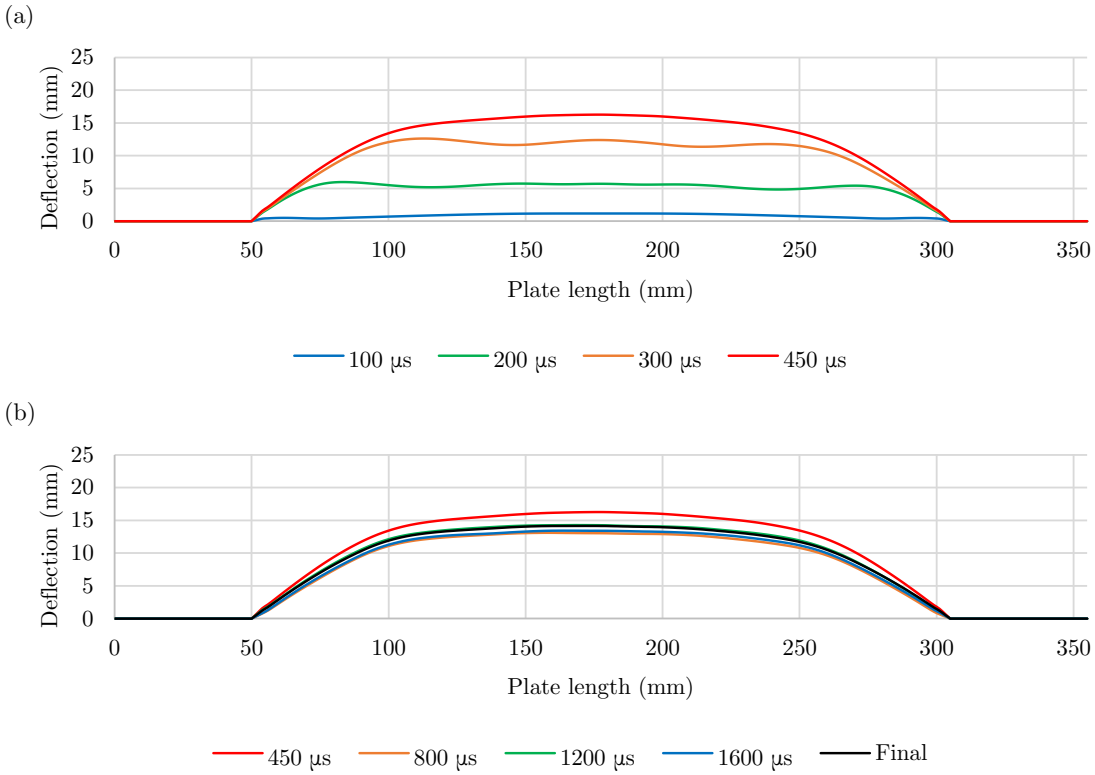

Figure A.8: Graphs of the transient midline profile for a fully-vented ($\zeta = 0.7$) blast simulation with a 15 g charge, deforming from (a) undeformed to peak deformation and (b) peak to final deformation.

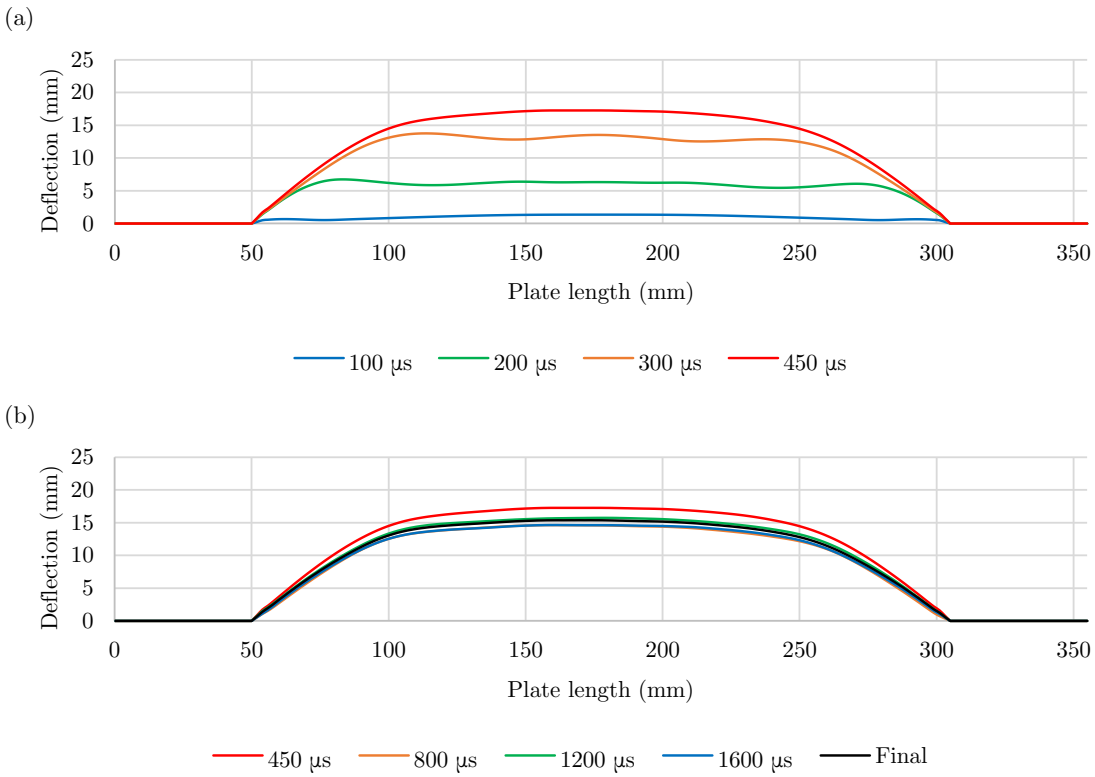

Figure A.9: Graphs of the transient midline profile for a fully-vented ($\zeta = 0.7$) blast simulation with a 17 g charge, deforming from (a) undeformed to peak deformation and (b) peak to final deformation.

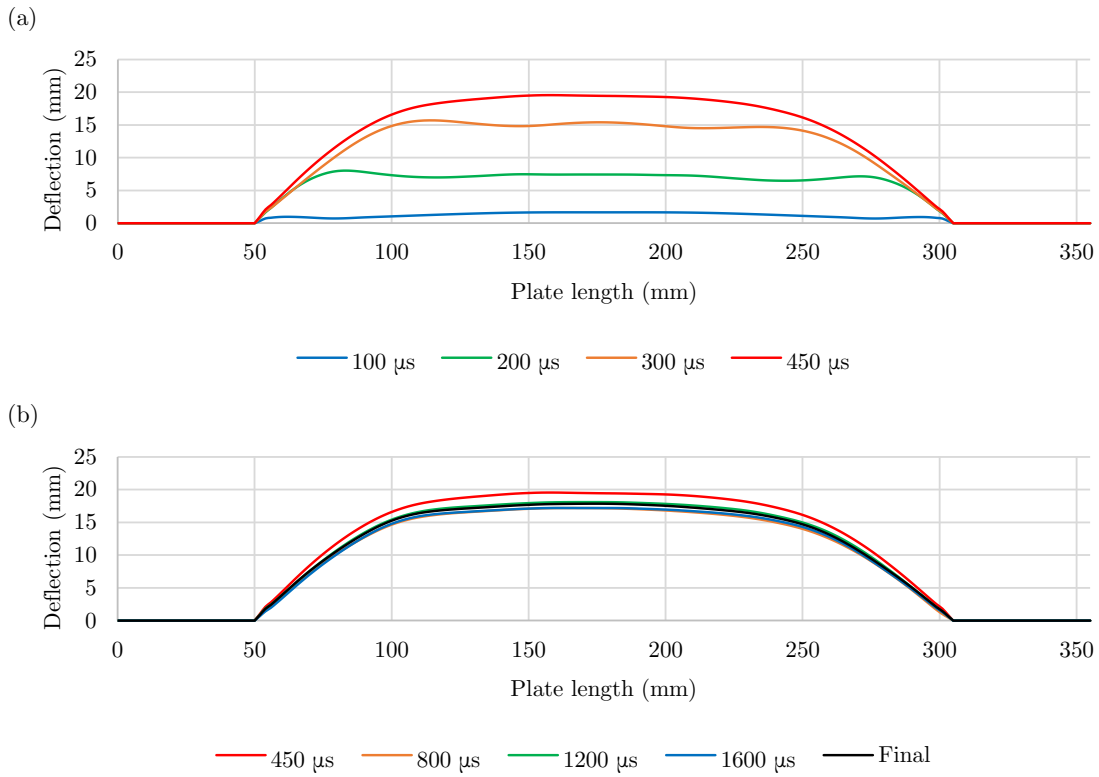

Figure A.10: Graphs of the transient midline profile for a fully-vented ($\zeta = 0.7$) blast simulation with a 20 g charge, deforming from (a) undeformed to peak deformation and (b) peak to final deformation.

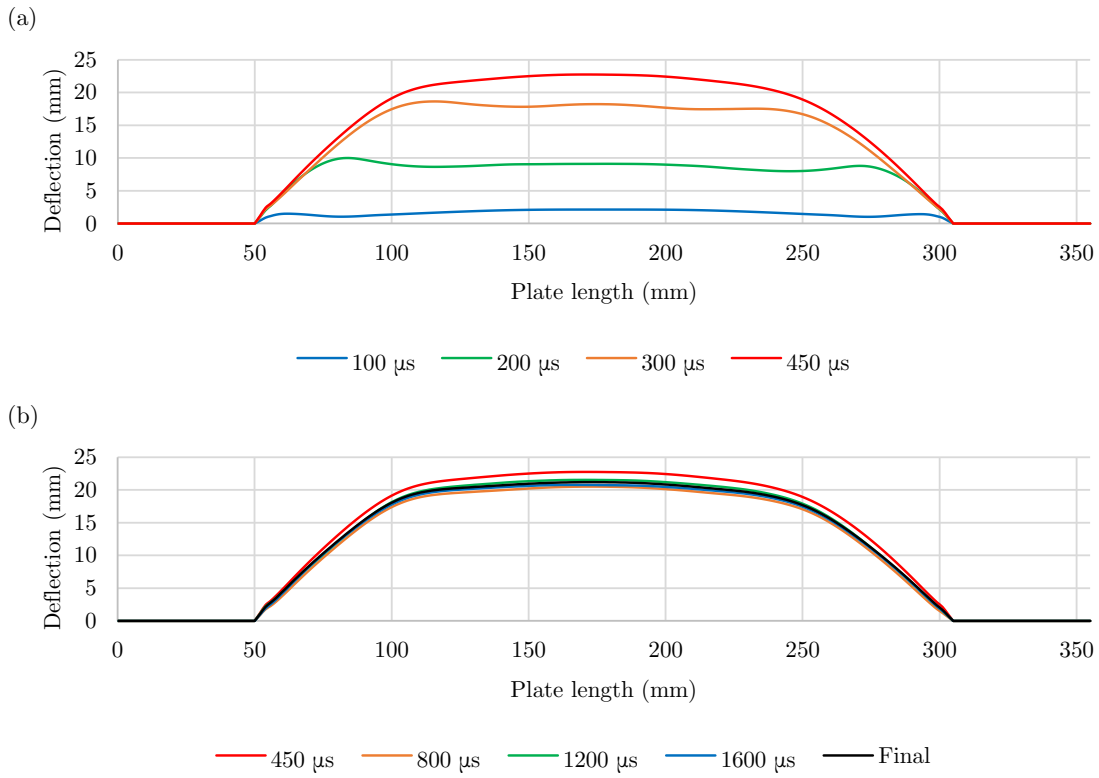

Figure A.11: Graphs of the transient midline profile for a fully-vented ($\zeta = 0.7$) blast simulation with a 25 g charge, deforming from (a) undeformed to peak deformation and (b) peak to final deformation.

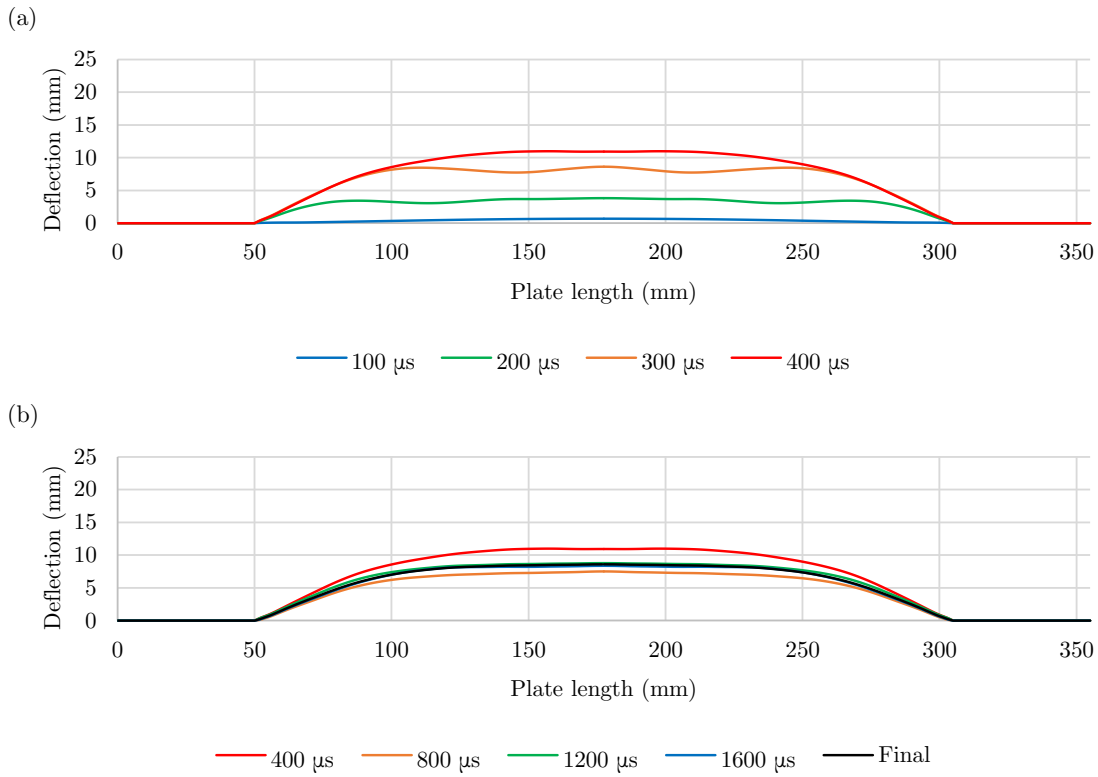

Figure A.12: Graphs of the transient midline profile for a fully-vented ($\zeta = 1.4$) blast simulation with a 10 g charge, deforming from (a) undeformed to peak deformation and (b) peak to final deformation.

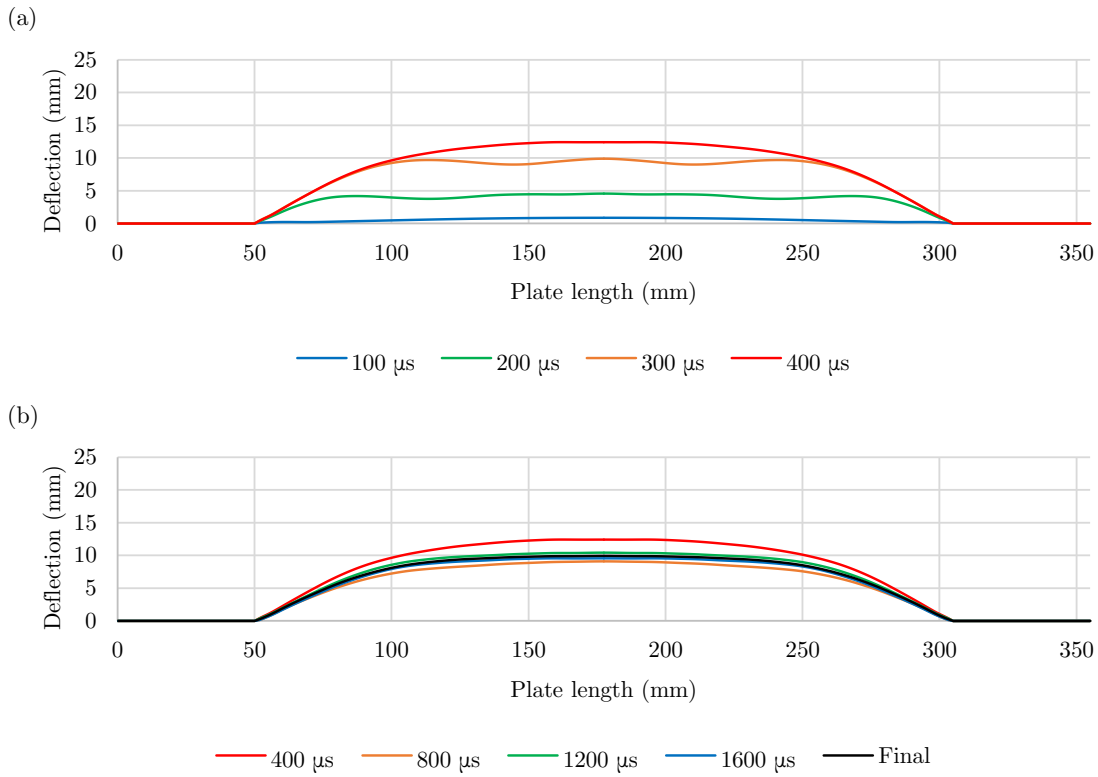

Figure A.13: Graphs of the transient midline profile for a fully-vented ($\zeta = 1.4$) blast simulation with a 12 g charge, deforming from (a) undeformed to peak deformation and (b) peak to final deformation.

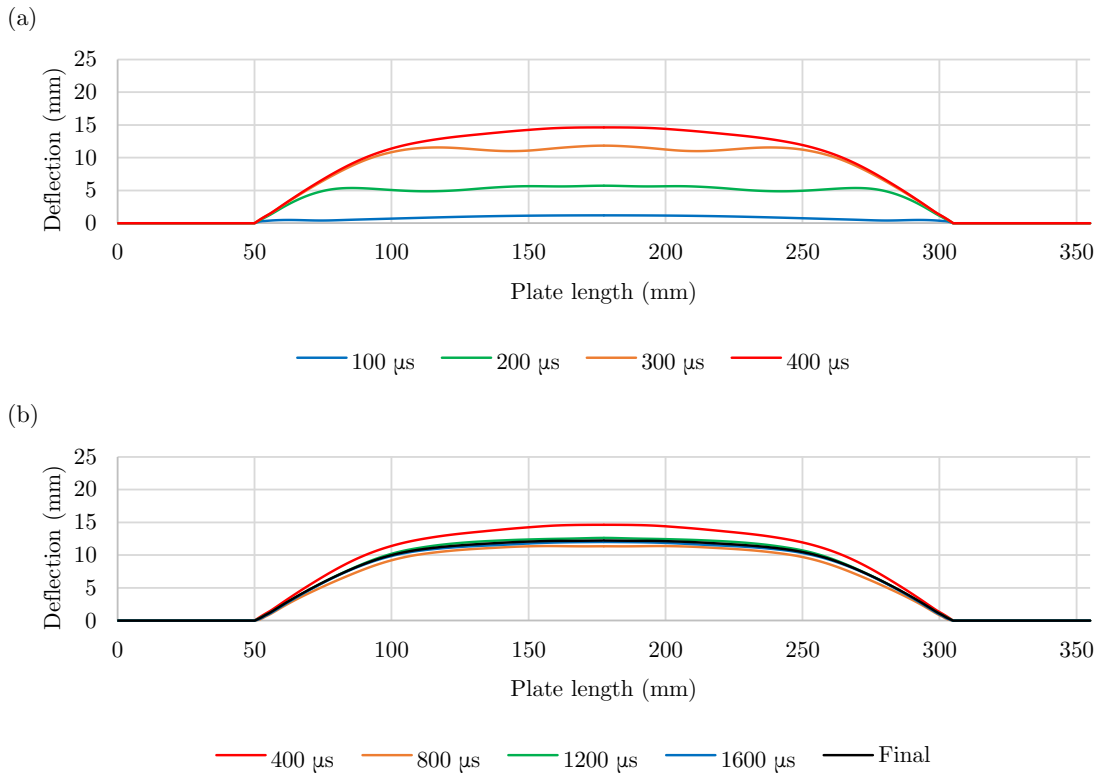

Figure A.14: Graphs of the transient midline profile for a fully-vented ($\zeta = 1.4$) blast simulation with a 15 g charge, deforming from (a) undeformed to peak deformation and (b) peak to final deformation.

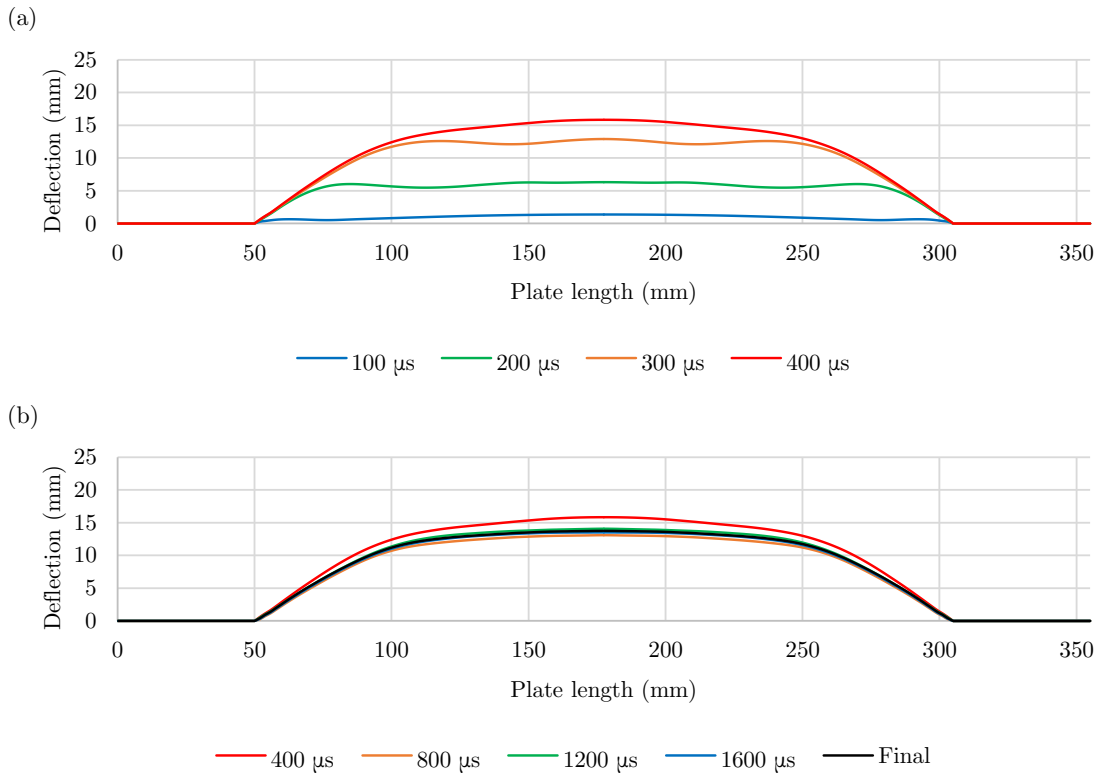

Figure A.15: Graphs of the transient midline profile for a fully-vented ($\zeta = 1.4$) blast simulation with a 17 g charge, deforming from (a) undeformed to peak deformation and (b) peak to final deformation.

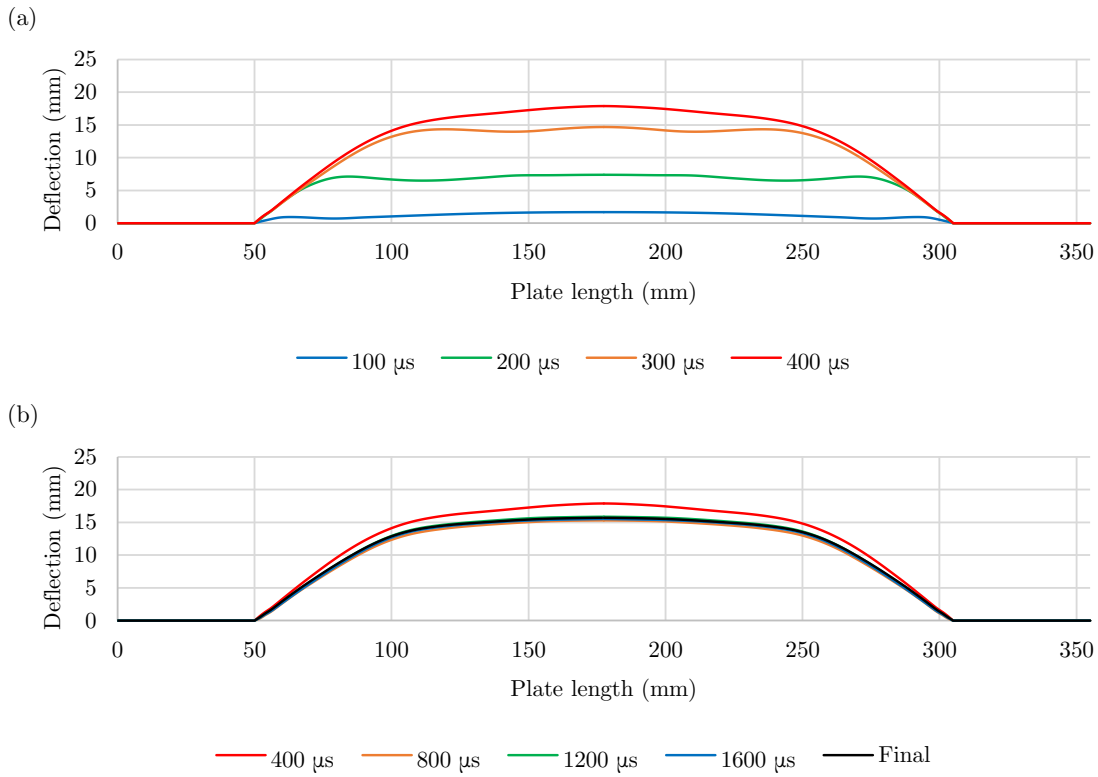

Figure A.16: Graphs of the transient midline profile for a fully-vented ($\zeta = 1.4$) blast simulation with a 20 g charge, deforming from (a) undeformed to peak deformation and (b) peak to final deformation.

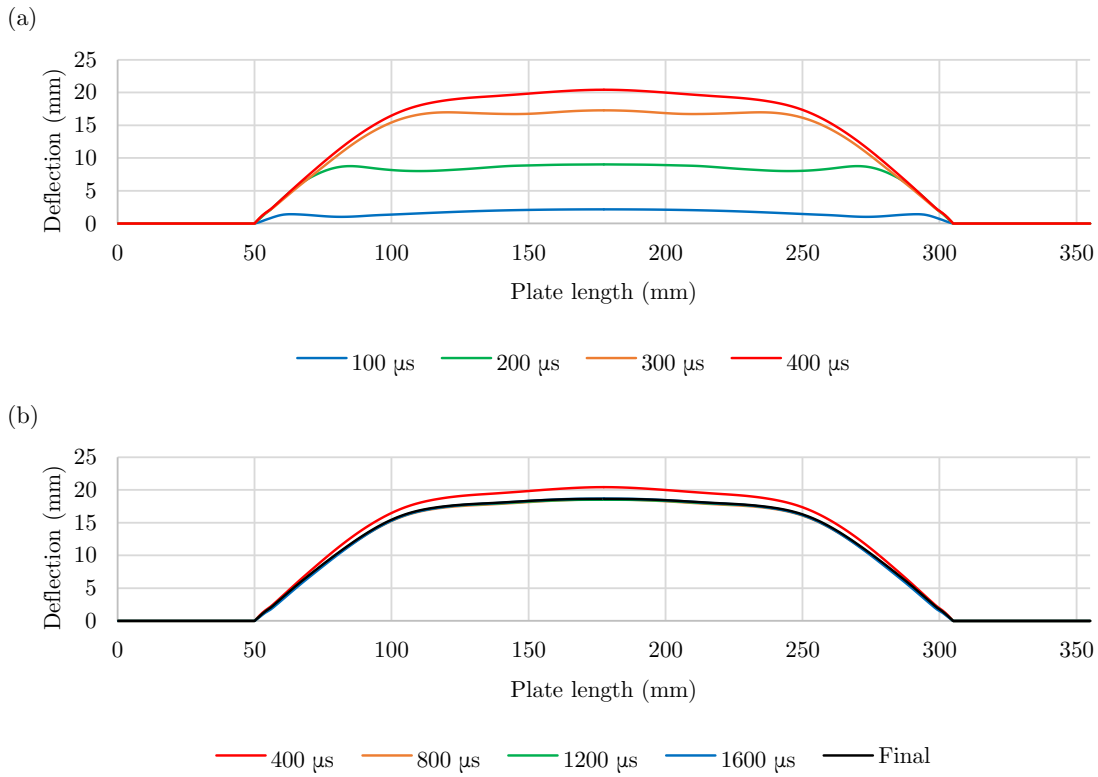

Figure A.17: Graphs of the transient midline profile for a fully-vented ($\zeta = 1.4$) blast simulation with a 25 g charge, deforming from (a) undeformed to peak deformation and (b) peak to final deformation.

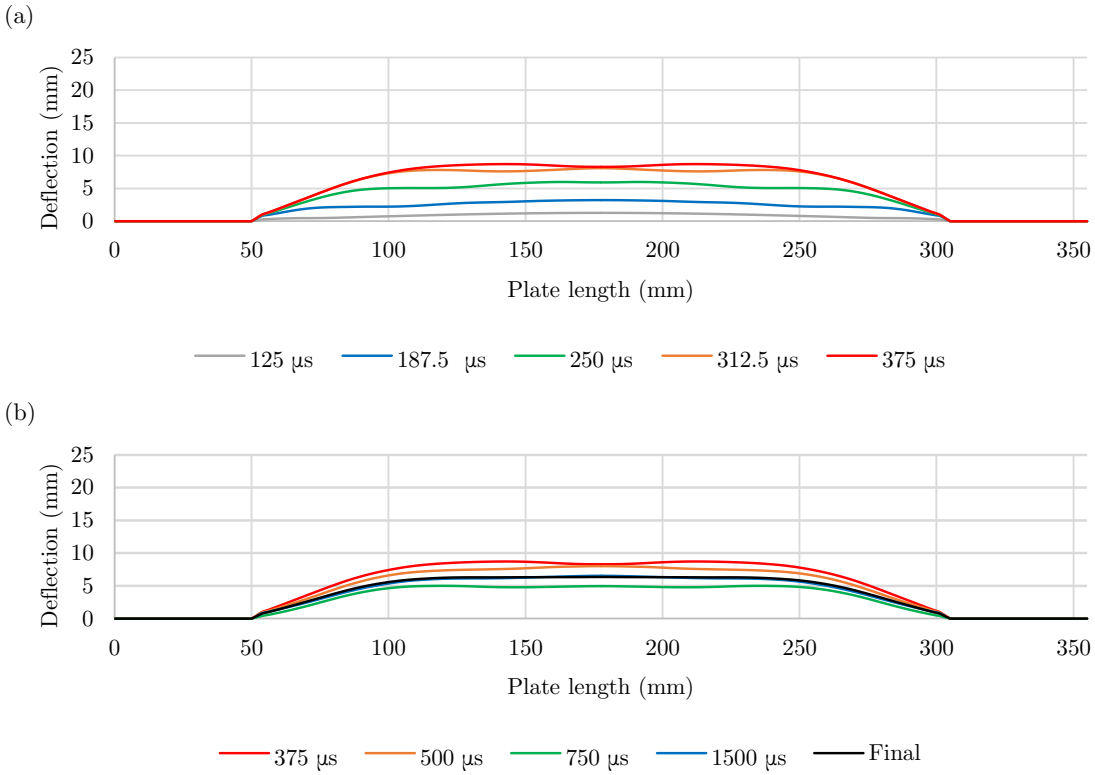

Figure A.18: Graphs of the transient midline profile for an unconfined blast simulation with a 10 g charge, deforming from (a) undeformed to peak deformation and (b) peak to final deformation.

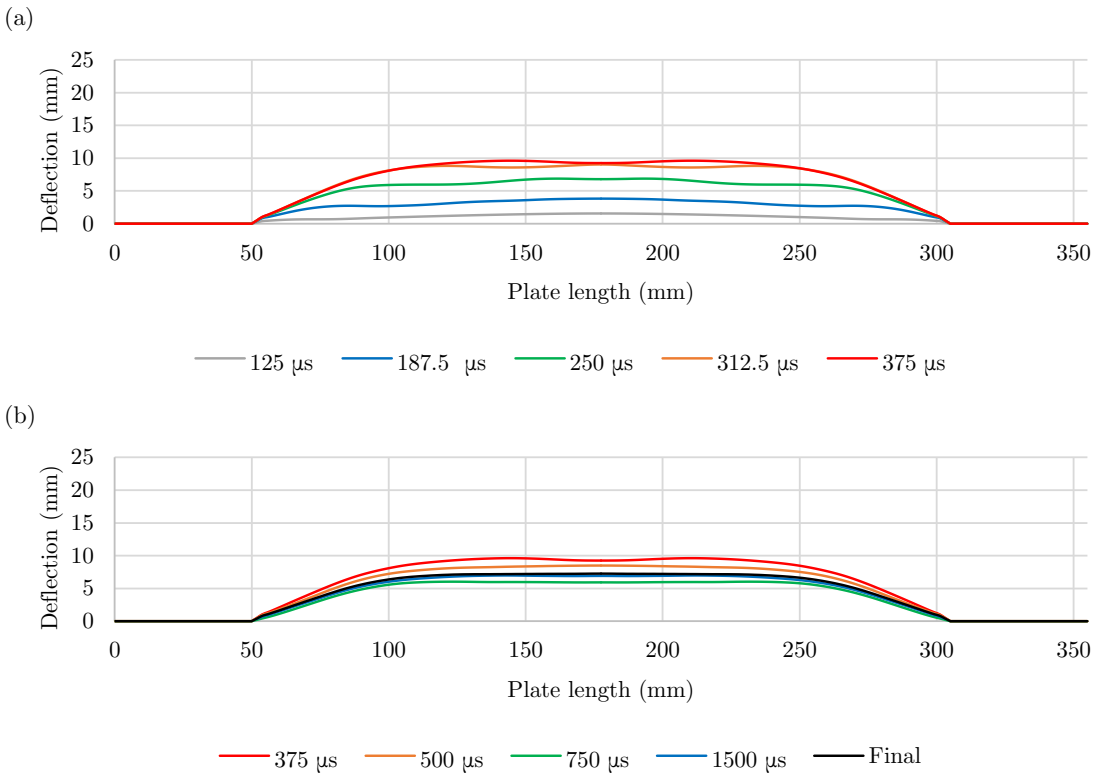

Figure A.19: Graphs of the transient midline profile for an unconfined blast simulation with a 12 g charge, deforming from (a) undeformed to peak deformation and (b) peak to final deformation.

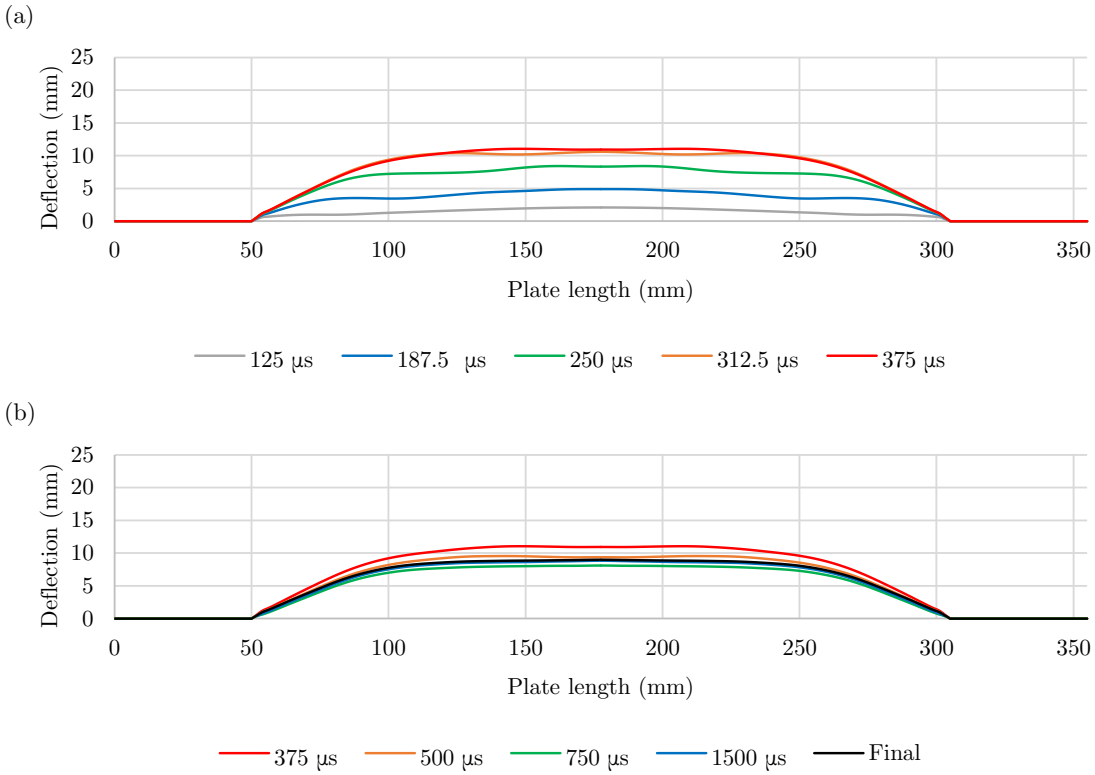

Figure A.20: Graphs of the transient midline profile for an unconfined blast simulation with a 15 g charge, deforming from (a) undeformed to peak deformation and (b) peak to final deformation.

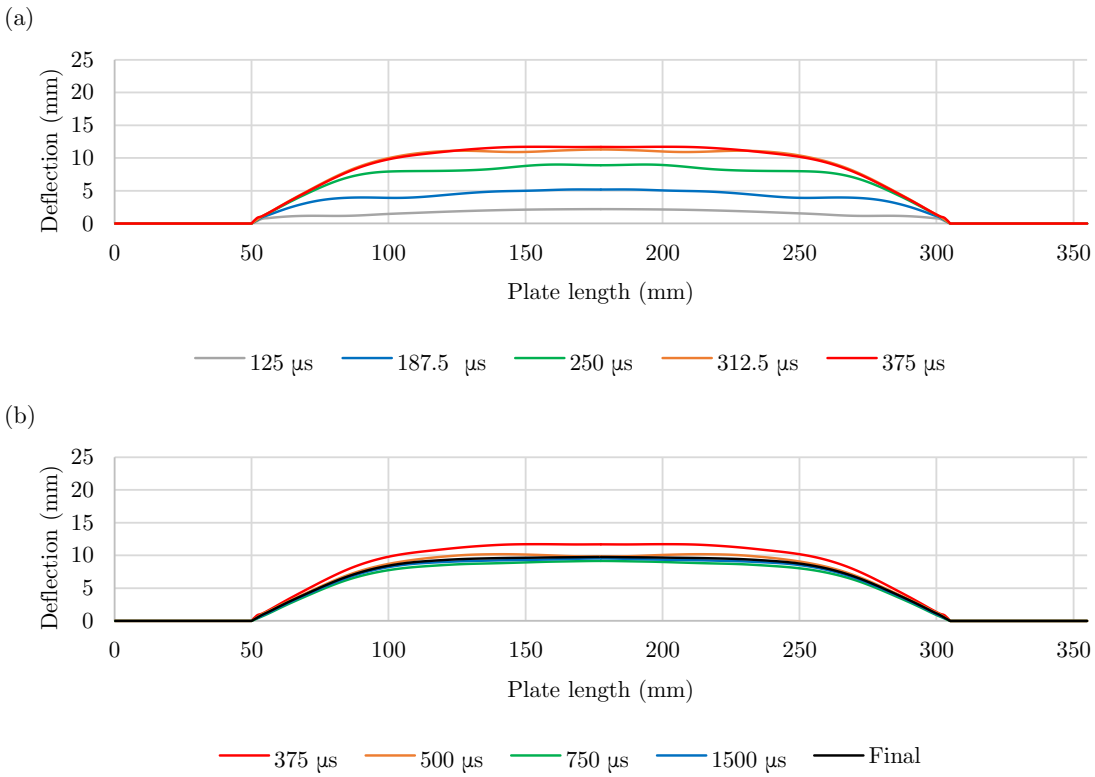

Figure A.21: Graphs of the transient midline profile for an unconfined blast simulation with a 17 g charge, deforming from (a) undeformed to peak deformation and (b) peak to final deformation.

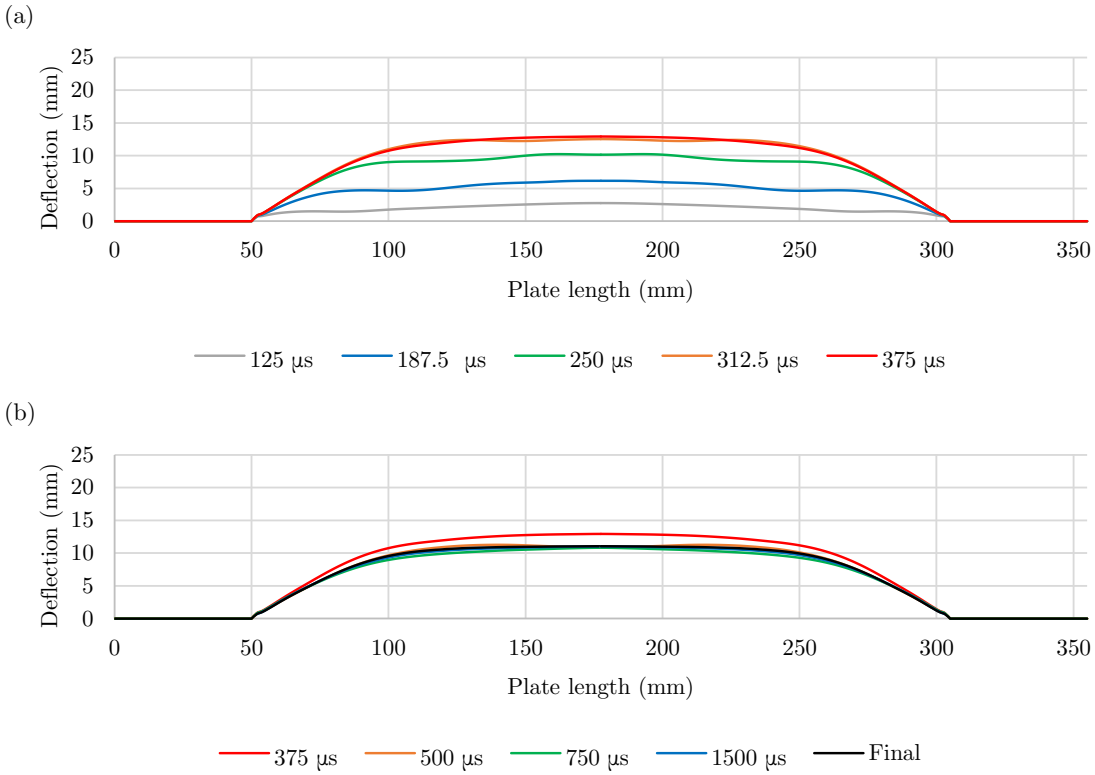

Figure A.22: Graphs of the transient midline profile for an unconfined blast simulation with a 20 g charge, deforming from (a) undeformed to peak deformation and (b) peak to final deformation.

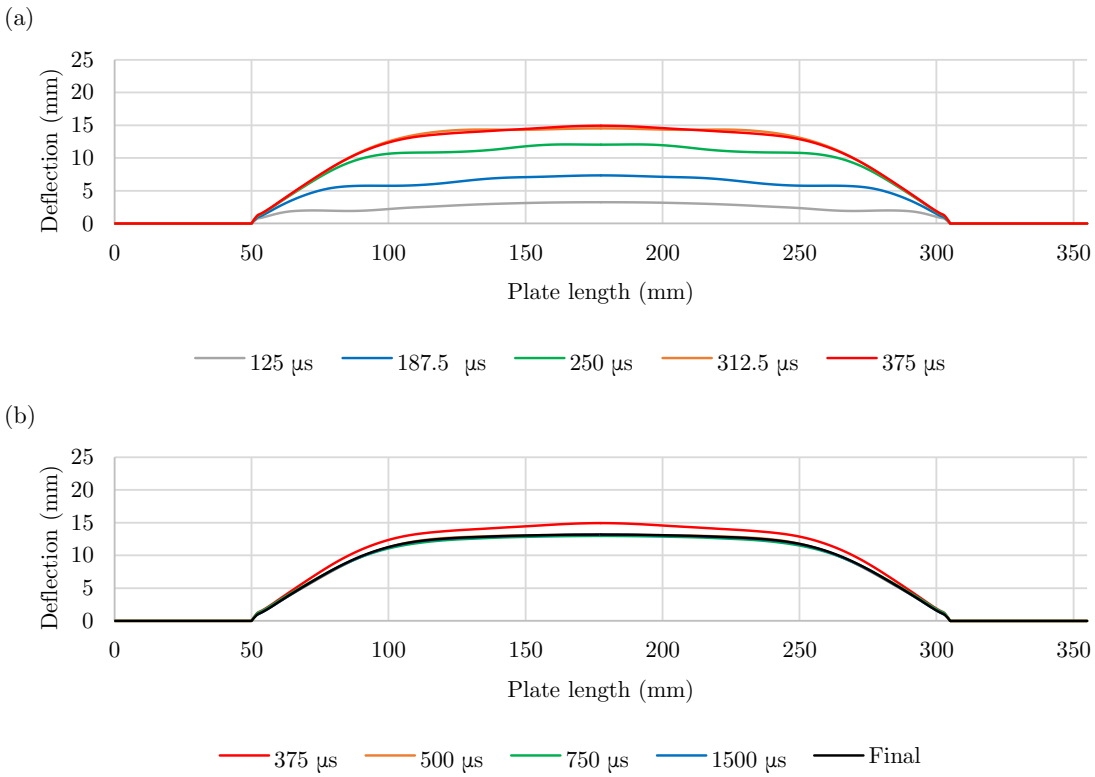

Figure A.23: Graphs of the transient midline profile for an unconfined blast simulation with a 25 g charge, deforming from (a) undeformed to peak deformation and (b) peak to final deformation.

This page is intentionally left blank.

Appendix B Blast Simulation Input Deck

The numerical blast models each comprised six keyword files: main.k, air.k, plate.k, box.k, clamp.k, and restart.k. The main keyword file was used to establish the control cards of the simulation, and the boundary conditions of and interactions between the parts. Specified within the keyword file of each of the parts (air, target plate, ULD box and clamp frame) were the section and material properties, and (where relevant) the equation of state parameters. A restart keyword file was used to restart the analysis without the air domain and FSI interactions once the loading phase of the simulation was complete. The main and restart keyword files, as well as abridged versions of the air, plate, box and clamp keyword files (which exclude the node and element definitions) are presented here.

```
*TITLE
$#   main.k
LS-DYNA keyword deck by LS-Prepost
*CONTROL_ALE
$#        dct       nadv       meth       afac       bfac       cfac       dfac       efac
         -1          1         -2         -1          0          0          0          0
$#      start        end      aafac      vfact       prit        ebc       pref   nsidebc
          0    1.00E20          1   1.00E-06          0          0     0.1013          0
$#       ncpl       nbkt     imascl     checkr     beamin   mmgpref    pdifmx   dtmufac
          1         50          0          0          0          0          0          0
*CONTROL_ENERGY
$#       hgen       rwen      slnten     rylen
          2          2          1          1
*CONTROL_SOLUTION
$#       soln        nlq      isnan      lcint      lcacc      ncdcf
          0          0          1        100          0          1
*CONTROL_TERMINATION
$#     endtim     endcyc       dtmin     endeng     endmas       nosol
         1.0          0          0          0   1.00E+08          0
*CONTROL_TIMESTEP
$#     dtinit     tssfac       isdo     tslimt     dt2ms       lctm     erode     ms1st
   1.00E-05       0.67          0          0          0          0         0         0
$#     dt2msf    dt2mslc      imscl     unused     unused     rmscl
          0          0          0          0
*DATABASE_BNDOUT
$#         dt     binary       lcur      ioopt
   1.00E-05          0          0          1
*DATABASE_GLSTAT
$#         dt     binary       lcur      ioopt
   1.00E-05          0          0          1
*DATABASE_MATSUM
$#         dt     binary       lcur      ioopt
   1.00E-05          0          0          1
*DATABASE_NODOUT
$#         dt     binary       lcur      ioopt    option1    option2
   1.00E-05          0          0          1          0          0
*DATABASE_TRHIST
$#         dt     binary       lcur      ioopt
   1.00E-05          0          0          1
*DATABASE_BINARY_D3PLOT
$#         dt       lcdt       beam      npltc     psetid
         0.02          0          0          0          0
$#      ioopt
          0
*DATABASE_HISTORY_NODE_SET
$#        id1        id2        id3        id4        id5        id6        id7        id8
        200          0          0          0          0          0          0          0
```

*DATABASE_TRACER

$#	time	track	x	y	z	ammg	nid	radius
	0	1	56.0	67.0	2.0	0	0	0
	0	1	20.0	113.0	127.5	0	0	0
	0	1	90.0	20.0	127.5	0	0	0

*BOUNDARY_SPC_SET

$#	nsid	cid	dofx	dofy	dofz	dofrx	dofry	dofrz
	101	0	0	0	1	1	1	0
$#	nsid	cid	dofx	dofy	dofz	dofrx	dofry	dofrz
	201	0	0	0	1	1	1	0
$#	nsid	cid	dofx	dofy	dofz	dofrx	dofry	dofrz
	301	0	1	1	1	1	1	1
$#	nsid	cid	dofx	dofy	dofz	dofrx	dofry	dofrz
	401	0	1	1	1	1	1	1

*CONTACT_AUTOMATIC_SURFACE_TO_SURFACE_ID

$#	cid	title						
	500	Plate – box contact						
$#	ssid	msid	sstyp	mstyp	sboxid	mboxid	spr	mpr
	202	302	0	0	0	0	0	0
$#	fs	fd	dc	vc	vdc	penchk	bt	dt
	0.61	0.61	0	0	0	0	0	1.00E+20
$#	sfs	sfm	sst	mst	sfst	sfmt	fsf	vsf
	1	1	0	0	1	1	1	1

*CONTACT_AUTOMATIC_SURFACE_TO_SURFACE_ID

$#	cid	title						
	600	Plate – clamp contact						
$#	ssid	msid	sstyp	mstyp	sboxid	mboxid	spr	mpr
	202	402	0	0	0	0	0	0
$#	fs	fd	dc	vc	vdc	penchk	bt	dt
	0.61	0.61	0	0	0	0	0	1.00E+20
$#	sfs	sfm	sst	mst	sfst	sfmt	fsf	vsf
	1	1	0	0	1	1	1	1

*INITIAL_VOLUME_FRACTION_GEOMETRY

$#	fmsid	fmidtyp	bammg	ntrace				
	100	1	1	3				
$#	conttyp	fillopt	fammg	vx	vy	vz	radvel	unused
	6	0	2	0	0	0	0	
$#	xc	yc	zc	radius	unused	unused	unused	unused
	185.0	164.1667	0.0	15.5				

*INITIAL_DETONATION

$#	pid	x	y	z	lt
	10	185.0	164.1667	0.0	0

*DEFINE_TRANSFORMATION_TITLE

	Clamp translation							
$#	tranid							
	400							
$#	option	a1	a2	a3	a4	a5	a6	a7
	TRANSL	-1.6	-1.2	0	0	0	0	0

```
*ALE_MULTI-MATERIAL_GROUP
$#         sid      idtype      gpname
           100           1         Air
            10           1   Explosive
*CONSTRAINED_LAGRANGE_IN_SOLID_TITLE
$#      coupid       title
           310 Plate in air
$#      Slave      master       sstyp       mstyp       nquad       ctype       direc       mcoup
           200         110           1           0           2           4           2           0
$#      start         end        pfac        fric      frcmin        norm     normtyp        damp
             0  1.00E+10         0.1         0.4         0.5           0           0           0
$#         cq        hmin        hmax       ileak       pleak     lcidpor       nvent    blockage
             0           0           0           2         0.1           0           0           0
$#     iboxid     ipenchk     intforc     ialesof      lagmul      pfacmm        thkf
             0           0           0           0           0           0           0
*CONSTRAINED_LAGRANGE_IN_SOLID_TITLE
$#      coupid       title
           410 Box in air
$#      slave      master       sstyp       mstyp       nquad       ctype       direc       mcoup
           300         110           0           0           2           4           3           0
$#      start         end        pfac        fric      frcmin        norm     normtyp        damp
             0  1.00E+10         0.1           0         0.5           0           0           0
$#         cq        hmin        hmax       ileak       pleak     lcidpor       nvent    blockage
             0           0           0           0         0.1           0           0           0
$#     iboxid     ipenchk     intforc     ialesof      lagmul      pfacmm        thkf
             0           0           0           0           0           0           0
*SET_MULTI_MATERIAL_GROUP_LIST_TITLE
       Air & explosive
$#     ammsid
           110
$#   ammgid1     ammgid2     ammgid3     ammgid4     ammgid5     ammgid6     ammgid7     ammgid8
             1           2           0           0           0           0           0           0
*INCLUDE
$#    filename
      air.k
*INCLUDE_TRANSFORM
$#    filename
      plate.k
$#       idnoff      ideoff      idpoff      idmoff      idsoff      idfoff      iddoff
         3000000     3000000           0           0           0           0           0
$#       idroff
             0
$#      fctmas      fcttim      fctlen      fcttem     incout1      unused
             1           1           1           1           1
$#      tranid
             0
```

```
*INCLUDE_TRANSFORM
$#     filename
       box.k
$#      idnoff      ideoff      idpoff      idmoff      idsoff      idfoff      iddoff
      4000000     4000000           0           0           0           0           0
$#      idroff
           0
$#      fctmas      fcttim      fctlen      fcttem     incout1      unused
           1           1           1           1           1
$#      tranid
           0
*INCLUDE_TRANSFORM
$#     filename
       clamp.k
$#      idnoff      ideoff      idpoff      idmoff      idsoff      idfoff      iddoff
      5000000     5000000           0           0           0           0           0
$#      idroff
           0
$#      fctmas      fcttim      fctlen      fcttem     incout1      unused
           1           1           1           1           1
$#      tranid
         400
*END
```

```
*TITLE
$#    air.k
LS-DYNA keyword deck by LS-Prepost
*PART
$#                title
       Air block
$#                pid       secid         mid       eosid        hgid        grav     adpopt        tmid
                  100         110         100         100         110           0          0           0
$#                title
       Explosive
$#                pid       secid         mid       eosid        hgid        grav     adpopt        tmid
                   10         110          10          10         110           0          0           0
*SECTION_SOLID_TITLE
       Solid MMALE
$#             secid      elform         aet
                110          11           0
*MAT_NULL_TITLE
       Air
$#                mid          ro          pc          mu       terod       cerod          ym          pr
                  100    1.00E-03           0           0           0           0           0           0
```

```
*MAT_HIGH_EXPLOSIVE_BURN_TITLE
     PE4 EOS
$#              mid                ro                 d               pcj              beta                 k                 g              sigy
                 10          0.001601              8193             28000                 0                 0                 0                 0
*EOS_LINEAR_POLYNOMIAL_TITLE
     Air EOS
$#            eosid                c0                c1                c2                c3                c4                c5                c6
                100                 0                 0                 0                 0               0.4               0.4                 0
$#               e0                v0
            0.2533                 1
*EOS_JWL_TITLE
     PE4 EOS
$#            eosid                 a                 b                r1                r2              omeg                e0                vo
                 10            609770             12950               4.5               1.4              0.25              9000                 1
*HOURGLASS_TITLE
     Standard HG
$#             hgid               ihq                qm               ibq                q1                q2            qb/vdc                qw
                110                 2          1.0E-06                 0               1.5              0.06               0.1               0.1
*SET_PART_LIST_TITLE
     Air & explosive
$#              sid               da1               da2               da3               da4            solver
                110                 0                 0                 0                 0              MECH
$#             pid1              pid2              pid3              pid4              pid5              pid6              pid7              pid8
                 10               100                 0                 0                 0                 0                 0                 0
*SET_NODE_LIST_TITLE
     XY Symmetry
$#              sid               da1               da2               da3               da4            solver
                101                 0                 0                 0                 0              MECH
*END
```

```
*TITLE
$#  plate.k
LS-DYNA keyword deck by LS-Prepost
*PART
$#                title
     Plate
$#              pid             secid               mid             eosid              hgid              grav           adpopt              tmid
                200               200               200                 0                 0                 0                 0                 0
*SECTION_SHELL_TITLE
     Shell section
$#            secid            elform              shrf               nip             propt           qr/irid             icomp             setyp
                200                 2                 1                 2                 1                 0                 0                 1
$#               t1                t2                t3                t4              nloc            marea              idof            edgset
                 2                 2                 2                 2                 1                 0                 0                 0
```

*MAT_JOHNSON_COOK_TITLE
Aluminium JC

$#	mid	ro	g	e	pr	dtf	vp	rateop
	200	0.0027	27000	70000	0.33	0	0	0
$#	a	b	n	c	m	tm	tr	epso
	160.5	339.8	0.5206	0.003	2.519	600	298.15	3.33E-07
$#	cp	pc	spall	it	d1	d2	d3	d4
	900	0	2	0	0	0	0	0
$#	d5	c2/p	erod	efmin	numint			
	0	0	1.00E-06	0				

*SET_NODE_LIST_TITLE
Nodout nodes of plate

$#	sid	da1	da2	da3	da4	solver
	200	0	0	0	0	MECH

*SET_NODE_LIST_TITLE
XY Symmetry

$#	sid	da1	da2	da3	da4	solver
	201	0	0	0	0	MECH

*SET_SEGMENT_TITLE
Clamped region on plate

$#	sid	da1	da2	da3	da4	solver
	202	0	0	0	0	MECH

*END

*TITLE
$# box.k
LS-DYNA keyword deck by LS-Prepost
*PART
$# title
Main

$#	pid	secid	mid	eosid	hgid	grav	adpopt	tmid
	301	300	300	0	0	0	0	0

$# title
Side1

$#	pid	secid	mid	eosid	hgid	grav	adpopt	tmid
	302	300	300	0	0	0	0	0

$# title
Flange1

$#	pid	secid	mid	eosid	hgid	grav	adpopt	tmid
	303	300	300	0	0	0	0	0

$# title
Side2

$#	pid	secid	mid	eosid	hgid	grav	adpopt	tmid
	304	300	300	0	0	0	0	0

```
$#                title
      Flange2
$#              pid      secid        mid      eosid       hgid       grav     adpopt       tmid
                305        300        300          0          0          0          0          0
*SECTION_SOLID_TITLE
      Solid
$#            secid     elform        aet
                300          1          0
*MAT_ELASTIC_TITLE
      Steel
$#              mid         ro          e         pr         da         db   not used
                300    0.00785     210000        0.3          0          0          0
*SET_PART_LIST_TITLE
      ULD box
$#              sid        da1        da2        da3        da4     solver
                300          0          0          0          0       MECH
$#             pid1       pid2       pid3       pid4       pid5       pid6       pid7       pid8
                301        302        303        304        305          0          0          0
*SET_NODE_LIST_TITLE
      Fixed nodes of box
$#              sid        da1        da2        da3        da4     solver
                301          0          0          0          0       MECH
*SET_SEGMENT_TITLE
      Clamped region of flange
$#              sid        da1        da2        da3        da4     solver
                302          0          0          0          0       MECH
*END
```

```
*TITLE
$#    clamp.k
LS-DYNA keyword deck by LS-Prepost
*PART
$#                title
      Clamp
$#              pid      secid        mid      eosid       hgid       grav     adpopt       tmid
                400        400        400          0          0          0          0          0
*SECTION_SOLID_TITLE
      Solid
$#            secid     elform        aet
                400          1          0
*MAT_ELASTIC_TITLE
      Steel
$#              mid         ro          e         pr         da         db   not used
                400    0.00785     210000        0.3          0          0          0
```

```
*SET_NODE_LIST_TITLE
      Fixed nodes of clamp
 $#             sid       da1       da2       da3       da4     solver
               401         0         0         0         0      MECH
*SET_SEGMENT_TITLE
      Clamped region on clamp
 $#             sid       da1       da2       da3       da4     solver
               402         0         0         0         0      MECH
*END
```

```
*TITLE
 $#   restart.k
LS-DYNA keyword deck by LS-Prepost
*CONTROL_TERMINATION
 $#     endtim    endcyc     dtmin    endeng    endmas      nosol
         3.00         0         0         0 1.00E+08
*DATABASE_BINARY_D3PLOT
 $#        dt      lcdt      beam      npltc     psetid
        0.200         0         0         0         0
 $#     ioopt
         0.0
*DELETE_FSI
 $#      id1       id2       id3       id4       id5       id6       id7       id8
        310       410         0         0         0         0         0         0
*DELETE_PART
 $#      id1       id2       id3       id4       id5       id6       id7       id8
        100        10         0         0         0         0         0         0
*END
```

This page is intentionally left blank.

Appendix C Tension Test Simulation Input Deck

The tension test simulation was performed to assess the accuracy of the material model at representing the response of the aluminium. An implicit solver was used to develop the simulation because of the long duration of the quasi-static tension test. A single keyword file was used since only one part (the test specimen) was present in the simulation. The input deck of the tension test simulation is presented here.

```
LS-DYNA keyword deck by LS-Prepost
*CONTROL_IMPLICIT_AUTO
$#     iauto     iteopt     itewin      dtmin      dtmax      dtexp     kfail    kcycle
         1         11          5          0       5000          0         0         0
*CONTROL_IMPLICIT_GENERAL
$#   imflag        dt0     imform       nsbs        igs      cnstn      form    zero_v
         1          5          2          1          2          0         0         0
*CONTROL_IMPLICIT_SOLUTION
$#   nsolvr     ilimit     maxref      dctol      ectol      rctol     lstol    abstol
         2         11         15      0.001       0.01   1.00E+10       0.9  1.00E-10
$#   dnorm     diverg      istif    nlprint    nlnorm     d3itctl    cpchk
         2          1          1          0          2          0         0
$#   arcctl     arcdir     arclen     arcmth     arcdmp     arcpsi    arcalf    arctim
         0          0          0          1          2          0         0         0
$#   lsmtd      lsdir       irad       srad       awgt       sred
         1          2          0          0          0          0
*CONTROL_IMPLICIT_SOLVER
$#   lsolvr     lprint      negev      order       drcm     drcprm   autospc   autotol
         4          2          2          0          4          0         1         0
$#   lcpack     mtxdmp
         2          0
*CONTROL_TERMINATION
$#   endtim     endcyc       dtmin     endeng     endmas
      600000          0          0          0   1.00E+08
*DATABASE_NODFOR
$#       dt     binary       lcur      ioopt
      10000          0          0          1
*DATABASE_NODOUT
$#       dt     binary       lcur      ioopt    option1    option2
      10000          0          0          1          0          0
*DATABASE_BINARY_D3PLOT
$#       dt       lcdt       beam      npltc     psetid
      10000          0          0          0          0
$#    ioopt
         0
*DATABASE_NODAL_FORCE_GROUP
$#     nsid        cid
       300          0
*DATABASE_HISTORY_NODE_SET
$#      id1        id2        id3        id4        id5        id6       id7       id8
       300          0          0          0          0          0         0         0
*BOUNDARY_PRESCRIBED_MOTION_SET_ID
$#       id    heading
       300    Tensile test strain rate
$#     nsid        dof        vad       lcid         sf        vid     death     birth
       300          1          0       1000          1          0  1.00E+28         0
```

*BOUNDARY_SPC_SET

$#	nsid	cid	dofx	dofy	dofz	dofrx	dofry	dofrz
	100	0	0	1	0	1	0	1
	200	0	1	0	0	0	1	1
	400	0	0	0	1	0	0	0

*SET_NODE_LIST_TITLE

XZ Symmetry

$#	sid	da1	da2	da3	da4	solver
	100	0	0	0	0	MECH

YZ Symmetry

$#	sid	da1	da2	da3	da4	solver
	200	0	0	0	0	MECH

Nodes in motion

$#	sid	da1	da2	da3	da4	solver
	300	0	0	0	0	MECH

Out-of-plane motion

$#	sid	da1	da2	da3	da4	solver
	400	0	0	0	0	MECH

*PART

$#	title

Tensile specimen

$#	pid	secid	mid	eosid	hgid	grav	adpopt	tmid
	1	1	1	0	0	0	0	0

*SECTION_SHELL

$#	secid	elform	shrf	nip	propt	qr/irid	icomp	setyp
	1	2	1	5	1	0	0	1
$#	t1	t2	t3	t4	nloc	marea	idof	edgset
	2	2	2	2	0	0	0	0

*MAT_JOHNSON_COOK_TITLE

Johnson-Cook AA5754h22

$#	mid	ro	g	e	pr	dtf	vp	rateop
	1	0.0027	27000	70000	0.33	0	0	0
$#	a	b	n	c	m	tm	tr	epso
	160.5	339.8	0.5206	0.003	2.519	600	298.15	3.33E-07
$#	cp	pc	spall	it	d1	d2	d3	d4
	900	0	2	0	0	0	0	0
$#	d5	c2/p	erod	efmin				
	0	0	1.00E-06					

*DEFINE_CURVE_TITLE

Velocity curve

$#	lcid	sidr	sfa	sfo	offa	offo	dattyp	lcint
	1000	0	1	1	0	0	0	0
$#	a1	o1						
	0	-8.33E-06						
	600000	-8.33E-06						

*END

This page is intentionally left blank.

Appendix D Detailed Drawings for Manufacturing

The detailed drawings of the ULD box assembly and components are presented in this section. These include:

- Assembly of fully-confined test rig
- Assembly of ULD box
- ULD box assembly instructions
- Flange detailed drawing
- Side panel detailed drawing
- Front panel detailed drawing
- Back panel detailed drawing
- Bottom panel detailed drawing
- Top panel detailed drawing

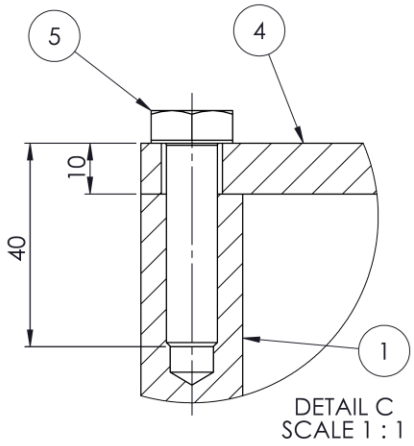

DETAIL C
SCALE 1 : 1

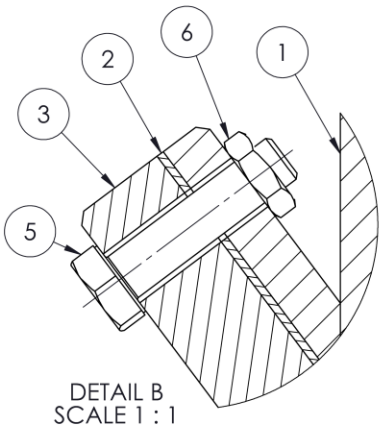

DETAIL B
SCALE 1 : 1

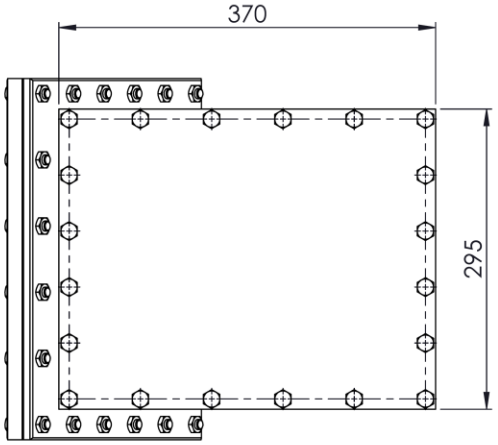

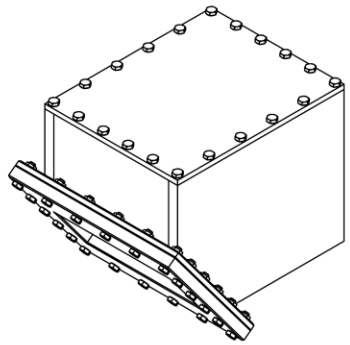

SCALE 1 : 8

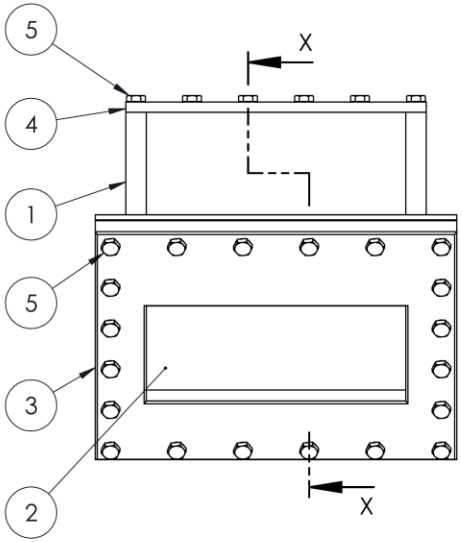

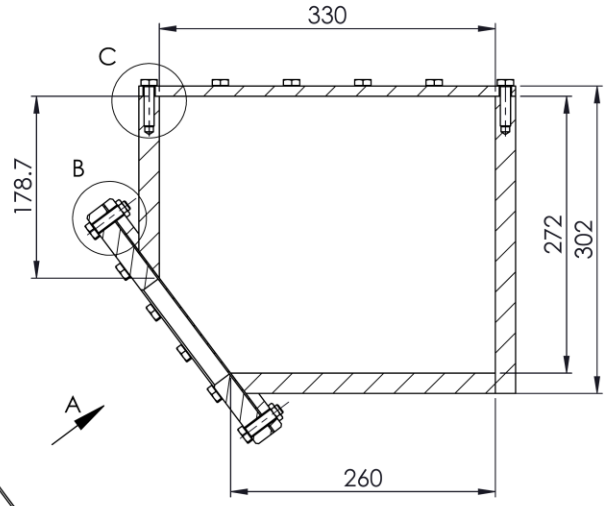

SECTION X-X

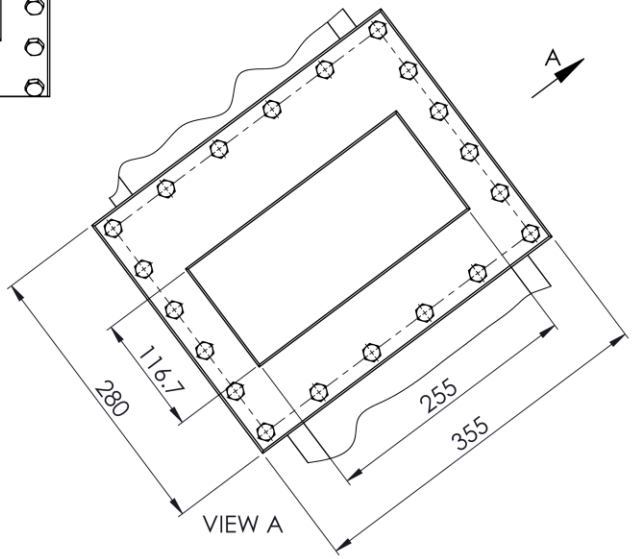

VIEW A

TOTAL MASS = 82.0 kg

ITEM NO.	PART	DESCRIPTION	QTY.
6	ISO - 4035 - M10 - N	M10 HEX NUTS	20
5	ISO 4017 - M10 x 40-N	M10 HEX BOLTS	40
4	Top Plate	MILD STEEL	1
3	Clamp Frame	MILD STEEL	1
2	Aluminium Plate	ALUMINIUM	1
1	Box Assembly	MILD STEEL	1

A3 Landscape	University of Cape Town Department of Mechanical Engineering			
	Title: ULD Assembly			
	All dimensions in mm			
Assembly Drawing	Scale: 1:5	Date: 2017/05/04	Sheet1	of 1
	Drawn By: Shaun Kriek 079 958 7542		Drawing Number DG1	

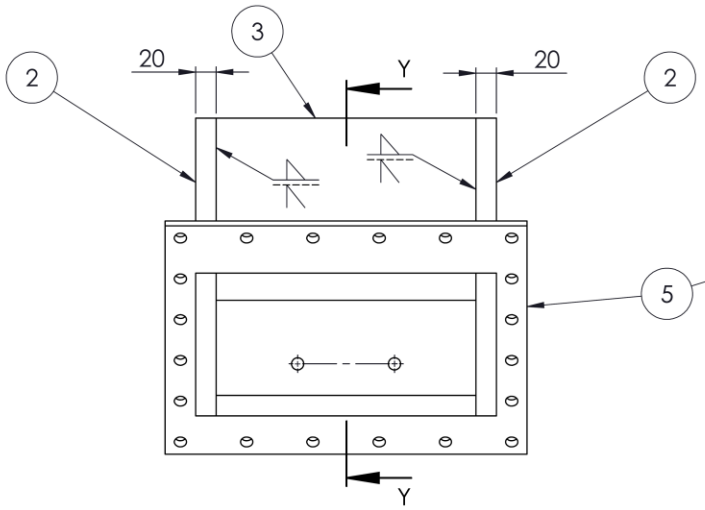

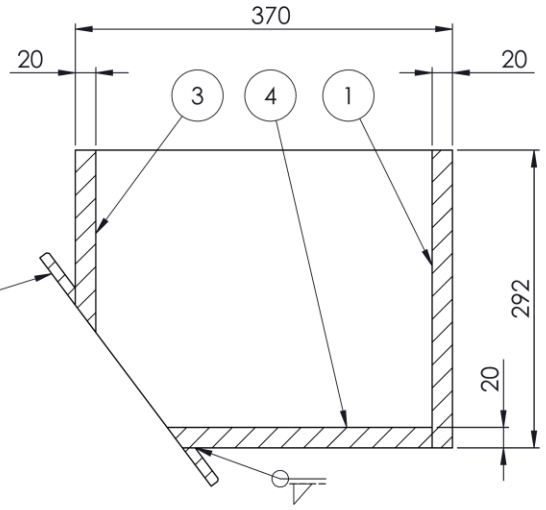

SECTION Y-Y

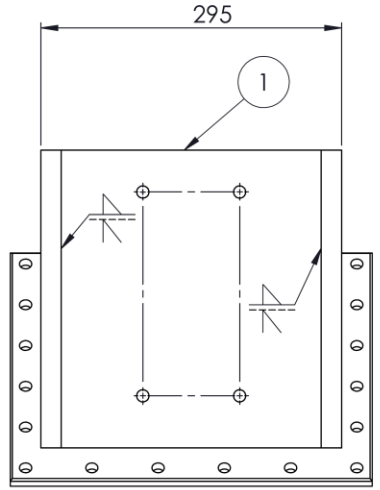

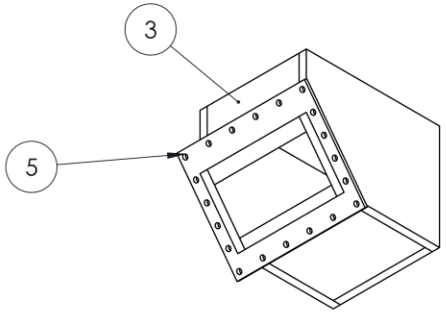

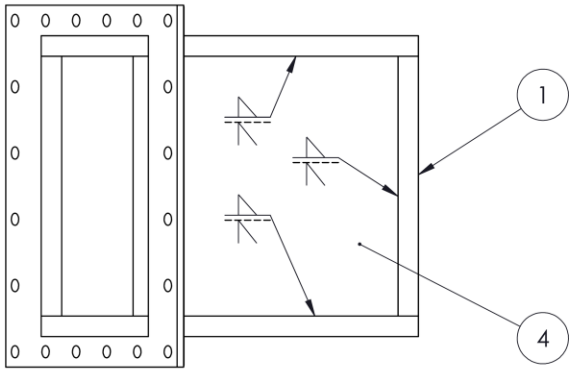

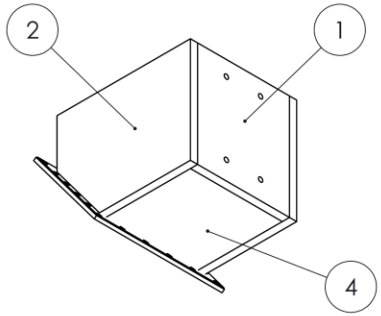

TOTAL MASS = 62.6 kg

ITEM NO.	PART NUMBER	DESCRIPTION	QTY.
5	Flange	MILD STEEL	1
4	Bottom Plate	MILD STEEL	1
3	Front Plate	MILD STEEL	1
2	Side Plate	MILD STEEL	2
1	Back Plate	MILD STEEL	1

A3 Landscape	University of Cape Town Department of Mechanical Engineering		
	Title: Box Assembly		
	All dimensions in mm		
Assembly Drawing	Scale: 1:5	Date: 2017/05/04	Sheet1 of 1
	Drawn By: Shaun Kriek 079 958 7542		Drawing Number DG1.1

1

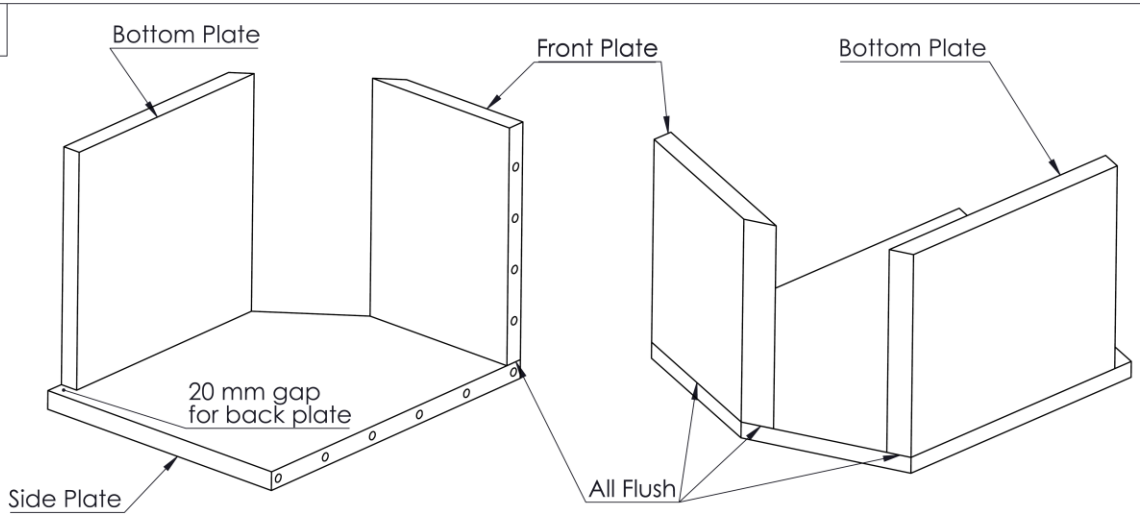

2

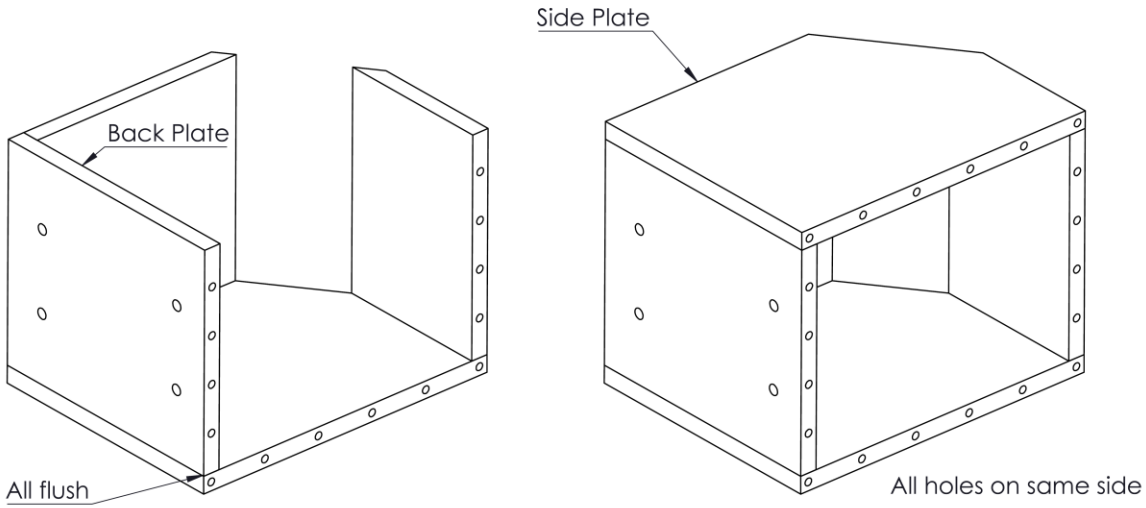

3

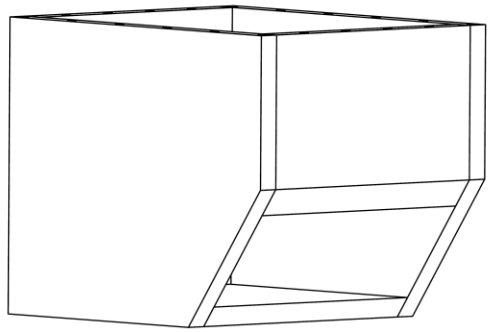

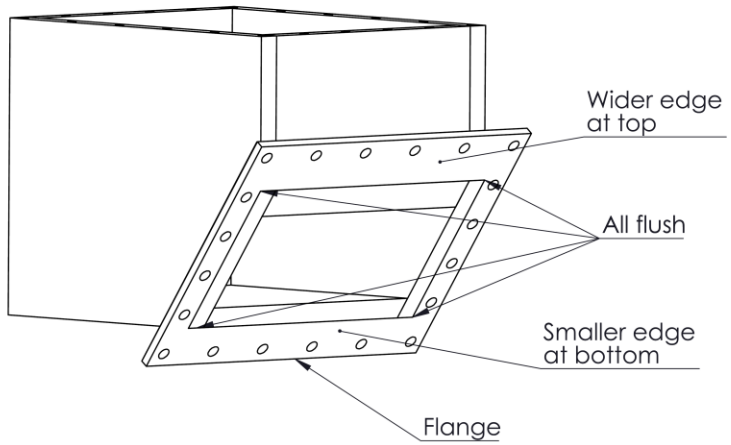

A3 Landscape	University of Cape Town Department of Mechanical Engineering			
	Title: Box Assembly			
Part Finish	Scale: 1:5	Date: 2018/11/08	Sheet1	of 1
Material: Mild Steel	Drawn By: Shaun Kriek 079 958 7542		Drawing Number DG05	

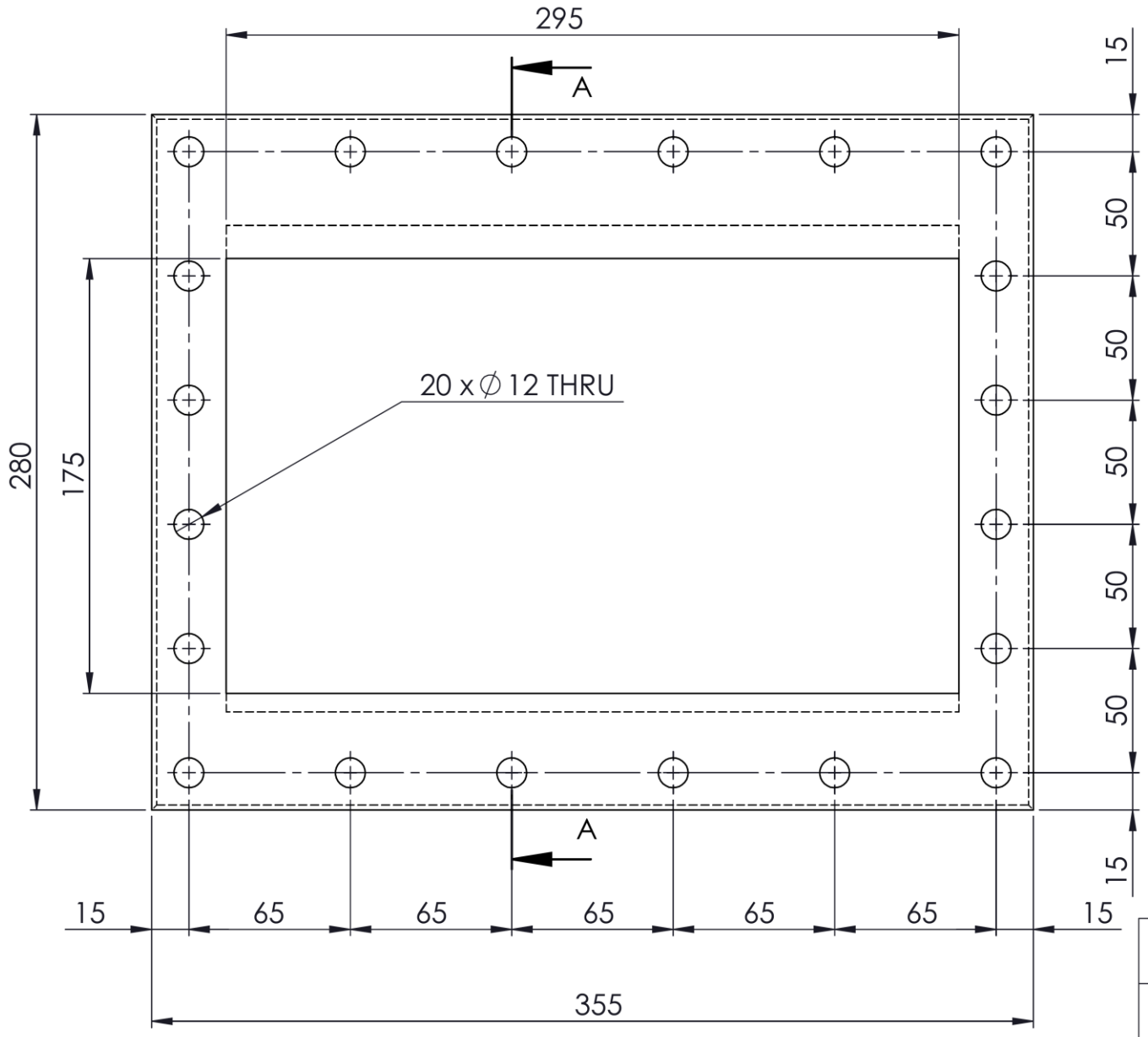

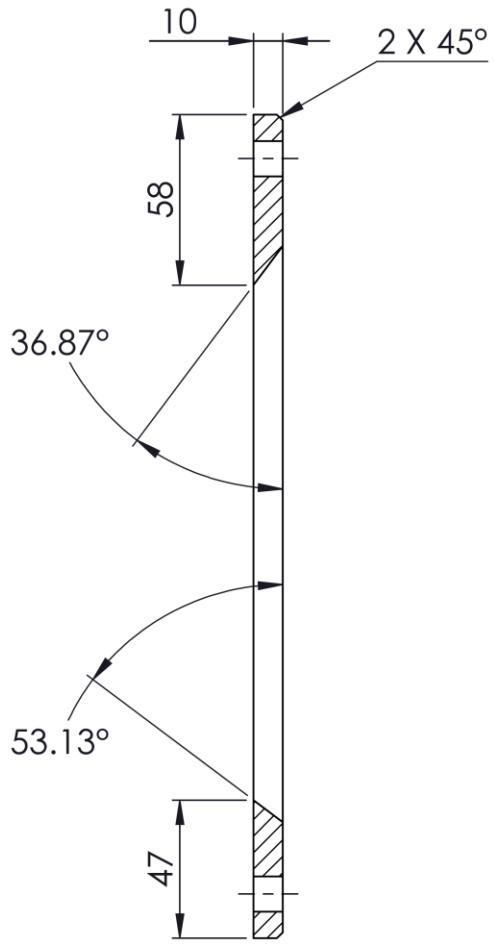

SECTION A-A

A4 Landscape	University of Cape Town Department of Mechanical Engineering			
	Title: Flange			
	All dimensions in mm			
Part Finish	Scale: 1:5	Date: 2018/11/08	Sheet1	of 1
Material:	Drawn By: Shaun Kriek 079 958 7542		Drawing Number DG1.1.5	

QTY: 2

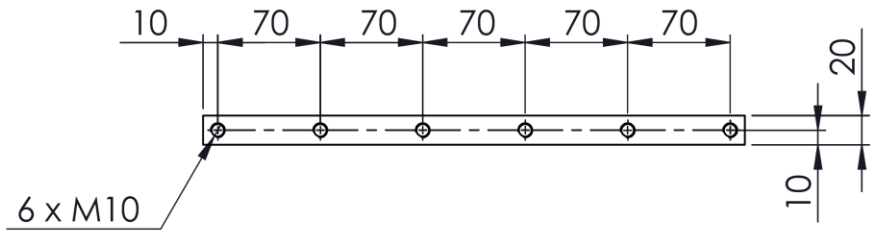

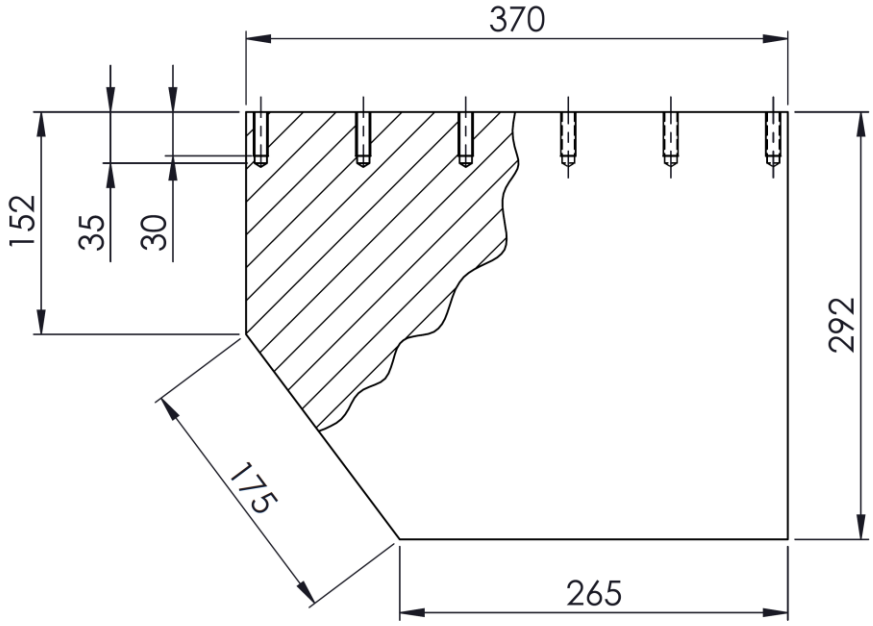

MASS = 15.6 KG

A4 Landscape	University of Cape Town Department of Mechanical Engineering			
	Title: Side Plate			
	All dimensions in mm			
Part Finish	Scale: 1:5	Date: 2018/11/08	Sheet1	of 1
Material:	Drawn By: Shaun Kriek 079 958 7542		Drawing Number DG1.1.2	

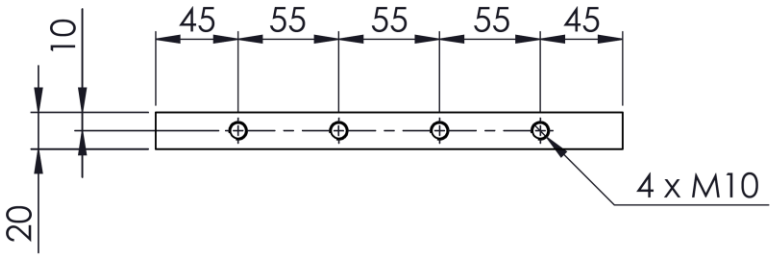

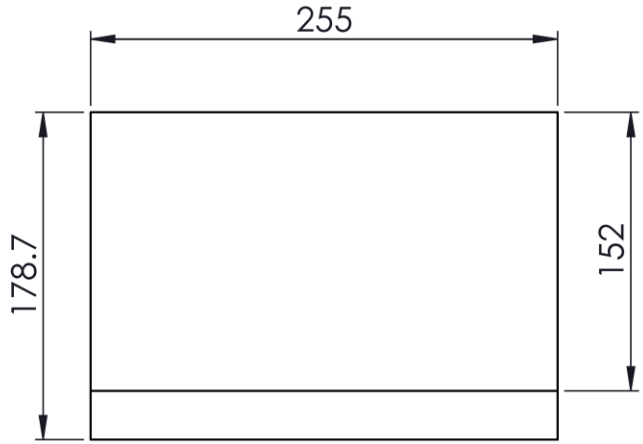

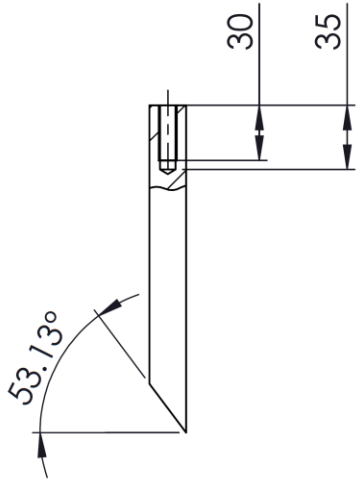

MASS = 6.51 KG

A4 Landscape	University of Cape Town Department of Mechanical Engineering			
	Title: Front Plate			
	All dimensions in mm			
Part Finish	Scale: 1:4	Date: 2018/11/08	Sheet1	of 1
Material:	Drawn By: Shaun Kriek 079 958 7542		Drawing Number DG1.1.3	

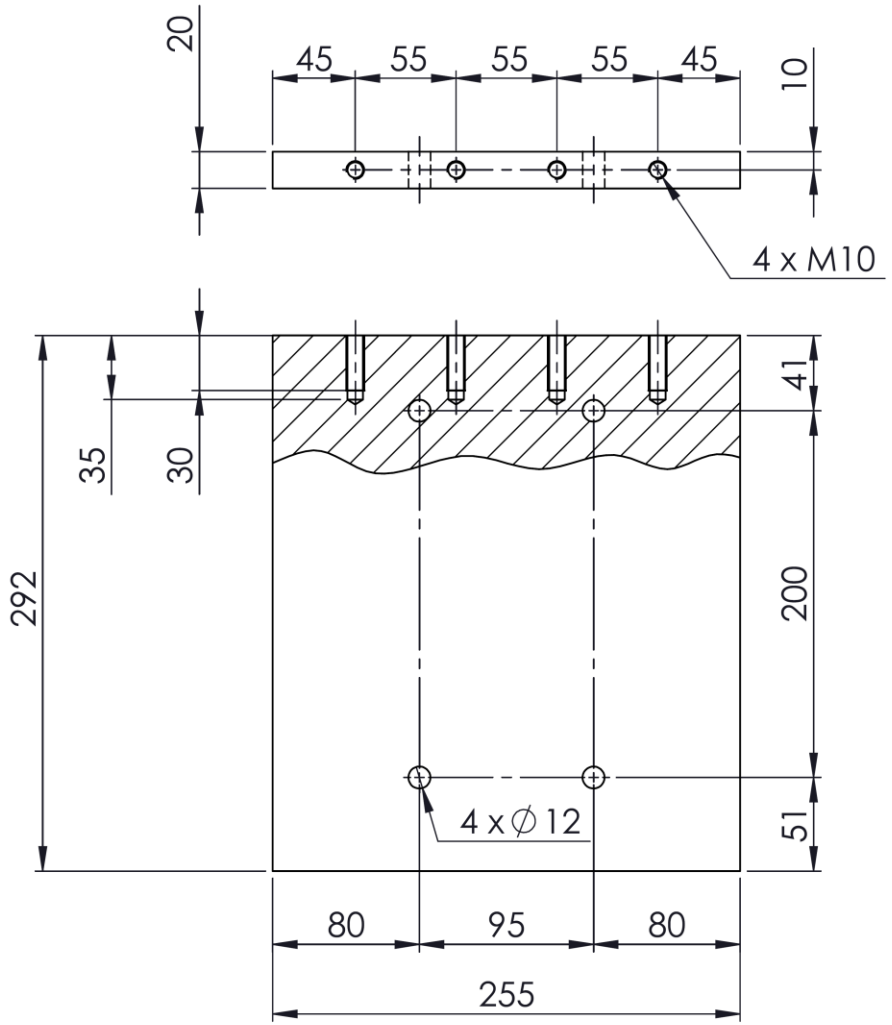

MASS = 11.5 KG

A4 Landscape	University of Cape Town Department of Mechanical Engineering			
	Title: Back Plate			
	All dimensions in mm			
Part Finish	Scale: 1:4	Date: 2018/11/08	Sheet1	of 1
Material:	Drawn By: Shaun Kriek 079 958 7542		Drawing Number DG1.1.1	

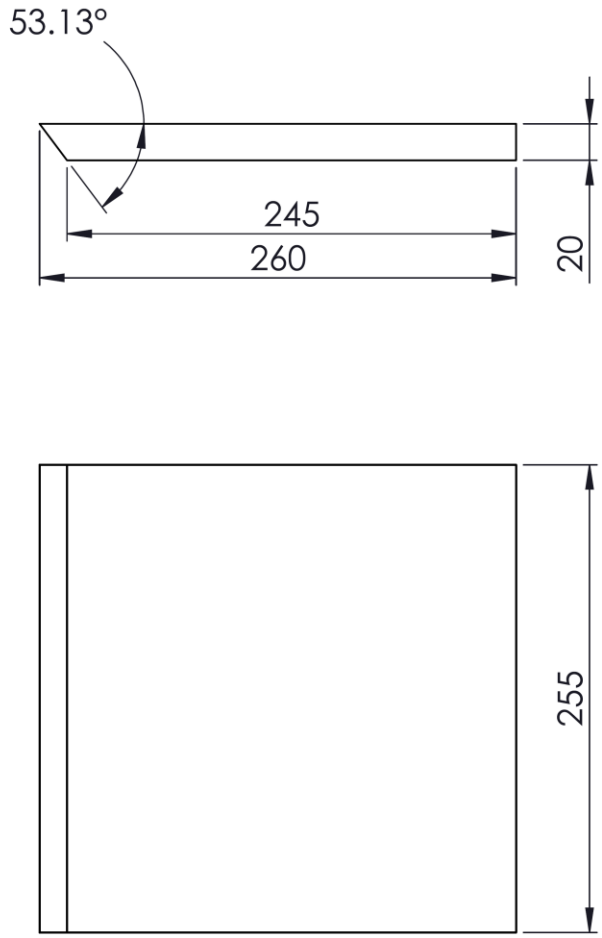

MASS = 10.0 KG

A4 Landscape	University of Cape Town Department of Mechanical Engineering			
	Title: Bottom Plate			
	All dimensions in mm			
Part Finish	Scale: 1:4	Date: 2018/11/08	Sheet1	of 1
Material:	Drawn By: Shaun Kriek 079 958 7542		Drawing Number DG1.1.4	

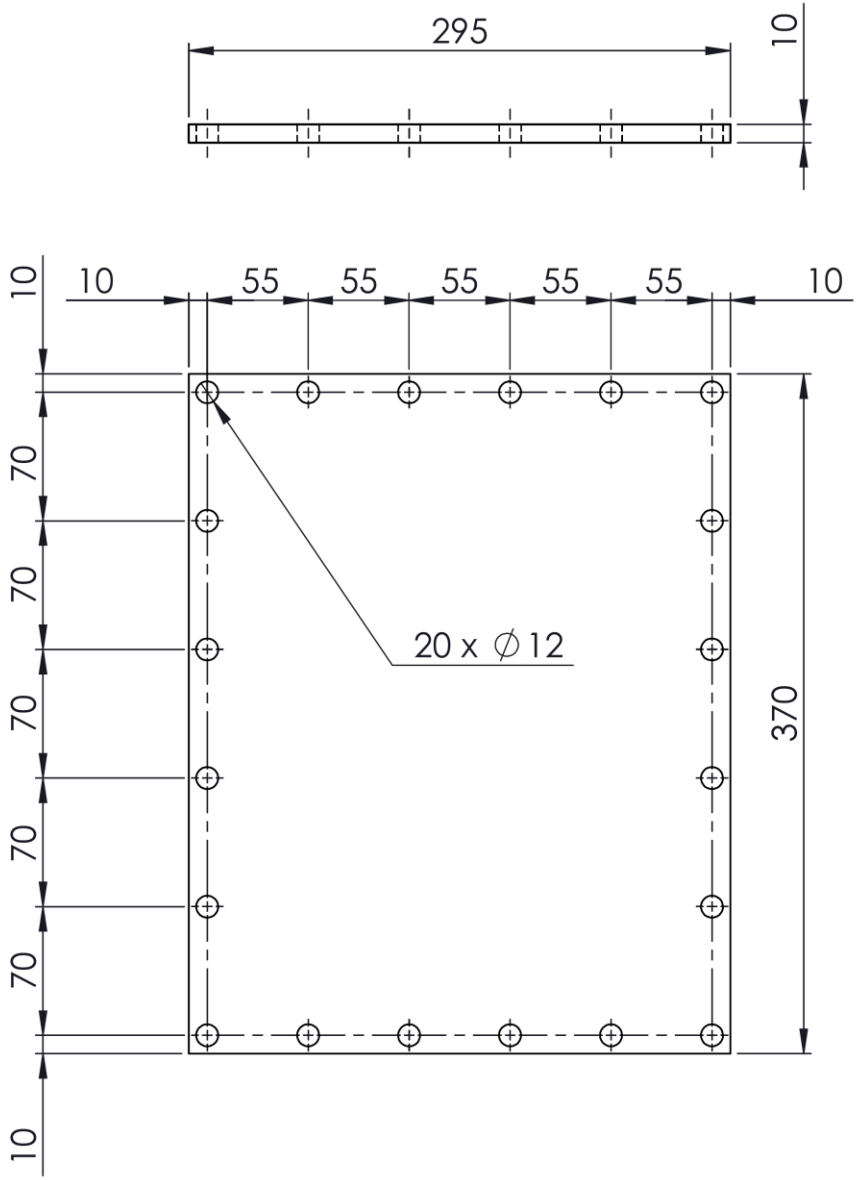

MASS = 8.34 KG

A4 Landscape	University of Cape Town Department of Mechanical Engineering			
	Title: Top Plate			
	All dimensions in mm			
Part Finish	Scale: 1:4	Date: 2018/11/08	Sheet1	of 1
Material:	Drawn By: Shaun Kriek 079 958 7542		Drawing Number DG1.4	